Dublin City University
School of Physical Sciences

Growth and characterisation studies of MgO and Mg silicate dielectric layers on Si and InP surfaces

Patrick Casey B.Sc.
Doctor of Philosophy

April 2010

Supervised by Professor Greg Hughes

Dedications and Acknowledgements

Firstly and most importantly I would like to thank my family, in particular my mother, for the help and support they have given me throughout my education.

I would also like to thank my supervisor Greg Hughes for all of his help and everything he has taught me, and especially for the respect and lack of restrictions he placed on me during the project.

I would like to express my gratitude to everyone in DCU, Barry, Stephen, Justin, Sergey, Ian, Rob, Catherine, Kumar, for the help they gave me during the project but in particular for the craic we had everyday and for ensuring that I always looked forward to coming to work. I would also like to thank everyone in the Tyndal institute in Cork, especially Paul, Éamon, Rathnait, Karim and Enrique for helping me and teaching me so much. I would also like to thank Simon Newcombe in Glebe Scientific for TEM analysis.

I would like to thank all my friends in Dublin and in Waterford, especially Paddy, Zack and Wayne for their friendship throughout all the years up in Dublin.

Finally I would like to acknowledge the Irish Research Council for Science Engineering and Technology and Intel Ireland for the financial support of this work.

Declaration

I hereby certify that this material, which I now submit for assessment on the program of study leading to the award of doctor of Philosophy is entirely my own work and has not been taken from the work of others save and to the extent that such work has been cited and acknowledged within the text of my work.

Signed:_______________________________________(Candidate)

ID No.: 56114346

Date:_________________________

Abstract

This thesis investigates the suitability of magnesium oxide (MgO) and magnesium silicate as possible high-*k* dielectric materials on both silicon and indium phosphide (InP) surfaces. Given that the emphasis of this study was controlling the semiconductor/high-*k* interface formation, the principle experimental technique used in these studies was x-ray photoelectron spectroscopy (XPS), however, additional techniques such as atomic force microscopy (AFM) and electrical characterisation have also been employed. XPS studies have shown that exposure to ambient conditions results in the rapid formation of magnesium hydroxide and carbonate species on the surface of MgO thin films. In order to prevent the detrimental affect of ambient exposure MgO/Si MOS devices were fabricated using an optimised metallisation procedure, called the FUSI process. Electrical characterisation of FUSI devices show low ($< 10^{12}$ cm^{-2}) interfacial state densities, and allowed the dielectric constant of MgO (~10) to be calculated. Transmission electron microscopy (TEM) and high resolution synchrotron based XPS have identified the presence of thin (< 1 nm) amorphous magnesium silicate layers at the MgO/Si interface. Studies show no evidence for the formation of SiO_2 upon MgO deposition with Mg silicate forming preferentially following MgO deposition onto both H-terminated and oxidised Si surfaces, and also following high temperature annealing. The mechanism by which Si oxide surfaces can be converted into Mg silicate has also been investigated. It has been shown that room temperature deposition of metallic Mg results in the formation of Mg silicide which decomposes during UHV annealing at 300 °C. Subsequent annealing to 500 °C results in the complete conversion of SiO_2 to Mg silicate. As Mg silicide growth has been shown to be a vital intermediate step to silicate formation, the growth and stability of Mg silicide thin films on Si has also been investigated. InP studies have focused on the preparation of oxide free, chemically stable surfaces prior to MgO deposition. The effectiveness of different chemical wet etch preparation procedures are compared to that of *in-situ* atomic hydrogen cleaning based on both the removal of oxide species and the chemical stability of the cleaned surface. The deposition of Si and Mg silicate interfacial control layers (ICL) onto InP has been shown to effectively passivate the InP surface, inhibiting the growth of In and P oxide species upon MgO deposition and subsequent 500 °C annealing.

Publications arising from this work

Interfacial analysis of InP surface preparation using atomic hydrogen cleaning and Si interfacial control layers prior to MgO deposition

P. Casey, G. Hughes

Applied Surface Science (2010) Available on-line from June 2010.

Photoemission study of the SiO_2 conversion mechanism to magnesium silicate

P. Casey, G. Hughes

Journal of Applied Physics **107** (2010) 074107

Growth, ambient stability and electrical characterisation of MgO thin films on silicon surfaces

P. Casey, É. O'Connor, R. Long, B. Brennan, S.A. Krasnikov, D. O'Connell, P.K. Hurley and G. Hughes

Microelectronic Engineering, **86** (2009) 1711-1714

Growth and Characterisation of Thin MgO Layers on Si (100) surfaces

P. Casey, É. O'Connor, R. Long, P.K. Hurley and G. Hughes

Journal of Physics: Conference Series **100** (2008) 042046

Structural analysis, elemental profiling, and electrical characterization of HfO2 thin films deposited on In0.53Ga0.47As surfaces by atomic layer deposition

R.D. Long, É. O'Connor, S.B. Newcomb, S. Monaghan, K. Cherkaoui, P. Casey, G. Hughes, K.K. Thomas, F. Chalvet, I. M. Povey, M.E. Pemble, P.K. Hurley

Journal of Applied Physics **106** (2009) 084508

Degradation and breakdown characteristics of thin MgO dielectric layers

R. O'Connor, G. Hughes, P. Casey, S. Newcombe

Journal of Applied Physics **107** (2010) 024501

Electrical characterization of the soft breakdown failure mode in MgO layers

E. Miranda, É. O'Connor, K. Cherkaoui, S. Monaghan, R. Long, D. O'Connell, P.K. Hurley, G. Hughes, P. Casey

Applied Physics Letters **95** (2009) 012901

Degradation dynamics and breakdown of MgO gate oxides

E. Miranda, É. O'Connor, G. Hughes, P. Casey, K. Cherkaoui, S. Monaghan, R. Long, D. O'Connell, P.K. Hurley

Microelectronic Engineering **86** (2009) 1715–1717

Effects of the electrical stress on the conduction characteristics of metal gate/MgO/InP stacks

E. Miranda, J. Martin-Martinez, É. O'Connor, G. Hughes, P. Casey, K. Cherkaoui, S. Monaghan, R. Long, D. O'Connell, P.K. Hurley

Microelectronics Reliability **49** (2009) 1052–1055

Publications in Preparation

High Resolution Photoemission Study of Mg Silicide Formation and Thermal Stability on Si

P. Casey, G. Hughes

Thin Solid Films, Under Review

Table of Contents

Dedication and Acknowledgements.. 2

Declaration.. 3

Abstract.. 4

Publications arising from this work.. 5

Table of Contents... 7

Figure Captions... 10

1. **Introduction**……………………………………………………………… 23
    - 1.1. MOSFET operation…………………………………………………… 23
    - 1.2. Challenges facing transistor technology……………………………… 24
    - 1.3. Factors in considering high-*k* candidates……………………………... 27
    - 1.4. Alternative semiconductors to replace Si…………………………….. 31
    - 1.5. Thesis Layout and Organisation……………………………………… 32
    - 1.6. References……………………………………………………………… 34

2. **Principles of experimental techniques**………………………………….. 37
    - 2.1. X-ray photoelectron spectroscopy……………………………………. 37
        - 2.1.1. Basic Principles…………………………………………….. 37
        - 2.1.2. Element Identification……………………………………… 41
        - 2.1.3. Chemical Shifts…………………………………………….. 42
        - 2.1.4. Quantification………………………………………………. 43
        - 2.1.5. Depth Profiling using ARXPS……………………………… 44
        - 2.1.6. Thickness Calculations……………………………………… 45
    - 2.2. Synchrotron based photoemission……………………………………... 47
    - 2.3. Atomic Force Microscopy……………………………………………... 48
    - 2.4. Temperature programmed desorption………………………………… 51
    - 2.5. Transmission electron microscopy……………………………………. 52
    - 2.6. Electrical Characterisation…………………………………………… 53
        - 2.6.1. Capacitance – Voltage (C-V)……………………………….. 54
        - 2.6.2. Current-Voltage (I-V)……………………………………… 61
    - 2.7. References……………………………………………………………... 64

3. **Experimental Details**……………………………………………………... 67
    - 3.1. Ultra High Vacuum Chambers………………………………………... 67
    - 3.2. Deposition Techniques………………………………………………... 71
        - 3.2.1. Electron Beam Deposition………………………………….. 71
        - 3.2.2. Thermal/hot wire deposition………………………………… 73
    - 3.3. Spectral analysis of photoemission peaks…………………………….. 73
    - 3.4. Surface Preparation methods………………………………………….. 77
        - 3.4.1. Standard organic cleaning of semiconductor surfaces……… 77
        - 3.4.2. Flash cleaning………………………………………………. 78
        - 3.4.3. Atomic hydrogen cleaning………………………………….. 78
    - 3.5. MOS Device Fabrication……………………………………………… 79

3.6. Electrical Characterisation of MOS devices………………………….. 81
3.7. References……………………………………………………………...82

4. Characterisation of MgO as a high-*k* candidate on silicon…………….. 84
4.1. Introduction……………………………………………………………84
4.2. Experimental Procedure……………………………………………… 85
4.3. Initial electrical characterisation and ambient stability of MgO thin films on Silicon………………………………………………………………………... 86
4.3.1. Initial electrical characterisation of Pd/MgO/Si (100) MOS structures………………………………………………………………………86
4.3.2. The Growth and ambient stability of e-beam deposited MgO thin films on Si……………………………………………………………………..94
4.3.3. Conclusions…………………………………………………..102
4.4. Electrical Characterisation of MgO based MOS devices fabricated using the FUSI metallisation technique……………………………………………...103
4.4.1. Electrical Characterisation…………………………………... 103
4.4.2. TEM analysis………………………………………………... 107
4.4.3. Conclusions…………………………………………………..110
4.5. High Resolution Photoemission study of MgO film growth on H-terminated Si (111) and thermally grown ultra-thin silicon oxide surfaces………...110
4.5.1. MgO on H-terminated Si (111)………………………………110
4.5.2. MgO on ultra-thin thermally grown Si oxide……………….. 114
4.5.3. Conclusions…………………………………………………. 119
4.6. Chapter Conclusions…………………………………………………... 120
4.7. References……………………………………………………………...120

5. The growth mode and characterisation of magnesium silicate films formed on modified silicon surfaces……………………………………………... 126
5.1. Introduction……………………………………………………………126
5.2. Experimental Procedures……………………………………………… 127
5.3. The growth and thermal stability of Mg silicate on Si native oxide surfaces……………………………………………………………………….. 128
5.3.1. Photoemission study of the SiO_2 conversion mechanism to Mg silicate………………………………………………………………………... 128
5.3.2. High temperature annealing studies of thin Mg silicate films formed on Si native oxide surfaces……………………………………………... 138
5.3.3. Conclusions…………………………………………………. 141
5.4. The growth and stability of magnesium silicide films grown on Si….. 142
5.4.1. Mg Silicide thin film growth……………………………….... 143
5.4.2. Thermal Stability of Mg silicide on Si oxide surfaces……… 147
5.4.3. Thermal Stability of Mg silicide on H-terminated Si surfaces 149
5.4.4. Chemical Stability of Mg silicide…………………………… 152
5.4.5. Conclusions…………………………………………………. 156
5.5. Investigations into the growth parameters of magnesium silicate films on silicon surfaces……………………………………………………………….. 156
5.5.1. Growth of Mg silicate on Hydrogen Terminated Si (111) surfaces………………………………………………………………………. 157
5.5.2. Mg silicate growth on Si oxide films of greater thickness….. 161
5.5.3. Mg silicate growth on SiON surfaces……………………….. 163
5.5.4. Conclusions…………………………………………………. 165

5.6. Chapter Conclusions………………………………………………….. 166
5.7. References…………………………………………………………….. 167

6. **The effects of Oxide Removal and Chemical Modification of InP surfaces prior to MgO deposition**………………………………………………………… 173
6.1. Introduction………………………………………………………… 173
6.2. Experimental Procedures…………………………………………... 175
6.3. Photoemission and electrical characterisation of MgO films deposited onto InP native oxide and wet chemically etched surfaces………………………... 176
6.3.1. Composition and Stability of InP native oxide surfaces……. 176
6.3.2. Wet Chemical Etching……………………………………… 181
6.3.3. Electrical characterisation of MgO films on native oxide and wet chemically etched InP (100) surfaces……………………………………………… 187
6.3.4. Conclusions………………………………………………… 192
6.4. Atomic Hydrogen Cleaning of InP native oxide surfaces……………. 193
6.4.1. Oxide removal and chemical stability of the cleaned surface. 193
6.4.2. The effect of thermal annealing on the native oxide composition and surface roughness of InP…………………………………………………..... 201
6.4.3. Conclusions………………………………………………… 209
6.5. InP interface modification using Si interlayers………………………. 211
6.5.1. Si interfacial control layers on InP native oxide surface…… 212
6.5.2. InP interface Modification using Mg silicate interlayers…... 217
6.5.3. Conclusions………………………………………………… 223
6.6. Chapter Conclusions………………………………………………… 224
6.7. Appendix to Chapter 6……………………………………………….. 226
6.8. References…………………………………………………………… 228

7. **Conclusions and Future Work**………………………………………….. 235
7.1. Conclusions………………………………………………………….... 235
7.1.1. MgO thin films on Si………………………………………. 235
7.1.2. Growth of magnesium silicate thin films on Si…………….. 236
7.1.3. InP surface preparation methods…………………………… 237
7.2. Future Work………………………………………………………….. 239
7.2.1. MgO as part of gate oxide stack…………………………… 239
7.2.2. Electrical characterisation of Mg silicate thin films……….. 239
7.2.3. Electrical characterisation of Si ICL on InP………………... 240
7.3. References…………………………………………………………… 240

Figure Captions

Figure 1.1 Schematic diagram of a silicon n-type channel MOS transistor……….. 23

Figure 1.2 Application of a positive gate voltage induces negative charge carriers to gather at the semiconductor surface. This creates a conductive "n-type" channel, turning the transistor "On"………………………………………………………… 24

Figure 1.3 Diagram showing electron quantum tunnelling through a potential barrier. It can be seen that the probability of tunnelling is increased by reducing the thickness (d) of the barrier layer……………………………………………………………25

Figure 1.4 Energy band diagram illustrating the direct injection of charge carriers from the semiconductor to the dielectric layer. The work of John Robertson [8] has shown that band offsets less than 1 eV allow for high leakage currents, making the bandgap of the dielectric vital to device efficiency……………………………... 29

Figure 1.5 Plot showing that, in general, an inverse relationship exists between the bandgap and dielectric constant of many gate dielectric candidates [16]…………. 29

Figure 2.1 A schematic diagram showing the experimental set-up for conventional XPS [2]……………………………………………………………………….. 37

Figure 2.2 Energy level diagram for the photoemission process showing a sample and spectrometer in electrical contact [3]……………………………………………39

Figure 2.3 Universal mean free path (MFP) curve, showing a range of materials… 40

Figure 2.4 Survey scan taken from an air exposed 700 nm SiO_2 surface. By analysing the binding energy positions of the photoemission peaks the elements Si, O and C can be identified…………………………………………………………….… 41

Figure 2.5 Si 2p spectrum showing a 4 eV chemical shift between component peaks which indicates the presence of Si and SiO_2………………………………………… 42

Figure 2.6 O 1s and Mg 2p spectra taken from a 20 nm MgO thin film………….. 43

Figure 2.7 (A) Schematic diagram showing reduced sampling depth at angle θ. (B) Si 2p spectra taken from Si native oxide surface showing the increased surface sensitivity using ARXPS……………………………………………………….. 45

Figure 2.8 Schematic diagram showing how an electron beam emits synchrotron radiation when accelerated around the curved sections of a storage ring…………. 48

Figure 2.9 Operational diagram for AFM which shows how tip deflections are measured using laser light reflected from the back surface of the tip [16]…..…… 49

Figure 2.10 Typical TPD desorption curve [18]………………………………... 51

Figure 2.11 C-V characteristics of 5 nm MgO on p-type Si showing accumulation, depletion and inversion regions within the curve profile………………………….. 54

Figure 2.12 Energy band diagram for ideal p-type MOS capacitor……………….. 55

Figure 2.13 Application of a negative voltage on the metal gate causes the accumulation of holes at the semiconductor/oxide interface which results in a maximum capacitance value within the measured C-V profile…………………… 56

Figure 2.14 Energy band diagram showing depletion in MOS capacitors. Application of a positive voltage depletes the semiconductor surface of majority carriers……. 57

Figure 2.15 Inversion is achieved once the Fermi level at the semiconductor surface lies above the intrinsic level, forming an "inverted" n-type surface………………. 58

Figure 2.16 C-V profile, taken from 5 nm MgO on Si, showing "bump" due to interfacial defect states……………………………………………………………… 59

Figure 2.17 Frequency dispersions C-V profiles showing the increased interface state contribution with decreasing measurement frequency……………………………. 60

Figure 2.18 I-V characteristics of 20 nm MgO on p-type Si showing dielectric breakdown at ~ 17 V………………………………………………………………. 63

Figure 3.1 Three chambered dedicated XPS system shown in figure 3.1A. Surface analysis chamber in figure 3.1B is equipped with XPS, mass spectrometer, H-cracker, mini e-beam evaporator and thermal evaporation system………………………… 67

Figure 3.2 Diagram showing the operation of a dual anode X-ray source [1]…….. 68

Figure 3.3 Schematic diagram of an XPS analysis system, showing how electrons are focused into the analyser system [4]………………………………………..69

Figure 3.4 Diagram of the ASTRID synchrotron in Aarhus, Denmark……………70

Figure 3.5 Schematic diagram of e-beam deposition showing the generation of electrons which are accelerated towards the source material using high voltage and a system of electro magnets [6]……………………………………………………71

Figure 3.6 Diagram of the multi-pocket Oxford Applied Research EGC04 mini e-beam evaporator used in this study [7]…………………………………………….. 72

Figure 3.7 Raw and curve fitted Si 2p spectra taken from an ultra-thin Si oxide layer using SRXPS. Curve fitting allows contributions from bulk Si (Si^o) and each of the four silicon oxidation states to be identified……………………………………… 74

Figure 3.8 Raw and curve fitted Si 2p spectra taken from a Si native oxide surface using conventional XPS………………………………………………………… 76

Figure 3.9 Si 2p spectra taken from the same ultrathin SiO_x layer, using both synchrotron based and conventional XPS. Differences between the spectra clearly show the increased resolution & surface sensitivity achieved with SRXPS……… 77

Figure 3.10 Schematic diagram of the Applied Research TC-50 Thermal Gas Cracker. The capillary tube design allows for higher efficiency and lower temperature operation than the conventional W filament design……………………………….. 79

Figure 4.1 I-V characteristics taken from n-type (A) and p-type (B) Si(111)/20 nm MgO/Pd MOS structures, without post deposition anneal. The measurements are taken from films deposited on Si native oxide and hydrogen terminated Si surface..86

Figure 4.2 I-V characteristics taken from n-type (A) and p-type (B) Si(111)/5 nm MgO/Pd MOS structures, without post deposition anneal. The measurements are taken from films deposited on Si native oxide and hydrogen terminated Si surface..87

Figure 4.3 C-V characteristics taken from 20 nm and 5 nm MgO films deposited on n-type Si (100) native oxide (A) and H-terminated surfaces (B). High (>1 × 10^{12} cm^{-2}) interface state density) is indicated by "bumps" on C-V and frequency dispersion measurements taken from the 5 nm devices are also shown (inset)………………. 88

Figure 4.4 Native oxide (A) and H-terminated (B) p-type devices, corresponding to those shown in figure 4.3. Positive charge trapping is evidenced by large voltage shifts in the 5 nm and 20 nm devices……………………………………………… 90

Figure 4.5 Si 2p spectrum taken from 5 nm H-terminated n-type device showing the presence of a ~ 0.7 nm interfacial oxide……………………………………………92

Figure 4.6 O 1s and Mg 2p spectra, taken from a 20 nm MgO film on Si, showing the affects of 5 minute exposure to ambient conditions……………………………….. 94

Figure 4.7 Curve fitting of O 1s spectrum, taken after 5 minute ambient exposure, shows the presence of magnesium hydroxide and carbonate species………………95

Figure 4.8 Evolution of O 1s spectra showing the continual growth of hydroxide and carbonate species over an exposure period of 34 days…………………………..…96

Figure 4.9 Valence band and O 2s spectra taken from MgO thin film after 2200 L water dose showing the evolution of peaks indicative of the presence of $Mg(OH)_2$.Arrows identify the position of water induced changes in the spectrum.. 97

Figure 4.10 TPD spectra taken from 20 nm MgO film after ambient exposure, showing the desorption profile of $Mg(OH)_2$ and $MgCO_3$. O 1s core level spectra normalised to the lattice oxygen peak (inset) show a corresponding decrease in the HBE peak………………………………………………………………….. 98

Figure 4.11 AFM images (5 μm × 5 μm) with corresponding O1s core level spectra insets showing the growth and removal of hydroxide/carbonate islands on the MgO surface. (A) after minimal air exposure (B) after 21 days ambient exposure and (C) after 700^{o}C anneal……………………………………………………………… 99

Figure 4.12 Graph showing the growth of the O 1s hydroxide peak on MgO films deposited on silicon at room temperature and 200 °C…………………………….. 101

Figure 4.13 I-V characteristics taken from n-type (A) and p-type (B) Si(111)/20 nm MgO/FUSI Ni MOS structures……………………………………………………..103

Figure 4.14 C-V characteristics taken from native oxide(A) & H-terminated(B) p-type devices suggest a reduction in charge trapping due to FUSI metallisation process.. 105

Figure 4.15 FUSI 5 nm n-type devices show a considerable reduction in interface state density and increased maximum capacitance compared to Pd lift off devices……. 106

Figure 4.16 Cross sectional TEM images taken from FUSI 5 nm (A) and 20 nm (B) MgO devices on H-terminated Si………………………………………………….. 107

Figure 4.17 Further TEM image taken from the 20 nm MgO film clearly showing the presence of crystalline regions within the MgO…………………………………… 108

Figure 4.18 Si 2p spectra taken at 130 and 260 eV, showing the passivation of Si (111) surface states due to H-termination. The high binding tail to the above H-terminated spectra are attributed to Si oxide peaks associated with the presence of sub-monolayer oxygen on the surface………………………………………………….. 111

Figure 4.19 Curve fitted Si 2p spectra indicating the presence of Si-H bonds (peak S) at the surface of H-terminated Si (111). Spectral components D and B are attributed to surface defects and bulk Si respectively……………………………………………… 112

Figure 4.20 Curve fitted Si 2p spectra showing the growth of Mg silicate as a function of MgO deposition on H-terminated Si (111)…………………………………………112

Figure 4.21 O 1s spectra (hν = 1253.6 eV) and Valence band/O 2s spectra (hν = 130 eV) both suggest the formation of interfacial hydroxyl groups due to MgO deposition on H-terminated Si……………………………………………………………………113

Figure 4.22 Raw Si 2p spectra (hν = 130 eV) showing the growth of interfacial Si oxide as a function of MgO deposition on an ultra thin (~ 0.3 nm) Si oxide layer... 115

Figure 4.23 Curve fitted Si 2p spectra indicate the growth of a Mg silicate interfacial layer due to MgO deposition onto Si oxide……………………………………….. 115

Figure 4.24 Corresponding Si 2p spectra (hν = 260 eV) for the sample shown in figure 4.23……………………………………………………………………………… 117

Figure 4.25 Mg 2p (hν = 79 eV) and O 1s spectra (hν = 1253.6 eV) showing the initial stages of MgO thin film formation on a Si oxide surface…………………………. 117

Figure 4.26 Si 2p spectra (hν = 200 eV) showing the preferential growth of Mg silicate at the MgO/Si oxide interface as a result of 500 °C annealing……………. 118

Figure 5.1 Curve Fitted Si 2p spectra showing the growth of Mg silicide and sub-stoichiometric silicon oxide species after Mg deposition (2 nm) onto Si native oxide surfaces. The growth of Mg silicide on 700 nm SiO_2 surfaces suggests disruption of the SiO_2 structure resulting in Mg atoms taking the place of the O atoms……….. 129

Figure 5.2 Si 2p spectra taken after UHV annealing to 300 °C show the complete removal of Mg silicide and Si sub-oxide species, and reduction in SiO_2 from 17 % to 10 % of the signal. Further annealing to 500 °C results in a chemical shift in the Si oxide peak, which is indicative of the transformation of SiO_2 to Mg silicate…….. 130

Figure 5.3 Mg 2p spectra of the core level following Mg deposition and the subsequent 300 °C anneal which results in the oxidation of the Mg. A reduction in the integrated area of the peak by a factor of 2.5, along with mass spectrometry data (inset) suggest desorption of excess Mg from the surface during annealing……… 131

Figure 5.4 Normalised O 1s core level spectra show the presence of both SiO_2 and partially oxidised Mg species after a 300 °C anneal. The reduction in the SiO_2 peak after a 500 °C anneal provides further evidence for the transformation of SiO_2 into Mg silicate………………………………………………………………………… 133

Figure 5.5 Si 2p spectra taken after 1 nm Mg deposition onto Si native oxide surface show the growth of less Mg silicide than that seen in figure 1. Subsequent UHV annealing to 500 °C resulted in only partial transformation of SiO_2 into Mg silicate, indicating the importance of silicide formation as an intermediate step in Mg silicate growth……………………………………………………………………………….. 135

Figure 5.6 Si 2p spectra taken from Si native oxide surface after MgO deposition and subsequent 500 °C anneal showing no change in peak profile which suggests the importance of Mg silicide growth as an intermediate step in Mg silicate formation.136

Figure 5.7 Raw and curve fitted Si 2p spectra showing that Mg deposition greatly increases the chemical reactivity of the Si native oxide surface………………….. 137

Figure 5.8 Curve fitted Si 2p spectra show that UHV annealing of Mg silicate to 750 °C causes the growth of interfacial Si oxide, while annealing to 850 °C results in the complete desorption of Mg silicate…………………………………………………138

Figure 5.9 Reduction in the Mg 2p peak area also suggests the desorption of Mg silicate at temperatures greater than 750 °C……………………………………… 140

Figure 5.10 Curve fitted Si 2p spectra, acquired using SRXPS, show the growth of Mg silicide due to step-wise deposition of Mg onto an ultra thin (~ 0.3 nm) thermally grown Si oxide surface………………………………………………………… 143

Figure 5.11 Mg 2p spectra, acquired at 79 eV photon energy, showing the initial stages of Mg silicide growth followed by the formation of metallic Mg………….. 144

Figure 5.12 Comparison of Si 2p (130 eV) and Mg 2p (79 eV) spectra taken after step-wise and continuous deposition of ~ 1 nm Mg show increased levels of Mg silicide growth due to step-wise deposition……………………………………….. 146

Figure 5.13 Annealing to 300 °C results in the removal of Mg silicide and oxidation of surface magnesium……………………………………………………………… 147

Figure 5.14 The growth of an additional peak due to thermal annealing, separated from the Si bulk peak by 3.25 eV, is attributed to the presence of Mg silicate……. 148

Figure 5.15 Curve fitted Si 2p and Mg 2p spectra taken using conventional XPS, showing that the growth of Mg silicide on H-terminated silicon surfaces upon deposition of ~ 2 nm Mg. Subsequent annealing to 300 °C promotes silicide growth, in contrast to the result seen on oxidised Si surfaces……………………………… 149

Figure 5.16 The chemical stability of Mg silicide is investigated using controlled exposure to O_2. Si 2p and Mg 2p spectra show that room temperature exposure reduces the presence of Mg silicide and partially oxidises excess metallic Mg. Annealing to 300 °C in an O_2 partial pressure of 5×10^{-7} mbar removes all evidence of Mg and Mg silicide, producing stoichiometric MgO, while further annealing to 500 °C partially converts this MgO to Mg silicate……………………………………. 152

Figure 5.17 Si 2p spectra showing the effect of Mg deposition and 175 °C annealing on H-terminated Si (111) surfaces…………………………………………………. 157

Figure 5.18 Curve fitted Si 2p spectra showing the growth of Mg silicate due to high temperature annealing of Mg on H-terminated surface in an O_2 partial pressure of 5 × 10^{-7} mbar………………………………………………………………………….. 158

Figure 5.19 Mg 2p core level spectra show that annealing to 200 °C in 5 × 10^{-7} mbar of O_2 causes the growth of stoichiometric MgO and inhibits Mg desorption. Subsequent annealing to 500 °C causes Mg silicate growth as shown by a shift to LBE…………………………………………………………………………………….. 159

Figure 5.20 Curve fitted O 1s and Mg 2p spectra show the presence of both MgO and Mg silicate on the H-terminated surface after 500 °C………………………….. 160

Figure 5.21 Curve fitted Si 2p and O 1s spectra showing the growth of Mg silicate on a 700 nm SiO_2 surface. The integrated area of the Si 2p Mg silicate component suggests that the thickness of the silicate layer is greater than that formed on the Si native oxide surface…………………………………………………………….. 162

Figure 5.22 Curve fitted Si 2p spectra showing the growth of Mg silicate on a ~ 2 nm SiON layer. The binding energy position of the silicate component following 500 °C annealing may indicate that N atoms remain integrated within the film………… 164

Figure 6.1 Curve fitted In 3d and P 2p spectra taken from the InP native oxide surface. Fitting parameters for the In 3d spectrum were determined based on the B.E. separation between the P 2p bulk and oxide signals, and the work of Hollinger *et al.* [40]. The origin of the In 3d satellite peaks is discussed in the appendix section at the end of this chapter…………………………………………………………………… 178

Figure 6.2 P 2p and In 3d spectra showing a change in the chemical composition of the InP native oxide surface as a result of MgO deposition……………………… 180

Figure 6.3 In 3d, P 2p and O 1s spectra showing the removal of surface oxide after 2-stage wet chemical etching. The spectra suggest the subsequent MgO deposition resulted in interfacial In oxide growth…………………………………………… 182

Figure 6.4 In 3d and P 2p spectra show no evidence for surface oxide after 2-stage etching, and indicate the preferential growth of In oxide after MgO deposition….. 183

Figure 6.5 In 3d, P 2p and O 1s spectra showing the removal of surface oxide using sulphur passivation. In 3d spectra show increased levels of In oxide growth upon MgO deposition………………………………………………………………………. 185

Figure 6.6 Curve fitted In 3d and P 2p spectra showing the complete removal of In and P oxide due to s-pass etching and the preferential growth of In oxide upon MgO deposition………………………………………………………..…………... 186

Figure 6.7 I-V characteristics taken from 20 nm MgO films on n-type (A) and p-type (B) InP surfaces. The results suggest 2-stage etch devices have on average higher leakage currents than native oxide and s-pass substrates…………………………. 188

Figure 6.8 CV characteristics taken from 20 nm MgO films on n-type (A) and p-type (B) InP, showing lower values than expected for the difference (ΔC) between C_{max} and C_{min} attributed to Fermi level pinning………………………………………… 189

Figure 6.9 CV characteristics taken from 5 nm MgO films on n-type InP. The dependence of measured capacitance on the surface preparation techniques is similar to that seen from 20 nm devices…………………………………………………… 191

Figure 6.10 In 3d and P 2p spectra show large decreases in surface oxide upon H* cleaning at 300°C, & slight decreases upon subsequent cleaning at 350 & 400 °C.. 194

Figure 6.11 Curve fitted spectra taken after H* cleaning at 400 °C which show complete removal of In and P oxide species along with evidence for the growth of In-In bonds………………………………………………………………………………. 194

Figure 6.12 XPS O 1s, C 1s and survey (0 – 600 eV) spectra which show considerable decreases in surface contaminants after H* cleaning……………………………... 195

Figure 6.13 In 3d and P 2p spectra showing the large scale growth of In oxide as a result of MgO deposition after H* cleaning at 300°C, considerably greater than that seen after wet chemical etching……………………………………………………… 197

Figure 6.14 Curve fitted In 3d spectra showing the continued growth of In oxide as a function of MgO deposition……………………………………………………….. 198

Figure 6.15 2 μm × 2μm AFM images taken from an InP native oxide surface before (A) and after H* cleaning at 300 °C (B). The H* cleaned surface clearly shows the presence of island structures which can be linked to the high levels of In oxide growth seen in figure 6.14………………………………………………………………… 199

Figure 6.16 I-V characteristics taken from a 10 nm MgO film deposited on a n-type InP (100) substrate after H* cleaning at 300°C. Extremely high leakage current is indicative of nonuniformity in the dielectric layer caused by similar island features to that seen in 6.15……………………………………………………………….... 200

Figure 6.17 MgO deposition onto native oxide surfaces subsequent to 200 °C annealing causes a shift to HBE in the P oxide peak. The binding energy separation of the P 2p bulk and oxide peaks is indicative of a phosphorous rich oxide species… 202

Figure 6.18 P 2p spectra taken after 300 °C annealing and subsequent MgO deposition show a shift to HBE in the P oxide peak, indicative of segregation in the oxide layer…………………………………………………………………… 203

Figure 6.19 10 μm × 10 μm & 2 μm × 2 μm AFM images taken from InP native oxide surface after annealing to 300 °C shows evidence for considerable surface roughening & the presence of island structures evenly distributed across the surface………… 205

Figure 6.20 XPS core level spectra suggest the desorption of surface oxide at 500 °C, while subsequent MgO deposition results in preferential In oxide growth similar to that seen at 300 °C……………………………………………………………… 206

Figure 6.21 O 1s spectra offer further evidence for the desorption of surface oxygen at 500 °C……………………………………………………………………………207

Figure 6.22 A 5 μm × 5 μm AFM image showing evidence for considerable island growth and surface disruption after 500 °C annealing. Due to their size, the island structures seen in AFM image are more easily seen using a 3 dimensional representation of the image……………………………………………………... 208

Figure 6.23 TPD spectra taken from an InP native oxide surface suggests accelerated thermal desorption of P at temperatures above 460 °C…………………………… 209

Figure 6.24 Si 2p core level spectra taken after Si control layer deposition on InP native oxide surfaces show the transfer of O from the substrate. A peak at the LBE side of the Si-Si peak is attributed to Si-InP bonds……………………………….. 212

Figure 6.25 In 3d and P 2p spectra both indicate the transfer of O from the substrate to the Si control layer, and offer further evidence for the presence of S-P and Si-In bonds……………………………………………………………………………… 214

Figure 6.26 XPS spectra suggest the presence of a Si ICL layer prevented the growth of interfacial InP oxide upon MgO deposition and subsequent 500 °C annealing…215

Figure 6.27 Si 2p core level spectra show the continued oxidation of the Si CL layer due to MgO deposition and 500 °C annealing. Curve fitting of the spectra also indicate the presence of Mg silicate within the film……………………………… 216

Figure 6.28 Si 2p spectra show evidence for the growth of Mg silicide after Mg deposition on the Si ICL on InP native oxide. Subsequent annealing to 500 °C results in Mg silicate growth, in agreement with studies on Si native oxide surfaces……..218

Figure 6.29 Modification of Si ICL via Mg silicate formation is seen to inhibit the growth of Si oxide after ~ 1.5 nm MgO deposition and 500 °C annealing………. 219

Figure 6.30 In 3d and P 2p spectra, relating to the Si 2p spectra in figures 6.28 & 6.29, suggest the formation of direct Mg-In and Mg-P bonds as a function of Mg deposition onto the ~ 1 nm silicon overlayer. XPS data suggests these bonds are successfully removed from the surface at 500 °C.. 221

Figure 6.31 2 µm × 2 µm AFM images show no evidence for discontinuity in Si control layers on InP native oxide, suggesting that Mg-InP bonds are caused by Mg diffusion through the Si film... 222

Figure 6.32 In 3d spectrum showing the correlation between the In 3d $_{3/2}$ main peak and the satellite peaks which form part of the overall In 3d $_{5/2}$ peak profile......... 226

Figure 6.33 curve fitted In 3d spectrum taken from a InP native oxide surface. The LBE side of the peak profile is enlarged to more clearly show the curve fitting components which were used throughout this study to identify the satellite peaks labelled S1 and S2.. 227

Chapter 1

Introduction

The focus of this thesis is to investigate some of the challenges currently facing the transistor technology industry and how new materials may be used to deal with these problems. In this section the importance of both the semiconducting substrate and the gate dielectric layer, to the operation of metal oxide semiconductor field effect transistors (MOSFET) will be discussed.

1.1 MOSFET operation

Transistor devices have traditionally been fabricated using silicon semiconducting substrates and thermally grown silicon dioxide (SiO_2) insulating layers. This is primarily due to the ease with which high quality insulating layers can be formed on atomically clean Si surfaces using controlled oxidation [1]. Therefore, the basic operation of Si/SiO_2 transistor devices will first be discussed before the limitations of these materials are analysed in further detail. A schematic diagram showing the operation of a silicon n-type channel MOS transistor can be seen in figure 1.1.

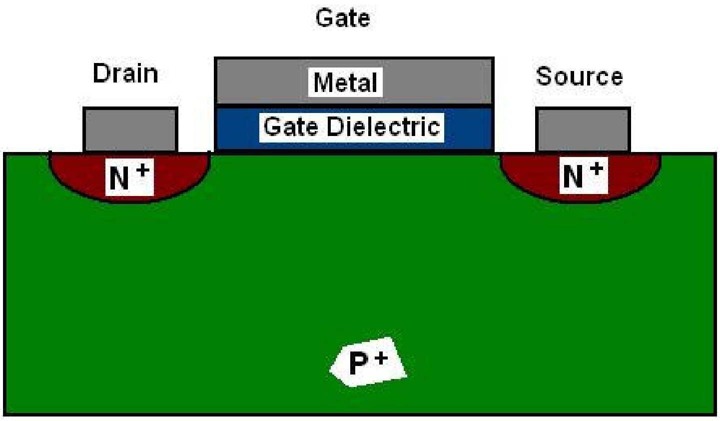

Figure 1.1 Schematic diagram of a silicon n-type channel MOS transistor.

A transistor device within an electron circuit may be simply viewed as an On/Off switch, which is switched "On" when a current flows between the source and drain regions of the device. The diagram in figure 1.1 shows that the n-type source and drain regions are separated by the p-type substrate material, creating a series of p-n junctions which inhibit current flow. Therefore, it can be said that the device defaults to the "Off" position even when a potential difference is applied between the source and the drain, and in order to turn it "On" a conducting n-type channel must be formed between the source and drain regions. The formation of this conduction path is controlled by applying a voltage to the metallic gate electrode, which is separated from the channel region by an insulating dielectric layer as shown in figure 1.2 [2].

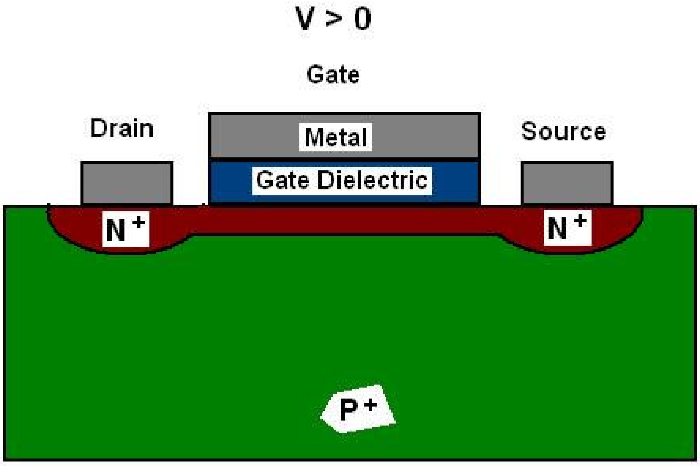

Figure 1.2 Application of a positive gate voltage induces negative charge carriers to gather at the semiconductor surface. This creates a conductive "n-type" channel, turning the transistor "On".

The application of a positive gate voltage induces negative charges to accumulate at the surface of the underlying Si substrate. The abundance of negative carriers at the substrate surface due to the applied voltage effectively makes them the majority carriers within the surface region. This local electrically induced change in majority carriers is known as inversion, and allows an n-type conductive channel region to be created within a p-type semiconducting substrate (or vice versa) [3]. As such, when inversion is achieved current is allowed to flow from the source to the drain region, turning the device "On". The process of substrate inversion, along with the related phenomena depletion and accumulation, are discussed in greater detail in Chapter 2 of this study.

1.2 Challenges facing transistor technology

As mentioned previously, transistor fabrication has traditionally been based on Si/SiO_2 devices. However, the challenges currently facing the semiconductor industry have meant that a great deal of study has focused on replacing SiO_2 as the gate dielectric material. These challenges can be summarised in two main points;

1) The need to improve computer performance has demanded the integration of more transistor devices within the processor chip. This has necessitated the down scaling of device dimensions.
2) The desire for higher efficiency requires the power consumption of computers to be lowered.

As the number of transistor devices per unit area continues to increase, in accordance with Moore's law [4], the dimensions of transistor devices must be decreased accordingly. This reduction must occur equally on all dimensions of the device [5], and as such must include a decrease in the thickness of the insulating gate dielectric layer. As the thickness of the dielectric is decreased below 5 nm, power consumption is negatively affected by an increase in gate leakage current, which occurs due to direct quantum tunnelling through the dielectric layer [6]. The mechanism of direct quantum tunnelling in MOS capacitors is graphically represented in figure 1.3.

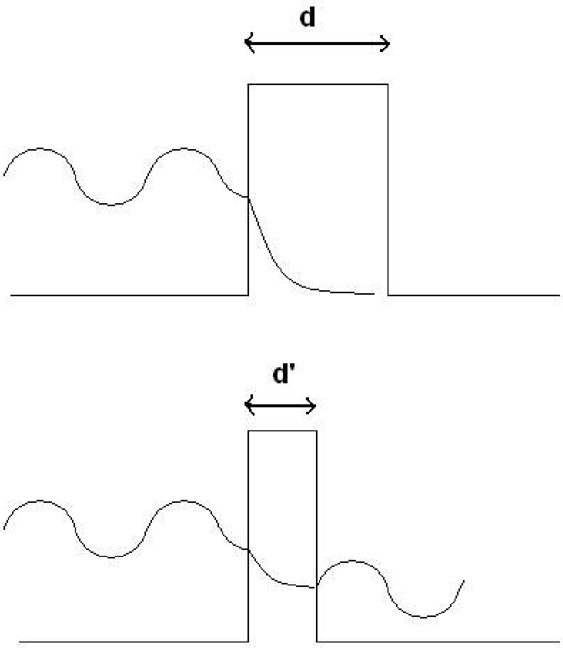

Figure 1.3 Diagram showing electron quantum tunnelling through a potential barrier. It can be seen that the probability of tunnelling is increased by reducing the thickness (d) of the barrier layer.

The schematic diagram clearly indicates that the probability of electron quantum tunnelling is inversely related to the thickness of the barrier layer (d). This dependence is further shown by the following equation for the electron quantum tunnelling probability (T) [7];

$$T \cong 16\left(\frac{E}{V_0}\right)\left(1-\frac{E}{V_0}\right)\exp\left(-2\left[\sqrt{\frac{2m(V_0-E)}{\hbar}}\right]d\right) \tag{1.1}$$

It can be seen from equation 1.1 that for an electron with energy (E) and mass (m) the tunnelling probability (T) depends on both the barrier thickness (d) and the barrier height (V_0).

It can therefore be stated that decreasing the physical thickness of the dielectric layer results in an increased gate leakage current, which negatively affects the efficiency and power consumption of the device. By approximating the MOS device as a parallel plate capacitor, the capacitance (C) of the dielectric layer can be expressed using the following equation;

$$C = \frac{\varepsilon_0 \kappa A}{d} \tag{1.2}$$

where ε_0 is the permittivity of free space, *k* the dielectric constant of the material, A is the capacitor area and d the thickness. Based on this equation it can be seen that the physical thickness of the dielectric layer (d) can be increased by using a different material of higher dielectric constant (*k*), while still maintaining the capacitance (C) achieved using a given SiO_2 thickness. This would have the effect of reducing the tunnel current which has direct implications for power consumption. The relationship between the thickness of dielectric layers formed from SiO_2 and alternative materials is often referred to as the effective oxide thickness (EOT) [8]. This is the thickness of SiO_2 that would result in the same capacitance as that achieved by a particular thickness of high-*k* dielectric. This can also be expressed as;

$$EOT = \left(\frac{k_{SiO_2}}{k}\right)d_{physical} \tag{1.3}$$

where *k* is the dielectric constant, and d is the physical thickness, of the alternative dielectric layer [8]. This basic analysis is the fundamental motivation behind the field of high-*k* dielectric research, however, there are a number of other factors beyond simply the *k* value of the material which must be considered when attempting to replace SiO_2 as the gate dielectric material.

1.3 Factors in considering high-*k* candidates

The following are the criteria upon which possible high-*k* candidates should be judged, as suggested by the work of John Robertson [8];

I) The *k* value must be large enough to be used for a reasonable number of years of future device scaling.
II) The oxide is in direct contact with the Si channel so it must be thermodynamically stable.
III) It must be kinetically stable and be compatible to processing to 1000 °C for 5s (in present process flows).
IV) It must act as an insulator, by having band offsets with Si of over 1 eV to minimize carrier injection into its bands.
V) It must form a good electrical interface with Si.
VI) It must have few bulk electrically active defects.

These criteria can be summarised individually with reference to specific dielectric materials currently under investigation.

I) High-k Requirements

The reasons for introducing materials with a dielectric constant higher than that of SiO_2 (3.9) have been outlined. However, in order to make the cost of implementing any new material economically feasible, then its *k* value must be large enough for it to last for several generations (3-4 years as defined by Moore's law [4]). It is reported that a *k* value between 25-30 is required [8], and while there are several available candidates with *k* values as large and larger than this (Ta_2O_5 [9], $SrTiO_3$ [10]) these materials do not satisfy some of the following criteria such as band offsets and thermal stability [11].

II) Chemical stability of the Si/dielectric interface

Upon deposition the dielectric material should not react with the Si to form interfacial SiO_2 or a metal silicide species. Given that it is the dielectric constant of the over all dielectric layer which determines the EOT, the formation of a low-*k* SiO_2 layer at the Si/dielectric interface is to be avoided, as the interfacial oxide layer will act as a separate capacitor in series with that of the deposited dielectric layer. The growth of interfacial SiO_2 is a serious obstacle to reducing EOT and work of Zeman *et al.* [12] has shown this tendency for numerous metal oxide materials such as HfO_2 and ZrO_2. Conversely, the formation of direct metal-silicon bonds, in the form of a metal silicide, reduces the insulating properties of the dielectric layer, analogous to the creation of a "short circuit" through the insulator.

III) Thermal Stability

Any alternative gate oxide must be thermally stable in contact with Si, and must be able to withstand processing up to ~ 1000 °C during rapid thermal annealing (RTA) treatments [8]. The primary difficulty for many high-*k* candidates (HfO_2 [8,13], ZrO_2 [8,14]) is the formation of crystalline regions within the film during annealing. The grain boundaries of these regions are known to act as effective paths for dielectric breakdown through the oxide, increasing power consumption and reducing the lifetime of the device [8, 15].

IV) Insulating properties (Band-offsets)

Previous discussions have addressed the probability of an electron tunnelling through the dielectric layer is dependant on both the thickness and height of the potential barrier. While the physical thickness of the barrier (gate dielectric) can be increased through the use of high-*k* materials, this improvement can be fully negated by a reduction in the band off-sets between the energy bands of the semiconductor and the dielectric [8]. The effect of energy band offset on leakage current flow is graphically represented in figure 1.4.

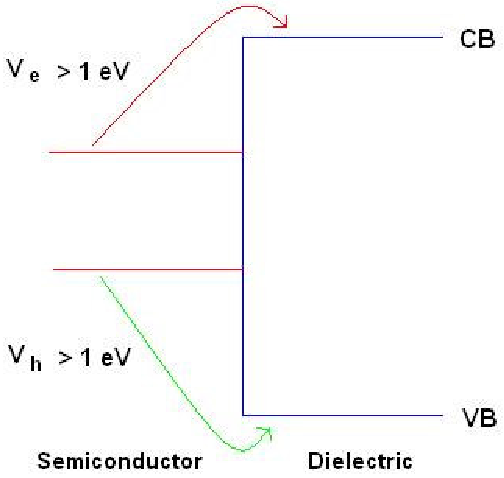

Figure 1.4 Energy band diagram illustrating the direct injection of charge carriers from the semiconductor to the dielectric layer. The work of John Robertson [8] has shown that band offsets less than 1 eV allow for high leakage currents, making the bandgap of the dielectric vital to device efficiency.

As indicated by the diagram, direct carrier injection between the semiconductor and dielectric energy bands can easily occur for energy offsets less than 1 eV. While the large bandgap of SiO_2 (9 eV) ensured large band offsets with silicon [8], many high-*k* candidates have bandgaps less than 5 eV. Figure 1.5 shows that, in general, an inverse relationship exists between the dielectric constant (*k*) value and the bandgap of metal oxide dielectric materials [16].

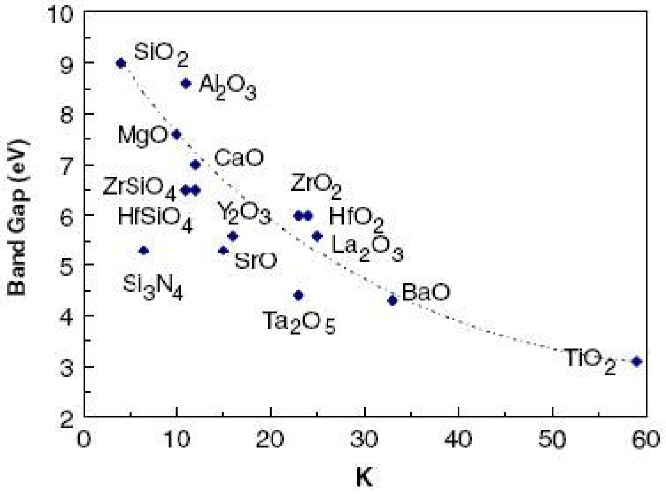

Figure 1.5 Plot showing that, in general, an inverse relationship exists between the bandgap and dielectric constant of many gate dielectric candidates [16].

V) Electrical Interfacial Properties

Given that the dielectric material is in direct contact with the Si channel, the properties of this interface can greatly affect factors such as carrier mobility and the number of electrically active defects. Therefore, it is crucially important to reduce the surface roughness and defect density at this interface. While it has been reported that defects such as unsatisfied dangling bond sites may be passivated using thermal annealing processes [17], any additional thermal processing can adversely affect the insulating properties of the layer. It is suggested by Robertson [8] that favourable interfacial properties are best achieved using either fully epitaxial or fully amorphous dielectric layers, therefore both the chemical and thermal stability of the layer are of key importance.

VI) Bulk defects

Electrically active defects are defined as atomic configurations which give rise to electronic states in the band gap of the oxide [8]. For metal oxide dielectric materials these defects commonly arise due to incorrect film stoichiometry, in the form of an excess or deficiency of oxygen atoms. Such defects can cause charge trapping within the layer which can result in a reduction in carrier mobility, a (variable) shift in the gate voltage required to turn the device on, and also increase the probability of dielectric breakdown within the film reducing the lifetime of the device.

While the above criteria for the selection of dielectric materials are well known, to date no one material has been found to fully satisfy each of them. For example, materials such as Ta_2O_5 and $SrTiO_3$ have high k values, but are also reported to have small band gaps [18] and poor thermal stability with Si [11]. Another popular candidate, HfO_2, which has recently been integrated into commercial devices has been shown to have a k value ~ 8 times that of SiO_2 [16] and also forms high quality interfacial regions with Si. However, it has a tendency to crystallise at low temperature [8,13]. In response to this problem the use of mid-k materials such as MgO [19], Al_2O_3 [20] and various metal silicates [11,21] has been proposed. While these materials have comparatively low k values (~8 to 15) it has been reported that they form abrupt and thermally stable interfaces with Si, along with favourable band offset to reduce leakage current flow.

In this study two such materials, namely MgO and Mg silicate were investigated as possible dielectric candidates on silicon and indium phosphide substrates. Their suitability is discussed primarily in terms of the ability to form abrupt and stable interfacial regions, which is analysed using photoemission spectroscopy. Other analysis techniques, such as atomic force microscopy (AFM), temperature programmed microscopy (TPD) and electrical characterisation measurements were also used to characterise the dielectric films.

1.4 Alternative semiconductors to replace Si

While the above discussion has described challenges facing transistor technology in terms of alternative gate dielectric materials for use on silicon, a great deal of investigation has also centred on replacing Si as the semiconducting substrate. As mentioned previously, one of the main advantages offered by Si is the ease with which high quality SiO_2 dielectric layers can be grown. Therefore, if SiO_2 is replaced as the gate dielectric, then the main benefit of using Si may also be gone. The alternative semiconducting substrates which are currently being investigated include the group IV material Ge, and a group of composite materials referred to as III-V semiconductors including InAs, GaAs, InP and InGaAs. III-V semiconductors are known to have higher carrier mobility than Si and as such may allow faster transistor devices to be fabricated [22]. Other materials, such as GaN, have wider band gaps than Si and have been used in high power applications [23]. While the advantages of these materials are well known, the main obstacle to the integration of alternative semiconductors remains controlling the interfacial properties between the substrate and the deposited gate dielectric [24].

InP has shown some promise in high frequency operations due to its high carrier mobility [25], while its band offsets to numerous dielectrics including HfO_2 and Al_2O_3 are reported to be larger than that of Si [18]. Also, unlike Si, InP has a direct band gap meaning that it is more suitable for optoelectronic devices [26]. It has also been suggested that InP is less susceptible to Fermi level pinning than other III-V candidates such as GaAs [27].

In this study, initial investigations into the preparation and modification of InP surfaces were undertaken. Wet chemical etching techniques such as sulphur passivation [28] and the 2-stage etching technique suggested by Sun *et al.* [29] are known to remove surface oxides from InP. However, given that dielectric layers must be deposited after etching, the chemical stability of the cleaned surface must also be determined. The chemical stability of native oxide and wet chemically etched InP surfaces were also investigated by depositing MgO and monitoring interfacial oxide growth using *in-situ* XPS analysis. Along with wet chemical etching, the technique of atomic hydrogen (H*) cleaning has also been used extensively on III-V materials such as GaAs [30] and InP [31]. The chemical stability of H* cleaned surfaces was also analysed using MgO deposition, with the effect of elevated substrate temperature during H* cleaning being investigated in some detail.

In addition to processes designed for removing surface oxide from InP, attempts to modify the chemical composition of the surface will also be described. This was achieved via the deposition of a Si interfacial control layers (ICL) onto the InP surface prior to dielectric deposition, a technique which has recently shown great promise [32]. Using conventional photoemission spectroscopy, Si deposition onto InP native oxide surfaces was studied, along with the affect of subsequent MgO deposition and high temperature vacuum annealing.

1.5 Thesis Layout and Organisation

Chapter 2 introduces the analysis techniques used in this study, along with the principles behind their operation. The primary technique used in this work was conventional X-ray photoelectron spectroscopy (XPS), however, other techniques such as synchrotron based XPS, atomic force microscopy (AFM), temperature programmed desorption (TPD), transmission electron microscopy (TEM) and electrical characterisation were also used and are described in Chapter 2.

Chapter 3 describes the ultra high vacuum (UHV) systems used for these experiments, along with the thin film deposition and semiconductor surface cleaning techniques employed throughout the study. The deposition techniques used in this study include electron beam (e-beam) evaporation and thermal deposition which were primarily used to deposit thin films of MgO and Si. The curve fitting parameters used for both synchrotron and conventional XPS spectra are also outlined in this chapter.

Chapter 4 focuses on the suitability of MgO as an alternative gate dielectric on Si. The three main factors investigated in this study were the ambient stability, electrical characterisation and interfacial properties of MgO thin films on Si. It is shown that exposure to ambient conditions results in the rapid formation of hydroxide and carbonate species, negatively affecting the electrical characteristics of air exposed MgO films. However, subsequent MOS structures fabricated by depositing an *in-situ* Si cap on the MgO films prior to ambient exposure showed very promising electrical results. High resolution synchrotron based XPS studies have shown that MgO deposition onto Si results in the formation of an Mg silicate interfacial region.

In Chapter 5 the conversion of SiO_2 native oxide surfaces into magnesium silicate is investigated. Studies relating to the Mg silicate growth mechanism indicate that the initial formation of Mg silicide is a vital intermediate step in silicate formation. Further investigation into the growth and stability of Mg silicide using high resolution synchrotron XPS were also undertaken and suggest that Mg silicide has lower thermal and chemical stability than other metal silicide species.

Chapter 6 presents an initial investigation into how the interfacial chemistry of MgO/InP interfaces can be modified and improved. Using conventional XPS the effectiveness of wet chemical etching techniques are analysed, based both on the removal of oxide species and the chemical stability of the etched surfaces. The use of atomic hydrogen cleaning and silicon interfacial control layers on InP has also been investigated.

Each of the experimental results chapters are sub-divided into three sections, which relate to different aspects of the study. At the end of each section a brief summary is given in an attempt to highlight the main results and place them in context within the over all chapter.

1.6 References

[1] M.M. Atalla, U.S. Patent 2899344, (1959)

[2] Ben G. Streetman, Solid State Electronic Devices, 2nd Edition, Prentice-Hall Inc., Englewood Cliffs, New Jersey 07632.

[3] Adir Bar-Lev, Semiconductors and Electronic Devices 2nd Edition, Prentice-Hall International

[4] G. E. Moore, Cramming more components onto integrated circuits, Electronics **38** (8) (1965) 114

[5] S. H. Voldman, Microelectronics Reliability **38** (1998) 1649 -1668

[6] D.R. Wolters, H.L. Peek, Solid-State Electronics, **30** (1987) 835

[7] D. A. Neamen Semiconductor Physics and Devices: Basic Principles 2nd edition Irwin Book Team (1997)

[8] J. Robertson, Reports on Progress in Physics, **69** (2006) 327–396

[9] I. C. Kizilyalli, R. Y. S. Huang, and P. K. Roy, IEEE Electron Device Letters. **19**, (1998) 423

[10] B. He, T. Ma, S. A. Campbell, and W. L. Gladfelter, Technical Digest - International Electron Devices Meeting, 1038 (1998)

[11] G. D. Wilk and R. M. Wallace, Appl. Phys. Lett. **74**, 19 (1999) 2854

[12] M. C. Zeman, C. C. Fulton, G. Lucovsky, R. J. Nemanich, W.-C. Yang, J. Appl. Phys. **99** (2006) 023519

[13] Tae-Hyoung Moon, Moon-Ho Ham, Myoung-Seok Kim, Ilgu Yun, Jae-Min Myoung, App. Surf. Sci. **240** (2005) 105–111

[14] Shuying Shao, Zhengxiu Fan, Jianda Shao, Hongbo He, Thin Solid Films **445** (2003) 59–62

[15] R. O'Connor, G. Hughes, P. Casey, S. Newcombe, J. Appl. Phys **107** 024501 (2010)

[16] J. Robertson J. Vac. Sci. Technol. B **18** (2004) 1785

[17] M. Schmidt, M. C. Lemme, H. Kurz, T. Witters, T. Schram, K. Cherkaoui, A. Negara and P.K. Hurley, Microelectronic Engineering **80** (2005) 70–73

[18] J. Robertson, and B. Falabretti, J. Appl. Phys. **100** (2006) 014111

[19] L. Yan, C.M. Lopez, R.P. Shrestha, E.A. Irene, A.A. Suvorova, M. Saunders, Appl. Phys Letts **88** (2006) 142901

[20] Changhai Lin, Jinfeng Kang, Dedong Han, Dayu Tian, Wei Wang, Jinghua Zhang, Meng Liu, Xiaoyan Liu, Ruqi Han, Microelectronic Engineering **66** (2003) 830–834

[21] J. J. Chambers and G. N. Parsons, J. Appl. Phys. **90**, (2001) 918-933

[22] S. Sze, Semiconductors Devices, Physics and Technology, Wiley, NY, (2003) 537.

[23] P. D. Ye, B. Yang, K. K. Ng, J. Bude, G. D. Wilk, S. Halder, and J. C. M. Hwang, Appl. Phys. Lett. **86**, 063501 (2005)

[24] M. Passlack, J.K. Abrokwah, R. Droopad, Yu Zhiyi, C Overgaard, S. In Yi, M. Hale, J. Sexton, A.C. Kummel, *Electron* Device Letters, IEEE **23**, no.9, (2003) 508-510

[25] P. van Staa, H. Rombach, R. Kassing J. Appl. Phys. **54** (1983) 4014

[26] F. J. Leonberger, P. F. Moulton, Appl. Phys. Lett., **35**, 9, (1979) 712

[27] Y. Q. Wu, Y. Xuan, T. Shen, P. D. Ye, Z. Cheng, A. Lochtefeld, Appl. Phys. Lett. **91**, (2007) 022108

[28] T. Chass, H. Peisert, P. Streubel, R. Szargan, Surface Science **331-333** (1995) 434-440

[29] Y. Sun, Z. Liu, F. Machuca, P. Pianetta, W. Spicer, J. Appl. Phys. **97** (2005) 124902

[30] T. Sugaya, M. Kawabe, Jpn. J. Appl. Phys. **30** (1991) L402-L 404

[31] T. Muranaka, C. Jiang, A. Ito, H. Hasegawa, Jpn. J. Appl. Phys. **40** (2001) 1874-1877

[32] Y-T Chen, H. Zhao, J. H. Yum, Y. Wang, J. C. Lee, Appl. Phys. Lett. **94** (2009) 213505

Chapter 2

Principles of experimental techniques

2.1 X-ray photoelectron spectroscopy

The principle analytical technique used in this study was X-ray photoelectron spectroscopy (XPS). XPS is a surface analysis technique used to probe the chemical composition of roughly the first 6nm of a material. Surface analysis by XPS is accomplished by irradiating a sample with mono-energetic soft x-rays and analysing the kinetic energy of the electrons which are subsequently emitted from the material due to the photoelectric effect [1].

2.1.1 Basic Principles

The basic experimental set up for conventional XPS analysis is shown in figure 2.1, consisting of a sample under analysis, electron collection lens, electron kinetic energy analyser and output display monitor.

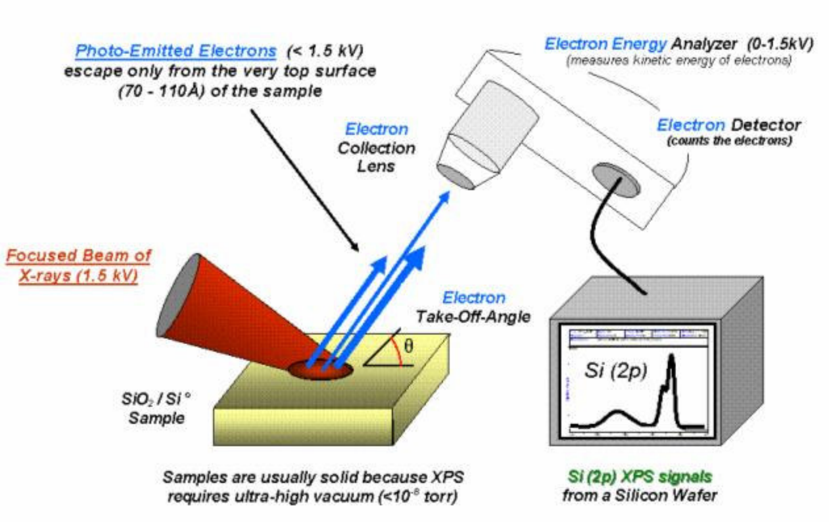

Figure 2.1 A schematic diagram showing the experimental set-up for conventional XPS [2].

In conventional XPS systems x-rays are commonly generated from a twin anode x-ray source that can provide two different excitation energies. Electrons from a hot tungsten filament are accelerated using a high voltage, ranging from 10 – 15 kV, towards a water cooled Mg or Al anode. Upon striking the selected cathode, x-rays of either 1256.6 eV (Mg Kα) or 1486.6 eV (Al Kα) are emitted. These photon energies are used to excite electrons from the near surface region of the sample and the kinetic energy of the excited electrons are measured using an electron energy analyser apparatus similar to that shown in figure 4.1. In its simplest form the kinetic energy (KE) of electrons emerging from the surface is given by Einstein's equation;

$$KE = h\nu - E_b \qquad (2.1)$$

It can be seen that the kinetic energy of the electron is equal to the photon energy ($h\nu$) of the incident x-ray minus the binding energy (E_b) of that electron, which is measured with respect to the Fermi level. As such, the binding energy value can be obtained by measuring the kinetic energy of the emitted electron. Given that every energy level of each element has a discrete binding energy, the elemental composition of a sample can be determined by comparing the measured binding energies to known values.

Figure 2.2 shows an energy level diagram for the full photoemission and analysis process, taken from a sample and spectrometer which are in electrical contact. From figure 2.2 it is clear that the sum of the electron's initial binding energy measured up to the Fermi level (E_B^F), and its kinetic energy after being emitted (E_{kin}^1), does not equal the photon energy of the impinging x-rays.

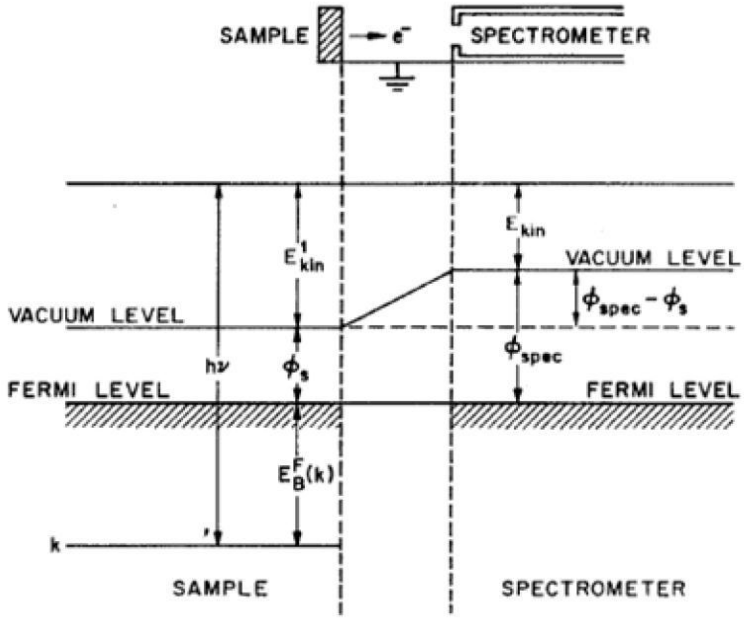

Figure 2.2 Energy level diagram for the photoemission process showing a sample and spectrometer in electrical contact [3].

It can be seen from equation 2.2 that the workfunction of the sample Φ_s, defined as the energy difference between the vacuum level and Fermi level ($E_{\text{vac}} - E_{\text{F}}$), must be considered when defining the actual kinetic energy of electrons emitted from the sample.

$$h\nu = E_B^F + E_{kin}^1 + \Phi_s \tag{2.2}$$

While this equation relates to the actual kinetic energy of the emitted electrons, Feldman and Mayer [3] explain how the measured kinetic energy value (E_{kin}) may differ from this. It has been shown that an electron passing from the sample to the spectrometer experiences a potential difference equal to the difference between the workfunction of the sample Φ_s and that of the spectrometer Φ_{spec}. The measured kinetic value can therefore be defined by equation 2.3.

$$E_{kin} = E_{kin}^1 + (\Phi_s - \Phi_{spec}) \tag{2.3}$$

By substituting this into equation 2.2, the expression given in equation 2.4 can be found.

$$h\nu = E_B^F + E_{kin} + \Phi_{spec} \quad (2.4)$$

This equation allows the binding energy of an electron to be obtained once the x-ray photon energy and spectrometer workfunction values are known. The spectrometer workfunction is commonly determined using a reference sample such as gold or copper, with measured spectra being shifted to compensate for this value.

The kinetic energy of electrons emitted from the sample may be changed by atomic collisions and phonon interactions which can occur within the solid before the photo-excited electrons emerge from the surface. The probability of such interactions can be statistically predicted based on the inelastic mean free path (IMFP) of the material, which is the distance an electron will travel in a material before its kinetic energy drops to 1/e of its initial value, where e is the exponential function. This is represented by the universal mean free path curve in figure 2.3.

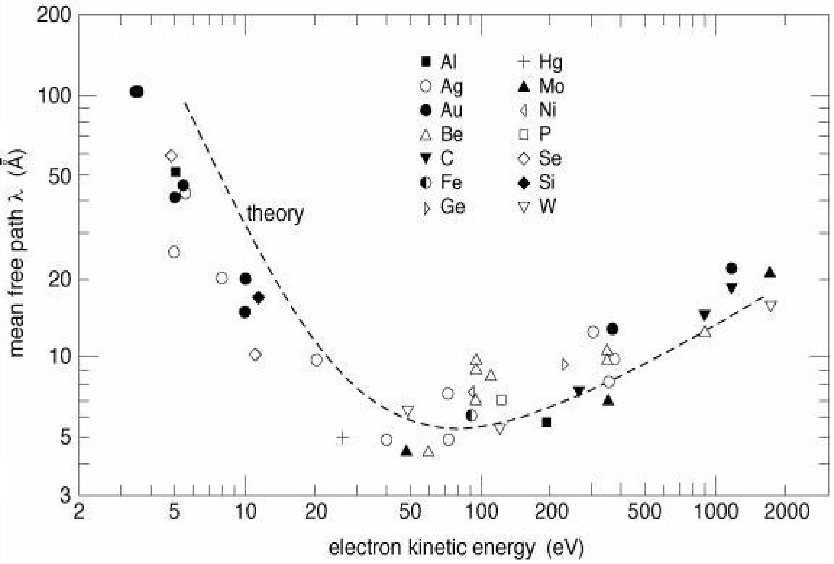

Figure 2.3 Universal mean free path (MFP) curve, showing a range of materials [4].

Only electrons which reach the analyser without suffering inelastic collisions have kinetic energies which can be related back to the original binding energy value. Therefore, in photoemission experiments useful information may only be obtained from the first 5 – 10 nm of the surface, making the technique highly surface sensitive. Unscattered electrons produce narrow and intense photoemission peaks, such as those shown in the survey scan of silicon dioxide in figure 2.4, and the binding energy of these peaks can be related to the elements present at the surface.

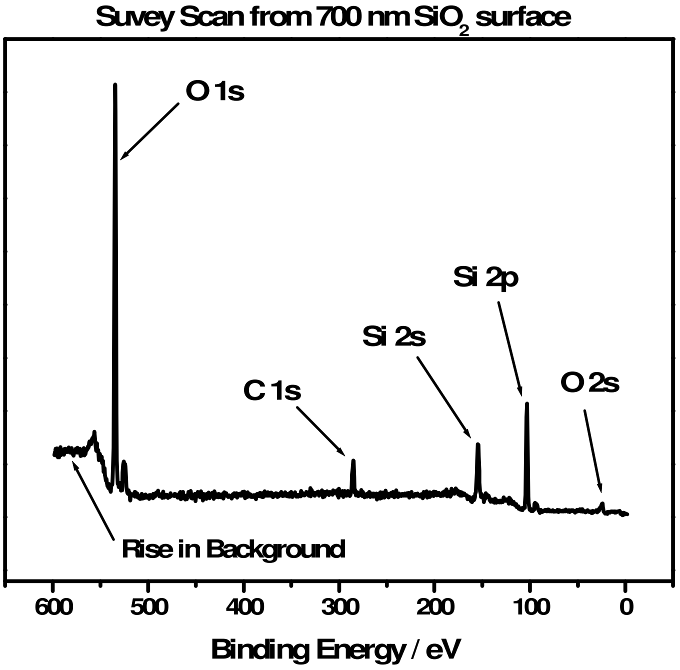

Figure 2.4 Survey scan taken from an air exposed 700 nm SiO_2 surface. By analysing the binding energy positions of the photoemission peaks the elements Si, O and C can be identified.

Electrons which have lost energy due to inelastic collisions emerge from the sample with random kinetic energies, and simply add to the background of the spectrum.

2.1.2 Element Identification

Standard XPS can be used to identify the presence of elements which are at atomic concentration levels greater than approximately 0.1 – 1 %. Elements are commonly identified by the presence of their strongest spectral feature, in the case of silicon this is the Si 2p peak (figure 2.4). However, binding energy positions are not unique to specific elements and different peaks may often overlap within the spectrum i.e. the Ga 3p and Si 2p peaks at ~ 103 eV [5]. In this situation the presence of secondary core level features, such as the Si 2s, may be used to identify the sample.

2.1.3 Chemical Shifts

In addition to identifying the elements present on the surface, one of the most important aspects of XPS is the ability to distinguish between different chemical environments of the same element. This is possible because the binding energy of an electron within an atom depends on the bonding environment of that atom. Therefore, changes in chemical bonding can result in changes in the charge density around the atoms, which causes a "chemical shift" in the binding energy of the electrons which emerge from these atoms. This process is described in greater detail with reference to the silicon/silicon dioxide system, using the Si 2p spectrum in figure 2.5.

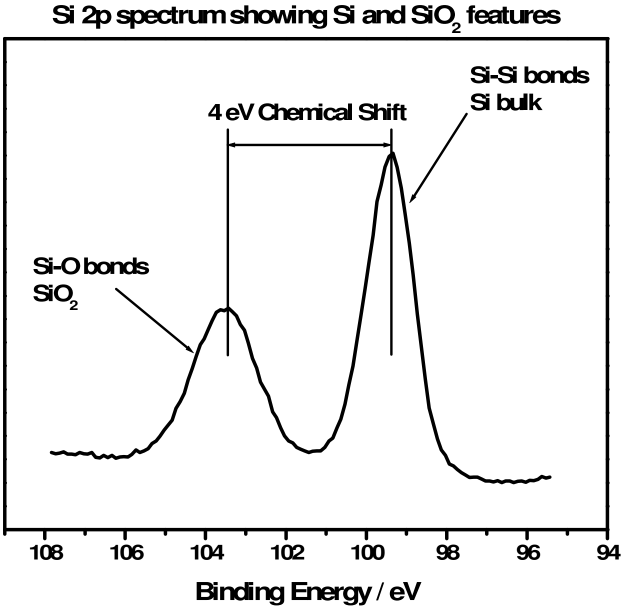

Figure 2.5 Si 2p spectrum showing a 4 eV chemical shift between component peaks which indicates the presence of Si and SiO_2.

Figure 2.5 shows a Si 2p spectrum taken from a thin (~ 4 nm) SiO_2 layer which was thermally grown on a Si (111) substrate. It can be seen that electrons excited from the Si substrate appear at a binding energy of ~ 99.3 eV, while those from the SiO_2 over layer appear at a higher binding energy position, chemically shifted from the bulk by ~ 4 eV. This is due to the different bonding environment present within the two chemical species. The covalent Si-Si bonding system seen within the Si bulk allows the valence electrons to be shared equally among each of the Si atoms involved in the bond structure. However, the incorporation of O atoms, which have considerably greater electronegativity than Si, results in the transfer of electron density toward the

O atoms. As such, Si-O bonds are more ionic and electrons which are excited from these silicon atoms are leaving an atom which has a slightly greater positive charge than those within the Si bulk. The effect of this positive charge is to reduce the kinetic energy of the emitted electrons, which is apparent from the increased binding energy of the SiO_2 peak seen in figure 2.5. As such, the relative electronegativity values of the elements within a sample can be used to identify chemical composition. For example, the formation of a spectral component at the lower binding energy (LBE) side of the Si bulk peak indicates that Si atoms are bonded to an element with a lower electronegativity than that of Si, commonly seen in the form of a metal silicide as will be shown in Chapter 5 of this study.

2.1.4 Quantification

Semi-quantitative analysis of the relative concentration of different elements in a material can be achieved by comparing the intensity of the relevant core level peaks. However, there are a number of factors which must be taken into account in order to accurately quantify chemical composition using XPS peak intensities. This is analysed in further detail in reference to Mg 2p and O 1s spectra taken from an MgO thin film deposited on Si (111), shown in figure 2.6.

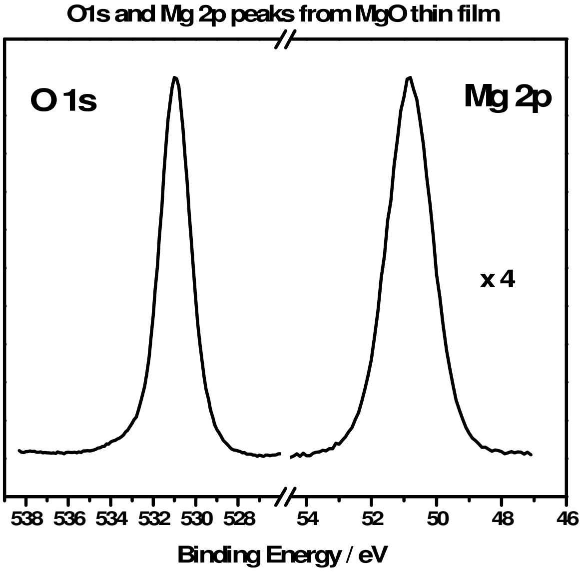

Figure 2.6 O 1s and Mg 2p spectra taken from a 20 nm stoichiometric MgO thin film.

In order to determine stoichiometry using the spectra in figure 2.6 it must be assumed that the MgO film is homogenous, as if the chemical composition perpendicular to the surface is non-uniform within the XPS sampling depth, no definitive elemental ratios can be extracted. The relative binding energies of the two peaks must also be taken into account given that electron IMFP is strongly dependant on kinetic energy. As such, it can be said that electrons emerging from the Mg 2p peak (BE ≈ 50 eV, KE ≈ 1200 eV) may emerge from a greater depth than O 1s electrons (BE ≈ 531 eV, KE ≈ 720 eV). Further factors include the photo-ionisation cross-section of that specific core-level which is the probability that an electron of that core-level will be excited [6], and finally the transmission function of the analyser which determines the sensitivity of the analyser to electrons of that kinetic energy.

Based on these criteria relative sensitivity factors (RSF) can be obtained for the core level peaks of each element, and using these RSF values, chemical composition can be analysed. Published RSF values are available from XPS reference manuals [7] and allow semi-quantitative analysis of chemical composition to be achieved. In reference to the spectra in figure 2.6, the published RSF values of O 1s and Mg 2p are 0.711 and 0.129 respectively [7]. Therefore, for stoichiometric MgO the integrated area of the O 1s peak should be ~ 5.5 times greater than that of the Mg 2p. This analysis is at best semi-quantitative and the use of reference materials is common for more accurate quantification studies. In this study, quantitative analysis has been performed in an attempt to directly compare differently prepared samples, rather than for the purpose of extracting absolute values.

2.1.5 Depth Profiling using ARXPS

Angular resolved XPS (ARXPS) allows non-destructive depth profiling to be achieved for a thickness into the sample surface which is comparable to the sampling depth. Previous discussions relating to the emission of photoelectrons assume that they escape using the shortest path, which is that perpendicular to the sample surface. Therefore, the maximum sampling depth is achieved by aligning the sample so that the electrons which emerge normal to the surface are detected by the analyser. However, electrons emerging from shallower angles with respect to the surface may also be analysed by rotating the sample relative to the analyser. This is graphically represented in figure 2.7a for a thin SiO_2 layer on Si.

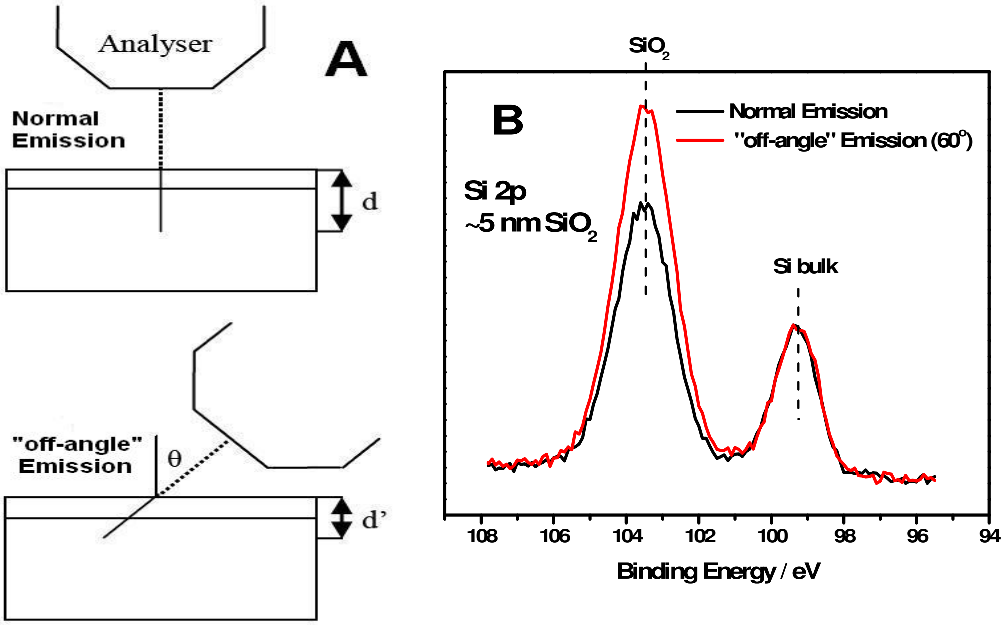

Figure 2.7 (A) Schematic diagram showing reduced sampling depth at angle θ. (B) Si 2p spectra taken from Si native oxide surface showing the increased surface sensitivity using ARXPS.

It can be seen from figure 2.7a that electrons emerging perpendicular to the surface have the same sampling depth as those emerging at the angle θ, however, the perpendicular depth d' into the sample is considerably less than d. As such, core level spectra taken at angle θ are more surface sensitive than those taken at normal emission. This is further evidenced by Si 2p spectra in figure 2.7b which are taken from a SiO_2 surface (~ 5 nm) at emission angles equal to 0 ° (normal emission) and 60 °. It can be clearly seen that the spectrum taken at 60 ° shows an increased intensity from the Si oxide overlayer.

2.1.6 Thickness Calculations

XPS may be used to approximate the thickness of thin (less than approximately 10 nm) overlayers by comparing the intensity of core level peaks taken from the substrate and overlayer, respectively.

XPS thickness calculations used in this study can be divided into two categories. The overlayer thickness can be estimated based on the suppression of the substrate peak by the presence of an overlayer. Alternatively, when the same element is present in distinguishably different chemical environments in the overlayer and substrate, the overlayer thickness calculations are simplified.

For a sample of material A which forms a thin uniform layer of thickness d on a substrate of material S, the following equation can be written for the relative intensity of the substrate (I_S) and overlayer (I_A) XPS signals (assuming exponential attenuation of the overlayer) [8,9].

$$\frac{I_A}{I_S} = \frac{I_A^{\infty}\left\{1 - \exp\left[\frac{-d}{\lambda_{A,A}(Cos\theta)}\right]\right\}}{I_S^{\infty}\exp\left[\frac{-d}{\lambda_{S,A}(Cos\theta)}\right]} \qquad (2.5)$$

The angle θ in this equation is the emission angle of the excited electrons and is measured with respect to the surface normal. Factors I_A^{∞} and I_S^{∞} are peak intensities taken from samples of materials A and B of effectively infinite thickness. The parameters $\lambda_{A,A}$ and $\lambda_{S,A}$ are the effective attenuation lengths of electrons emerging from the overlayer and the substrate respectively [10]. The effective attenuation length (EAL) is known to differ from the inelastic mean free path (IMFP) due to elastic-scattering which causes the photoelectrons signal to decay in a non-exponential manner [11]. This variation from the IMFP value is dependant on the composition of the sample but, in general, changes in physical properties such as an increased density will result in a reduction of the EAL.

For the case of SiO_2 on Si, where the kinetic energy of the substrate and overlayer signals differ by approximately 4 eV the values $\lambda_{A,A}$ and $\lambda_{S,A}$ are approximately equal and can be replaced by a single term λ [10], making d the subject of the expression equation 2.6 is found.

$$d = \lambda\cos\theta\ln\left[1 + \frac{\left(\frac{I_A}{I_A^{\infty}}\right)}{\left(\frac{I_S}{I_S^{\infty}}\right)}\right] \qquad (2.6)$$

The ratio $\frac{I_S^\infty}{I_A^\infty}$ can be referred to as K [10,12,13] leaving;

$$d = \lambda \cos\theta \ln\left[1 + K\left(\frac{I_A}{I_S}\right)\right] \qquad (2.7)$$

As stated previously, equation 2.7 relates only to situations where the kinetic energy of the substrate and overlayer peaks are comparable. In this study equation 2.7 was used to calculate the thickness of Si oxide overlayers on Si, with the parameter K being found experimentally using SiO_2 and Si samples of effectively infinite thickness. A value for λ can be found in the literature [10].

Thickness calculations based on this method can be achieved using software such as NIST Electron EAL Database [14].

2.2 Synchrotron based photoemission

The principle of synchrotron based photoemission (SRXPS) is similar to that of conventional XPS, with the energy of emitted photoelectrons being analysed to determine the composition of a material. However, SRXPS allows for considerably improved resolution and greater surface sensitivity than conventional XPS.

Synchrotron radiation is characterised by:

- High brightness and high intensity, many orders of magnitude more than that offered by X-rays produced in conventional X-ray tubes
- High brilliance, exceeding other natural and artificial light sources by many orders of magnitude: 3rd generation sources typically have a brilliance greater than 10^{18} photons/s/mm^2/mrad^2/0.1%BW, where 0.1% BW denotes a bandwidth 10^{-3} ω centred on the frequency ω.
- High collimation, i.e. small angular divergence of the beam
- Low emittance, i.e. the product of source cross section and solid angle of emission is small
- Widely tuneable in energy/wavelength by monochromatisation (sub eV up to the MeV range)
- High level of polarization (linear or elliptical)

- Pulsed light emission (pulse durations at or below one nanosecond, or a billionth of a second)

Electrons are linearly accelerated and subsequently “injected” into a storage ring as shown in figure 2.8.

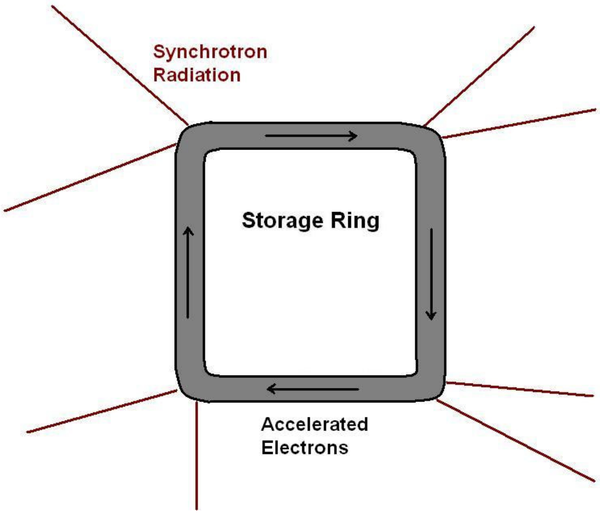

Figure 2.8 Schematic diagram showing how an electron beam emits synchrotron radiation when accelerated around the curved sections of a storage ring.

The change in electron momentum which occurs at the curved corners of the ring results in the emission of a broad spectral range of synchrotron radiation. This radiation is then extracted for use in beamlines, for a variety of techniques. The use of monochromators allows specific photon energies to be selected allowing for high resolution spectroscopy and maximum surface sensitivity, as the appropriate photon energy may be selected for a particular core level.

2.3 Atomic Force Microscopy

Atomic force microscopy (AFM) is a surface imaging technique, used to obtain topographical information from a sample surface at near atomic resolution [15]. The main benefit of AFM over other more sensitive techniques such as scanning tunnelling microscopy (STM) is that AFM may be used on a broader range of samples, including insulators, and may also be used in air. In the simplest terms, AFM operates by placing an atomically sharp tip at the end of a cantilever in close proximity to a sample surface and measuring the resultant force acting on the tip.

When two materials are brought into close proximity, inter-atomic forces are exerted between the two materials. AFM measures the magnitude of these forces, which include Van der Waals, electrostatic or magnetic forces, and uses it to determine characteristics of the surface being investigated [16].

The three modes of operation used for AFM are contact mode, tapping mode and non-contact mode. Contact mode AFM operates by scanning a tip, which is attached to the end of a cantilever, across the sample surface and monitoring the changes in cantilever deflection. The force acting on the tip and the resulting cantilever deflection can be related using Hooke's law; $F = -kx$, where k is the spring constant of the cantilever and x is the deflection. The value of k may range from 0.01 N/m to 1.0 N/m, resulting in forces ranging from nN to μN for ambient AFM [16]. The tip is brought to its operating position in two stages. Firstly, the user brings the tip to a height above the surface of approximately 1 mm, using an optical microscope system which is designed to focus on surface features at an image distance of 1 mm. The tip is then engaged using a piezoelectric motor which lowers the tip in increments of 10 μm (i.e. ~ 100 "steps"). The sample surface is then scanned by moving it under the tip using a piezoelectric scanner.

As the surface is moved beneath the tip the cantilever is deflected by forces exerted on it by the surface. These deflections are detected using laser light which is reflected from the back of the cantilever and onto a split photodetector, as shown in the diagram of operation in figure 2.9.

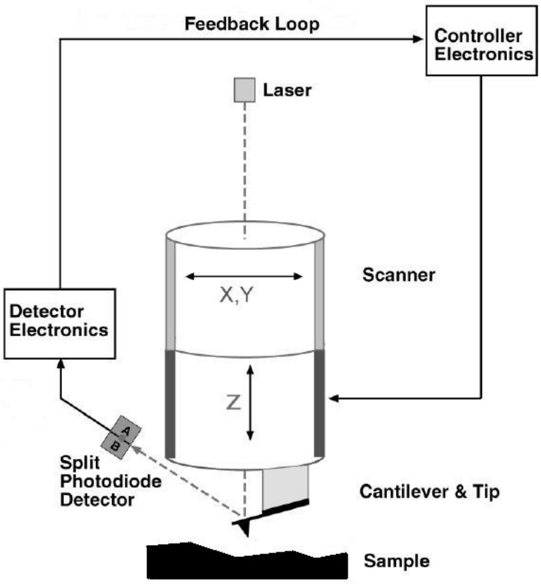

Figure 2.9 Operational diagram for AFM which shows how tip deflections are measured using laser light reflected from the back surface of the tip [16].

The deflection of the tip, as measured using the photodetector, and the measured force between the tip and the surface allow a topographic image of the surface to be generated.Using contact mode the surface may be scanned in two ways; either by keeping the tip position constant and monitoring the changes in cantilever reflection (constant height mode) or by maintaining a constant cantilever deflection by altering the position of the tip relative to the surface so as to keep a constant force between the two (constant force mode). Constant height mode is only used when the surface is known to be relatively flat so as to avoid tip damage due to surface contamination or abrupt changes in topography.

In tapping mode, the tip is scanned across the surface at the end of an oscillating cantilever. The frequency of oscillation is kept constant by altering the position of the tip relative to the surface, which is again monitored using the position of the deflected laser beam. The cantilever oscillates at or near its resonance frequency, with amplitude ranging typically from 20 nm to 100 nm [16]. The tip lightly taps the surface during scanning and only contacts the surface at the bottom of its swing. As such it is in contact with the surface less frequently that contact mode and is less susceptible to damage due to surface contamination. Non-contact mode is commonly used for soft samples, such as biological material, where physical contact may damage the surface. In this mode the cantilever oscillates above the surface, slightly beyond its resonant frequency. It operates by measuring the attractive Van der Waals forces which extend from 1 nm to 10 nm above the surface, altering the tip position in order to maintain constant oscillation frequency.

The atomic force microscope used in this study was a Dimension 3100 SPM equipped with an acoustic and vibration isolation hood and an anti-vibration table. All AFM images presented in this study were acquired using tapping mode. WSxM free software [17] was used to process the images, allowing information such as surface roughness and feature height to be acquired. Root mean square (RMS) surface roughness values quoted in this study are average values taken from a minimum of 8 sites across the sample surface.

2.4 Temperature programmed desorption

Thermal annealing of samples in UHV conditions increases the desorption rate of chemical species adsorbed on the surface, allowing them to be detected in the gas phase using conventional mass spectroscopy. By studying the temperature dependence of this desorption rate, information can be gained relating to the desorption energies of the surface adsorbates. As such, information relating to both surface composition and the nature of adsorbate-substrate bonding can be acquired using temperature programmed desorption (TPD) measurements [1].

In TPD experiments the temperature ramp rate is slow enough (~2 °C per second) to allow the desorbed species to be removed using the conventional vacuum pumping systems. As such the desorption of chemical species at a particular binding energy results in a peak in the pressure-temperature curve, as shown in figure 2.10.

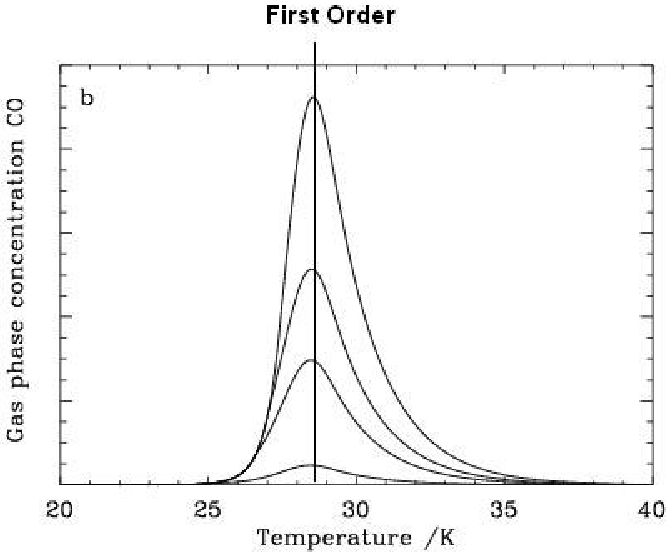

Figure 2.10 Typical TPD desorption curve [18]

Therefore, a peak in the thermal desorption spectrum at temperature T indicates a maximum desorption rate at that temperature. The spectra in figure 2.10 shows an asymmetric TPD peak which is indicative of first order desorption. First order desorption is characterised by a linear dependence of desorption rate on the number of surface species available for desorption [1]. While increased temperature increases the likelihood of desorption, this is counteracted by the continual decrease in surface coverage. These competing factors cause the peak asymmetry seen in figure 2.10 [19].

The main feature of first order desorption is that the peak position is independent of surface coverage.

If a species desorbs reassociatively (i.e. subsequent to a chemical reaction) then a requirement for desorption is the presence of suitable atoms adjacent to each other [1]. The probability of this is depends on the concentration of surface atoms squared, which defines the process of second order desorption. As such second order desorption peaks may vary considerably with surface concentration, moving to lower temperature with higher concentration level. The binding energy (E_d) of desorbed species can be related to the desorption peak temperature in Kelvin (T_{max}) using the Redhead equation [20];

$$E_d = RT_{\max}\left[\ln\left(\frac{\nu T_{\max}}{\beta}\right) - 3.46\right] \qquad (2.10)$$

where R is the gas constant (8.314 J mol^{-1} K^{-1}), and β is the heating rate $\left(\beta = \frac{dT}{dt}\right)$.

The term ν is the frequency factor, which is assumed to be of the same order of magnitude as the molecular vibrational frequency (10^{13} s^{-1}) [19]. It should be noted that Eqn. 2.10 relates only to first order desorption where the value of ν/β is between 10^8 and 10^{13} K^{-1}, and also makes the assumption that the frequency factor is not dependant on surface coverage [1]. However, despite such assumptions the equation is widely used, and forms the basis for quantitative analysis of TPD spectra [19]. It has been shown that factors such as non-uniform heating rate and inadequate pumping speed can broaden desorption peaks and prevent accurate analysis of desorption binding energies [1]. Therefore, it is vital to ensure that the method used to heat the sample provides a heating rate which is linear with time. Also, heating should ideally be restricted to the sample, so as to avoid thermal desorption from other surfaces within the vacuum chamber.

2.5 Transmission electron microscopy

Cross-sectional transmission electron microscopy (TEM) allows the metal oxide/semiconductor interfacial regions investigated in this thesis to be imaged using near atomic resolution. The resolution achieved using TEM is most simply explained using the classical Rayleigh criterion for light microscopy, which gives the minimum distance which can be resolved (δ) using light of wavelength λ.

$$\delta = \frac{0.61\lambda}{n \sin \theta} \tag{2.11}$$

where n is the refractive index and θ the collecting angle of the lens.

This equation shows that the resolution of an instrument may be improved by reducing the wavelength λ. Therefore, the comparatively small wavelength of high velocity electrons allows far greater resolution than that achieved using optical microscopy. While the resolution of the technique can be explained by comparison with visible light, it should be remembered that the electron is a charged particle and as such can be easily deflected or scattered when passing close to other electrons or the positively charged nucleus of an atom [21]. Electrons are commonly generated using thermionic emission and accelerated using high voltage (100 ~ 300 kV), before being focused towards the sample using a system of magnetic lenses [21].

Image contrast in TEM images can be obtained based on both the particle and wave properties of the electron. Electrons passing atoms of higher atomic number or thicker regions within the sample may not reach the detector due to absorption events. This will result in dark regions within the TEM image, allowing investigation of the structure and atomic composition of the sample. Diffraction contrast uses the Bragg scattering of electrons from crystalline regions within the sample. Scattering changes the angular distribution of the electrons, allowing them to be detected separately from unscattered electrons. As such, crystalline regions may be identified as bright regions within the image [21].

2.6 Electrical Characterisation

In Chapter 1 the concept of MOSFET devices was introduced, along with the motivations for introducing new semiconductor and gate dielectric materials. The electrical measurement techniques used to characterise devices fabricated from these new materials are outlined in this section. In this study the electrical characteristics of metal oxide semiconductors (MOS) capacitors are discussed in terms of capacitance-voltage (C-V) and current-voltage (I-V) measurements. The techniques are discussed in terms of the theoretical basis for the measurements, and the information which can be derived from them.

2.6.1 Capacitance – Voltage (C-V)

A typical C-V curve, taken from a high-*k* dielectric (5 nm MgO) on Si, is shown in figure 2.11.

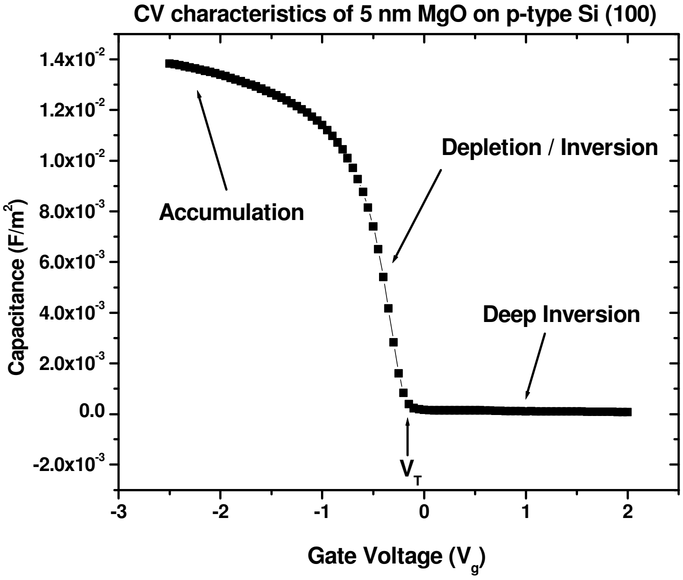

Figure 2.11 C-V characteristics of 5 nm MgO on p-type Si showing accumulation, depletion and inversion regions within the curve profile.

Measured C-V curves such as this allow information to be deduced relating to the dielectric constant of the gate oxide, the interfacial state density, the effects of charge trapping and the presence of Fermi level pinning at the dielectric/semiconductor interface. This information is obtained by analysing the changes in the MOS capacitance as the polarity and magnitude of the applied voltage is varied to sweep the device between the accumulation, depletion and inversion regions, as shown in figure 2.11.

The concept of accumulation, depletion and inversion within a MOS device can be described using electron energy band diagrams. Initially it is best to consider the idealised case of a perfect MOS device and subsequently discuss the problems caused by real surfaces. Figure 2.12 shows the band diagram for an ideal p-type MOS device, which may be essentially viewed as a parallel plate capacitor.

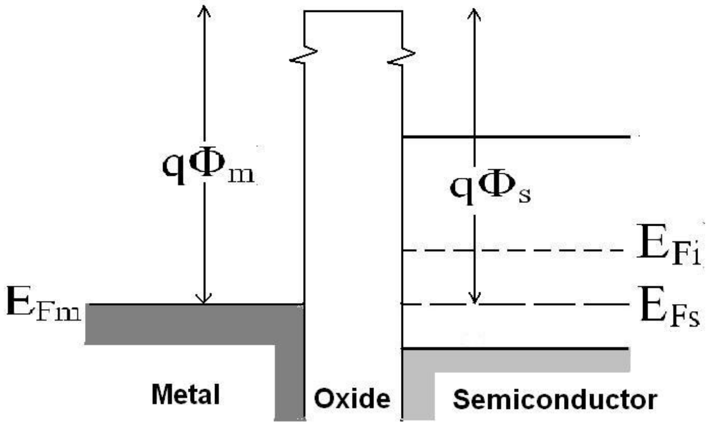

Figure 2.12 Energy band diagram for ideal p-type MOS capacitor.

While the workfunction of a metal is usually defined as the energy required to move an electron from the electron Fermi level (E_{Fm}) to outside the metal, in this case it is more relevant to define a modified work function ($q\Phi_m$) measured from E_{Fm} to the conduction band of the oxide. It should be noted that in this idealised case the metal and semiconductor workfunctions are taken to be equal ($q\Phi_m = q\Phi_s$) [22]. Given that this is a p-type semiconductor it can be seen that its Fermi level (E_{Fs}) lies close to the valence band and below the intrinsic level (E_{Fi}). This is of some importance to subsequent discussions, as it is the Fermi level position relative to the intrinsic level which defines the conduction properties of the device.

If on the above device a negative voltage is applied to the metal, electrons accumulate on the “metal plate” of the capacitor. This causes a corresponding number of positively charged holes to accumulate at the semiconductor-oxide interface, referred to as accumulation [23] as shown in figure 2.13.

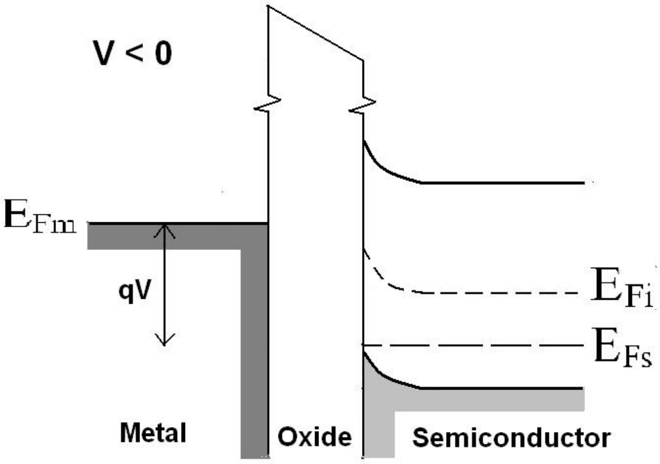

Figure 2.13 Application of a negative voltage on the metal gate causes the accumulation of holes at the semiconductor/oxide interface which results in a maximum capacitance value within the measured C-V profile.

The applied voltage (V) acts to raise the metal Fermi level above that of the semiconductor by a value qV, however, the work function values do not change with applied voltage thus causing a slope in the oxide conduction band. The bending of the semiconductor energy bands, seen in figure 2.13, can be explained in reference to the increased concentration of holes at the semiconductor surface. Using the density of states function (which gives the number of available energy states within the band structure) and the Fermi-Dirac equation (which gives the probability that these states will be occupied by an electron) an equation for hole concentration (p) can be found

$$p = n_i e^{\left(\frac{E_i - E_F}{kT}\right)} \tag{2.12}$$

where k is the Boltzman constant, T is the temperature in Kelvin and n_i is the intrinsic electron concentration [22].

Given that no current passes through the oxide layer, there can be no variation in the semiconductor Fermi level [22]. As such, the value of E_i - E_F in eqn. 2.12 may only be increased by the intrinsic level moving up the bandgap. This results in the band bending seen in figure 2.13, and essentially means that in accumulation the semiconductor surface becomes more “strongly” p-type as E_F now lies closer to the valence band edge.

Accumulation in MOS capacitors is evidenced by a maximum capacitance (C_{max}) level in the C-V curve (figure 2.11). In the ideal case the C_{max} in accumulation should be determined by the dielectric properties of the oxide, allowing the dielectric constant (*k*) of the oxide to be obtained using the simple parallel plate capacitor equation;

$$C_{\max} = \frac{\kappa \varepsilon_0 A}{d} \qquad (2.13)$$

where A is the device area, d is the thickness of the oxide and ε_0 is the permittivity of free space. However, the presence of a low *k* interfacial oxide region may place another capacitance value in series with that of the oxide making it more difficult to determine the dielectric properties of the oxide.

If the polarity of the voltage is changed the Fermi level of the metal is lowered with respect to that of the semiconductor, tilting the oxide conduction band in the opposite direction to that seen previously (figure 2.14).

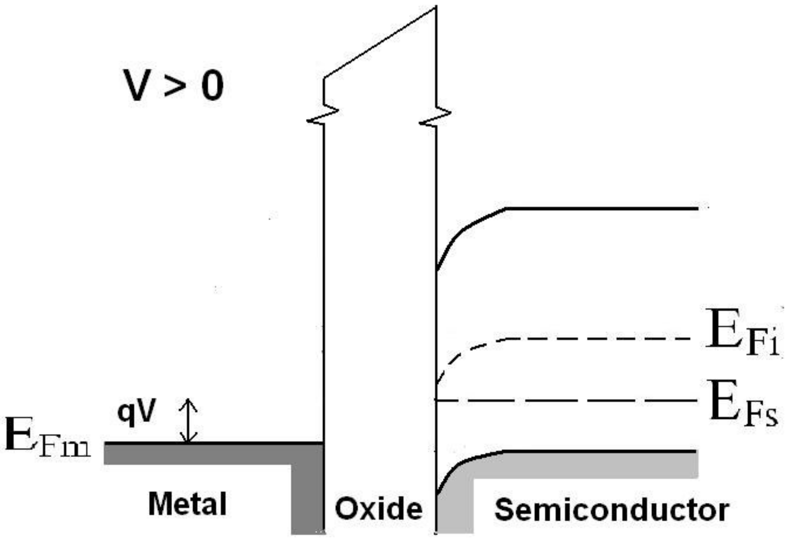

Figure 2.14 Energy band diagram showing depletion in MOS capacitors. Application of a positive voltage depletes the semiconductor surface of majority carriers.

This voltage applies a positive charge to the metal plate, and attempts to form a corresponding negative charge at the semiconductor-oxide interface. As electrons are the minority carriers in p-type semiconductors this negative charge is formed by the "depletion" of holes from the region near the surface, which leave behind uncompensated, negatively charged acceptors [22]. The creation of hole/electron pairs forms a depletion region which is analogous to that seen for p-n junction diodes [23]. The formation of this deletion region means that the concentration of holes at the semiconductor surface is reduced. This causes E_i to be lowered closer to E_F, as seen in equation 2.12. If the strength of this voltage is further increased the bands continue to bend, causing E_i to bend below E_F as shown in figure 2.15.

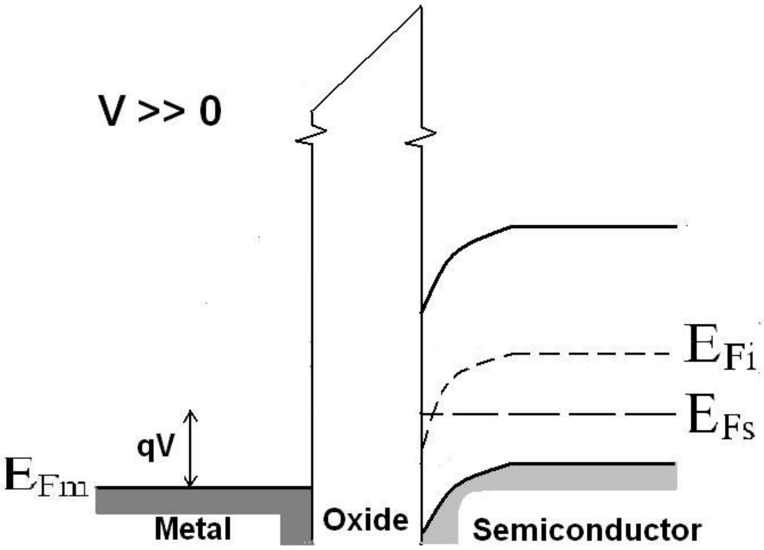

Figure 2.15 Inversion is achieved once the Fermi level at the semiconductor surface lies above the intrinsic level, forming an "inverted" n-type surface.

In this situation it can be said that the conduction properties of the surface have been inverted and are now the same as an n-type material. This results in an inversion region at the semiconductor surface which is separated from the p–type bulk by a depletion region. The case of strong inversion occurs when the surface region becomes as strongly n-type as the bulk material is p-type. Therefore, by moving the semiconductor Fermi level with respect to the intrinsic position, a p-type device may be converted into an n-type device (or vice-versa) by simply applying a voltage. Depletion and inversion are shown by a reduction in the measured capacitance of the C-V curve. In the ideal case the minimum capacitance value indicates strong inversion, which occurs at a threshold inversion V_T (figure 2.11). Thus far the operation of MOS capacitors has been discussed in terms of ideal structures. However, the following discussion will focus on common electrical defects and how they can be identified using C-V measurements.

In the ideal case, shown in figure 2.12, it can be seen that no band bending occurs prior to the application of an external voltage. However, factors such as differences in the metal and semiconductor workfunctions, and the presence of interfacial charge, can result in band bending under equilibrium conditions (V = 0). Therefore, a voltage must be applied in order to return the device to flat band conditions. The voltage required to achieve this is referred to as the flat band voltage (V_{FB}) and is discussed again in this chapter in reference to I-V characterisation. In extreme cases the band bending may be large enough to create an inversion region at the surface without applying an external voltage, which may lead to the transistor device defaulting to the "On" position. Such band bending in equilibrium is indicated by a "horizontal" voltage shift in the C-V curve [22].

Defects at the semiconductor-oxide interface may create a measurable capacitance that may be viewed as another parallel plate capacitor, in series with the oxide capacitance and in parallel with that of the semiconductor. While the measured capacitance in accumulation will still be dominated by the oxide properties, if the density of interfacial defects (D_{IT}) is sufficiently large it may contribute to the measured total capacitance during depletion and inversion. This deforms the profile of the C-V curve, creating bumps similar to that shown in figure 2.16.

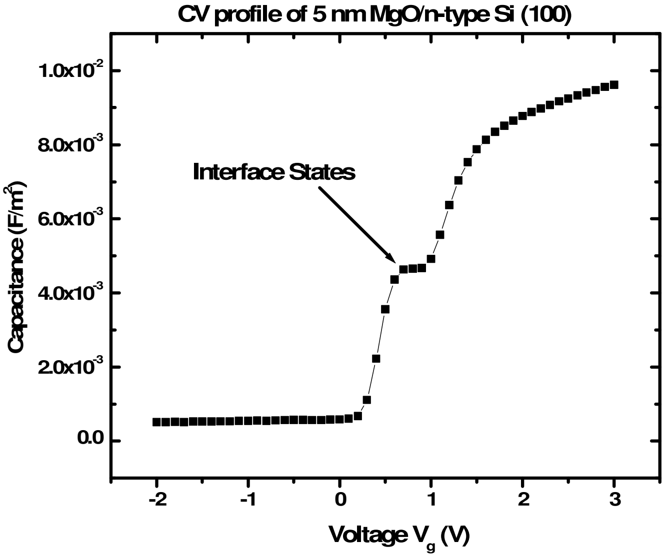

Figure 2.16 C-V profile, taken from 5 nm MgO on Si, showing "bump" due to interfacial defect states.

While conductance measurements are more commonly used to determine D_{IT} [24], densities higher than ~ 10^{12} cm^{-2} may be easily measured using C-V. The effect of these defects states can be further analysed using C-V curves taken successively over a range of measurement frequencies (e.g. 1 kHz – 1 MHz). The frequency dispersion measurements in figure 2.17 show how defect states become more prominent at low frequency, as more charge can "follow" the voltage variation as the frequency of oscillation is reduced.

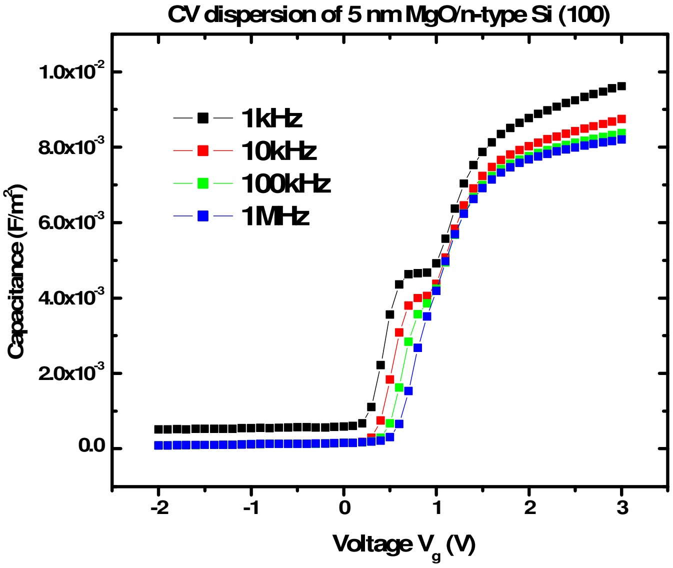

Figure 2.17 Frequency dispersions C-V profiles showing the increased interface state contribution with decreasing measurement frequency.

Frequency dispersion such as that shown in figure 2.17 can be quantified based on the capacitance change measured as a function of changing frequency. This value is then expressed as a percentage, as shown in equation 2.14;

$$\Delta v = \frac{C_{low} - C_{high}}{C_{low}} \times 100 \qquad (2.14)$$

where C_{low} and C_{high} respectively refer to the C_{max} values recorded for the lowest and highest measurement frequencies used, i.e. with respect to figure 2.17 C_{low} corresponds to 1 kHz and C_{high} corresponds to 1 MHz.

High defect state densities are commonly seen for high-*k* materials on Si, and may be reduced by the use of forming gas annealing which acts to passivate interfacial dangling bonds [25].

C-V characterisation is also commonly used to measure the effects of Fermi level pinning in MOS devices. As shown previously, in order to achieve inversion the semiconductor Fermi level must be moved through the band gap with respect to the intrinsic level. However, the presence of defect energy states within the bandgap may prevent this movement, acting to "pin" the Fermi level. As such, the device may not be able to reach accumulation or inversion or indeed both, depending on the density and energy position of defect states within the bandgap. This is evidenced by a reduction in the difference between the maximum and minimum capacitance values measured from the C-V curve [26]. As such, in pinned devices the C_{min} value may not represent true inversion in the device, and may simply represent the lowest level of depletion achievable. Similarly C_{max} values taken from pinned devices may not represent the dielectric properties of the oxide layer as the Fermi level may not be free to move across the band gap and allow majority carriers to accumulate at the interface. Fermi level pinning is most commonly seen subsequent to metal oxide deposition onto III-V semiconducting materials, and is indicative of high interface state density (D_{IT}) and poor interface quality [27,28].

2.6.2 Current-Voltage (I-V)

I-V characterisation of MOS capacitors measures the leakage current which occurs as a result of direct electron tunnelling through the oxide layer. The bandgap of the oxide material creates a potential energy barrier to the flow of electrons. As such, the band off-sets between the semiconductor and oxide act to determine the probability of electron tunnelling. Also, as described in Chapter 1, the probability of quantum mechanical electron tunnelling is also exponentially dependant on the thickness of the potential barrier and as such is strongly affected by the physical thickness of the oxide.

While the exact mechanisms of leakage current flow are beyond the scope of this study, the insulating properties of the dielectric material may be investigated by determining leakage current density using I-V measurements. Leakage current values quoted in this study are measured at "V_{FB}+1" i.e. 1 volt beyond the flat-band voltage towards accumulation. The flat-band voltage is found from the measured C-V curve, using a theoretical calculation of the flat-band capacitance, C_{FB};

$$C_{FB} = \frac{C_{OX} C_{Si-FB}}{C_{OX} + C_{Si-FB}} \tag{2.15}$$

where C_{OX} is the maximum capacitance value taken from the C-V curve and $C_{Si\text{-}FB}$ is the theoretically calculated capacitance contribution from the Si substrate in flat-band conditions;

$$C_{Si-FB} = \frac{\varepsilon_0 \kappa_{Si}}{L_{D-Si}} \tag{2.16}$$

where ε_0 is the permittivity of free space (8.854 × 10^{-12} F/m) and κ_{Si} is the relative permittivity of Si (11.8). The term L_{D-Si} is the Debye length of silicon, a value which relates to the distribution of charge carriers within highly doped substrates, calculated using the following equation;

$$L_{D-Si} = \sqrt{\frac{\varepsilon_0 \kappa_{Si} kT}{q^2 N_d}} \tag{2.17}$$

where, k is Boltzman's constant (1.38 × 10^{-23} m^2 kg s^{-2-} K^{-1}), T is the measurement temperature in Kelvin, q is the electronic charge (1.6 × 10^{-19} C) and N_d is the substrate doping. Using equations 2.15 – 2.17 the flatband capacitance can be calculated, and this value can be related to the flatband voltage using C-V characteristics measured from the device.

As current flow through the oxide increases a direct conduction path may be formed, resulting in dielectric breakdown. This is evidenced by a sharp increase in the slope of the I-V plot, as shown in figure 2.18.

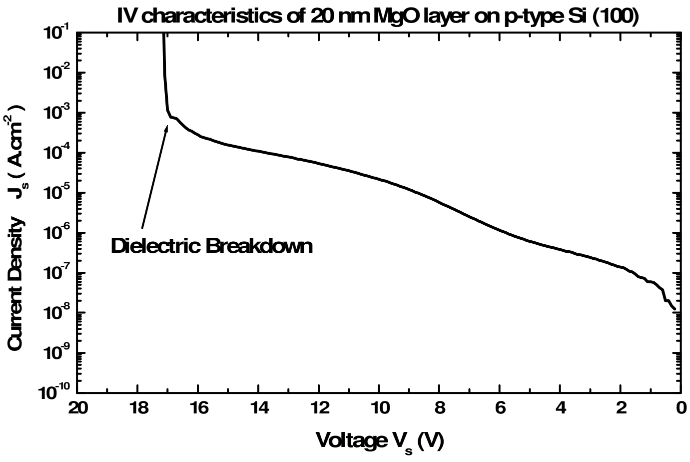

Figure 2.18 I-V characteristics of 20 nm MgO on p-type Si showing dielectric breakdown at ~ 17 V.

The mechanism by which dielectric breakdown occurs is again beyond the scope of this study, however, the dielectric strength of the oxide may be investigated based on the measured breakdown voltage. The measured breakdown voltage is a direct measure of the lifetime of potential MOS devices, and as such is important in the analysis of dielectric materials.

I-V characteristics are of particular relevance to investigating the structural morphology of gate dielectric materials. For example, certain metal oxide thin films have been shown to crystallise during rapid thermal annealing, as described in Chapter 1. The grain boundaries associated with these poly-crystalline films are known to act as effective breakdown paths, which reduce the lifetime of potential MOS devices. As such, the effects of sample processing can be investigated using I-V characterisation, based on both the leakage current density and breakdown voltage values measured from the device. While several of the papers which have emerged from this thesis [29-32] focus on the dielectric breakdown properties of MgO, these experimental results are not included as they were performed by colleagues elsewhere.

2.7 References

[1] D.P. Woodruff, T.A. Delchar, Modern techniques of surface science, Cambridge Solid State Science Series (1986)

[2] http://upload.wikimedia.org/wikipedia/commons/f/f2/System2.gif

[3] L. C. Feldman, J. W. Mayer, Fundamentals of surface and thin film analysis, Elsevier Science Publishing Co., Inc. (1986)

[4] D. Briggs, J. T. Grant. “Surface Analysis by Auger and X-ray Photoelectron Spectroscopy” IM Publications, (2003)

[5] S. Oktyabrsky, V. Tokranov, M. Yakimov, R. Moore, S. Koveshnikov, W. Tsai, F. Zhu, J.C. Lee, Materials Science and Engineering B **135**, 3 (2006) 272-276

[6] G. Alvarez, H.J. Silverstone, Phys. Rev. A, **40** (1989) 3690

[7] C. D. Wagner, L. E. Davis, M. V. Zeller, J. A. Taylor, R. M. Raymond and L. H. Gale, Surf. Interface Anal. **3** (1981) 211

[8] M.P. Seah and S. J. Spencer, Surf. Interface Anal. **33** (2002) 640

[9] D. Briggs, M.P. Seah, Practical Surface Analysis: volume 1, Auger and X-ray Photoelectron Spectroscopy, Wiley, Chichester, 1990

[10] R.G. Vitchev, J.J. Pireaux, T. Conard, H. Bender, J. Wolstenholme, Chr. Defranoux, Appl. Surf. Sci. **235** (2004) 21–25

[11] A. Jablonski, C.J. Powell, Surface Science Reports **47** (2002) 33

[12] F. J. Himpsel, F.R. McFreely, A. Taleb-Ibrahimi, J.A. Yarmoff and G. Hollinger, Phys. Rev. B **38**, (1988) 6084

[13] R.G. Vitchev , Chr. Defranoux , J. Wolstenholme, T. Conard, H. Bender, J.J. Pireaux, Journal of Electron Spectroscopy and Related Phenomena **149** (2005) 37–44

[14] C.J. Powell, A. Jablonski, W.S.M. Werner, W. Smekal, Appl. Surf. Sci., **239** (2005) 470

[15] J. C. Vickerman, Surface analysis : the principal techniques, Wiley, (1997)

[16] Digital Instruments, Veeco Metrology Group, Nanoscope scanning probe microscope training manual (1999)

[17] http://www.nanotec.es/products/wsxm/index.php

[18] Astronomy and Astro physics anada.org

[19] G. Attard and C. Barnes, Surfaces, Oxford Chemistry Primers (1998)

[20] P.A. Redhead, Vacuum **12** (1962) 203

[21] D.B. Williams and C.B. Carter, Transmission Electron Microscopy, Volume 1, Plenum Publishing Corporation (2001)

[22] Ben G. Streetman, Solid State Electronic Devices, 2nd Edition, Prentice-Hall Inc., Englewood Cliffs, New Jersey 07632.

[23] Adir Bar-Lev, Semiconductors and Electronic Devices 2nd Edition, Prentice-Hall International

[24] L. Yan, C. M. Lopez, R. P. Shrestha, E. A. Irene, A. A. Suvorova and M. Saunders, Appl. Phys. Lett. **88** (2006) 142901

[25] M. Schmidt, M. C. Lemme, H. Kurz, T. Witters, T. Schram, K. Cherkaoui, A. Negara and P.K. Hurley, Microelectronic Engineering **80** (2005) 70–73

[26] Z. Fu, S. Kasai, H. Hasegawa, Applied Surface Science **190** (2002) 298–301

[27] M. Passlack, J.K. Abrokwah, R. Droopad, Yu Zhiyi, C Overgaard, S. In Yi, M. Hale, J. Sexton, A.C. Kummel, *Electron* Device Letters, IEEE **23**, no.9, (2003) 508-510

[28] J. Robertson, Reports on Progress in Physics, **69** (2006) 327–396

[29] R. O'Connor, G. Hughes, P. Casey, S. Newcombe Journal of Applied Physics **107** (2010) 024501

[30] E. Miranda, É. O'Connor, K. Cherkaoui, S. Monaghan, R. Long, D. O'Connell, P.K. Hurley, G. Hughes, P. Casey Applied Physics Letters **95** (2009) 012901

[31] E. Miranda, É. O'Connor, G. Hughes, P. Casey, K. Cherkaoui, S. Monaghan, R. Long, D. O'Connell, P.K. Hurley Microelectronic Engineering **86** (2009) 1715–1717

[32] E. Miranda, J. Martin-Martinez, É. O'Connor, G. Hughes, P. Casey, K. Cherkaoui, S. Monaghan, R. Long, D. O'Connell, P.K. Hurley Microelectronics Reliability **49** (2009) 1052–1055

Chapter 3

Experimental Details

3.1 Ultra High Vacuum Chambers

XPS analysis carried out in this study was performed in the two separate ultra high vacuum chambers located in Dublin City University, shown in figure 3.1.

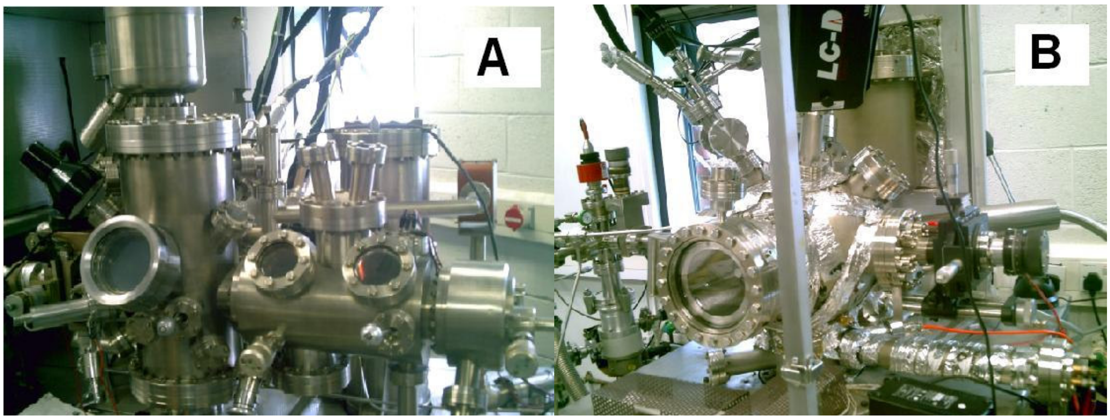

Figure 3.1 Three chambered dedicated XPS system shown in figure 3.1A. Surface analysis chamber in figure 3.1B is equipped with XPS, mass spectrometer, H-cracker, mini e-beam evaporator and thermal evaporation system.

The UHV system seen in figure 3.1A is a three chambered UHV system consisting of a load lock (~10^{-2} mbar), preparation chamber (~10^{-7} mbar) and analyser chamber (~10^{-10} mbar). A standard bakeout procedure of ~ 140 °C for 12 hours was used to achieve the optimum vacuum. This system allows for comparatively fast introduction of *ex-situ* prepared samples into UHV, and was used in this study for the ambient stability investigations in Chapter 4. The system is pumped using diffusion pumps backed by rotary pumps and was used as a dedicated XPS analysis system, as no surface preparation or thin film deposition was carried out in this chamber.

The system shown in figure 3.1B is a dedicated surface analysis chamber which allows for *in-situ* sample preparation and analysis. A base pressure of approximately 10^{-10} mbar was routinely achieved following a similar bakeout procedure to that described above, with pumping carried out by a turbo molecular pump backed by a rotary roughing pump and a titanium sublimation pump. Sample heating was achieved *in-situ* in two ways, and was used for surface cleaning and annealing studies. Using the first method Si (111) and InP (100) wafers were fixed to a sample stub, which could be heated *in-situ* up to ~ 550 °C using resistive current heating. Sample temperature was measured by calibrating the heating stub using a thermocouple attached directly to the sample. *In-situ* annealing of Si samples to higher temperatures ($\leq$ 1200 °C) was achieved by passing a current directly through boron doped (2-5 $\times 10^{19}$ cm^{-3}) Si (111) wafers with a resistivity of 1-3 mΩ·cm. A pyrometer was used to measure sample temperatures greater than 550 °C. The chamber is also equipped with a multipocket mini e-beam and thermal evaporation sources for thin film deposition, as well as a hydrogen cracker used for surface preparation and mass spectrometer used to monitor thermal desorption.

The XPS system consisted of a dual anode X-ray source (Mg and Al) and a Vacuum Generators (VG) CLAM electron energy analyser operating at a 20 eV pass energy, yielding an overall resolution of 1.2 eV. A graphic representation of the X-ray source is shown in figure 3.2.

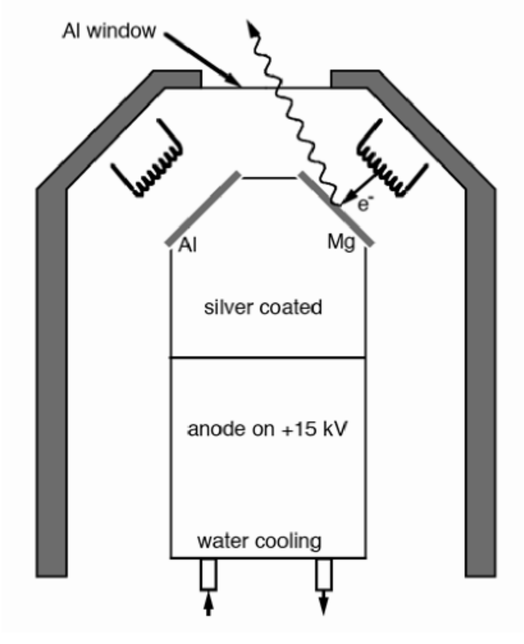

Figure 3.2 Diagram showing the operation of a dual anode X-ray source [1]

High voltage (10 - 15 keV) cathodes bombard the Mg and Al sources with high energy electrons, creating a continuous Bremstrahlung energy distribution. The anode source must be watercooled during operation in order to avoid damage due to excess heating. X-rays are emited at peak intensities from the respective sources (Mg $K\alpha$ =

1253.6 eV and Al *Kα* = 1486.6 eV). While the use of an X-ray monochromator can reduce the line width to ~ 0.3 eV, the non-monochromated system used in these studies has a line width of ~ 0.7 eV for the Mg source and ~ 0.85 for the Al source [2,3]. Bremshtralung radiation produced along with the x-ray signal is partially removed by placing an Al foil (~ 2 μm thick) at the exit aperture of the X-ray source, while radiation which is not removed adds to the background of the spectrum.

X-rays striking the sample surface result in the emission of photoelectrons, as described in Chapter 2. These photoelectrons are collected and analysed using a VG CLAM electron energy analyser, similar to that schematically shown in figure 3.3.

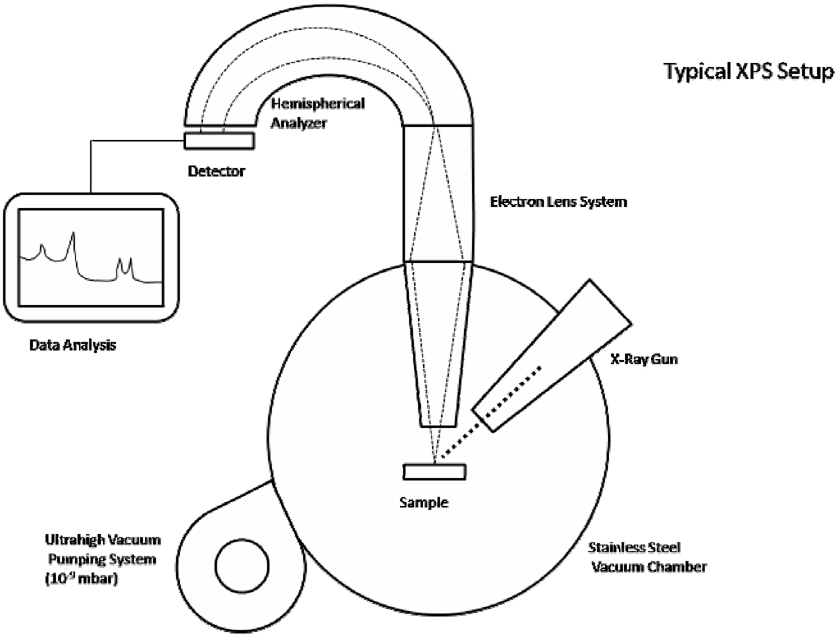

Figure 3.3 Schematic diagram of an XPS analysis system, showing how electrons are focused into the analyser system [4].

The electrostatic field generated by a system of two electron lenses acts to successively focus electrons to a point within the analyser system [5]. As the kinetic energy of the electrons greatly affects the focal point of the lens system, electrons first pass through a fine mesh grid which is held at a negative potential known as the retarding voltage. This restricts the kinetic energy of the electrons to a range called the pass energy, which is in this study was 20 eV. Given that the kinetic energy of electrons emitted from the sample commonly varies by up to ~ 1100 eV, the retarding voltage applied to the grid must be continually changed in order to ensure that all electrons have the same pass energy which is essential to achieve uniform resolution across the spectrum.

Electrons focused by the lens system then enter a hemispherical electron energy analyser, as shown in figure 3.3. The voltage applied to the two hemispheres is adjusted to ensure that only electrons which enter the analyser with the correct pass energy are allowed through the analyser to be detected and amplified in the channeltron. Electrons which enter with kinetic energies different from the pass energy are lost to collisions within the hemispheres, and as such do not contribute to the measured photoelectron signal.

Synchrotron based photoemission vacuum system

SRXPS studies were performed at the Astrid synchrotron in the University of Aarhus, Denmark, using the SGM1 beamline. The ultrahigh vacuum system consists of a preparation chamber (5×10^{-10} mbar) and an analysis chamber (2×10^{-10} mbar). A schematic diagram of the Astrid synchrotron is shown in figure 3.4.

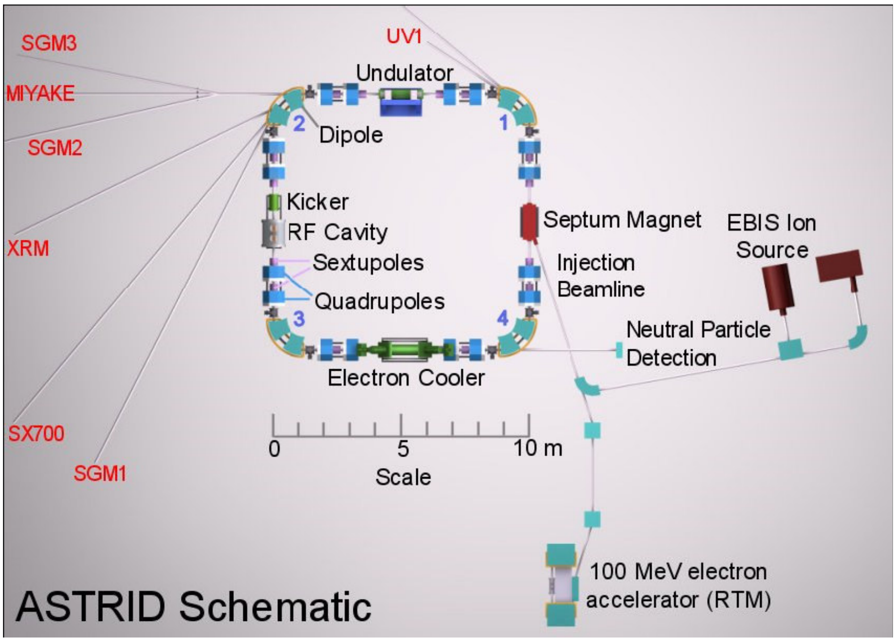

Figure 3.4 Diagram of the ASTRID synchrotron in Aarhus, Denmark.

In the photoemission system, the SCIENTA SES-200 electron energy analyzer collects photoelectrons over a solid angle of 8 ° centered at 40 ° from the direction of the incoming photons. The SGM monochromator and the SCIENTA analyzer were set up such that the combined instrumental resolution was 70 meV for the Si 2p acquired with 130 eV photons. A conventional XPS system, similar to that described above, was used to acquire the O 1s (BE ≈ 530 eV) core level spectra, due to the limited energy range of the synchrotron radiation produced in the SGM1 beamline.

3.2 Deposition Techniques

3.2.1 Electron Beam Deposition

Electron beam (e-beam) evaporation is a physical vapour deposition technique. The target material is thermally heated and evaporated using a high energy electron beam. Electrons are generated by passing a current (~ 5 A) through a tungsten filament, and accelerated towards the source using high voltage (2-5 kV). The electron beam is directed towards the source using a system of electro-magnets which bend the beam through an angle of ~ 270 °, as shown in figure 3.5, in order to prevent line of site contamination of the source material from the tungsten filament. The hearth, in which the crucible used to hold the source material sits, is generally water cooled in order to prevent excess heating.

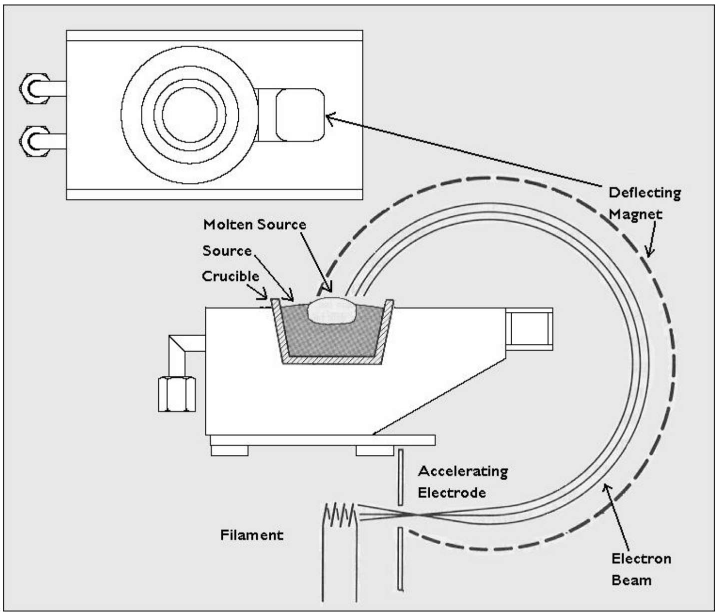

Figure 3.5 Schematic diagram of e-beam deposition showing the generation of electrons which are accelerated towards the source material using high voltage and a system of electro magnets [6].

Three different e-beam systems were used in this study. The first is a Ferrotec EV-1-8 electron beam evaporator, held within a dedicated deposition chamber which allowed the deposition of films at a base pressure of ~ 1×10^{-6} mbar. Given that this system was not equipped with any analysis techniques, all films were exposed to air after deposition, and as such this system was used to deposit films for the ambient stability studies in Chapter 4. The second e-beam evaporator used in this study was a similar system located in the Tyndall National Institute, in University College Cork, which was primarily used in the fabrication of metal-oxide-semiconductor (MOS) structures for electrical characterisation. This system was equipped with a double pocket source which allowed for the sequential deposition of two different materials without breaking vacuum. In both of these systems, the electron beam was focused directly onto the source material, with the size and direction of the electron beam being altered as required to achieve uniform heating of the source. The deposition rate, typically 0.01 nm/s, was monitored using a thin film deposition monitor which could be calibrated for each material used.

The final e-beam system used in this study was an Oxford Applied Research EGC04 mini e-beam evaporator four pocket source, which allowed for *in-situ* deposition and analysis of various thin films in the UHV chamber described above. The mini e-beam differed from those mentioned previously in that the electron beam did not impinge directly onto the source material, instead heating the crucibles which contained the evaporant. A diagram of the mini e-beam evaporator is shown in figure 3.6.

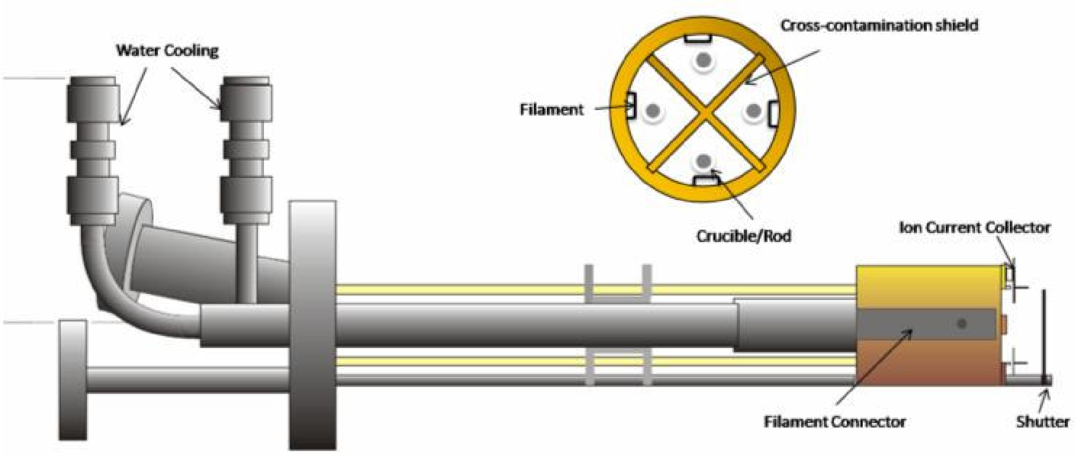

Figure 3.6 Diagram of the multi-pocket Oxford Applied Research EGC04 mini e-beam evaporator used in this study [7].

During the experimental studies carried out in this work, it was found that when the electron beam is focused directly onto polycrystalline MgO pellets stoichiometric MgO films are deposited. However, when the same source material is used in the mini-beam system just described, non-uniform heating of the pellets within the crucible occurs, resulting in dissociation of the MgO which resulted in the deposition of partially metallic films. This is attributed to the fact that the MgO pellets do not melt during deposition, and therefore thermal energy from the crucible is not uniformly distributed throughout the source. Materials such as Cu, Si and Mn were all successfully deposited using the mini e-beam system.

3.2.2 Thermal/hot wire deposition

In this process the source material is contained in a tantalum pouch which is wrapped in a tungsten or tantalum filament, and resistively heated by passing a current through the filament [8]. This thermal deposition method is appropriate for metals with low melting temperatures (e.g. Mg), and the use of high purity (typically >99.9%) source material results in the deposition of highly pure thin films. Metal oxide films were grown by the evaporation of metals in an oxygen background pressure (5×10^{-7} mbar) which allows the metal to oxidise on the sample surface and form metal oxide films, which were measured to be stoichiometric using conventional XPS. Given that stoichiometric MgO films could not be deposited using the mini e-beam system described in section 3.2.1, *in-situ* analysis of MgO films was achieved by evaporating metallic Mg in an oxygen partial pressure using the hot wire deposition method.

3.3 Spectral analysis of photoemission peaks

Curve fitting of photoemission spectra is used to obtain information relating to both the elemental and chemical composition of the sample surface. It has been shown in chapter 2 that it is often possible to identify elements using the binding energy position of the photoemission peaks. However, given that contributions from different chemical species within a core level spectrum tend not to be separated by more than 5 eV, these peaks are often unresolved within the spectrum.

Therefore, in order to further analyse the different chemical states contained within the peak profile the spectrum must be de-convolved into a series of component peaks, each of which relating to a specific bonding environment. All curve fitting analysis presented in this study was carried as an iterative process using the AAnalyser software [9]. XPS core level spectra were curve fitted using Voigt profiles composed of Gaussian and Lorentzian line shapes in a 3:1 ratio and using a nonlinear Shirley-type background to account for the rise in the spectral background due to the emission of secondary electrons.

To achieve an accurate curve fit it is important to obtain accurate fitting parameters as a starting point. An example of this is the Si 2p spectrum shown in figure 3.7, which was acquired from an ultra-thin (~ 1 ML) Si oxide on a silicon surface using synchrotron based XPS. It can be seen from figure 3.7 that the measured "raw" spectrum is difficult to identify as the sum of the component peaks overlays it almost completely. It should be noted that curve fitted spectra presented throughout this study do not distinguish between the raw spectrum and the sum of the component peaks. As such, it situations where the sum overlays the raw spectrum it is taken to be a measure of the accuracy of the peak fit.

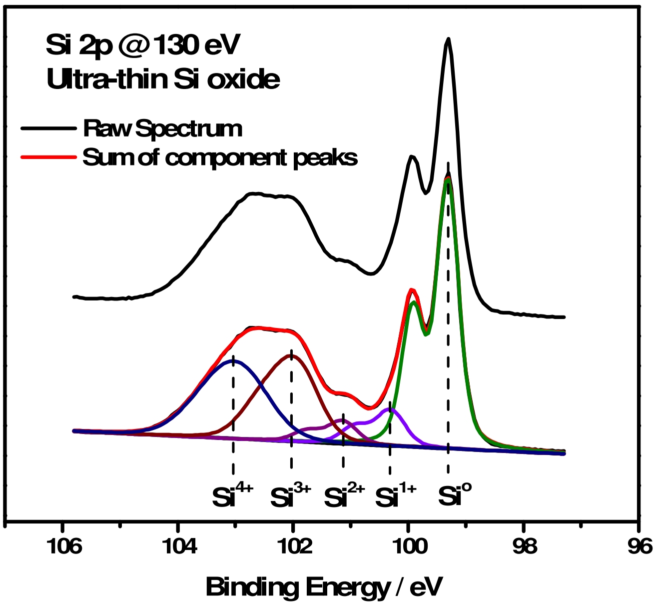

Figure 3.7 Raw and curve fitted Si 2p spectra taken from an ultra-thin Si oxide layer using SRXPS. Curve fitting allows contributions from bulk Si (Si^{o}) and each of the four silicon oxidation states to be identified.

It is known that each component within the Si 2p spectrum is a doublet, with a spin-orbit splitting of 0.61 eV and an intensity ratio of 2:1 for the 2p 3/2 and 1/2 features. The full width half maximum (FWHM) of each component peak is a combination of both Lorentzian and Gaussian components. The Lorentzian width is related to the intrinsic lineshape which relates to a specific core level independent of chemical composition. As such, for the spectra in figure 3.7, the Lorentzian line width can be linked and will be the same for each component. The Gaussian width is principally affected by instrumental broadening but may also depend on the chemically homogeneity of a particular bonding state. As such, the Gaussian profile acts as a direct measure of the disorder within the local bonding environment, with more chemically disordered surfaces showing broader Gaussian peak widths.

Himpsel *et al.* have reported a binding energy separation of ~0.9 eV between the Si bulk peak (Si^o) and each of the four Si oxidation states [10], however variations of ± 0.2 eV have also been reported [11]. Therefore, these separation values were fixed only for the initial stages of analysis, before allowing a best fit to be obtained. The curve fitting parameters used in figure 3.7 are summarised in table 3.1.

	Position	**Gaussian FWHM**	**Lorentzian FWHM**	**Peak Area**	**Spin-Orbit Splitting**
Si^o	99.33 eV	0.33 eV	0.18 eV	43.9 %	0.61 eV*
Si^{1+}	100.32 eV	0.45 eV	0.18 eV *	6.8 %	0.61 eV*
Si^{2+}	101.15 eV	0.44 eV	0.18 eV *	4.4 %	0.61 eV*
Si^{3+}	101.95 eV	0.79 eV	0.18 eV *	22.8 %	0.61 eV*
Si^{4+}	102.90 eV	1.02 eV	0.18 eV *	22.1 %	0.61 eV*

Table 3.1 Peak fitting parameters relating to the Si 2p spectrum in figure 3.7, with * indicating a value which was fixed during the fitting process.

These parameters are used throughout this study as the starting point for curve fitting Si 2p spectra obtained using SRXPS. While increases in the Gaussian width can be attributed to chemical disorder, excessively large widths often indicate the presence of another chemical state. This may necessitate the addition of further component peaks, which must be justified with reference to published results, electronegativity values or thermodynamic data. As instrumental broadening may greatly affect photoemission line widths, the parameters used for synchrotron studies may differ substantially from those used for spectra taken using standard XPS. Curve fitted Si 2p spectra taken from a Si native oxide surface using standard XPS, and the relevant fitting parameters, are shown in figure 3.8 and table 3.2.

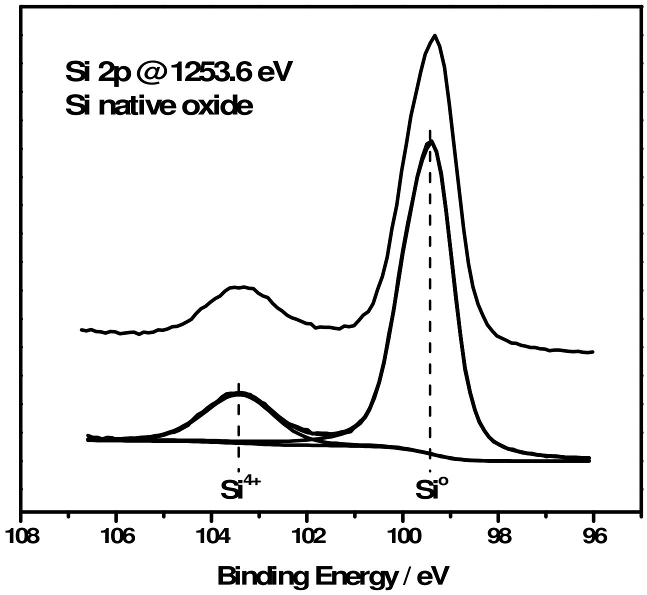

Figure 3.8 Raw and curve fitted Si 2p spectra taken from a Si native oxide surface using conventional XPS.

	Position	**Gaussian FWHM**	**Lorentzian FWHM**	**Peak Area**	**Spin-Orbit Splitting**
Si°	99.30 eV	0.77 eV	0.30 eV	82.8 %	0.61 eV*
Si^{4+}	103.23 eV	1.28 eV	0.30 eV *	17.2 %	0.61 eV*

Table 3.2 Peak fitting parameters relating to the spectrum in figure 3.8. The reduced surface sensitivity of conventional XPS allows on the Si^{4+} oxidation state to be resolved.

It can be seen that only the Si^{4+} oxidation component is used for the curve fit in figure 3.8. This is due to a combination of reduced resolution and decreased surface sensitivity of standard XPS compared to SRXPS. This is further evidenced by curve fitted Si 2p spectra taken from the same surface using both conventional and synchrotron based XPS (figure 3.9).

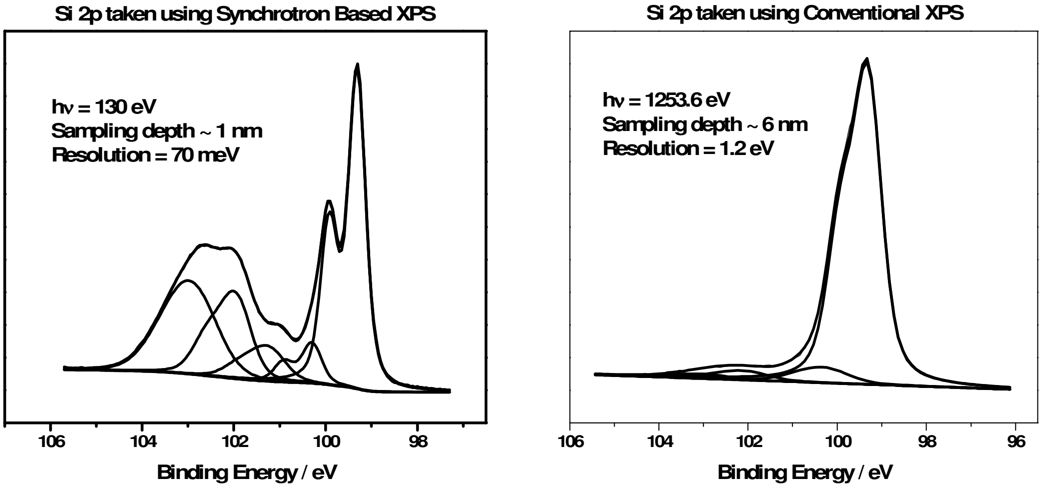

Figure 3.9 Si 2p spectra taken from the same ultra-thin (~ 0.3 nm) Si oxide layer, using both synchrotron based and conventional XPS. Differences between the spectra clearly show the increased resolution and surface sensitivity achieved using SRXPS.

The parameters in table 3.2 are again used throughout this study for Si 2p spectra taken using standard XPS.

Apart from the Si 2p, the main core level spectra analysed in this study using curve fitting are the In 3d and P 2p peaks taken from InP. As there are comparatively few photoemission studies within the literature which relate to InP, in comparison to the Si system, both oxidised and oxide free InP surfaces were studied in order to obtain reliable peak fitting parameters for the In 3d and P 2p spectra, as discussed in further detail in Chapter 6.

3.4 Surface Preparation methods

3.4.1 Standard organic cleaning of semiconductor surfaces

Prolonged exposure to ambient conditions results in the formation of predominantly carbon based impurities on the surface of semiconducting substrates. In this study the cleaning method used to remove these impurities consisted of successive 1 minute dips in acetone, methanol and isopropyl alcohol (IPA), with samples being subsequently dried using N_2 gas. This procedure was used to clean both Si and InP native oxide surfaces, however, it should be noted that XPS spectra taken in this study suggest that the procedure does not remove or alter the chemical composition of the oxide layers.

3.4.2 Flash cleaning

Atomically clean Si surfaces were prepared, for *in-situ* analysis in the UHV systems shown in figure 3.1B and 3.4, using a method referred to as flash cleaning. Low resistivity boron doped p-type Si (111) samples of resistivity 1-3 mΩ·cm (doping concentration 2-5 × 10^{19} cm^{-3}) were used for flash cleaning experiments. Following standard organic cleaning the native SiO_2 was removed by *in-situ* direct current flash heating of the silicon sample to temperatures greater than 1100 °C. This results in desorption of the SiO_2 leaving an oxygen free surface, as previously reported [10,12,13]. It should be noted that SRXPS spectra taken at ASTRID beam line showed no evidence for the presence of either O 2s or C 1s core level spectra after flash cleaning, suggesting that surfaces prepared using this method were in fact atomically clean.

3.4.3 Atomic hydrogen cleaning

Atomic hydrogen (H*) cleaning of III-V semiconducting materials allows surface contaminants (commonly oxide and carbonate) to be removed at lower temperatures than that found for thermal annealing alone [15]. Exposing GaAs native oxide surfaces to atomic hydrogen at high temperature has been shown to form volatile surface oxides [15] while further studies have examined the desorption mechanism which takes place during cleaning [16]. Commonly used atomic hydrogen sources operate by passing H_2 gas through a hot tungsten filament, and the atomic hydrogen created is subsequently directed onto the sample surface.

In this study atomic hydrogen was generated using an Oxford Applied Research TC-50 Thermal Gas Cracker, using a total hydrogen partial pressure ($H^* + H_2$) equal to 1 × 10^{-7} mbar. A schematic diagram of the TC-50 cracker is shown in figure 3.10.

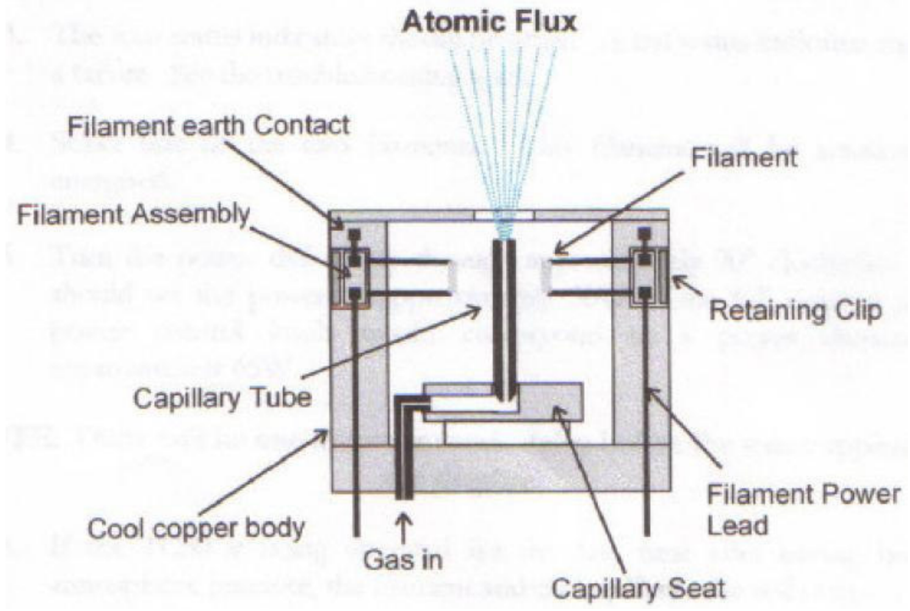

Figure 3.10 Schematic diagram of the Applied Research TC-50 Thermal Gas Cracker. The capillary tube design allows for higher efficiency and lower temperature operation than the conventional W filament design.

The instrument uses electron-beam induced heating of a metallic capillary through which H_2 gas is passed before entering the UHV chamber, a design which is in contrast to the commonly employed W filament based systems. The capillary tube acts to confine the gas species, whilst creating a large surface area and long path length for high efficiency cracking at lower temperature than that achieved by W filament devices. The cracker system is water cooled in order to prevent outgassing due to excessive thermal heating.

3.5 MOS Device Fabrication

Electrical results presented in this study were acquired from n and p-type Si (100) wafers with a doping concentration of 10^{15} cm^{-3}, and n and p-type InP (100) wafers with a doping concentration of 3-5 × 10^{18} cm^{-3}. MgO based MOS capacitors were fabricated at the Tyndall National Institute, Cork, using two procedures, namely Pd metallisation and fully silicided (FUSI) Ni metallisation. The Pd metallisation process was used for initial electrical characterisation of MgO thin films on silicon, discussed in Chapter 4. The FUSI process was used in all subsequent electrical characterisation studies in Chapter 4, along with the analysis of MgO films on InP which are presented in Chapter 6. In both cases MgO thin films were deposited onto Si or InP semiconducting substrates using electron beam evaporation, in the deposition chamber described in section 3.2.1. MgO deposition was carried out using polycrystalline MgO pellets (purity 99.9 %) at an elevated temperature of ~ 180 °C, a chamber pressure of 1×10^{-6} mbar, a deposition rate of 0.01 nm/s and without the addition of O_2 to the chamber. Using the Pd metallisation technique MgO films were subsequently exposed to ambient conditions for approximately 10 minutes prior to metallisation. This process involved wet chemical surface preparation followed by the deposition of Pd (~ 100 nm) using e-beam evaporation. Individual capacitor structures were subsequently defined using wet chemical lithography.

The FUSI metallisation process involved the *in-situ* deposition of a (~ 100 nm) Si capping layer immediately after MgO deposition, ensuring that the MgO films were not exposed to ambient conditions. Electrical characterisation of these structures was facilitated by depositing Ni (~ 80 nm) onto the Si capping layer and annealing to 500 °C for ~ 30 seconds, to form Ni silicide. Individual capacitor structures were again defined using wet chemical lithography, however, it is important to stress that the wet chemicals used do not contact the measured devices during the lithographic processing of FUSI devices. Figure 3.11 shows an optical microscope image of the lithographical mask used to define capacitor structures.

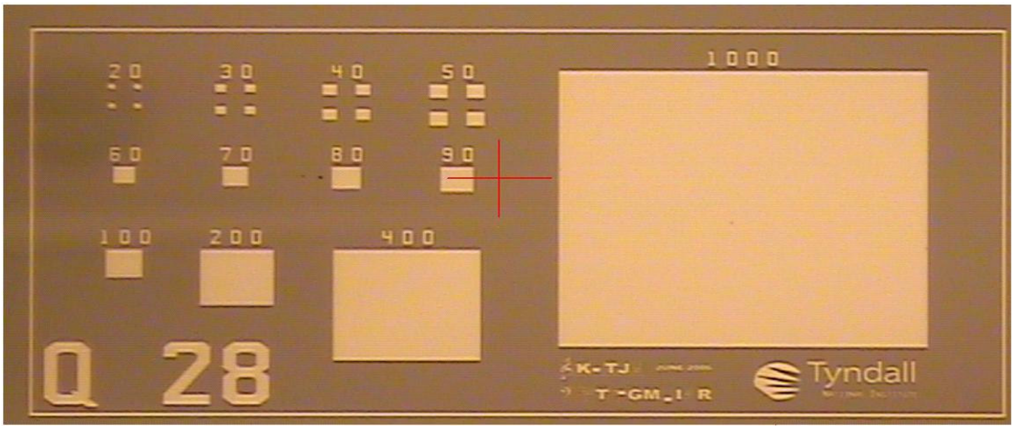

Chapter 3.11 An Optical microscope image of the lithographical mask which was used in this study to define individual capacitor structures ranging in device area between 20 μm × 20 μm and 1000 μm × 1000 μm.

While capacitor structures ranging between 20 µm × 20 µm and 1000 µm × 1000 µm were defined, all C-V and I-V measurements presented in this study were acquired from sites with a device area of 50 µm × 50 µm. The FUSI process used in this study is similar to that outlined by Shickova *et al.* [17].

The differences between the FUSI and Pd metallisation processes can be summarised as follows;
MgO films metallised using the FUSI process were not exposed to ambient conditions, or to wet chemical surface preparation. However, FUSI devices did experience thermal annealing (500 °C for ~ 30 seconds) as part of the FUSI process. Conversely MgO films metallised using the Pd process were exposed to both ambient conditions and wet chemical surface treatments, and did not experience any post deposition annealing.

The singular exception to the fabrication procedures outlined above is that of a MgO/InP based device prepared using atomic hydrogen (H*) cleaning, the I-V characteristics of which are presented in Chapter 6 figure 6.16. This alternative fabrication process was necessary as the deposition chamber used to fabricate all other devices, could not attain the vacuum levels required to perform H* cleaning. The device was prepared using the InP H* cleaning procedure outlined in Chapter 6, followed by subsequent deposition of ~10 nm MgO using the thermal evaporation of metallic Mg in an oxygen partial pressure (as described in section 3.2.2). The sample was then exposed to ambient conditions for ~10 minutes prior to the deposition of a Ni gate electrode (~ 100 nm) through a shadow mask, using electron beam evaporation. The shadow mask was used to define individual transistor devices with an area 50 µm × 50 µm, which allowed subsequent I-V analysis.

3.6 Electrical Characterisation of MOS devices

The electrical measurements presented in this study were performed at room temperature in a microchamber controlled environment (Cascade Microtech Summit 12000 Theta) using a HP4156A and a HP4284A for I-V and C-V analysis. C-V characterisation was performed at a measurement frequency of 100 kHz, apart from frequency dispersion measurements performed in a range of 1 kHz to 1 MHz. The device area used for all electrical characterisation was 50 μm × 50 μm. For both C-V and I-V measurements a voltage was applied to a metal chuck which was in direct electrical contact with the semiconducting substrate under analysis, as this configuration is known to reduce noise within the measurement. While the I-V measurements shown in this study are plotted using the applied substrate voltage (V_s), capacitance measurements are plotted against gate voltage (V_g) in agreement with convention (where $V_g = V_s \times -1$). I-V characteristics in this study are typically taken for negative substrate voltage ranges on n-type devices, and positive V_s ranges on p-type devices i.e. "towards accumulation". It should also be noted that all capacitance measurements presented in this study are plotted as a function of device area, i.e. in units of F/m^2.

3.7 References

[1] http://eapclu.iap.tuwien.ac.at/~werner/images/t_exp_pho.gif

[2] J. C. Vickerman, Surface analysis : the principal techniques, Wiley, (1997)

[3] D.P. Woodruff, T.A. Delchar, Modern techniques of surface science, Cambridge Solid State Science Series (1986)

[4] http://iramis.cea.fr/Images/astImg/508_2.jpg

[5] D.W.O. Heddle, Electrostatic Lens Systems, Adam Hilger, (1991)

[6] http://cleanroom.byu.edu/metal.parts/gun.jpg

[7] http://www.oaresearch.co.uk/oaresearch/brochures/EGSeries.pdf

[8] J.S. Corneille, J.W. He, D.W. Goodman, Surf. Sci., **306**, (1994) 269

[9] AAnalyzer: A. Herrera-Gomez, http://qro.cinvestav.mx/~aanalyzer/

[10] F. J. Himpsel, F.R. McFreely, A. Taleb-Ibrahimi, J.A. Yarmoff and G. Hollinger, Phys. Rev. B **38** (1988) 6084

[11] F. Jolly, F. Rochet, G. Dufour, C. Grupp, A. Taleb-Ibrahimi, Surface Science **463** (2000) 102–108

[12] P. Morgen, A. Bahari, U. Robenhagen, J. F. Anderson, J. –K. Hansen, K. Pedersen, M. G. Rao, Z. S. Li, J. Vac. Sci. Technol. A **23** (1) (2005) 201

[13] I. Jiménez J. L. Sacedón, Surface Science **482-485** (2001) 272-278

[14] G.R. Bell, N.S. Kaijaks, R.J. Dixon, C.F. McConville, Surface Science 401 (1998) 125–137

[15] M. Yamada, Y. Ide, K. Tone, Jpn. J. Appl. Phys. **31** (1992) L1157

[16] M. Yamada, Y. Ide, Jpn. J. Appl. Phys. **33** (1994) L671

[17] A. Shickova, B. Kaczer, A. Veloso, M. Aoulaiche, M. Houssa, H. Maes, G. Groeseneken, J.A. Kittl, Microelectronics Reliability **47** (2007) 505–507

Chapter 4

Characterisation of MgO as a high-*k* candidate on silicon

4.1 Introduction

Magnesium Oxide (MgO) has been proposed as an alternative gate dielectric due to its large bandgap (7.8 eV) and high thermal stability. While having a dielectric constant (8.6) which is just over twice that of silicon dioxide [1], it has the attribute of being chemically very stable which should reduce the chemical reactivity at the silicon surface promoting the formation of abrupt interfaces. The large bandgap has the potential to ensure band offsets of sufficient magnitude to minimise leakage currents. MgO has also been suggested as a possible high-*k* replacement for SiO_2 for high power transistor applications on SiC due to its relatively high thermal conductivity [2]. Yan *et al.* [1] have recently reported that MgO films deposited on silicon substrates, by sputter depositing magnesium metal in an oxygen partial pressure, reveal sharp interfaces with interface state densities comparable with the SiO_2/Si system.

In this study three main factors relating to electron beam (e-beam) deposited MgO deposition and dielectric characterisation were investigated. The ambient stability of MgO thin films deposited onto Si (111) substrates using e-beam evaporation was studied. These investigations show that exposure to ambient conditions results in the rapid formation of hydroxide and carbonate species on the MgO surface. Electrical characterisation of 5 nm and 20 nm MgO films exposed to ambient conditions show poor capacitance scaling and high ($>1 \times 10^{12}$ cm^{-2}) interface state density. Poor capacitance scaling is attributed to hydroxide and carbonate growth prior to metallisation.

MOS structures were subsequently fabricated using MgO/Si layers with fully silicided top contacts in order to prevent the effects of ambient exposure. Electrical characterisation of these structures show improved capacitance scaling and considerably reduced interfacial sate density. Chemical analysis of the MgO/Si interface formation was investigated using standard x-ray photoelectron spectroscopy (XPS) and high resolution synchrotron radiation based core level photoemission measurements. Results suggest that MgO deposition onto both H-terminated and silicon oxide surfaces results in the formation of a magnesium silicate interfacial region with an approximate thickness of less than 1 nm. Thermal annealing studies suggest the growth of Mg silicate at 500 °C, and show no evidence for the growth of interfacial SiO_2.

4.2 Experimental Procedure

Metal oxide semiconductor (MOS) capacitor structures were fabricated in the Tyndal national institute on native oxide and H-terminated Si surfaces, using the procedures described in Chapter 3, section 3.5. Hydrogen terminated Si (100) surfaces were prepared by dipping n and p type (100) Si wafers (10^{15} cm^{-3}) in a solution of 5 % hydrofluoric (HF) acid for 1 minute. Samples were subsequently dried using N_2 gas and loaded into the high vacuum (HV) e-beam deposition system where MgO films were deposited. Initial electrical characterisation was carried out on MOS structures fabricated using the Pd based metallisation process described in Chapter 3, section 3.5 which resulted in MgO films being exposed to ambient conditions for approximately 10 minutes prior to Pd deposition. The fully silicided (FUSI) metallisation process, described in the same section of Chapter 3, was used on subsequent devices to avoid the effects of ambient exposure on the MgO surface. The electrical measurements on the Si (100)/MgO/Pd structures were performed using the apparatus and procedure outlined in Chapter 3, section 3.6. X-ray photoelectron spectroscopy (XPS) was carried out on MgO films fabricated at the same time and subject to the same procedures as those prepared for electrical characterisation. The XPS analysis was carried using the VG Microtech electron spectrometer described in Chapter 3, section 3.1, using the Mg Kα (hν = 1253.6 eV) X-ray source. Synchrotron based photoemission studies were carried out on the SGM1 beamline at the Astrid synchrotron in the University of Aarhus in an ultrahigh vacuum (UHV) system, the operation of which has also been described in Chapter 3. Atomic Force Microscopy (AFM) analysis was performed in ambient conditions using a Digital Instruments Dimension 3100 AFM. All AFM images were acquired using tapping mode and the surface roughness data was taken from at least ten different 2 μm × 2 μm areas of the surface. Temperature programmed desorption (TPD) measurements were carried out by monitoring the intensities of atomic masses 61 ($Mg(OH)_2$) and 84 ($MgCO_3$) in a

Dycor quadrupole mass spectrometer during a thermal anneal at a heating rate of 2 °C per second.

Section 4.3 Initial electrical characterisation and ambient stability of MgO thin films on Silicon

4.3.1 Initial electrical characterisation of Pd/MgO/Si (100) MOS structures

In order to investigate the electrical characteristics of MgO thin films, MOS capacitors with nominal MgO thicknesses of 20 nm and 5 nm were fabricated on both native oxide and the hydrogen terminated silicon (100) surfaces. These structures were metallised using the Pd based procedure described in Chapter 3, and were not subjected to post deposition thermal annealing.

I-V characteristics, taken from both the n-type and p-type 20 nm devices, are shown in figure 4.1.

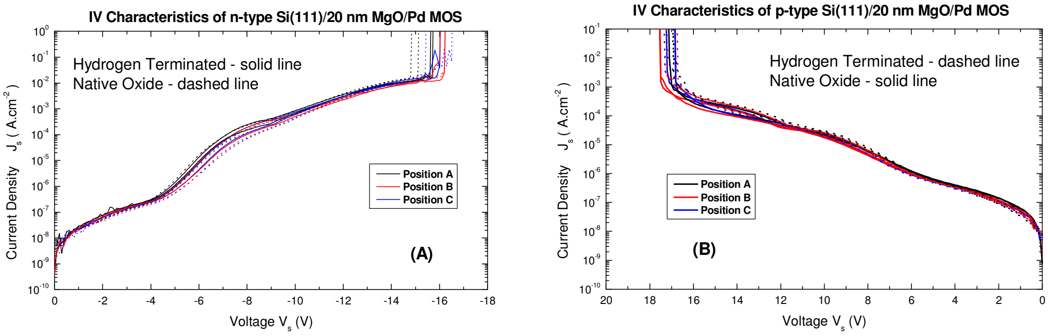

Figure 4.1 I-V characteristics taken from n-type (A) and p-type (B) Si(111)/20 nm MgO/Pd MOS structures, without post deposition anneal. The measurements are taken from films deposited on Si native oxide and hydrogen terminated Si surface.

The measurements show excellent repeatability across the wafer, indicating a consistent film uniformity resulting from the e-beam deposition technique. The I-V profiles of native oxide samples show no significant difference to those of the HF etched samples, possibly due to the thickness of the MgO film. There is also a strong correlation between the measurements taken from the p-type and n-type Si, both of which have a breakdown voltage of approximately 16 V. This relates to a dielectric breakdown field of ~ 8 × 10^6 V/cm for the 20 nm MgO films, a value close to that reported for SiO_2 (~ 10^7 V/cm) [3,4].

While 20 nm dielectric films are significantly thicker than the ideal thickness for transistor device application, the results are promising, particularly given that few studies exist within the literature for MgO films thinner than 100 nm [5]. I-V measurements taken from the 5 nm MgO films are displayed in figure 4.2, with the relevant leakage current density values shown in table 4.1.

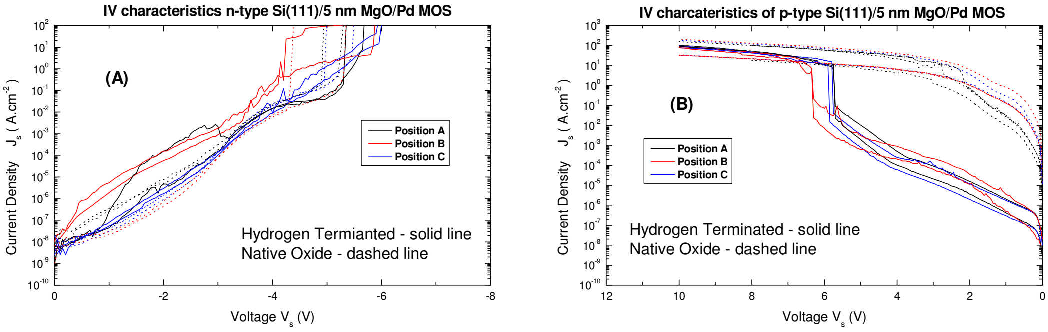

Figure 4.2 I-V characteristics taken from n-type (A) and p-type (B) Si(111)/5 nm MgO/Pd MOS structures, without post deposition anneal. The measurements are taken from films deposited on Si native oxide and hydrogen terminated Si surface.

Pd Lift-Off Devices	**Native Oxide (n) (A.cm^{-2})**	**H-Terminated (n) (A.cm^{-2})**	**Native Oxide (p) (A.cm^{-2})**	**H-Terminated (p) (A.cm^{-2})**
20 nm	2.5 × 10^{-8}	1.5 × 10^{-8}	6.6 × 10^{-8}	6.6 × 10^{-8}
5 nm	1.3 × 10^{-7}	1.6 × 10^{-7}	9 × 10^{-2}	8.2 × 10^{-7}

Table 4.1 Leakage current density values taken at V_{FB}+1 from 20 nm and 5 nm films on Si, metallised using Pd wet chemical lithography. The method by which the flatband voltage (V_{FB}) was calculated is described in Chapter 2, Section 2.6.2.

I-V curves show a greater variation in terms of repeatability with high levels of noise present in the curves. A pronounced difference is also observed between I-V profiles of the native oxide and HF etched samples for the p-type substrates, with the native oxide surfaces showing considerably higher leakage currents. This difference in behaviour is not understood and was not pursued in subsequent work. The breakdown field of these 5 nm films was calculated to be ~ 1 × 10^7 V/cm, a similar value to that found for the 20 nm films.

C-V measurements taken from the same 20 nm and 5 nm films deposited onto n-type native oxide and H-terminated surfaces, are shown in figure 4.3.

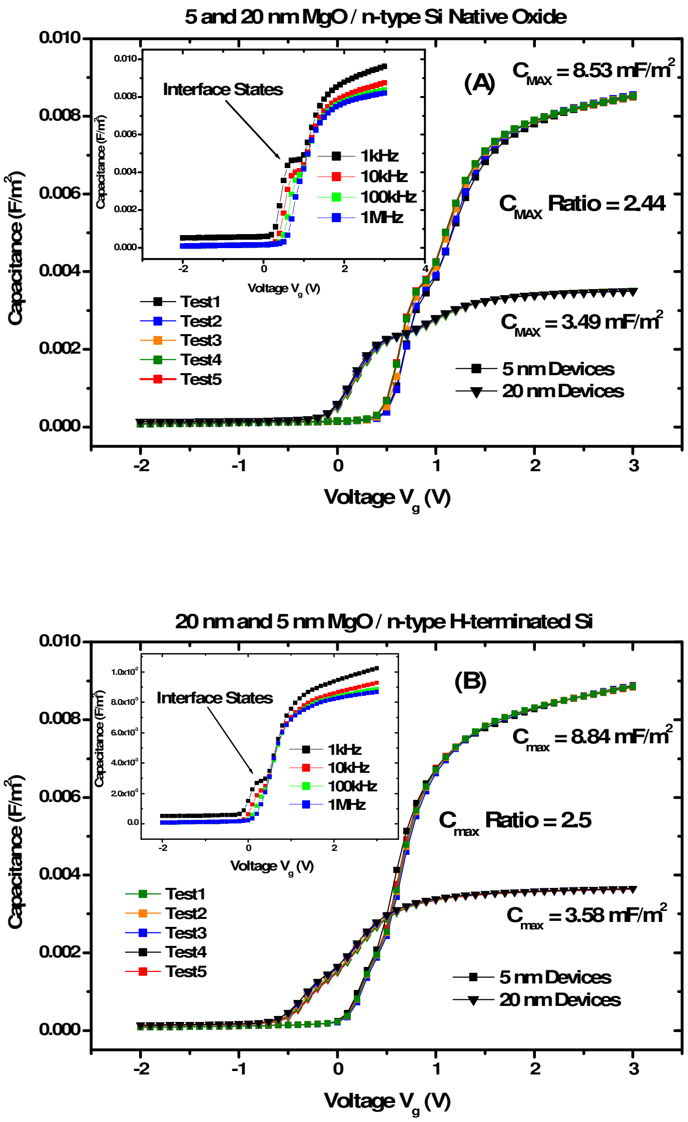

Figure 4.3 C-V characteristics taken from 20 nm and 5 nm MgO films deposited on n-type Si (100) native oxide (A) and H-terminated surfaces (B). High (>1 × 10^{12} cm^{-2}) interface state density is indicated by "bumps" on C-V and frequency dispersion measurements taken from the 5 nm devices are also shown (inset).

The C-V curves from the n-type devices show excellent repeatability for both the 20 nm and 5 nm films. The presence of interface states is evidenced by "bumps" within the C-V curves along with prominent frequency dispersion (inset). The total charge related to these interfacial states can be calculated as the product of the relevant capacitance and voltage values from the specific point on the C-V curve. The interfacial state density (D_{IT}) may then be estimated based on this interfacial charge value, along with the device area (2.5×10^{-5} cm^2) and the electronic charge (1.6×10^{-19} C). The D_{IT} of the 5 nm H-terminated device is calculated below based on the prominent bump within the CV curve (C = 2.70 F/m^2, V = 0.53 V);

$$2.70\ \mathrm{F/m^2} \text{ relates to } 6.75 \times 10^{-12}\ \mathrm{F} \text{ for } (50\ \mu\mathrm{m})^2 \text{ device}$$

$$Q = C \times V$$

$$Q = (6.75 \times 10^{-12}) \times (0.53) = 3.58 \times 10^{-12}\ \mathrm{C}$$

$$D_{IT} \approx \frac{3.58\times10^{-12}}{\left(1.6\times10^{-19}\right)\left(2.5\times10^{-5}\right)}$$

$$D_{IT} \approx 1 \times 10^{12}\ \mathrm{cm^{-2}}$$

Using this method the interfacial state density for these devices was estimated to be ~ 1×10^{12} cm^{-2}. Such levels of interface state density are commonly observed on films which have not been subjected to a post deposition forming gas (90 % N_2 + 10 % H_2) anneal, which acts to reduce D_{IT} by passivating electrically active interface defects [6].

The maximum capacitance (C_{max}) ratio taken from the 20 nm and 5 nm films is equal to 2.4. A C_{max} ratio of less than the ideal value of 4 would be expected from 20 nm and 5 nm films deposited onto native oxide surfaces, given that the dielectric constant of the native SiO_2 (3.9) reduces the overall capacitance of the device. However, the H-terminated devices show a similar trend to that seen by the native oxide surfaces. The C-V dispersion measurements also show evidence for frequency dependency in the measured maximum capacitance values, indicative of high interface state density. For the 5 nm H-terminated devices in figure 4.3 B, this C_{max} dispersion has been quantified as 14 % of the C_{max} value at 1 kHz. The C-V characteristics of 20 nm and 5 nm MgO films deposited onto p-type native oxide and H-terminated Si (100) surfaces, are displayed in figure 4.4.

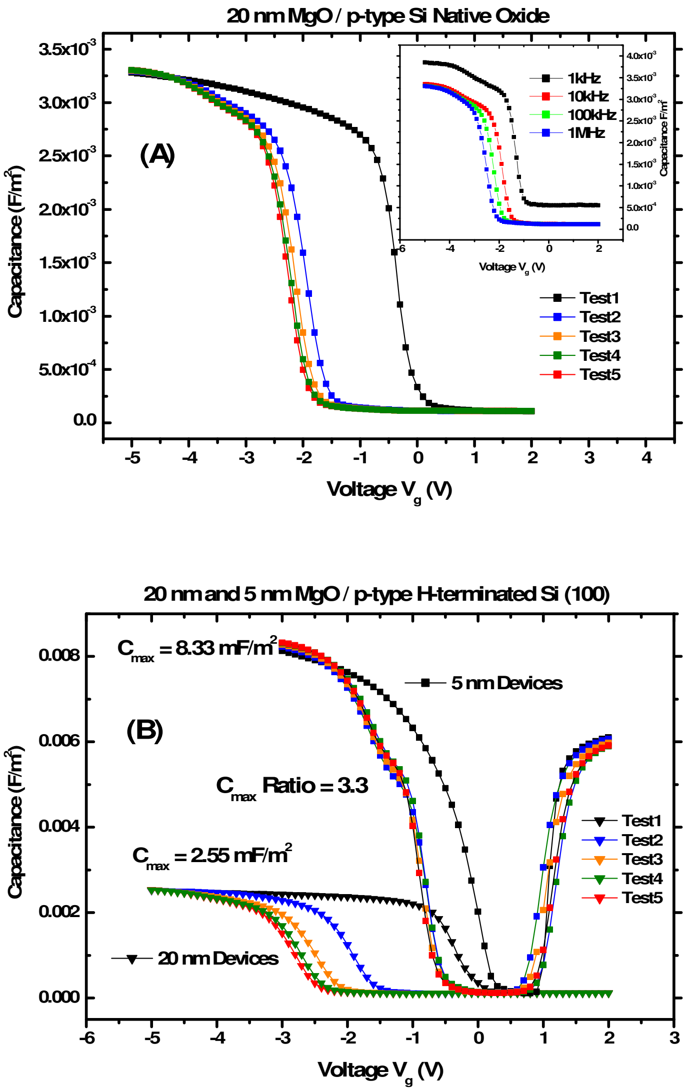

Figure 4.4 Native oxide (A) and H-terminated (B) p-type devices, corresponding to those shown in figure 4.3. Positive charge trapping is evidenced by large voltage shifts in the 5 nm and 20 nm devices.

The p-type devices show evidence for a large voltage shift between successive C-V measurements for both native oxide and H-terminated surfaces. This shift, not present in the n-type device profiles, has been attributed to positive charge trapping at the MgO/Si interface and is commonly seen in high *k* devices prior to post deposition annealing [7]. It should be noted that a measurable capacitance could not be obtained from the 5 nm MgO deposited onto p-type native oxide surface. This is in agreement with the high leakage current measured from the device, as shown in figure 4.2 B.

While leakage current values taken from the 5 nm p-type H-terminated surfaces devices are comparatively low, a measurable capacitance could only be obtained within the gate voltage biasing range of -2 to 2 volts. These structures also show evidence for a significant capacitance at positive gate voltage, which is attributed to peripheral inversion charging effects.

Peripheral inversion occurs due to the accumulation of charge at the surface and edges of the MOS device during measurement. In the case of the p–type devices in figure 4.4B, negative charge originating from outside the capacitor may be incorporated into the semiconductor surface upon application of a negative gate voltage, which allows this “peripheral” charge to add to the measured capacitance. Peripheral inversion effects have been identified in these MOS structures by measuring devices of larger surface area and with increasing measurement frequency, as the effect should was reduced in both cases. Surface charge often originates due to the metallisation process and as such does not depend on substrate doping.

The maximum capacitance values obtained from each of the devices shown in figures 4.3 and 4.4 can be found in table 4.2.

Pd Lift-Off Devices	**Native Oxide (n) (mF/m^2)**	**H- Terminated (n) (mF/m^2)**	**Native Oxide (p) (mF/m^2)**	**H- Terminated (p) (mF/m^2)**
20 nm	3.5	3.6	3.3	2.5
5 nm	8.5	8.8	-----	8.3
C_{max} Scaling	2.4	2.5	-----	3.3

Table 4.2 Maximum capacitance values taken from devices shown in figures 4.3 and 4.4 suggest poor capacitance scaling with thickness.

Using the H-terminated n-type device with a nominal thickness of 20 nm, the dielectric constant of MgO was calculated to be 8.1, a value which is in agreement with previous studies [1]. However, using the 5 nm devices the *k* value is calculated to be ~ 5. As such, C_{max} measurements taken from the 5 nm films do not scale linearly with that of the 20 nm devices, with a capacitance ratio of 2.5 obtained between the 20 nm and 5 nm H-terminated devices. Poor capacitance scaling can be attributed to the presence of a “low” dielectric constant region at the semiconductor/metal oxide interface, which is commonly in the form of SiO_x for silicon based devices. The interfacial chemistry of the 5 nm H-terminated device was analysed using conventional XPS, with the relevant Si 2p spectrum (figure 4.5) exhibiting evidence for the presence of silicon oxide at the interface.

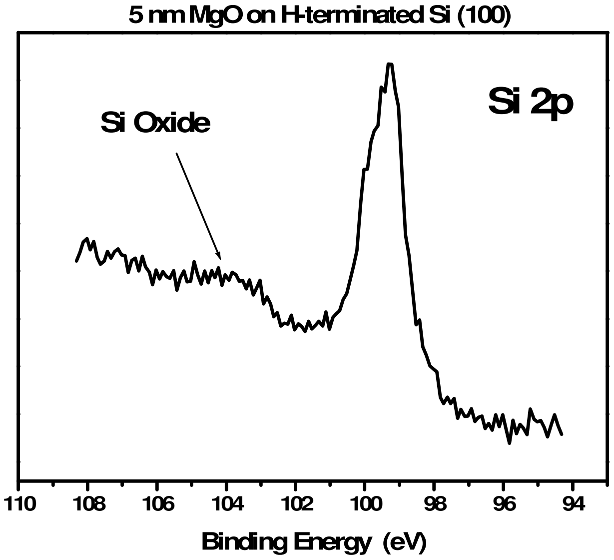

Figure 4.5 Si 2p spectrum taken from 5 nm H-terminated n-type device showing the presence of a ~ 0.7 nm interfacial oxide.

Using XPS curve fitting, and the XPS thickness calculation method outlined in Chapter 2, the thickness of the interfacial region was calculated to be 0.7 nm. Assuming this region is SiO_2 and using the dielectric constants of MgO (8.1) and SiO_2 (3.9), it is possible to calculate whether the poor capacitance scaling shown by the 5 nm & 20 nm devices can be explained by presence of a 0.7 nm interfacial oxide region. The measured capacitance values can be approximated using the simple capacitor equation;

$$C = \frac{\kappa \varepsilon_0 A}{d} \tag{4.1}$$

where C is the total capacitance

κ = dielectric constant

A = device area (50 μm × 50 μm)

d = oxide thickness

The total (measured) capacitance can be related to the capacitance of the interfacial layer (C_{int}) and MgO film (C_{MgO}) as follows;

$$\frac{1}{C_{total}} = \frac{1}{C_{MgO}} + \frac{1}{C_{\text{int}}} \tag{4.2}$$

The value C_{MgO} was calculated to be 2.2×10^{-11} F, using the measured dielectric constant of 8.1, and nominal film thickness of 5 nm.

Making C_{int} the subject of the equation;

$$\frac{1}{C_{\text{int}}} = \frac{1}{2.2\times10^{-11}} - \frac{1}{3.6\times10^{-11}} \tag{4.3}$$

$$C_{\text{int}} = 5.65 \times 10^{-11} \text{ F}$$

As such, for an MgO film with a nominal thickness of 5 nm and dielectric constant of 8.1, the measured total capacitance value can only be explained by an interfacial capacitance equal to 5.65×10^{-11} F. Once again assuming that the dielectric constant of this interfacial region is 3.9 (SiO_2), the interfacial oxide thickness (d_{int}) required to achieve this capacitance can be calculated as;

$$d_{\text{int}} = \frac{(3.9)(8.854\times10^{-12})(50\times10^{-6})^2}{5.65\times10^{-11}} \tag{4.4}$$

$$d_{\text{int}} = 1.53 \text{ nm}$$

Given that the Si 2p spectrum in figure 4.5 only shows evidence for a 0.7 nm interfacial region, it can be deduced that this interfacial oxide is insufficient to explain the poor capacitance scaling observed from the 20 nm and 5 nm devices. It may therefore be suggested that a further low-*k* region must exist within the film, reducing the overall dielectric constant measured from the device. It should also be noted that such a region would have a larger effect on the measured capacitance of thinner dielectric films (Eqn. 4.2), explaining the different *k* values obtained from the 5 nm ($\kappa = 5.0$) and 20 nm ($\kappa = 8.1$) films. Therefore, the effect which exposure to ambient conditions has on the top surface of deposited MgO thin films was investigated using XPS.

4.3.2 The Growth and ambient stability of e-beam deposited MgO thin films on Si

Poor scaling of capacitance measurements with MgO thickness, observed in the electrical measurements in section 4.3.1, suggested the presence of "low-k" layer on the MgO top surface possibly caused by ambient exposure. Therefore, the ambient stability of e-beam deposited MgO thin films was studied in order to determine if such contamination occurs upon exposure to air. All MgO films discussed in this section were deposited using e-beam evaporation, as described in Chapter 3, section 3.2.1. The affects of 5 minute ambient exposure on a 20 nm MgO film can be seen from the O 1s and Mg 2p core level XPS spectra in figure 4.6.

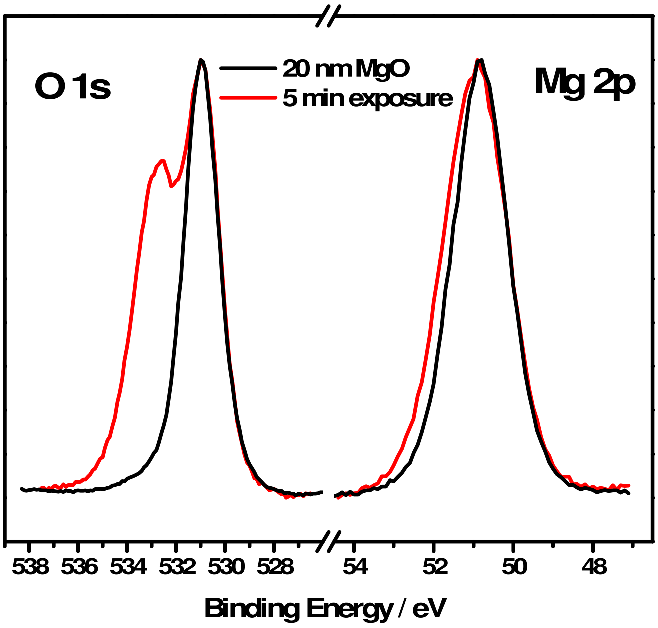

Figure 4.6 O 1s and Mg 2p spectra, taken from a 20 nm MgO film on Si, showing the affects of 5 minute exposure to ambient conditions.

It can be seen that brief exposure to ambient conditions has resulted in significant changes in the chemical composition of the MgO film, as evidenced by the growth of spectral features on the higher binding energy (HBE) side of both the O 1s and Mg 2p spectra. Curve fitting of the O 1s peak taken after exposure shows the presence of 3 distinct component peaks as seen in figure 4.7.

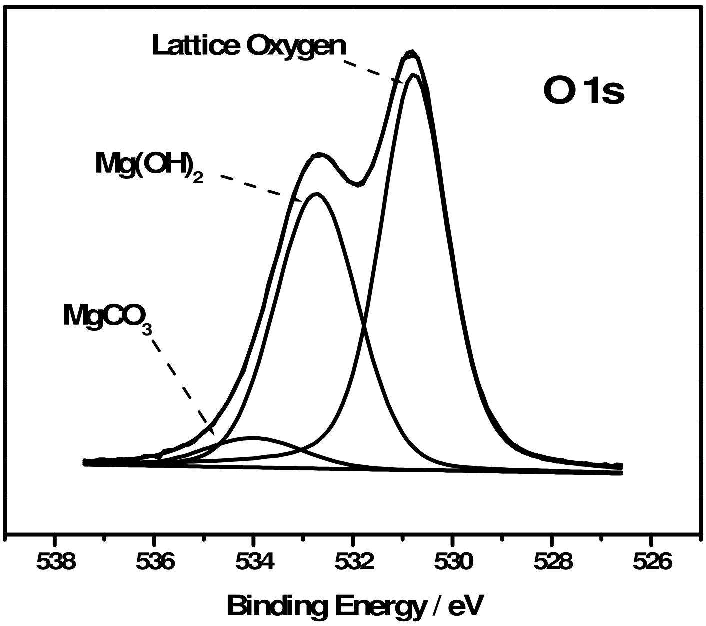

Figure 4.7 Curve fitting of O 1s spectrum, taken after 5 minute ambient exposure, shows the presence of magnesium hydroxide and carbonate species.

The lower binding energy (LBE) peak is attributed to the lattice oxygen of the MgO while the HBE peaks have been attributed to the presence of magnesium hydroxide ($Mg(OH)_2$) and magnesium carbonate ($MgCO_3$) in agreement with previous studies [8-15]. Angular resolved XPS spectra (not shown) suggest that the hydroxide and carbonate species are localised to the surface of the MgO film. The rate of hydroxide and carbonate growth over an exposure period of 34 days is shown by the evolution of the O 1s profile in figure 4.8, and indicates that long term exposure results in continuous growth of hydroxide and carbonate species in agreement with the work of Yao *et al.* [12].

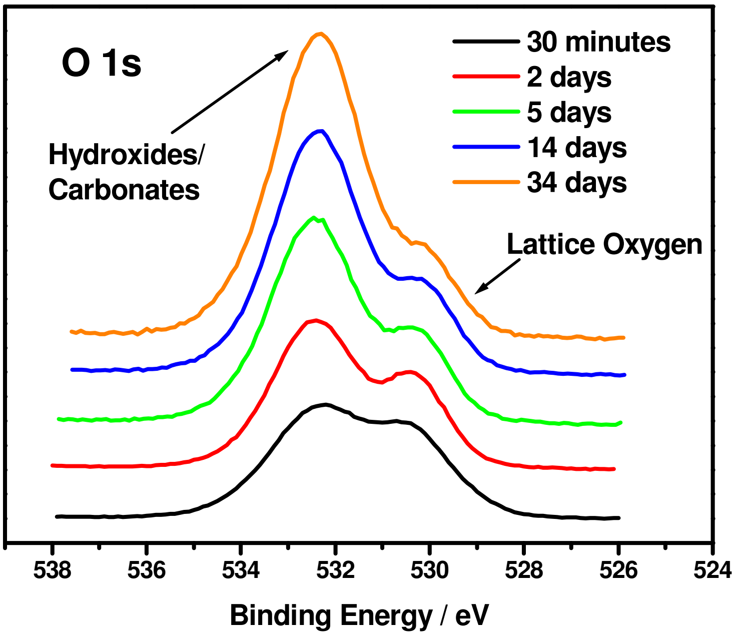

Figure 4.8 Evolution of O 1s spectra showing the continual growth of hydroxide and carbonate species over an exposure period of 34 days.

In order to further investigate the growth of magnesium hydroxide on the MgO surface in more controlled conditions, a study of the changes induced in the valence band photoemission spectra of UHV deposited MgO when exposed to water was undertaken. Prior to deposition of the MgO film, an ultra thin (0.3nm) SiO_2 layer was initially grown on an atomically clean p-type Si(111) wafer. An MgO layer was then deposited by the evaporation of magnesium metal from a resistively heated tantalum pouch which contained high purity magnesium chips in an oxygen partial pressure of 5×10^{-7} mbar. A similar evaporation technique was employed by Corneille *et al.* [16] to produce stoichiometric MgO films. Water vapour was then introduced into the chamber in a controlled and incremental fashion in order to determine the effect of water vapour on the MgO valence band spectra. A similar study was carried out by P. Liu *et al.* [8] in which a bulk MgO single crystal was used to study the reactivity of MgO and water. Figure 4.9 shows the evolution of the O 2s and valence band region as a result of water exposure.

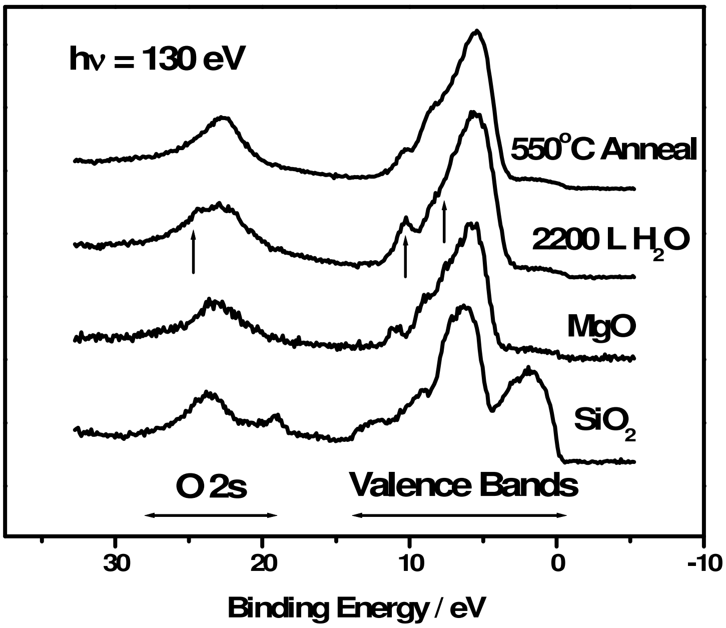

Figure 4.9 Valence band and O 2s spectra taken from MgO thin film after 2200 L water dose showing the evolution of peaks indicative of the presence of $Mg(OH)_2$. Arrows identify the position of water induced changes in the spectrum.

The suppression of SiO_2 valence band peaks in figure 4.9 suggests that the spectrum labelled MgO is almost entirely due to the MgO overlayer and not the underlying SiO_2. The growth of an additional peak in the O 2s core level, and two additional peaks in the valence band region (highlighted by arrows in figure 4.9), is evidence for the interaction of water with the surface. The additional peaks have been attributed to the presence of $Mg(OH)_2$, in agreement with previous studies [8], and show the high reactivity of MgO surfaces at extremely low exposure to water vapour. It should also be noted that the growth of hydroxide species occurred at much lower exposure levels in this study than that seen in the work of Liu *et al.* [8]. Given that the growth of $Mg(OH)_2$ has been linked to the density of surface defects [17] it is suggested that the increased reactivity seen in this experiment is due to a higher density of defects in thermally deposited MgO thin films, compared to the surfaces of MgO single crystals.

Temperature programmed desorption (TPD) results taken from a 20 nm MgO film after 7 days exposure (figure 4.10) give further direct evidence for the presence of both Mg(OH)2 and $MgCO_3$ on air exposed surfaces, and suggest that these species can be desorbed from the surface at temperatures below 500 °C.

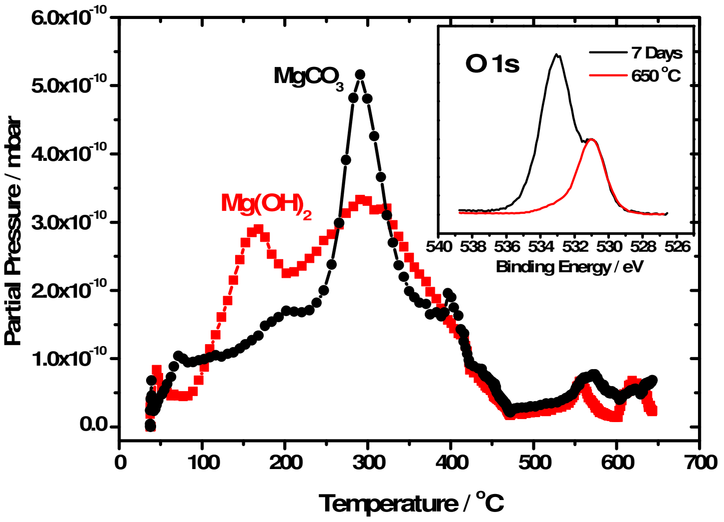

Figure 4.10 TPD spectra taken from 20 nm MgO film after ambient exposure, showing the desorption profile of $Mg(OH)_2$ and $MgCO_3$. O 1s core level spectra normalised to the lattice oxygen peak (inset) show a corresponding decrease in the HBE peak.

The presence of multiple desorption peaks for both $Mg(OH)_2$ and $MgCO_3$ is attributed to a surface coverage of greater than 1 ML, as species absorbed directly to the substrate surface are known to have higher binding energies than subsequently absorbed layers [18]. Prominent desorption peaks for both $Mg(OH)_2$ and $MgCO_3$ are seen at ~290 °C. Using the Redhead desorption model [19], desorption energies for these species can be calculated to be ~1.6 eV. It should be noted that monitoring the partial pressure of atomic masses 24 (Mg) and 40 (MgO) during the experiment showed no evidence of either species desorbing up to 500 °C. *In-situ* XPS analysis, seen in the inset of figure 4.10, shows that desorption of hydroxide and carbonate species resulted in a corresponding reduction in the O 1s HBE peak. XPS analysis also shows no evidence of changes in the stoichiometry of the underlying MgO film, which is in agreement with previous studies suggesting that MgO thin films on silicon are stable up to annealing temperatures of 740 °C [20]. While previous studies [21,22,23] have suggested that high temperature annealing of MgO surfaces results in the transformation of $Mg(OH)_2$ and $MgCO_3$ into H_2O/CO_2 and MgO, the results of this study show that the hydroxide and carbonate species are also desorbed in molecular form.

The effect of ambient exposure on the surface roughness of MgO films was investigated using AFM measurements. Initial analysis, performed less than one hour after film deposition, shows a flat MgO surface with a root-mean-square (RMS) roughness of 0.4 nm as shown in figure 4.11A.

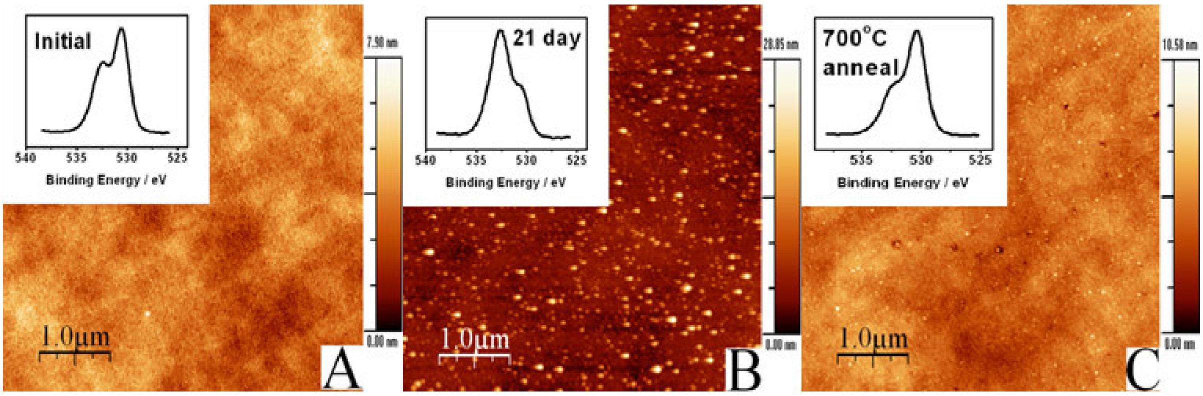

Figure 4.11 AFM images (5 µm × 5 µm) with corresponding O1s core level spectra insets showing the growth and removal of hydroxide/carbonate islands on the MgO surface. (A) after minimal air exposure (B) after 21 days ambient exposure and (C) after 700°C anneal.

An AFM image taken after 21 days exposure to ambient conditions displayed in figure 4.11B shows the growth of islands on the initially flat MgO surface, with an average height of 20 nm and average width of 50 nm. The XPS spectrum in the inset of figure 4.11B shows a corresponding growth in the O 1s HBE peaks, suggesting that these islands are due to magnesium hydroxide and carbonate species. This level of island growth is in agreement with the previous assertion that prolonged exposure results in hydroxide/carbonate coverages greater than 1 ML. High temperature annealing (700 °C) results in the removal of these islands features, returning the surface to a condition similar to that seen before ambient exposure, with an RMS roughness of 0.6 nm. This study displays results similar to those reported by Aswal *et al.* for their XPS-AFM study of the annealing of MgO crystals [24].

It should be noted that the XPS spectrum shown in Fig 4.11C corresponds to an MgO film which has been re-exposed to ambient conditions after annealing in order to perform AFM analysis. This is significant as the magnitude of the O 1s HBE peaks observed for a sample annealed *in-situ* (figure 4.10 inset) without ambient exposure are considerably lower than that shown in figure 4.11C.

The factors which affect the growth rate of hydroxide and carbonate species have also been investigated. Numerous studies, both theoretical and experimental, have investigated the factors which affect the growth of $Mg(OH)_2$ on MgO single crystals. [25-28]. As stated previously, it is suggested that while the MgO crystal structure is highly stable, defects such as step-edges and oxygen vacancies greatly increase the probability of hydroxide growth [17,26-28]. Given that thin (< 20 nm) MgO films will contain considerably more structural defects than bulk single crystals, the rapid growth of surface contaminants is to be expected. However, analysis of the MgO film growth may allow thin film stability to be improved. The work of Mather *et al.* [29] and Putkonen *et al.* [30] has suggested that while MgO films deposited at elevated temperature (~ 200 °C) have correct stoichiometry, films deposited at room temperature are oxygen deficient. XPS stoichiometry data obtained in this study is in agreement with this result, and also suggests that films deposited using e-beam evaporation at room temperature, in the presence of excess O_2 (1×10^{-5} mbar), are also oxygen deficient.

In order to determine whether surface oxygen deficiency affects the rate of hydroxide and carbonate growth on MgO, 20 nm films were simultaneously grown on silicon surfaces held at room temperature (RT) and elevated substrate temperature (200 °C). After initial XPS analysis both films were exposed to ambient conditions for increasing periods of time and re-scanned using XPS over a 300 hour period. The ratio of the O 1s peaks, lattice oxygen to hydroxide, is used as a measure of contaminant growth and is shown as a function of exposure time in figure 4.12.

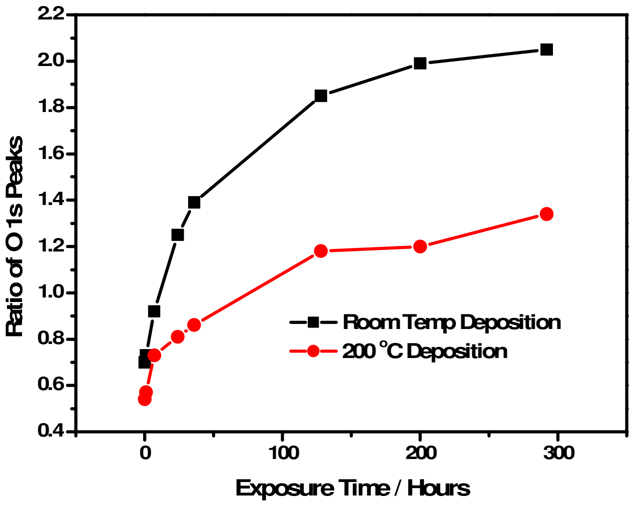

Figure 4.12 Graph showing the growth of the O 1s hydroxide peak on MgO films deposited on silicon at room temperature and 200 °C.

It can be seen from figure 4.12 that MgO films deposited at room temperature show a greatly increased growth rate for hydroxide and carbonate species. It should also be noted that the rate of hydroxide growth on both samples decreases as a function of time. This is related to the increasing formation of hydroxide and carbonate island structures, as seen in figure 4.11, acting as a barrier which inhibits the growth of further contaminants. The different levels of ambient stability seen after room temperature and 200 °C deposition can be directly related to the stoichiometry of the respective films throughout the exposure period, as shown in table 4.3.

Exposure Time	**RT (Mg : O)**	**200 °C (Mg : O)**
5 Minutes	1 : 0.9	1 : 1.0
6 Hours	1 : 0.9	1 : 1.0
43 Hours	1 : 0.85	1 : 1.0
100 Hours	1 : 0.85	1 : 1.1
300 Hours	1 : 0.85	1 : 1.1

Table 4.3 XPS stoichiometry values suggest that MgO films deposited at room temperature are oxygen deficient and remain so as a function of ambient exposure. Stoichiometry values are calculated using the O 1s and Mg 2p lattice components and the relevant atomic sensitivity factors [31].

Given the strong link between film stoichiometry and the rate of hydroxide growth, it can be suggested that the stability of MgO thin films is strongly dependant on structural defects such as oxygen deficiency, which is in agreement with results for MgO bulk crystals. Based on these results it can be implied that the stability of MgO thin films can be improved by changing the growth parameters used. It should be noted that Putkonen *et al.* [30] have suggested that the surface roughness of MgO thin films may be reduced by deposition at elevated temperature. While such a reduction in surface roughness may also act to inhibit hydroxide/carbonate growth, ambient AFM images taken in this study showed no evidence to support these results.

4.3.3 Conclusions

Initial electrical characterisation of MgO thin films on Si showed promising results, allowing the dielectric constant of MgO to be calculated as 8.1. However, poor scaling of capacitance and thickness values suggest the presence of "low-*k*" species within the film. XPS spectra show insufficient evidence of interfacial Si oxide to account for this poor scaling, suggesting the presence of contaminant species which grew on the MgO surface prior to metallisation. The ambient stability of MgO thin films deposited on Si has been studied, suggesting that exposure to ambient condition results in the rapid growth of magnesium hydroxide ($Mg(OH)_2$) and carbonate ($MgCO_3$) species in the form of island structures on the MgO surface. Thermal annealing studies suggest that these contaminant species can be desorbed from the surface at temperatures as low as 500 °C, returning the surface to a condition similar to that seen before exposure. The factors which affect contaminant growth have also been investigated and indicate that elevated temperature disposition of MgO improves film stoichiometry and inhibits the growth of hydroxide and carbonate species.

Section 4.4 Electrical Characterisation of MgO based MOS devices fabricated using the FUSI metallisation technique

While it has been shown in section 4.3.2 that the growth of hydroxide and carbonate species on the surface of MgO can be inhibited, brief exposure to ambient conditions will still result in contamination of the film. Given the detrimental effect of these contaminants on the electrical properties of the film, as shown in section 4.3, device fabrication must be achieved without exposure to ambient conditions. Also, the absence of a hydroxide and carbonate contamination layer would allow a more accurate determination of the MgO dielectric constant. MgO films with thicknesses of 5 nm and 20 nm were again deposited on native oxide and H-terminated Si (100) surfaces using the procedure outlined in section 4.2. In order to eliminate the affects of ambient exposure, an *in-situ* silicon cap (100 nm) was deposited onto the MgO films immediately following deposition. Electrical characterisation of these MgO layers was facilitated using the fully silicided (FUSI) process described in Chapter 3, Section 3.5. Electrical results presented for these FUSI devices should be considered with reference to the differences between the Pd and FUSI metallisation processes, which have been summarised in Chapter 3, Section 3.5.

4.4.1 Electrical Characterisation

The I-V characteristics taken from 20 nm MgO films deposited on both n-type and p-type Si(111), and metallised using the FUSI process are presented in figure 4.13.

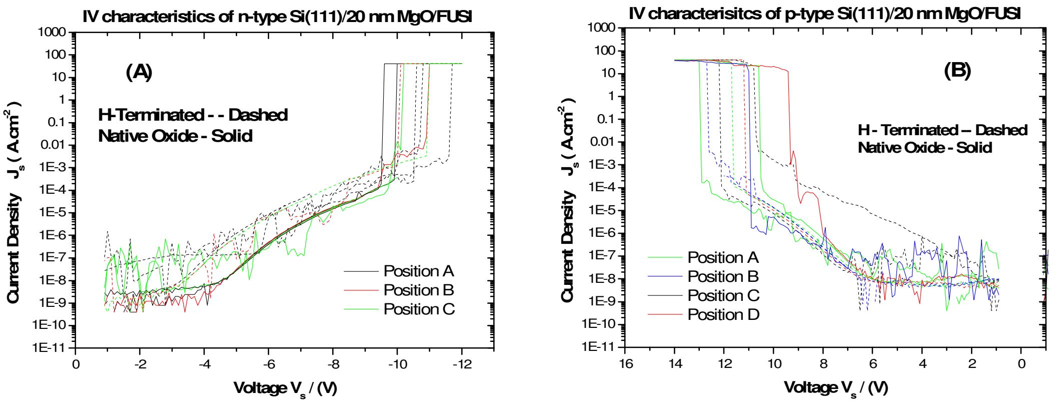

Figure 4.13 I-V characteristics taken from n-type (A) and p-type (B) Si(111)/20 nm MgO/FUSI Ni MOS structures.

These curves show a general increase in the noise signal compared to those metallised using the Pd contact, which are shown in figure 4.1. The origin of this noise signal is not fully understood and has not been determined in this study.

The leakage current values taken from these devices at V_{FB}+1 are shown in table 4.4, and exhibit a typical reduction equal to one order of magnitude compared to those seen for the Pd devices.

	Native Oxide (n) (A.cm^{-2})	**Hydrogen Terminated (n) (A.cm^{-2})**	**Native Oxide (p) (A.cm^{-2})**	**Hydrogen Terminated (p) (A.cm^{-2})**
20 nm FUSI	~1 × 10^{-9}	~1 × 10^{-9}	7 × 10^{-9}	6 × 10^{-9}
20 nm Pd	3 × 10^{-8}	2 × 10^{-8}	7 × 10^{-8}	7 × 10^{-8}

Table 4.4 Comparison of leakage current values taken from 20 nm MgO films on n and p-type Si using both Pd lift off and FUSI metallisation.

It should also be noted that I-V profiles taken from the 20 nm FUSI devices exhibit dielectric breakdown at ~ 11 V, which allows the dielectric field strength to be calculated as ~ 5 × 10^6 V/cm. This value is lower than that of the corresponding Pd devices (~ 8 × 10^6 V/cm) and possible reasons for this discrepancy are discussed later in this chapter. C-V characteristics taken from 5 nm and 20 nm MgO films deposited onto p-type H-terminated and native oxide Si (100), displayed in figure 4.14, show a considerable decrease in the presence of interfacial states compared to that seen from the Pd devices.

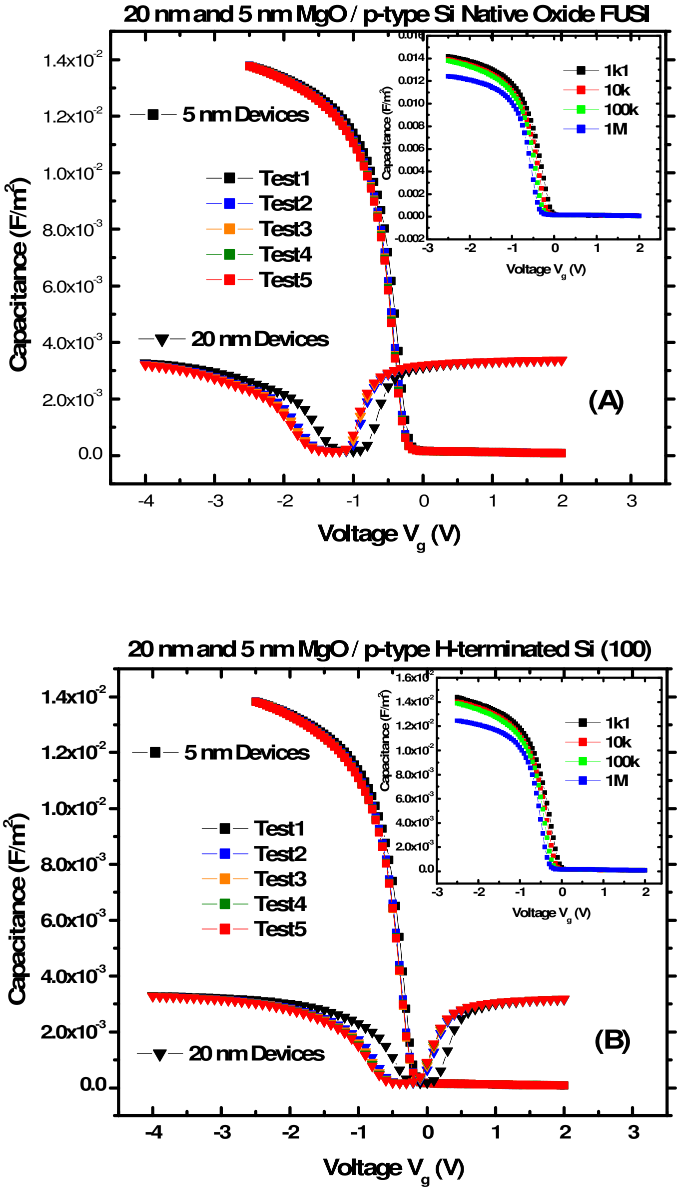

Figure 4.14 C-V characteristics taken from native oxide (A) and H-terminated (B) p-type devices suggest a reduction in charge trapping due to FUSI metallisation process.

This reduction is evidenced by the removal of bumps from the C-V curve and a slight reduction in C_{max} dispersion from 14 % to 12 % (inset). The p-type devices metallised using the FUSI method also show a considerably smaller voltage shift effect than those seen in figure 4.3, which may be attributed in part to the 500 °C annealing carried out during the FUSI process. However, given that this effect has been linked to the presence of OH ions [32,33], the growth of $Mg(OH)_2$ due to ambient exposure may have also contributed to the voltage shift shown in figure 4.3. The 20 nm p-type devices also show a large capacitance at inversion: given that this capacitance has been shown to be dependant on both device area and measuring frequency it is again attributed to the effect of peripheral inversion.

Figure 4.15 shows n-type devices fabricated using the FUSI process, which display similar improvements, including a significant reduction in interfacial state density.

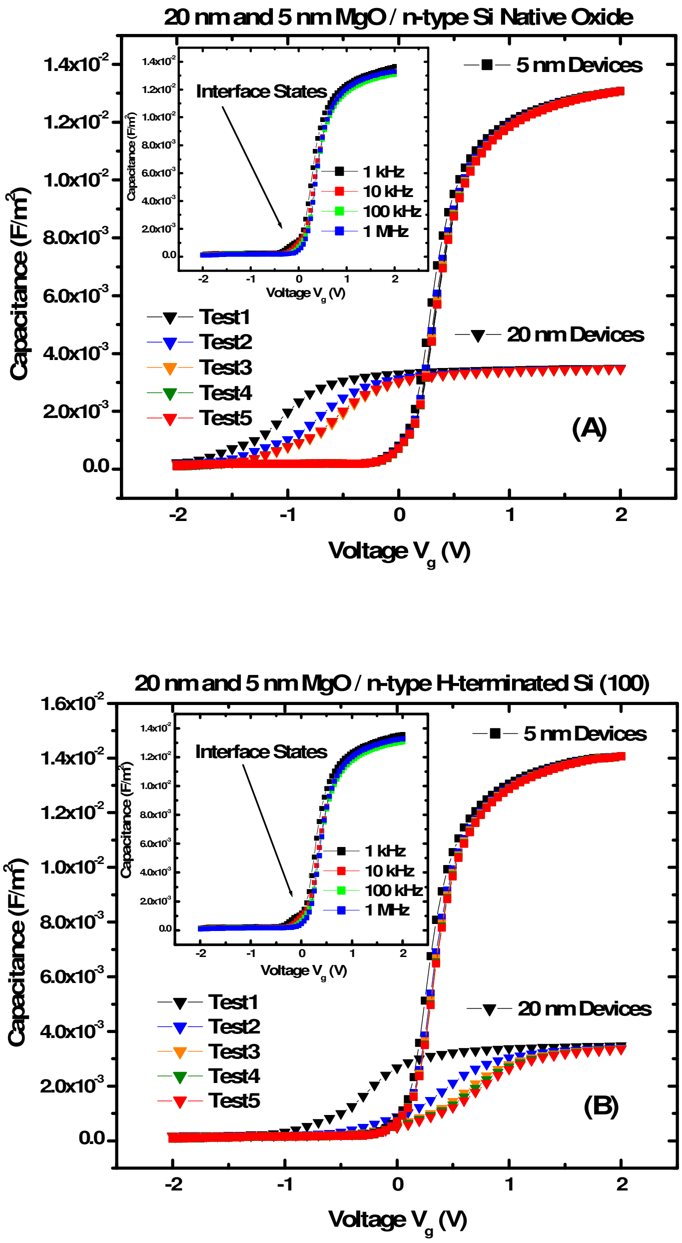

Figure 4.15 FUSI 5 nm n-type devices show a considerable reduction in interface state density and increased maximum capacitance compared to Pd lift off devices.

Frequency dispersion measurements (inset) show a C_{max} dispersion value of 4 %, decreased from 14 % in the Pd devices, which also indicates a reduction in D_{IT}. Low levels of interface state density have also been reported by Yan *et al.* [1], suggesting favourable MgO/Si interface characteristics.

The maximum capacitance values taken from the FUSI devices can be seen in table 4.5 and display a considerable increase on those taken from the Pd lift off devices (table 4.2), along with a considerable improvement in capacitance scaling. As the MgO deposition characteristics were identical for both the Pd and FUSI devices, this difference is attributed to the absence of low-*k* hydroxide and carbonate species due to the FUSI metallisation process.

FUSI Devices	**Native Oxide (n) (mF/m^2)**	**H- Terminated (n) (mF/m^2)**	**Native Oxide (p) (mF/m^2)**	**H- Terminated (p) (mF/m^2)**
20 nm	3.5	3.5	3.3	3.3
5 nm	13.1	14.1	13.8	13.9
C_{max} Scaling	3.8	4.0	4.2	4.2

Table 4.5 Increase in maximum capacitance values shown by FUSI devices is attributed to the absence of low-*k* hydroxide and carbonate species.

4.4.2 TEM analysis

The MgO/Si interface characteristics are further investigated using cross sectional transmission electron microscopy (TEM) images taken from the FUSI 20 nm and 5 nm MgO devices on n-type H-terminated Si, shown in figure 4.16.

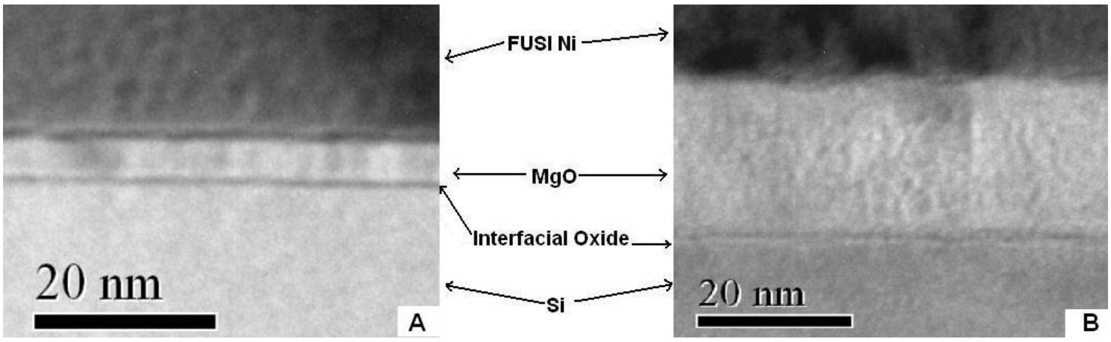

Figure 4.16 Cross sectional TEM images taken from FUSI 5 nm (A) and 20 nm (B) MgO devices on H-terminated Si.

These images show the presence of an amorphous interfacial layer between the Si substrate and the MgO overlayer, in agreement with the work of Yan *et al.* [1]. The measured thickness of the amorphous layer (< 1 nm) is in agreement with XPS calculations in section 4.3.1, and suggests the formation of an abrupt interfacial region. It should again be noted that samples shown in figure 4.16 were annealed to 500 °C as part of the FUSI process, indicating the thermal stability of the MgO thin films on Si. A high resolution TEM image (figure 4.17) taken from these samples clearly show the presence of crystalline columnar grain structures within the e-beam deposited MgO.

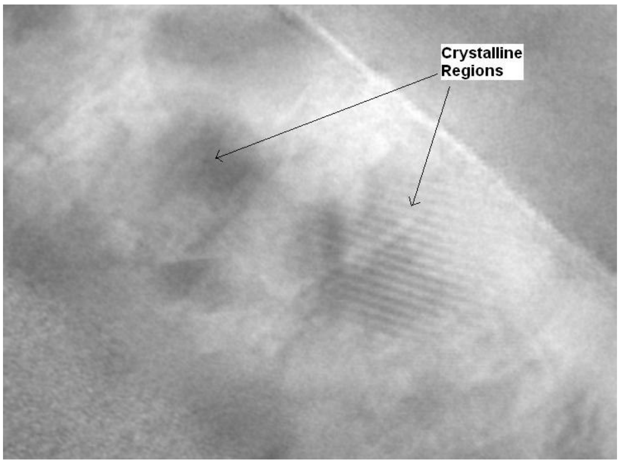

Figure 4.17 Further TEM image taken from the 20 nm MgO film clearly showing the presence of crystalline regions within the MgO.

The presence of columnar crystals has been reported for MgO films deposited using numerous deposition methods [34-36] and it has been suggested that the grain boundaries of these crystals act as effective paths for dielectric breakdown [37], dramatically reducing the life time of potential MgO transistor devices. This result may be linked to the reduced dielectric strength shown by the FUSI devices compared to that of the Pd devices, as the 500 °C anneal carried out during the FUSI process may have promoted the growth of such crystallites within the MgO. Thickness measurements taken from the TEM images in figure 4.16 are given in table 4.6. It should be noted that the nominally 20 nm MgO films show increased surface roughness, and as such an average value for MgO film thickness is quoted for this film. The dependence of MgO surface roughness on film thickness has previously been reported by Putkonen *et al.* [30].

Nominal Thickness of MgO film	20 nm	5 nm
TEM Thickness of MgO film	22.2 nm	4.60 nm
TEM Interfacial Layer Thickness	1 nm	0.65 nm
TEM Total over-layer Thickness	23.2 nm	5.25 nm

Table 4.6 TEM thickness values corresponding to figure 4.16.

As the chemical composition of the interfacial region is unknown, it is difficult to accurately determine the individual dielectric constant value of either the MgO film or the interfacial layer. However, given that the interfacial layer (IL) is vital to the electrical properties of the device it may be of greater interest to define the dielectric constant of the entire film i.e. the IL and MgO together. This is achieved using the total overlayer thickness and is analogous to measuring the combined *k* value of two capacitors in series. Using the measured C_{max} value in table 4.5, the average dielectric constant of the 23.2 nm film is calculated to be 9.7. While this value is larger than that calculated in section 4.3.1, the nominal thickness values used for the Pd devices may have affected the accuracy of this calculation. The value 9.7 is also in agreement with the work of Posasdas *et al.* [2] and Senzaki *et al.* [7], who have both reported a *k* value of 10 for MgO thin films.

Although the *k* value of MgO (9 - 10) found in this study is similar to that of Al_2O_3 [38,39] and PrO_2 [40], it is considerably lower than those reported for other metal oxides such Ta_2O_5 [41-43], TiO_2 [44], and $SrTiO_3$ [45]. However, the poor thermal stability of these materials in contact with Si has necessitated that they be deposited onto more stable “buffer” oxides for use in high-*k* dielectric gate stacks [46]. It is suggested that the favourable interfacial characteristics of MgO on Si shown in this study may make it a suitable candidate for use in such gate oxide stacks, as achieved by Mise *et al.* [47,48] who have reported promising results for MgO/HfO$_2$ dual oxide gate stacks. Therefore, the chemical interactions at the MgO/Si interface must be further investigated, in order to complement the understanding derived from the C-V and TEM analysis. The growth and thermal stability of MgO films on Si was investigated using high resolution synchrotron based photoemission in order to accurately determine the chemical composition of the interfacial region.

4.4.3 Conclusions

MgO/Si based devices metallised using the FUSI process show a considerable reduction in interface state density and improved maximum capacitance compared to Pd lift off structures. TEM images show the presence of abrupt amorphous oxide (0.7 - 1 nm) region at the MgO/Si interface. While results indicate favourable interfacial characteristics for MgO on Si, the chemical composition of the interfacial layer requires further investigation.

4.5 High Resolution Photoemission study of MgO film growth on H-terminated Si (111) and thermally grown ultra-thin silicon oxide surfaces

4.5.1 MgO on H-terminated Si (111)

Cross sectional TEM images taken from MgO films deposited onto H-terminated Si (100) surfaces clearly show the presence of an amorphous oxide region at the MgO/Si interface. However, given that the chemical composition of this interfacial region can not be examined using TEM it is difficult to analyse its impact on the electrical characteristics of the device. Therefore, high resolution synchrotron based photoemission studies of MgO thin film growth on H-terminated surfaces were carried out, in order to determine the chemical composition of the interfacial region. A study of MgO deposition onto an ultra thin thermally grown silicon oxide surface was also carried out using SR based photoemission, and the results compared to those seen on H-terminated surfaces.

Atomically clean, oxide free, Si surface were prepared using the flash cleaning procedure outlined in Chapter 3, section 3.4. Hydrogen termination of the oxide-free silicon surface was achieved by exposing the atomically clean surface, held at 200 °C, to molecular hydrogen (5000 L) in the presence of a hot tungsten filament. This had the effect of forming atomic hydrogen species which terminated the silicon surface in a process similar to that used in previous studies [49-51]. The effect of H exposure can be seen from the Si 2p spectra in figure 4.18, taken at photon energies of 130 and 260 eV.

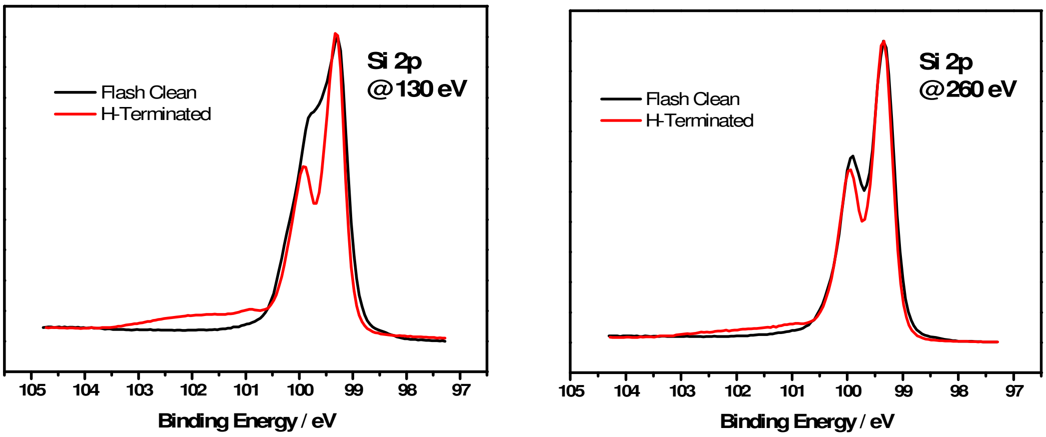

Figure 4.18 Si 2p spectra taken at 130 and 260 eV, showing the passivation of Si (111) surface states due to H-termination. The high binding tail to the above H-terminated spectra are attributed to Si oxide peaks associated with the presence of sub-monolayer oxygen on the surface.

The H-terminated spectra show evidence for the passivation of Si surface states on both the HBE and LBE sides of the Si bulk peak, narrowing the overall Si 2p profile. However, there is also evidence for the presence of Si oxide on the H-terminated surface on the HBE side of the substrate peak. This oxide layer, which is considerably less than 1 monolayer, is thought to be due to O_2 gas which was unintentionally introduced to the UHV chamber during H exposure. The smaller oxygen related signal on the spectrum acquired at 260eV reflects the larger sampling depth at this photon energy.

The effect of H-passivation is shown more clearly in the curve fitted spectra in figure 4.19, which is based on the parameters reported by Jolly *et al.* [51] and Mach *et al.* [52].

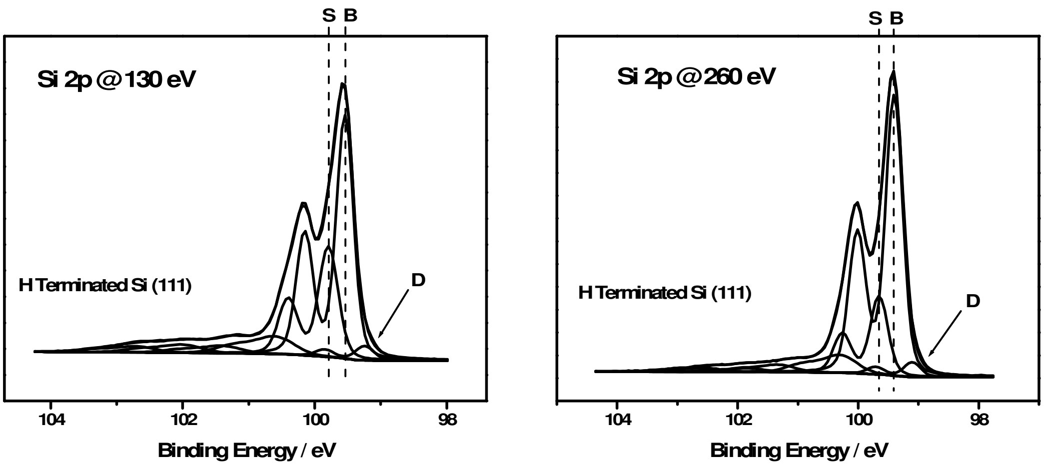

Figure 4.19 Curve fitted Si 2p spectra indicating the presence of Si-H bonds (peak S) at the surface of H-terminated Si (111). Spectral components D and B are attributed to surface defects and bulk Si respectively.

The spectra show the presence of two prominent peaks labelled B and S which are attributed to bulk and surface silicon atoms respectively, and have a binding energy separation equal to 0.23 eV. The peak labelled S is attributed to Si-H bonds and indicates that the surface has been H-terminated. The LBE peak labelled D has been attributed to surface defects, possibly in the form of Si dimers [49,51,52]. The effect of MgO deposition on the H-terminated Si (111) surface is shown in figure 4.20.

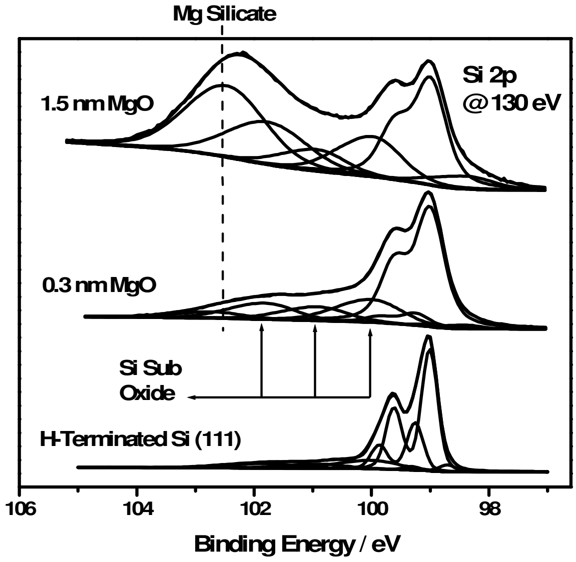

Figure 4.20 Curve fitted Si 2p spectra showing the growth of Mg silicate as a function of MgO deposition on H-terminated Si (111).

Curve fitting of spectra taken during the initial stages of MgO deposition showed the presence of Si sub-oxide peaks, separated from the Si ° peak by ~ 0.9, 1.8 and 2.7 eV in agreement with the work of Himpsel *et al.* [53]. Further MgO deposition resulted in the growth of a prominent peak separated from the Si ° peak by 3.4 eV. Given that this binding energy separation is considerably smaller than that reported for the Si $^{4+}$ oxidation sate, this peak has been attributed to the presence of Mg silicate in agreement with the work of Brennan *et al.* [54]. This result supports the finding of Posadas [2], and Goodrich *et al.* [20] who have both reported the growth of an Mg silicate interfacial layer upon MgO deposition on Si surfaces. Continued deposition shows evidence for the presence of a LBE peak previously attributed to interface defects [54,55], indicating that MgO deposition has resulted in disruption of the silicon substrate and an increase in the thickness of the interfacial oxide region.

It should be noted that curve fitting shows no evidence for the presence of the Si $^{4+}$ oxidation state on the H-terminated surface, suggesting that MgO deposition onto H-terminated Si (111) does not lead to the growth of interfacial SiO_2. This result may be of some importance in relation to the dielectric constant of the interface region. The chemical composition of this interfacial oxide region is further investigated using the O 1s spectra, acquired with a conventional X-ray source, and valence band/O 2s spectra, acquired at 130 eV photon energy (figure 4.21).

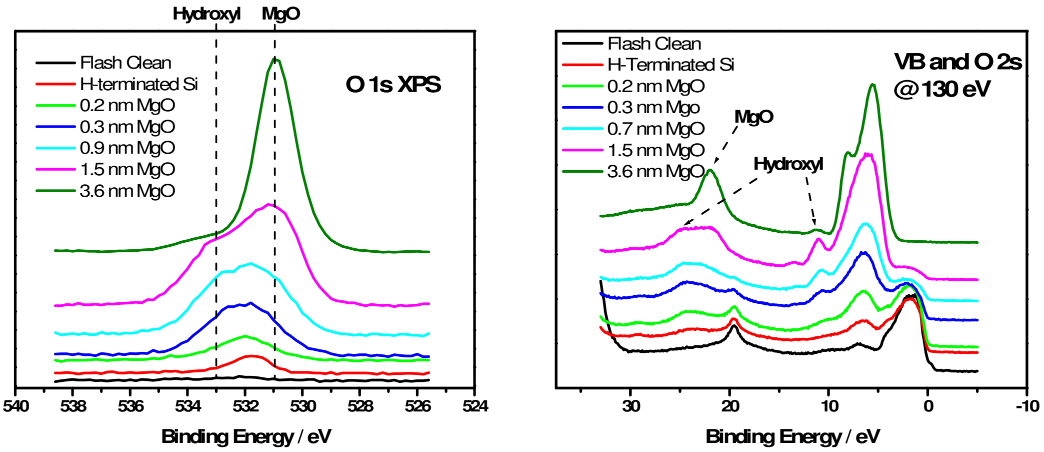

Figure 4.21 O 1s spectra (hν = 1253.6 eV) and Valence band/O 2s spectra (hν = 130 eV) both suggest the formation of interfacial hydroxyl groups due to MgO deposition on H-terminated Si.

The O 1s and O 2s spectra taken after 1.5 nm MgO deposition clearly show the presence of two oxygen component peaks. The LBE peak is attributed to MgO lattice oxygen in agreement with section 4.3.2, however, the origin of the HBE peak is less obvious. The work of Peterka *et al.* [56] has attributed a similar O 1s component to the existence of MgO_2 in MgO films less than 1 monolayer. However, the presence of the HBE peak at MgO thicknesses up to 1.5 nm suggests that the HBE O 1s peak is not due to MgO_2. Comparison with figures 4.8 and 4.9 in section 4.3.2 suggest that the HBE peaks in both the O 1s and O 2s spectra are due to the presence of a hydroxyl species, similar to $Mg(OH)_2$. The attenuation of these HBE peaks as a function of MgO deposition clearly indicates that these hydroxyl species are located at the MgO/Si interface. Therefore, based on the results in figures 4.20 and 4.21, it can be suggested that MgO deposition onto H-terminated Si surfaces results in the formation of a magnesium-hydroxy-silicate interfacial layer.

4.5.2 MgO on ultra-thin thermally grown Si oxide

In a separate experiment MgO was deposited on an ultra thin (~0.3 nm) SiO_2 film which was grown on an atomically clean, flash cleaned, Si surface. The oxide was grown in a partial pressure of 5×10^{-7} mbar oxygen at 500 °C for 30 minutes which resulted in a self limiting oxide similar to that reported by Morgen *et al.* [57]. The effect of MgO deposition onto an ultra-thin thermally grown Si oxide layer can be seen from the changes induced in the Si 2p spectra in figure 4.22, acquired at a photon energy of 130 eV for maximum surface sensitivity.

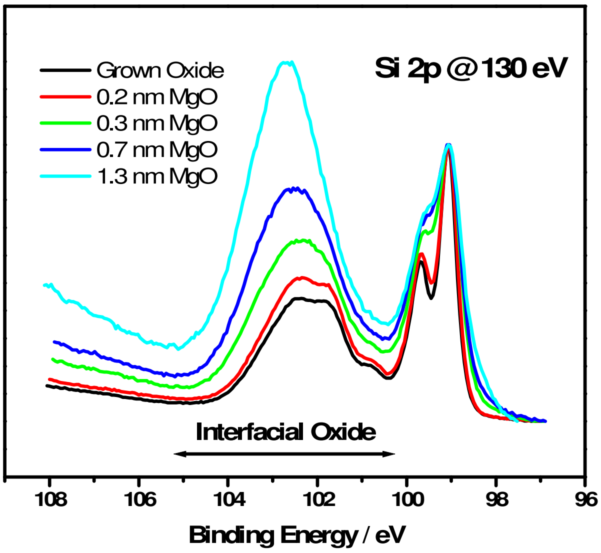

Figure 4.22 Raw Si 2p spectra (hν = 130 eV) showing the growth of interfacial Si oxide as a function of MgO deposition on an ultra thin (~ 0.3 nm) Si oxide layer.

The spectra show definite evidence for the growth of an interfacial silicon oxide region as a function of MgO deposition, as shown by a change in the intensity ratio of the oxide and substrate peaks. The chemical composition of this interfacial region is further investigated using the curve fitted Si 2p spectra in figure 4.23.

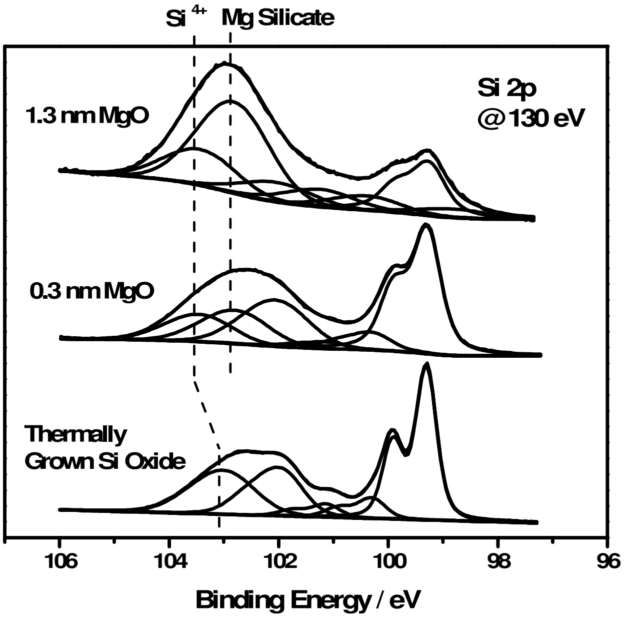

Figure 4.23 Curve fitted Si 2p spectra indicate the growth of a Mg silicate interfacial layer due to MgO deposition onto Si oxide.

The initially grown thermal Si oxide shows evidence for the presence of the four separate oxidation states, which are resolved by curve fitting in agreement with previous studies [53]. Using XPS thickness calculations [Chapter 2] the thickness of the self limiting oxide was calculated to be approximately 0.3 nm, effectively meaning that it is one monolayer thick, as previously reported by Miyata *et al.*. [58]. It should be noted that the position of the Si $^{4+}$ oxidation state shifts to higher binding energy after MgO deposition. It is known the binding separation of the Si $^{4+}$ peak from the Si ° signal is equal to ~ 4.0 eV for bulk SiO_2, but given that the thermally grown oxide in figure 4.23 is approximately 0.3 nm thick the Si $^{4+}$ signal is not representative of bulk silicon oxide [59]. As such, the binding energy separation seen for the thermally grown oxide before deposition is ~ 3.6 eV, in agreement with Himpsel *et al.* [53]. However, it can be seen from the raw spectra in figure 4.22 that the profile of Si 2p peak broadens considerably on the HBE side as a function of interfacial oxide growth. This broadening is attributed to the incorporation of additional oxygen atoms into the oxide film, which increases the net polarity of the Si-O bonds and results in the Si $^{4+}$ peak shifting to a position closer to that seen for bulk Si oxide.

Curve fitted spectra taken after MgO deposition also show evidence for the growth of an additional peak separated from the Si bulk peak (Si °) by 3.4 eV. This peak has again been attributed to magnesium silicate in agreement with the work of Brennan *et al.* [54]. The growth of Mg silicate can also be seen from corresponding Si 2p spectra taken at photon energy of 260 eV (figure 4.24), allowing for more bulk sensitive analysis.

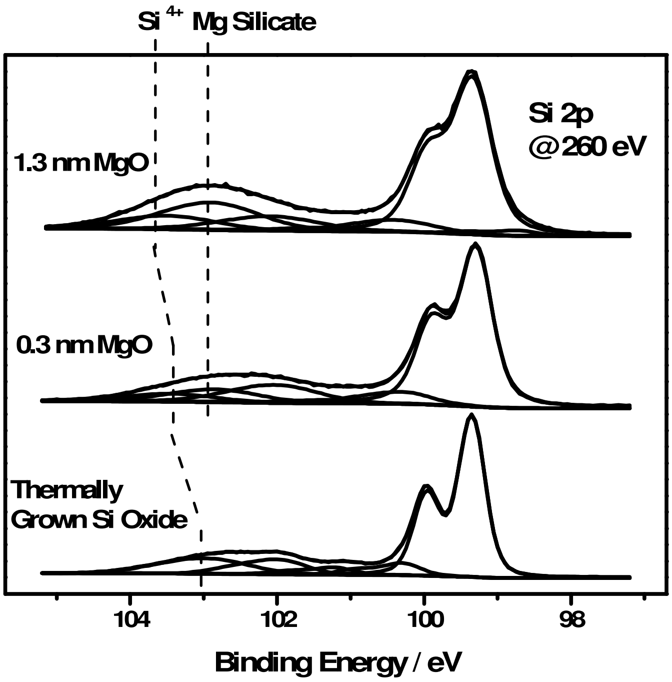

Figure 4.24 Corresponding Si 2p spectra (hν = 260 eV) for the sample shown in figure 4.23.

The interfacial oxide growth seen on the Si oxide surface can be further investigated using the Mg 2p and O 1s spectra in figure 4.25.

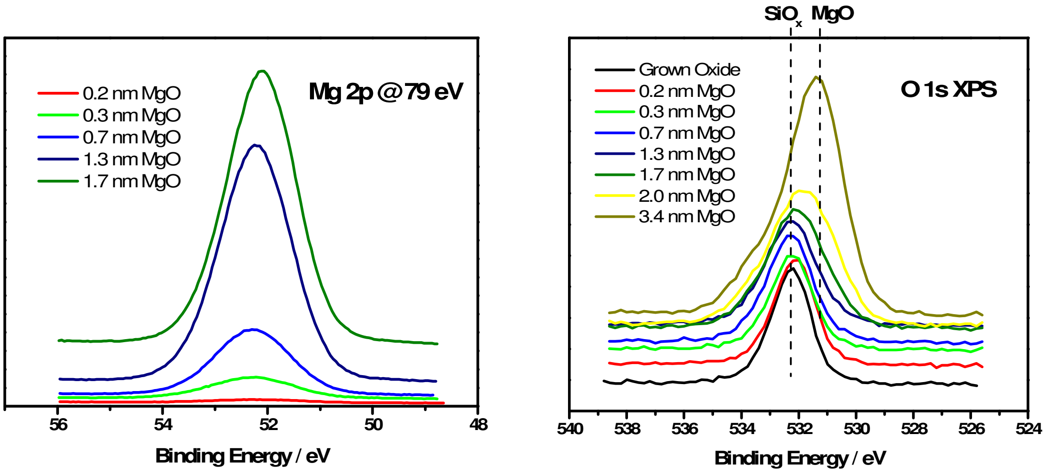

Figure 4.25 Mg 2p (hν = 79 eV) and O 1s spectra (hν = 1253.6 eV) showing the initial stages of MgO thin film formation on a Si oxide surface.

Analysis of the FWHM values of the Mg 2p spectra, exhibits a reduction in FWHM as a function of MgO deposition. This is attributed to the development of a more uniform chemical environment at thicknesses greater than ~ 1 nm [54]. It can be seen that MgO deposition results in the growth of the MgO component in the O 1s profile at ~ 531 eV in agreement with O 1s spectra in section 4.3.2, resulting in the attenuation of the Si oxide peak. It should also be noted that the O 1s spectrum taken from the thermally grown oxide surface may be fitted using one component peak, even though the Si 2p spectrum shows almost equal contributions from each of the 4 silicon oxidation states. As such it can be deduced that while it is possible for the silicon to be under coordinated, oxygen atoms should always be two fold coordinate.

The growth of Mg silicate on both H-terminated and oxidised silicon surfaces suggests that this oxide phase is energetically favourable within the MgO/Si system. This is further supported by the affect of thermal annealing on the Si oxide/MgO interface, as shown by the Si 2p spectra in figure 4.26.

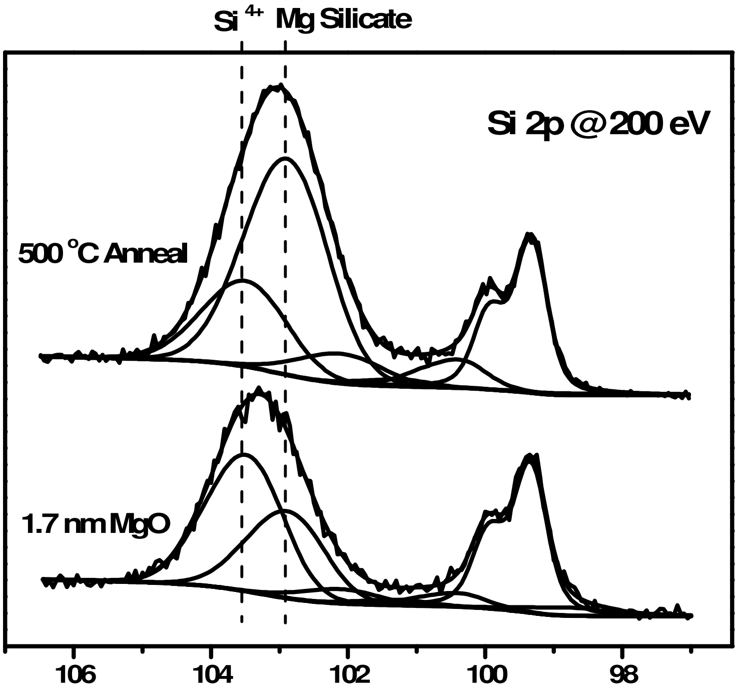

Figure 4.26 Si 2p spectra (hν = 200 eV) showing the preferential growth of Mg silicate at the MgO/Si oxide interface as a result of 500 °C annealing.

The spectra show clear evidence for the growth of Mg silicate as a result of a 500 °C anneal, suggesting that Mg silicate can increase in intensity at the expense of an SiO_2 component. Using XPS thickness calculations (Chapter 2) the thickness of the interfacial layer was calculated to be ~ 0.8 nm, in agreement with the TEM thickness values shown in table 4.6. Given that Wilk *et al.* [46] have suggested that the k of metal silicates commonly lie between that of SiO_2 and the relevant metal oxide, the preferential formation of Mg silicate over SiO_2 during thermal processing may be of some benefit to the electrical characteristics of MgO/Si based devices. These studies show that MgO deposition and subsequent annealing resulted in the formation of a predominantly Mg silicate based interfacial layer on both the native oxide and H-terminated surfaces.

4.5.3 Conclusions

The growth of Mg silicate interfacial layers after MgO deposition onto H-terminated and oxidised silicon has been shown using high resolution photoemission. Thermal annealing studies of MgO on silicon oxide show the preferential growth of Mg silicate, indicating the thermal stability of the MgO/Si interface. It is suggested that the formation of thin (< 1 nm) Mg silicate interlayers, which show no evidence for the presence of SiO_2, may be of benefit to the electrical characteristics of MgO/Si based devices.

4.6 Chapter Conclusions

Initial electrical characterisation of MgO films deposited on silicon, without post deposition annealing, allow the dielectric constant of MgO to be calculated as 8.1. These MOS devices also show evidence for high interface density and poor capacitance scaling with thickness. Investigations into the ambient stability of MgO suggest that this poor capacitance scaling is due to the rapid growth of magnesium hydroxide and carbonate species prior to metallisation. In order to prevent the detrimental effects of ambient exposure, an *in-situ* Si capping layer (~ 100 nm) was deposited onto MgO films prior to exposure. Electrical characterisation of these films was facilitated using the FUSI metallisation process. FUSI devices showed a considerable reduction in interfacial state density and increased maximum capacitance values. TEM images taken from n-type H-terminated FUSI devices show the presence of an amorphous interfacial oxide layer (IL) and columnar crystallite regions within the MgO films. High resolution synchrotron based photoemission studies identify this interfacial oxide as Mg silicate, which forms as a result of MgO deposition on both H-terminated and oxidised Si surfaces. Photoemission studies show no evidence for SiO_2 formation upon deposition of MgO, while thermal annealing has also been shown to result in the preferential growth of Mg silicate. While the dielectric constant of MgO thin films (~ 10) is less than that of other high-*k* metal oxides, it is suggested that the favourable interfacial characteristics and thermal stability of MgO on Si may make it a good candidate for use in gate oxide stacks along with high-k materials such as HfO_2 or ZrO_2.

4.7 References

[1] L. Yan, C. M. Lopez, R. P. Shrestha, E. A. Irene, A. A. Suvorova and M. Saunders, App Phys Lett, **88**, (2006) 142901.

[2] A. Posadas, F. J. Walker, C. H. Ahn, T. L. Goodrich, Z. Cai and K. S. Ziemer, Appl. Phys. Lett. **92** (2008) 233511.

[3] C. M. Osburn and D. W. Ormond, J. Electrochem. Soc: Solid-State Science and Technology, (1972) 591

[4] Y. Satoh, T. Shiota, H. Furuya, IEEE Transactions on Electron Devices, **47**, 2, (2000) 398

[5] T.W. Kim and Y.S. You, Appl. Surf. Sci. **180** (2001) 162-167

[6] M.Schmidt, M. C. Lemme, H. Kurz, T. Witters, T. Schram, K.Cherkaoui, A. Negara and P.K.Hurley, Microelectronic Engineering **80** (2005) 70–73

[7] J. Senzaki, K. Kurihara, N. Nomura, O. Mitsunaga, Y. Iwasaki, T. Ueno, Jpn. J. Appl. Phys. **37** (1998) 5150-5153

[8] P. Liu, T. Kendelewicz, G. E. Brown, Jr. and G.A. Parks, Surface Science **412/413** (1998) 287–314.

[9] M. Liu, S. Zanna, H. Ardelean, I. Frateur, P. Schmutz, G. Song, A. Atrens, P. Marcus, Corrosion Science **51** (2009) 1115–1127.

[10] S. Altieri, L. H. Tjeng, G. A. Sawatzky, Phys. Rev. B. **61**, 24, (2000) 948.

[11] J. Du, S. Gnanarajan, and A.Bendavid, Superconductor Sci & Tech **18** (2005) 1035

[12] H.B. Yao, Y. Li, A.T.S. Wee, Appl. Surf. Sci. **158** (2000) 112–119.

[13] V. Fournier, P. Marcus, I. Olefjord, Surf. Interface Anal. **34** (2002) 494–497.

[14] M. Kurth, P.C.J. Graat, E.J. Mittemeijer, Appl. Surf. Sci. **220** (2003) 60–78.

[15] M. Gajdardziska-Josifovska1, R. Sharma, Microsc. Microanal. **11** (2005) 524–533

[16] J.S. Corneille, J.W. He, D.W. Goodman, Surf. Sci., **306**, 269, (1994)

[17] C.A. Scamehorn, N.M. Harrison, M.I. McCarthy, J. Chem. Phys. **101**, 2 (1994) 1547.

[18] G. Attard and C. Barnes, Surfaces, Oxford Chemistry Primers (1998)

[19] P.A. Redhead, Vacuum **12** (1962) 203

[20] T.L. Goodrich, Z. Cai, M.D. Losego, J.-P. Maria and K.S. Ziemer, J. Vac. Sci. Technol. B **25,** 3 (2007) 1033.

[21] M.G. Kim, U. Dahmen, J. Am. Ceram. Soc. **70** (1987) 146.

[22] J. Green, J. Mater. Sci. **18** (1983) 637

[23] Z. Dohnalek, G. A. Kimmel, S. A. Joyce, P. Ayotte, R. Scott Smith, B. D. Kay, J. Phys. Chem. B **105** (2001) 3747-3751

[24] D.K. Aswal, K.P. Muthe, S. Tawde, S. Chodhury, N. Bagkar, A. Singh, S.K. Gupta, J.V. Yakhmi, Journal of Crystal Growth **236** (2002) 661–666.

[25] M. Odelius, Physical Review Letters **82**, 19 (1999) 3919.

[26] G. Pacchioni, A.M. Ferrari, Catalysis Today **50** (1999) 533-540.

[27] W. Langel, M. Parrinello, J. Chem. Phys. **103**, 8 (1995) 3240.

[28] W. Langel, M. Parrinello, Physical Review Letters **73**, 3 (1994) 504.

[29] P. G. Mather, J. C. Read, R. A. Buhrman, Phys. Rev. B. **73** (2006) 205412.

[30] M. Putkonen, T. Sajavaara, L. Niinisto, J. Mater. Chem. **10** (2000) 1857-1861.

[31] C. D. Wagner, L. E. Davis, M. V. Zeller, J. A. Taylor, R. M. Raymond and L. H. Gale, Surf. Interface Anal. **3** (1981) 211

[32] J. A. Gupta, D. Landheer, J. P. McCaffrey, G. I. Sproule, Appl. Phys. Lett. **78**, 12 (2001) 1718.

[33] S. Guha, E. Cartier, M. A. Gribelyuk, N. A. Bojarczuk, M. C. Copel, Appl. Phys. Lett. **77**, 17 (2000) 2710

[34] K.H. Kim, M.S. Lee, J.S. Choi, J.P. Ahn, Thin Solid Films **517**, (2009) 3995

[35] J.S. Lee, B.G. Ryu, H.J. Kwon, Y.W. Jeong, H.H. Kim, Thin Solid Films **354**, (1999) 82

[36] J.H. Boo, S.B. Lee, K.S. Yu, W. Koh, Y. Kim, Thin Solid Films **341**, (1999) 63

[37] R. O'Connor, G. Hughes, P. Casey, S.B. Newcomb, J. Appl. Phys. **107** (2010) 024501

[38] D.A. Buchanan, E.P. Gusev, E. Cartier, H**.** Okorn-Schmidt, K. Rim, M.A. Gribelyuk, A. Mocuta, A. Ajmera, M. Copel, S**.** Guha, N. Bojarczuk, A. Callegari, C. Demic, P. Kozlowski, K. Chan, R.J. Fleming, P.C. Jamison, J. Brown, R. Arndt, IEDM Tech. Digest (2000) 223–226

[39] L. Manchanda, W.H. Lee, J.E. Bower, F.H. Baumann, W.L. Brown, C.J. Case, R.C. Keller, Y.O. Kim, E.J. Laskowski, M.D. Morris, R.L. Opila, P.J. Silverman, T.W. Sorsch, G.R. Weber, Tech. Dig. Int. Electron Devices Meet., (1998) 605

[40] O. Seifarth, C. Walczyk, G. Lupina, J. Dabrowski, P. Zaumseil, G. Weidner, H.J. Müssig, T. Schroeder, **106**, (2009) 104105

[41] I. C. Kizilyalli, R. Y. S. Huang, and P. K. Roy, IEEE Electron Device Lett. **19**, (1998) 423

[42] D. Park, Y.-C. King, Q. Lu, T.-J. King, C. Hu, A. Kalnitsky, S.-P. Tay, and C. C. Cheng, IEEE Electron Device Lett. **19**, (1998) 441

[43] H. F. Luan, B. Z. Wu, L. G. Kang, B. Y. Kim, R. Vrtis, D. Roberts, and D. L. Kwong, Tech. Dig. Int. Electron Devices Meet., (1998) 609

[44] B. He, T. Ma, S. A. Campbell, and W. L. Gladfelter, Tech. Dig. Int. Electron Devices Meet., (1998) 1038

[45] R. A. McKee, F. J. Walker, and M. F. Chisholm, Phys. Rev. Lett. **81**, (1998) 3014

[46] G.D. Wilk, R.M. Wallace, Appl. Phys. Lett. **74**, 19 (1999) 2854

[47] N. Mise, M. Kadoshima, T. Morooka, T. Eimori, Y. Nara, Y. Ohji, Jpn. J. Appl. Phys. **47**, 10 (2008) 7780–7783

[48] N. Mise, T. Morooka, T. Eimori, S. Kamiyama, K. Murayama, M. Sato, T. Ono, Y Nara, and Y Ohji, IEEE Transactions on Electron Devices, Vol. **56**, 1, (2009) 85

[49] C.J. Karlsson, E. Landemark, L.S.O. Johansson, U.O. Karlsson, R.I.G. Uhrberg, Phys. Rev. B **41**, 3, (1990) 1521

[50] K. Yamamoto, M. Hasegawa, J. Vac. Sci. Technol. B. **12**, 4, (1994) 2493

[51] F. Jolly, F. Rochet, G. Dufour, C. Grupp, A. Taleb-Ibrahimi, Surface Science **463** (2000) 102–108

[52] J. Mach, J. Cechal, M. Kolíbal, M. Potocek, T. Sikola, Surface Science **602** (2008) 1898–1902

[53] F. J. Himpsel, F.R. McFreely, A. Taleb-Ibrahimi, J.A. Yarmoff and G. Hollinger, Phys. Rev. B **38**, (1988) 6084

[54] B. Brennan, S. McDonnell, G. Hughes, Thin Solid Films **518** (2010) 1980–1984

[55] S. McDonnell, B. Brennan, G. Hughes, Appl. Phys. Lett. **95**, (2009) 072903

[56] D. Peterka, C. Tegenkamp, K.M. Schroder, W. Ernst, H. Pfnur, Surface Science **431** (1999) 146–155

[57] P. Morgen, A. Bahari, U. Robenhagen, J. F. Anderson, J. –K. Hansen, K. Pedersen, M. G. Rao, Z. S. Li, J. Vac. Sci. Technol. A **23** (1) (2005) 201

[58] N. Miyata, M. Ichikawa, T. Nabatame, T. Horikawa, A. Toriumi, Jpn. J. Appl. Phys. **42** (2003) L 138

[59] S. Iwata, A. Ishizaka, J. Appl. Phys **79** (1996) 6653

Chapter 5

The growth mode and characterisation of magnesium silicate films formed on modified silicon surfaces

5.1 Introduction

Controlling the interfacial properties of silicon is one of the biggest challenges facing the integration of high-*k* materials in future silicon based transistor technology. The thermal stability of the interfacial region must be addressed in order to prevent the growth of interfacial SiO_2, which can adversely affect the equivalent oxide thickness (EOT) of the device [1]. The formation of thermally and chemically stable metal-silicates at the silicon surface may prevent the growth of SiO_2 [2]. Previous studies have shown that silicate layers can be formed by deposition of various metals including Yttrium [3] Lanthanum [4] and Erbium [5], and have been shown to produce promising electrical and physical characteristics. In this study the formation of a magnesium silicate interfacial layer is investigated as an alternative to SiO_2 due to its high reported thermal stability [6]. Previous studies have shown that MgO deposition onto Si results in the growth of a thin (< 1 nm) interfacial Mg silicate region [7,8]. Further studies also indicate that these films lead to favourable interface characteristics, including low interface state densities [9]. However, it has also been reported that the strong tendency for MgO to crystallise results in the film displaying a high density of columnar grains within the oxide films, independent of growth method [10-12]. The grain boundaries associated with these columnar structures may result in the rapid formation of breakdown paths, dramatically reducing the lifetime of the devices [13].

The focus of this chapter is to investigate methods by which the interfacial properties of silicon can be modified using the growth of magnesium silicate. The chapter is divided into three sections which address different aspects of how Mg silicate may be formed on silicon surfaces via the deposition of metallic magnesium. Photoemission spectroscopy is the primary analysis technique used in this study, with the curve fitting procedures outlined in Chapter 3 being used for both synchrotron and conventional XPS studies. Section 5.3 explores the mechanism by which silicon native oxide surfaces may be converted into Mg silicate at temperatures as low as 500 °C. *In-situ* XPS analysis of the Mg silicate growth mechanism has shown that the growth of Mg silicide, upon deposition of metallic Mg, acts as a vital intermediate step to silicate formation. Therefore the growth and stability of Mg silicide films on Si was studied in section 5.4. High resolution synchrotron based photoemission studies have shown that the step wise deposition of Mg onto an ultra-thin Si oxide surface, results in greater levels of silicide growth compared to that seen after continuous Mg deposition. Thermal annealing studies suggest that Mg silicide desorbs from silicon oxide surfaces at temperatures greater than 300 °C, however in contrast to this, it is possible to promote Mg silicide growth on H-terminated Si surfaces using UHV annealing. Low levels (900 L) of O_2 exposure have also been shown to result in removal of the Mg silicide, in contrast to the reported chemical stability of other metal silicide species.

The growth of Mg silicate on differently prepared Si surfaces is attempted in section 5.5. Magnesium silicate has been formed on oxide free H-terminated Si surfaces by depositing metallic Mg and subsequently annealing the surface in an O_2 partial pressure of 5×10^{-7} mbar. However, XPS analysis indicates that exposure to excess oxygen results in the formation of stoichiometric MgO which is not fully converted into Mg silicate by 500 °C annealing, forming a mixed phase Mg silicate/MgO film. Mg silicate films have also been successfully formed on 700 nm SiO_2 and silicon-oxy-nitride surfaces using the same procedure. At the end of each section a brief summary of the findings are given in an attempt to clarify the results and put them in context within the overall Mg silicate study.

5.2 Experimental Procedure

Si (111) native oxide surfaces were prepared using a standard degreasing procedure of successive dips in acetone, methanol and isopropyl alcohol (IPA) before being loaded into a UHV deposition and analysis system. Pure magnesium metal (99.9%) was deposited at room temperature at a pressure of 1×10^{-9} mbar onto the native oxide surface using thermal evaporation. The x-ray photoelectron spectroscopy (XPS) analysis was carried out using a VG Microtech electron spectrometer system described in Chapter 3. High temperature annealing studies were carried out in vacuum at a pressure of 1×10^{-9} mbar, with samples kept at the target temperature for 20 minutes. Information on the species which desorb from the surface during thermal annealing was acquired with Ametek Process Instruments - Dycor mass spectrometer, set to monitor atomic masses of 24 (Mg) and 40 (MgO). XPS core level spectra were curve fitted using Voigt profiles composed of Gaussian and Lorentzian line shapes in a 3:1 ratio and using a Shirley-type background. The full width at half maximum (FWHM) of the Si 2p substrate peak was 0.80eV and the oxides, silicides and silicate component peaks were in the range 1.2eV to 1.5eV. The corresponding O 1s core level spectra have FWHM values in the 1.75eV to 1.9eV range. All spectra were charge referenced to the Si 2p bulk signal at 99.3 eV and there was no evidence of differential charging effects for the native oxide covered surfaces.

The soft X-ray photoemission experiments were carried out on the SGM1 beamline at the Astrid synchrotron in the University of Aarhus in an ultrahigh vacuum (UHV) system described in Chapter 3. Prior to magnesium deposition, an ultra thin SiO_2 film was grown on atomically clean boron doped p-type Si(111) of resistivity 1–3 mΩ cm ($2–5\times10^{19}$ cm^{-3}) using the procedure outlined in Chapter 4. The metallic Mg component of the Mg 2p profile is fitted with an asymmetric doublet, with a spin orbit splitting of 0.28 eV. All other components within the Mg 2p (Mg silicide, oxidised Mg) were fitted using standard, symmetric, doublet peak again with a spin orbit splitting value of 0.28 eV.

5.3 The growth and thermal stability of Mg silicate on Si native oxide surfaces

5.3.1 Photoemission study of the SiO_2 conversion mechanism to Mg silicate

The curve fitted Si 2p spectra taken from a SiO_2 native oxide covered silicon surface before and after ~ 2 nm Mg deposition, shown in figure 5.1, illustrate that Mg deposition has resulted in the growth of peaks on both the higher binding energy (HBE) and lower binding energy (LBE) sides of the Si bulk peak.

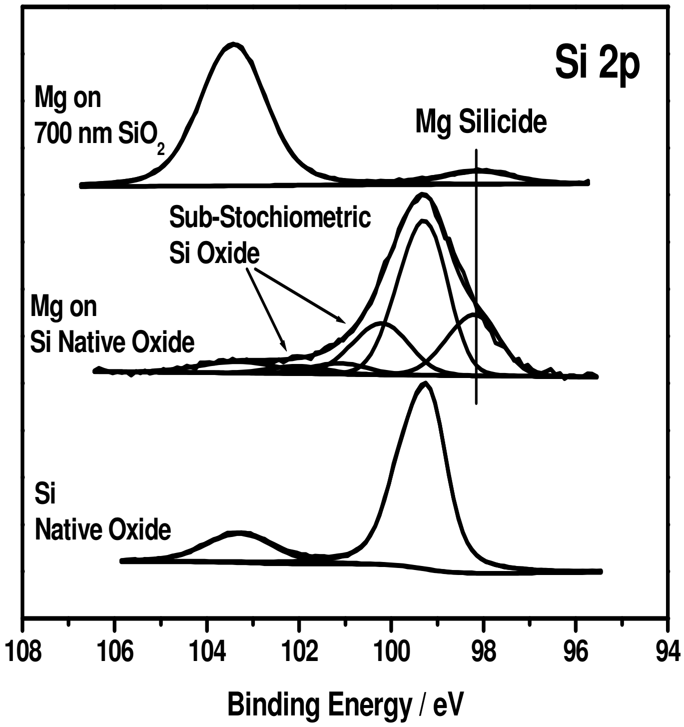

Figure 5.1 Curve Fitted Si 2p spectra showing the growth of Mg silicide and sub-stoichiometric silicon oxide species after Mg deposition (2 nm) onto Si native oxide surfaces. The growth of Mg silicide on 700 nm SiO_2 surfaces suggests disruption of the SiO_2 structure resulting in Mg atoms taking the place of the O atoms.

The HBE peaks have been attributed to sub-stoichiometric silicon oxide peaks which appear as the result of Mg incorporation within the SiO_2 layer. The LBE peak, separated from the Si substrate peak by 1.1 eV, has been attributed to the presence of magnesium silicide, which is consistent with the results reported by Brause *et al.* [14]. It should be noted that Si 2p spectra taken after successive Mg depositions suggest that silicide growth was self limiting, and could not be grown beyond a certain point. The formation of a metal silicide resulting from the deposition of a reactive metal onto a thin silicon surface oxide is usually associated with a reaction between the metal and the silicon substrate. This is because the normal thermodynamic trend for metal oxides used as high-*k* dielectrics is that the metal oxide is thermodynamically more stable than the silicide. Therefore, depositing these metals on thin Si oxide layers usually results in the preferential formation of a metal oxide by the reduction of SiO_2 [15] releasing silicon which can subsequently oxidise and contribute to the formation of an increased silicon oxide interlayer. In this case, the Mg preferentially reacts with the silicon atoms within the native oxide layer. This has been conclusively illustrated in a separate study where Mg was deposited on a SiO_2 layer of effectively infinite thickness (700nm) and, as shown in figure 5.1, the metal silicide was clearly observed. However, interface reactions are not necessarily predictable from bulk thermodynamic data as the non-equilibrium nature of the deposition process can have an impact on interface composition [16,17].

The growth of Mg silicide in the absence of bulk silicon suggests that the Mg atoms have disrupted the SiO_2 structure resulting in Mg atoms taking the place of the O atoms, creating Mg-Si bonds. Following the deposition of Mg on the native oxide surface, the samples were annealed in UHV to 300 °C and the changes in the Si 2p spectrum shown in figure 5.2 suggest the complete removal of Mg silicide, along with the removal of the Si sub oxide groups.

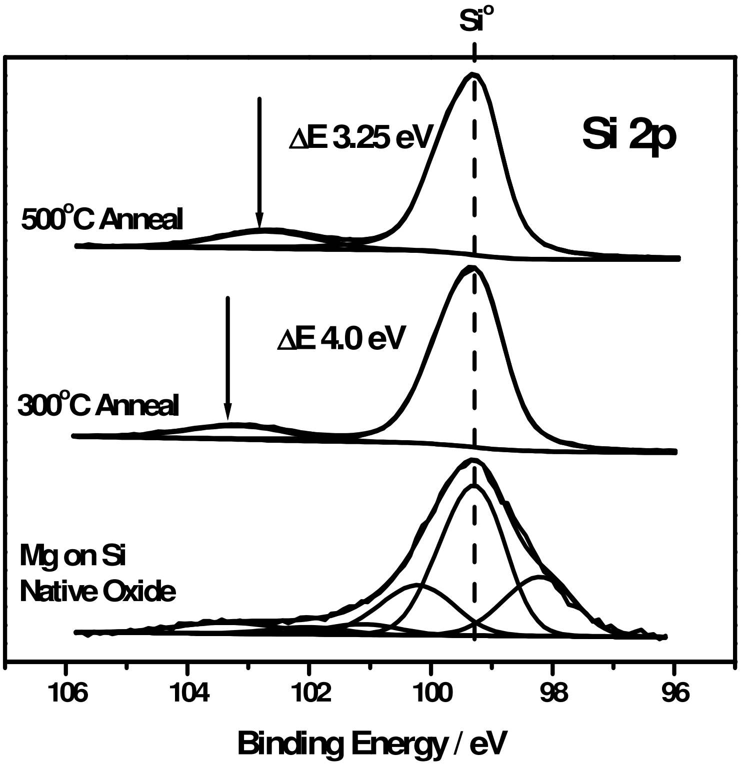

Figure 5.2 Si 2p spectra taken after UHV annealing to 300 °C show the complete removal of Mg silicide and Si sub-oxide species, and reduction in SiO_2 from 17 % to 10 % of the signal. Further annealing to 500 °C results in a chemical shift in the Si oxide peak, which is indicative of the transformation of SiO_2 to Mg silicate.

The thermal instability of Mg silicide has previously been reported [14,18]. The reduction in the SiO_2 peak area from 17 % to 10 % of the total signal is consistent with the removal of oxygen from the SiO_2 layer during Mg silicide formation, however there is no discernable shift in the peak position of the silicon oxide indicating that after this anneal the silicon within the oxide remains predominantly in the Si^{4+} oxidation state.

The Mg 2p spectrum in figure 5.3 relating to the deposition of Mg results in the appearance of an asymmetric peak indicative of metallic Mg [19].

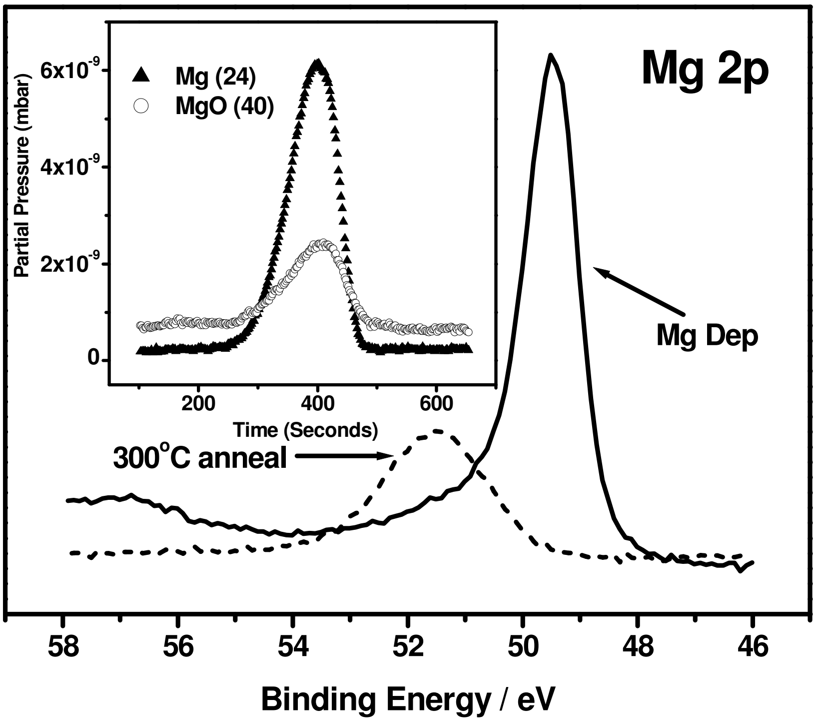

Figure 5.3 Mg 2p spectra of the core level following Mg deposition and the subsequent 300 °C anneal which results in the oxidation of the Mg. A reduction in the integrated area of the peak by a factor of 2.5, along with mass spectrometry data (inset) suggest desorption of excess Mg from the surface during annealing.

Annealing to 300 °C results in a 1.8 eV shift of the Mg 2p peak towards higher binding energy, which is indicative of the oxidation of the remaining Mg present on the SiO_2 surface. However this binding energy separation is less than the reported separation for metallic Mg and stoichiometric MgO (~2.1 eV) [20,21] indicating the presence of magnesium sub-oxide. The integrated area under the Mg 2p peak was also reduced by a factor of 2.5 as a result of the anneal suggesting desorption of excess Mg from the surface. This is substantiated by mass spectrometry data taken during annealing, shown in the inset of figure 5.3, where the predominant species desorbing from the surface at 300 °C is Mg with a smaller contribution from MgO.

The desorption of metallic Mg from the surface is in agreement with the work of Galkin *et al.* [18] which suggests that room temperature deposition of Mg onto Si initially results in the formation of silicide islands while continued deposition results in the growth of metallic Mg on top of these island structures. Other studies [22] have shown that metallic Mg will desorb from the Si surface at temperatures above 200 °C.

The changes induced in the Si 2p peak profile in figure 5.2 after subsequent annealing of the sample to 500 °C results in a significant shift in the Si oxide peak. The Si oxide peak now shows a separation from the bulk peak equal to 3.25 eV, which is indicative of Mg silicate and not SiO_2. The peak position of Mg silicate with respect to the silicon substrate peak has previously been found during MgO deposition onto the Si (111) surface (Chapter 4), and verified using Mg silicate reference materials. Using atomic sensitivity factors [23], the stoichiometry of the silicate film has been calculated to be $Mg_2Si_{0.8}O_{4.3}$ which is close to that of foresterite (Mg_2SiO_4) [24]. Peak fitting of the Si 2p spectrum in figure 5.2 suggests that the contribution of the Si^{4+} oxidation state has been reduced below the level of detection for standard XPS, which indicates a considerable reduction in the presence of the SiO_2 native oxide. Mg 2p spectra (not shown) taken after the 500 °C anneal show a 0.2 eV shift to lower binding energy, which is consistent with Mg silicate formation.

It should also be noted that there is no discernable change in Mg 2p peak area, indicating that the sub-oxidised Mg formed after at 300 °C does not desorb during the 500 °C anneal. Curve fitting of the Si 2p spectra in figure 5.2 indicate that the integrated area of the magnesium silicate peak is comparable to that of the silicon native oxide peak before Mg deposition. Given this result, and the self limiting nature of silicide formation, it can be suggested that only the native oxide layer is converted to Mg silicate and not the crystalline silicon bulk. This suggests that Mg silicate formation at 500 °C is a self limiting process and is determined by the initial thickness of the surface oxide film. Further evidence that the SiO_2 native oxide has been converted into Mg silicate comes from the evolution of the O 1s spectrum illustrated in figure 5.4.

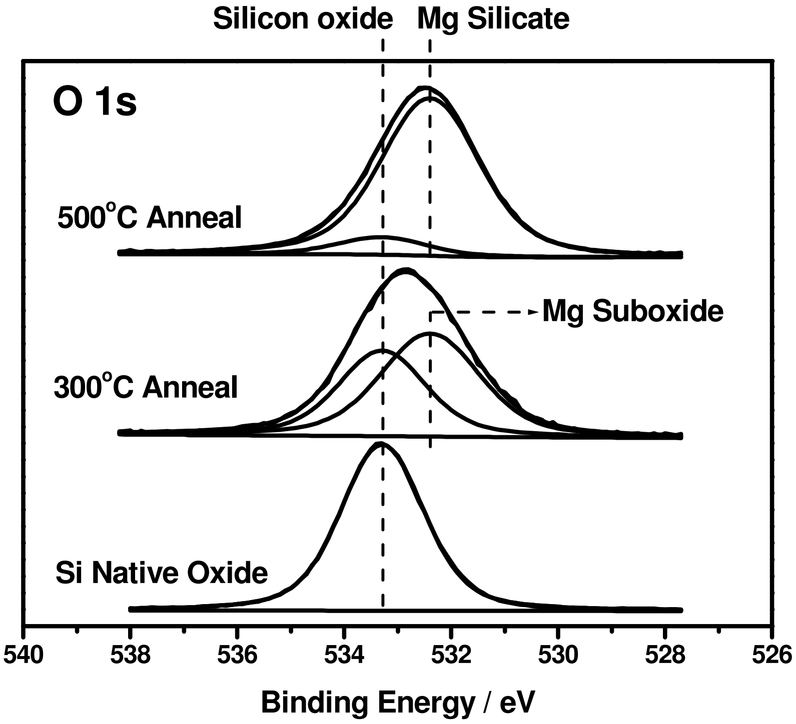

Figure 5.4 Normalised O 1s core level spectra show the presence of both SiO_2 and partially oxidised Mg species after a 300 °C anneal. The reduction in the SiO_2 peak after a 500 °C anneal provides further evidence for the transformation of SiO_2 into Mg silicate.

The deposition of Mg on the SiO_2 native oxide surface leaves the O1s peak profile unchanged which supports observations from the Si 2p core level that the room temperature interaction of Mg with the SiO_2 occurs preferentially with the silicon atoms in the SiO_2. It should be noted that the formation of sub-stoichiometric Si oxide peaks seen in the Si 2p spectra did not alter the O 1s spectrum. However, there is no inconsistency between seeing sub-stoichiometric silicon oxide states in the Si 2p spectrum and not seeing this reflected in the O 1s core level profile. For example when ultrathin oxides, which have almost equal contribution from the four silicon oxidation states, are grown on silicon (Chapter 4 figure 4.23) the oxygen peak can be fitted with a single peak (Chapter 4 figure 4.25). In addition, a study by Hirose *et al.*

[25] of the transition layer at the Si/SiO_2 interface which focused on the valence band region showed that there was no alteration to the O 2s peak profile when compared with a bulk SiO_2 layer other than a 0.2 eV shift in the binding energy.

Curve fitting of the broadened O 1s peak observed after 300 °C annealing reveals the presence of an oxidised Mg component shifted by 1.0 eV to lower binding energy in addition to the SiO_2 peak, which is consistent with the oxidation shown in the Mg 2p profile. This energy separation between the two oxide components of the O 1s spectrum is less than that seen between SiO_2 and fully stoichiometric MgO, which has been measured in separate experiments to be 1.54 eV. Therefore, although the Mg is in an oxidised state, it is not in the fully oxidised species MgO. It can also be said that the Mg atoms are not in a silicate bonding environment as the silicon oxide state shown in the Si 2p spectra (figure 5.2) is still indicative of the SiO_2 native oxide. After annealing to 500 °C there is a significant decrease in the presence of the SiO_2 related component within the O 1s core level profile. Given that there is no change in the total integrated area of the peak, this again indicates that the SiO_2 has been converted into Mg silicate consistent with the observations on the Si 2p core level. While the Mg 2p core level spectrum shifts by 0.2eV between the partially oxidised Mg and the Mg silicate, no corresponding binding energy shift is observed in the O 1s spectra. This would indicate that the binding energy position of the O 1s spectrum is insensitive to chemical changes between oxidised magnesium and magnesium silicate. The chemical shifts shown by the Si 2p, Mg 2p and O 1s spectra after Mg-silicate formation are in accordance with the electronegativities of magnesium, silicon and oxygen (1.31, 1.90 and 3.44 on the Pauling scale). These values would also suggest that the O 1s binding energy position of both suboxidised magnesium and magnesium silicate would exist between the SiO_2 (BE = 533.3 eV) and MgO (BE = 531.8 eV) which agrees with the above observations.

Subsequent studies have shown that the determining factor in silicate growth is the amount of Mg silicide initially formed on the SiO_2 surface. The importance of silicide formation as an intermediate step to silicate formation has previously been suggested by Chambers *et al.* [3] and can be conclusively shown here. The spectra in figure 1 showed the effect of ~ 2 nm Mg deposition onto SiO_2, which caused the growth of Mg-silicide and eventually led to the growth of Mg-silicate. However, if only 1 nm of Mg is deposited, an insufficient amount of Mg silicide is formed, and annealing to

500 °C results in only partial transformation of the SiO_2 into Mg-silicate as can be seen in the Si 2p spectra in figure 5.5.

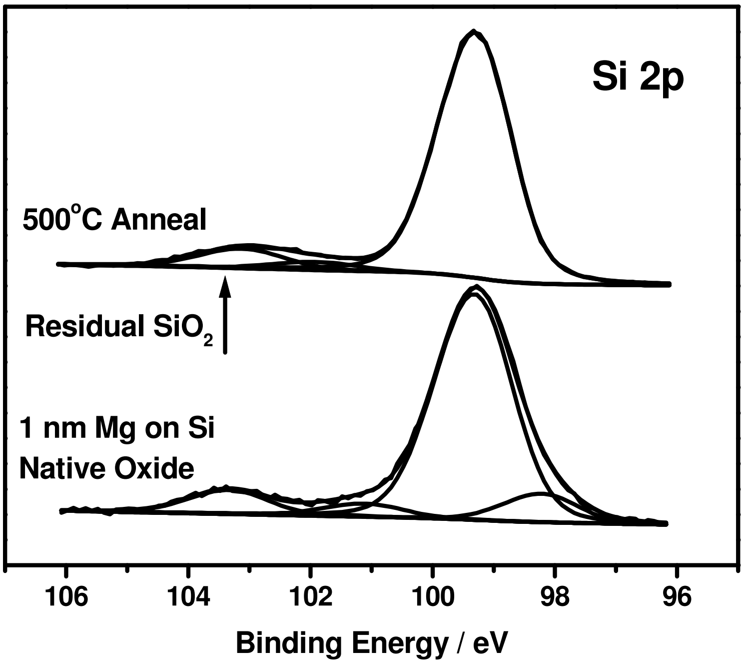

Figure 5.5 Si 2p spectra taken after 1 nm Mg deposition onto Si native oxide surface show the growth of less Mg silicide than that seen in figure 1. Subsequent UHV annealing to 500 °C resulted in only partial transformation of SiO_2 into Mg silicate, indicating the importance of silicide formation as an intermediate step in Mg silicate growth.

It should be noted that the depositing 1 nm of Mg reduced the integrated area of the SiO_2 peak from 17 % to 14 % of the total Si 2p signal, compared to a reduction of 17 % to 10 % seen in figure 5.3. This is again in agreement with the assertion that silicide formation results in the loss of silicon oxide. Further evidence for the importance of silicide formation comes from analysing the chemical species present on the surface after annealing to 300 °C. The Si 2p spectrum in figure 5.2 taken after the 300 °C anneal shows no evidence of Mg-silicide, while the silicon oxide present on the surface remains in the form of SiO_2. Also, it can be seen from figure 5.3 that the Mg present on the surface after the 300°C anneal is in the form of oxidised Mg. Therefore, while the only chemical species present are oxidised Mg and SiO_2, annealing the sample to 500 °C still results in silicate formation. This is in direct contrast to the result seen after the deposition of stoichiometric MgO onto the SiO_2 native oxide surface shown in figure 5.6, where the spectra taken after annealing to 500 °C show no evidence for the transformation of SiO_2 into Mg silicate.

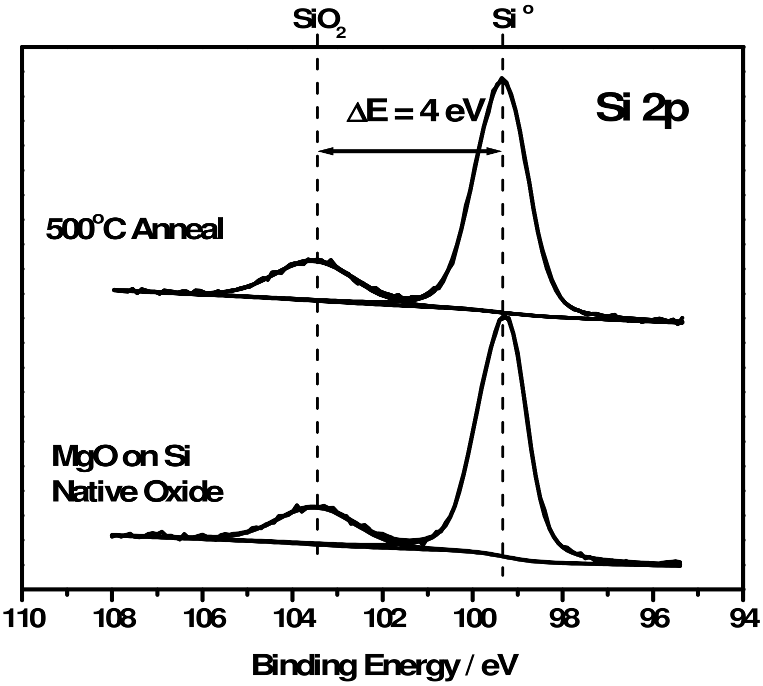

Figure 5.6 Si 2p spectra taken from Si native oxide surface after MgO deposition and subsequent 500 °C anneal showing no change in peak profile which suggests the importance of Mg silicide growth as an intermediate step in Mg silicate formation.

This would indicate that the presence of SiO_2 and stoichiometric MgO will not lead to silicate formation at 500 °C without the effect of the intermediate silicide formation at room temperature and subsequent decomposition at 300 °C prior to the 500 °C anneal. Further evidence for the assertion that Mg silicide formation increases the chemical reactivity of the Si native oxide surface is shown in figure 5.7.

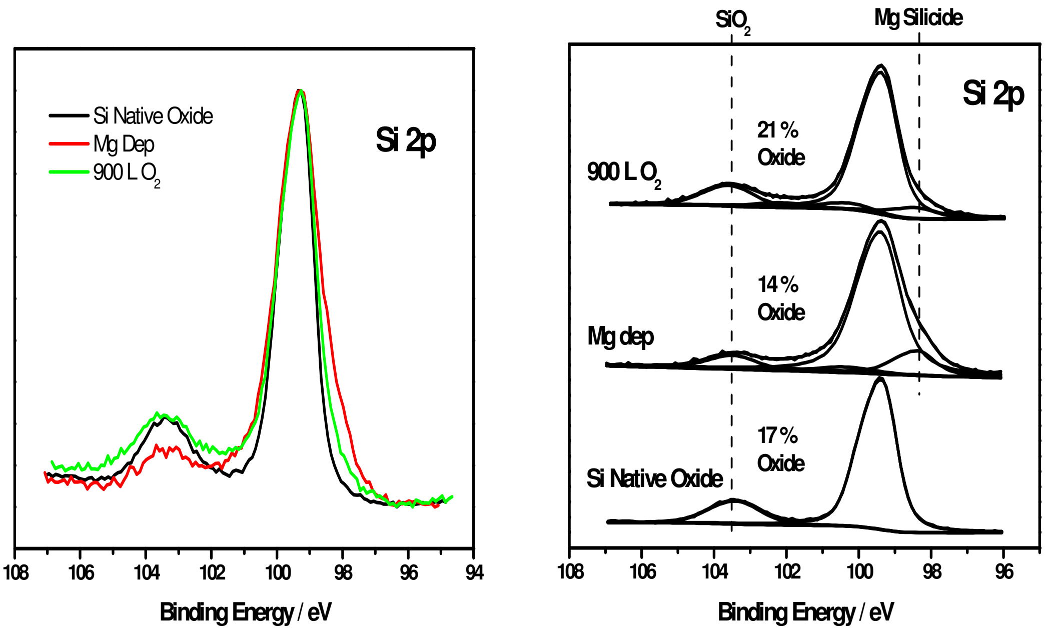

Figure 5.7 Raw and curve fitted Si 2p spectra showing that Mg deposition greatly increases the chemical reactivity of the Si native oxide surface.

The Si 2p spectra show that Mg deposition resulted in the growth of Mg silicide and associated reduction in the area of the SiO_2 peak, in agreement with figure 5.1. The sample was subsequently exposed to an O_2 partial pressure of 5×10^{-7} mbar, at room temperature, for 30 minutes (900 L). The Si 2p spectrum taken after room temperature O_2 exposure shows the re-growth of the SiO_2 peak. This is in direct contrast to the reactivity of native oxide, H-terminated and “flash cleaned” silicon surfaces, which show no comparable oxide growth after similar exposure periods at room temperature. This increased reactivity is again attributed the disruption caused to the surface during silicide growth, in agreement with the growth mechanism described previously. It should also be noted that there is no evidence for a binding energy shift in the Si oxide peak after O_2 exposure, this again suggests that while silicide growth is a vital intermediate step Mg silicate does not form as a direct result of Mg silicide oxidation.

Given the importance of silicide in silicate formation, it is suggested that the thermal instability of Mg-silicide offers an advantage over other metal-silicides. The thermal decomposition of Mg silicide prior to Mg silicate formation is in contrast to the silicide oxidation process developed for the formation other metal silicates such as Y silicate [3,26] and Hf silicate [27]. These studies have shown that the oxidation of Y silicide can only be achieved at high temperature (600° – 900 °C) and high pressures of N_2O (1 atm), while high pressure ozone oxidation has been used to form hafnium silicate from deposited hafnium silicide. The presence of excess oxygen in the high temperature annealing of rare earth silicates has been shown to result in the growth of interfacial Si-O-Si bonds [28]. However, it should also be noted from our studies that the desorption of excess metallic Mg from the silicon surface at 300 °C means that it is difficult to promote additional silicide formation above that which forms initially at room temperature. The thermal instability of Mg silicide therefore means that only those Si atoms which are involved in silicide formation after Mg deposition can be incorporated into Mg-silicate, placing a limit on the achievable thickness of the silicate film. This contrasts with the experimental observations reported by Baglin *et al.* [29] for the promotion of yttrium silicide growth at elevated temperature.

The results of this study may have relevance for the low temperature modification of silicon interlayers on III-V materials which have been deposited prior to high-*k* dielectric deposition, in an attempt to improve the interfacial electrical characteristics [30]. While Jiang *et al.* [31] have shown that thin amorphous silicon interlayers can be successfully converted into ytterbium silicide, high temperature annealing could detrimentally impact on the interface quality as III-V materials are unstable at high temperature [25]. The Mg silicate formation procedure at 500°C outlined in this work may make it more suitable for silicon interlayer modification on III-V semiconductor substrates than other metal silicates.

5.3.2 High temperature annealing studies of thin Mg silicate films formed on Si native oxide surfaces

The work of Wilk *et al.* [2] has suggested that while the dielectric constant of metal silicate films is typically less than that of metal oxides, silicate growth has the advantage of producing amorphous layers with improved thermal stability. The thermal stability of magnesium silicate films formed on SiO_2 native oxide surfaces was studied using a series of UHV high temperature anneals, between 500 °C and 850 °C, with samples remaining at the target temperature for 30 minutes. Annealing studies were carried out using direct current heating of low resistivity Si (111) samples similar to those used for flash cleaning procedure outlined in Chapter 3. Temperatures were measured with a pyrometer, using an average value of 0.61 for the emissivity of Si. Si 2p core level spectra taken from the surface after successive anneals between 750 °C and 850 °C are shown in figure 5.8. The Mg silicate film which was formed at 500 °C, showed no change to the Si 2p, Mg 2p or O 1s spectra at temperatures below 660 °C. This result is in agreement with the reported thermal stability of Zr silicate films [33].

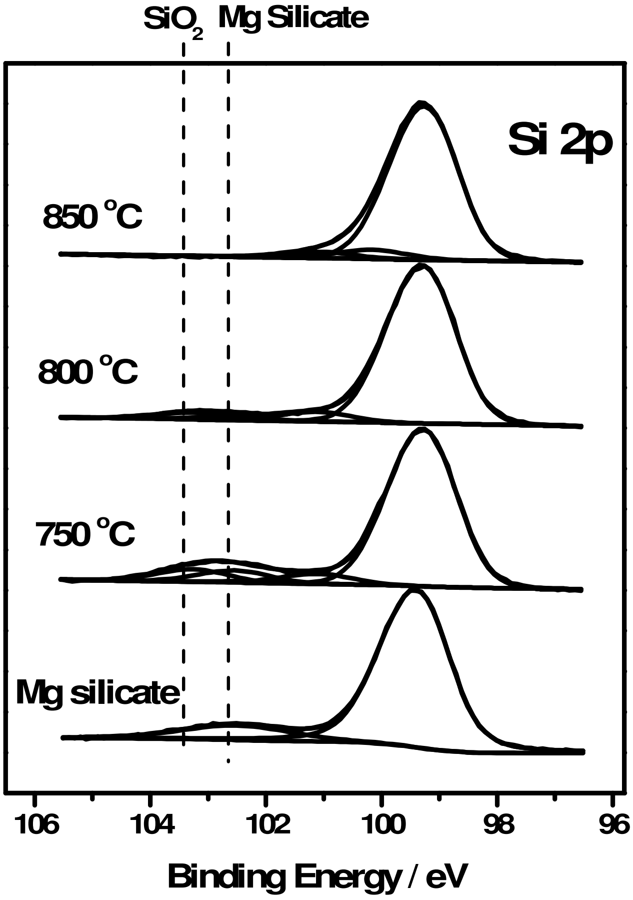

Figure 5.8 Curve fitted Si 2p spectra show that UHV annealing of Mg silicate to 750 °C causes the growth of interfacial Si oxide, while annealing to 850 °C results in the complete desorption of Mg silicate.

The Si 2p spectrum acquired after the 750 °C anneal shows evidence for growth in the Si 4^+ and 3^+ oxidation states. Given that the initial formation of Mg silicate results in the removal of the Si 4^+ oxidation state, the re-growth of this peak may be indicative of thermal decomposition within the Mg silicate film. This result is in agreement with the work of Ono *et al.* [28] who report an increase of Si-O-Si bonds at the interface between bulk silicon and metal silicate over layers, resulting from high temperature annealing. The effects of high temperature annealing on Mg silicate can also be seen from the Mg 2p spectra in figure 5.9.

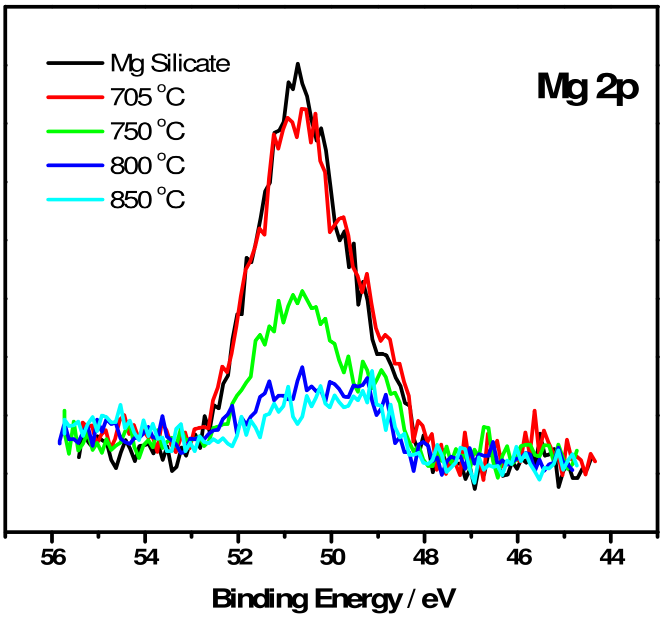

Figure 5.9 Reduction in the Mg 2p peak area also suggests the desorption of Mg silicate at temperatures greater than 750 °C.

Degradation in the silicate film, at temperatures above 750 °C, can be seen from a significant reduction in the Mg 2p peak area. At temperatures above 800 °C there is evidence for the loss of surface oxygen in both the Si 2p (figure 5.8) and O 1s spectra (not shown). The results suggest that thermal annealing to this temperature causes desorption of both silicon oxide and Mg silicate. Si 2p spectra taken after annealing to 850 °C suggest the complete removal of oxidised Si species, with only slight contribution from the Si $^{1+}$ oxidation state. This is in agreement with O 1s spectra, which show a 93 % reduction in the integrated peak area, and a similar a reduction in the area of the Mg 2p peak. While Mg 2p and O 1s spectra indicate the slight presence of residual Mg silicate above 850 °C, there is evidence for significant thermal desorption of Mg silicate below this temperature. Degradation of Mg silicate at temperatures below 800 °C is in contrast to the stability shown by Hf silicate films at this temperature [2], suggesting the thermal stability of Mg silicate thin films is less than that of Hf silicate. However, it should be noted that the reported thermal stability of Hf silicate was determined using a metal-oxide capping layer [2], which may greatly affect the result.

The results suggest Mg silicate is stable up to 700 °C, with no alterations in the Mg 2p, Si 2p and O 1s spectra. Between 705 ° and 800 °C there is evidence for the growth of Si-O-Si bonds along with a slight reduction in the presence of Mg silicate in agreement with published results. Temperatures above 800 °C show significant reduction in the presence of surface oxygen, suggesting the desorption of both silicon oxide and magnesium silicate.

5.3.3 Conclusions

The results presented here suggest that a SiO_2 native oxide layer can be converted into Mg silicate. Initial deposition of Mg onto the SiO_2 surface resulted in the growth of Mg silicide due to disruption of the SiO_2 and loss of oxygen from the surface. Annealing the sample to 300 °C resulted in removing the thermally unstable Mg silicide and desorption of excess Mg from the surface. It is believed that the decomposition of Mg silicide creates under co-ordinated silicon atoms which react with the oxidised Mg resulting in the formation of Mg silicate upon annealing to 500 °C. The study has also shown that the initial formation of Mg silicide is a necessary intermediate step in Mg silicate growth and can only be achieved by deposition of metallic Mg. The thermal stability of Mg silicate films has also been investigated using a series of high temperature anneals in ultra high vacuum. At temperatures above 800 °C there is evidence for desorption of both silicon oxide and magnesium silicate species.

Section 5.4 The growth and stability of magnesium silicide films grown on silicon

The growth of magnesium silicide as an intermediate step in the formation of magnesium silicate has been outlined. As such, the properties of Mg silicide and the factors which effect its growth are of great importance, and were therefore studied in further detail. The focus of this investigation is to determine the factors which effect the growth and stability of Mg silicide films formed on Si. The study has been informed by the work of Lee *et al.* [34] who have shown that the rate of Mg deposition onto oxide free Si (111) surfaces may determine the growth characteristics of both Mg silicide and metallic Mg thin films. It has been suggested that depositing Mg in a step-wise fashion, with at least 1 hour between deposition stages, results in the creation of round shaped Mg islands on the surface of an amorphous Mg silicide layer. However, deposition of Mg in a continuous fashion results in the formation of Mg islands with a hexagonal structure on a flat Mg silicide over layer. It is also suggested that the formation of such hexagonal structures may act as a barrier to further Mg atoms reaching the Mg silicide surface. While photoemission techniques have previously been used to analyse the growth of Mg silicide [35-37], the focus of this study is to use high resolution photoemission in order to characterise the growth mode of Mg silicide using both step-wise and continuous deposition, and determine if there is any difference in the amount of silicide formed using both approaches. The thermal stability of both metallic Mg and Mg silicide are of great importance in determining how the thickness of Mg silicide films can be increased beyond that formed during Mg deposition. While vacuum annealing has previously been used to promote the growth of metal silicide species on silicon surfaces [29,38,39], the thermal stability of both the metal and metal-silicide are crucial in determining the effectiveness of this technique. Once formed using Mg deposition, the thermal stability of Mg silicide and mechanism of silicide growth was investigated using standard x-ray photoelectron spectroscopy (XPS) after a series of high temperature vacuum anneals. The chemical stability of Mg silicide was also studied using controlled exposure to O_2 at low temperature and this was compared to data which has been published for other metal silicide species.

5.4.1 Mg Silicide thin film growth

The effect of step-wise Mg deposition onto an ultra thin grown Si oxide layer is shown using curve fitted Si 2p spectra in figure 5.10, taken at 130 eV photon energy using synchrotron based XPS. The acquisition of photoemission spectra resulted in a gap of at least 1 hour between successive depositions. The initially grown thermal oxide shows evidence of the presence of the four separate oxidation states, which are resolved by curve fitting in agreement with previous studies [40]. As stated in Chapter 4, the thickness of the self limiting oxide was calculated to be approximately 0.3 nm, effectively meaning that it is one monolayer thick [41].

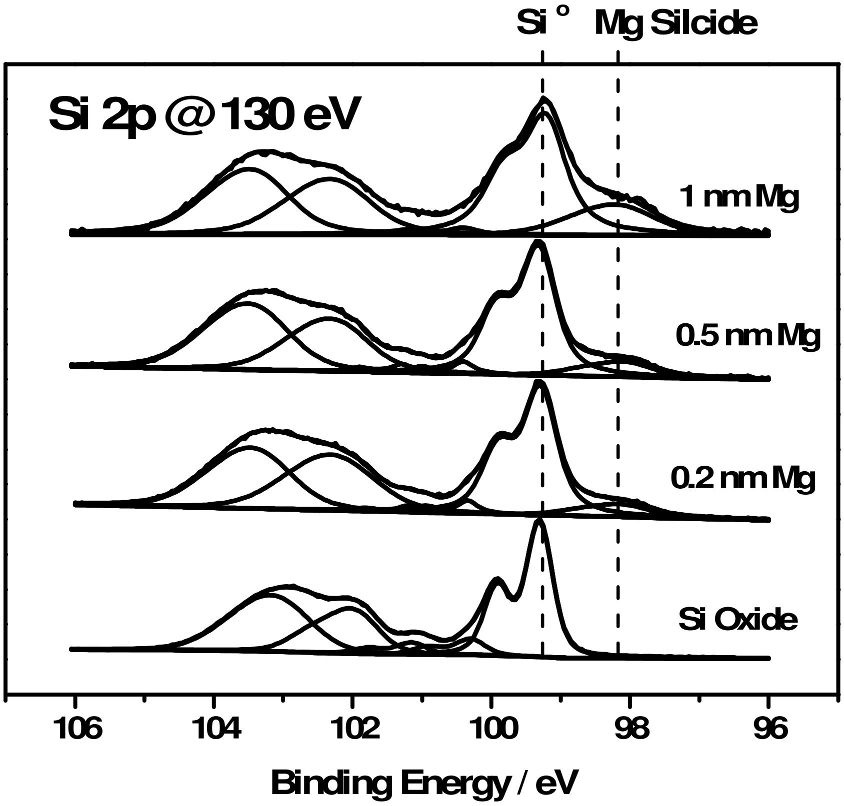

Figure 5.10 Curve fitted Si 2p spectra, acquired using SRXPS, show the growth of Mg silicide due to step-wise deposition of Mg onto an ultra thin (~ 0.3 nm) thermally grown Si oxide surface.

The spectra show that Mg deposition results in the growth of a peak at 1.1 eV lower biding energy (LBE) with respect to the Si bulk peak. This peak has been attributed to the presence of Mg silicide, in agreement with the work of Brause *et al.* [14] and van

Burren *et al.* [42]. While numerous silicide phases exist for metals such as Ni and Ti [43] the only reported phase of Mg silicide is the metal rich Mg_2Si [14,43], and as such a single silicide peak is used during curve fitting. Curve fitting data taken from the Si 2p spectra in figure 5.10 indicate a ~ 10 % reduction in the ratio of the Si oxide and bulk signals as a function of Mg deposition (i.e. (Σ oxide peaks)/bulk peak). An increase in the area of the Si $^{3+}$ oxidation state with respect to the Si $^{4+}$ state, from 0.6:1 to 1:1, is also observed. Both results indicate that oxygen has been lost from the Si oxide, due to the formation of Mg silicide involving Si atoms which initially lay within the SiO_x layer. This is in agreement with previous results which have shown that Mg can react with Si atoms in a fully oxidised environment (figure 5.1) and is consistent with the reported behaviour of other metals such as Ta and Ti [44]. However, given that the Si oxide layer had an initial thickness of only 1 ML, silicide growth may not have occurred exclusively within the oxide layer and may have also incorporated atoms from the Si bulk. The mechanism of silicide growth can be studied further by investigating the changes in the profile of the Mg 2p core level as a function of Mg coverage, as shown in figure 5.11.

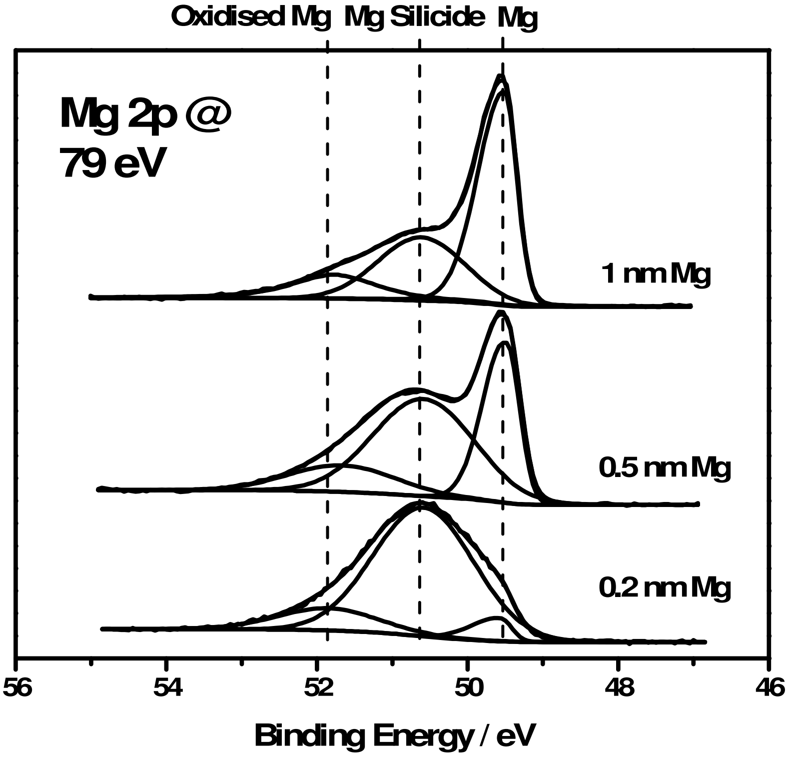

Figure 5.11 Mg 2p spectra, acquired at 79 eV photon energy, showing the initial stages of Mg silicide growth followed by the formation of metallic Mg.

The curve fitted spectra suggest that Mg deposition initially results in Mg silicide formation, as the binding energy of the principle peak at 50.6 eV is in agreement with that recorded in previous studies [45]. Continued deposition leads to the emergence of a metallic Mg component at 49.6 eV binding energy. A significantly smaller peak separated from the metallic Mg peak by 2.0 eV has been attributed to the presence of oxidised Mg [20,21]. This curve fitting analysis is in agreement with the work of Ndwandwea *et al.* [46] who have investigated the interaction between SiO_2 surfaces and a variety of metal species, and have shown that the deposition of reactive metals results in the formation of both metal-silicide and metal-oxide species. The growth of MgO upon Mg deposition is also in agreement with the removal of oxygen from the SiO_x layer seen in figure 5.10, while the relative intensities of the silicide and oxide peaks again indicates the preferential growth of Mg silicide.

The work of R. Pretorius [43] suggests that the growth of metal silicide thin films can be successfully predicted based both on bulk thermodynamic data and on the relative concentration of the Si and metal atoms. Therefore, the high heat of formation of Mg_2Si (-1661 kJ/mol) compared to either MgO (-602 kJ/mol) or SiO_2 (-859 kJ/mol) would suggest that metallic Mg would only be present on the surface if it was in contact with previously formed Mg silicide structures rather than on the Si oxide surface. If this is the case, the simultaneously observed growth of both metallic Mg and Mg silicide seen after the 2nd and 3rd Mg depositions may be consistent with the formation of silicide island structures on the oxidised silicon surface. The room temperature formation of metallic Mg on the surface of silicide island structures has previously been reported by Galkin *et al.* [18]. The effects of step-wise Mg deposition on a Si oxide surface can therefore be explained by the initial formation of Mg silicide islands, and the growth of metallic Mg on the surface of these islands.

Si 2p and Mg 2p spectra shown in figure 5.12 illustrate the differences in interfacial chemistry which result when Mg films, of ~ 1 nm, are grown using both step-wise and continuous deposition.

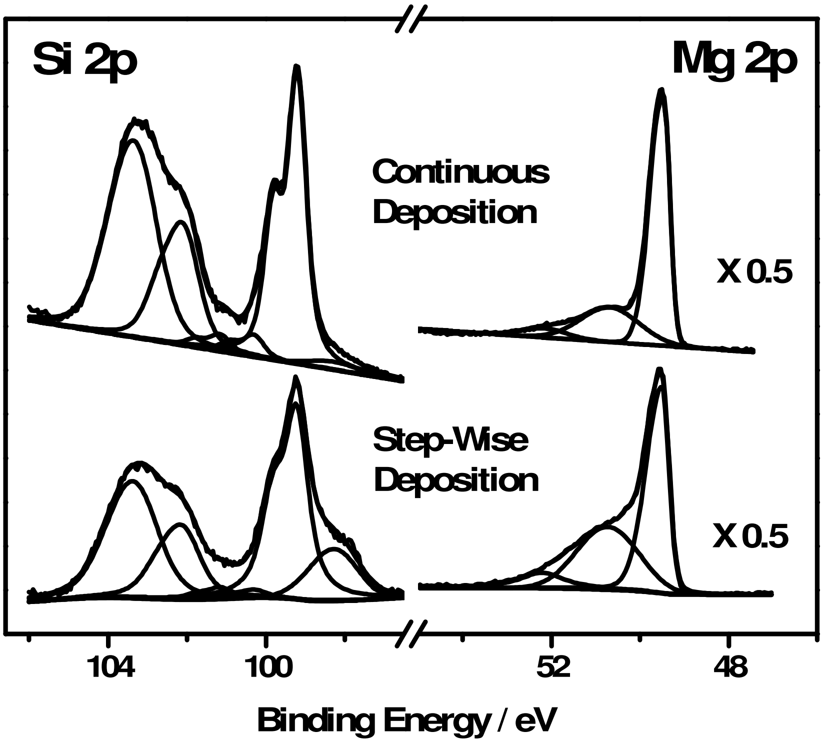

Figure 5.12 Comparison of Si 2p (130 eV) and Mg 2p (79 eV) spectra taken after step-wise and continuous deposition of ~ 1 nm Mg show increased levels of Mg silicide growth due to step-wise deposition.

The profiles of both the Si 2p and Mg 2p spectra show that the step wise deposition of Mg results in the growth of considerably more Mg silicide than that observed after the continuous deposition of Mg. An explanation for these different growth modes has been informed by the work of Lee *et al.* [34] who have previously reported differences in the growth mode of magnesium silicide on atomically clean silicon surfaces which relate to the flux of Mg atoms impinging on the Si surface. Their analysis suggests that a single step deposition process resulted in the formation of a uniform silicide layer, on top of which grew hexagonally shaped Mg structures which act as a barrier to further Mg atoms reaching the silicide surface. Should the formation of such a barrier also occur when Mg is deposited onto an oxidised Si surface it may act to limit the growth of silicide on the surface, explaining the results shown in figure 5.11. It may also be noted that the silicide formation is not as a result of the complete disruption of the original ultra-thin oxide which plays a critical role in preserving the electrical properties of the silicon which is in contrast to the observed interactions of MgO deposition onto the same surface [47].

5.4.2 Thermal Stability of Mg silicide on Si oxide surfaces

The thermal stability of magnesium silicide was subsequently studied using *in-situ* vacuum anneals. The effect of 300 °C annealing on the Mg silicide surface is shown in figure 5.13 for both Si 2p and Mg 2p core levels.

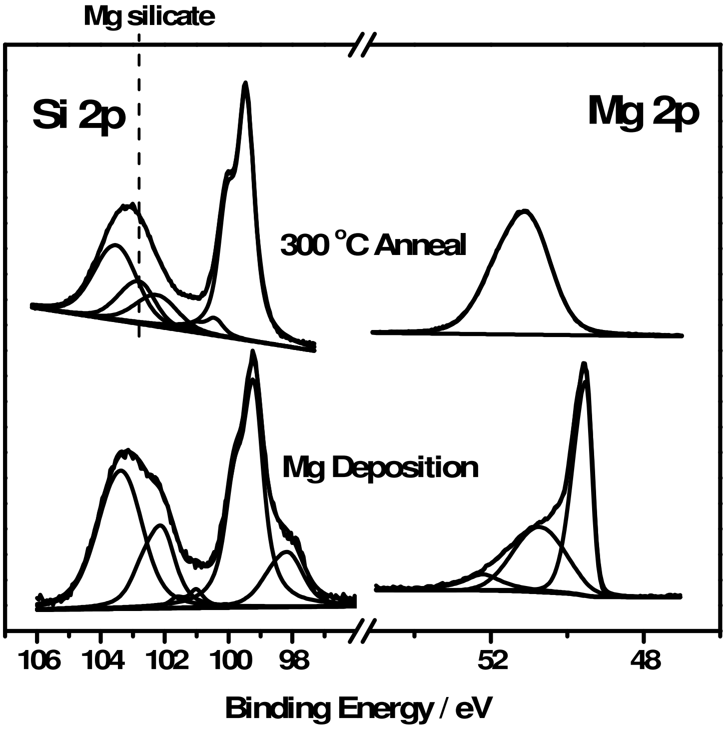

Figure 5.13 Annealing to 300 °C results in the removal of Mg silicide and oxidation of surface magnesium.

Si 2p spectra show no evidence for the presence of Mg silicide after annealing to 300 °C for 20 minutes. The thermal decomposition of Mg silicide has previously been reported by Galkin *et al.* [18] and observed in figure 5.2. Mg 2p spectra taken after annealing to 300 °C suggest the complete removal of metallic Mg from the surface in agreement with previously shown results (section 5.3. figure 5.3). The desorption of metallic Mg from Si surfaces at temperatures as low as 200 °C has previously been reported [22]. The removal of Mg silicide after vacuum annealing at temperatures below 300 °C is in marked contrast to that seen for the formation of other metal silicides such as Y [29], Ta [38], Dy [39] and Hf [48], which all result in the further silicide growth at elevated temperature. It should also be noted that annealing to 300 °C resulted in the growth of an additional peak separated from the Si° bulk peak by 3.25 eV, which has been attributed to the formation of Mg silicate in agreement with previous studies. The Si 2p spectrum taken after subsequent annealing to 500 °C in figure 5.14, shows evidence for the continued growth of Mg silicate along with Si sub-oxide growth.

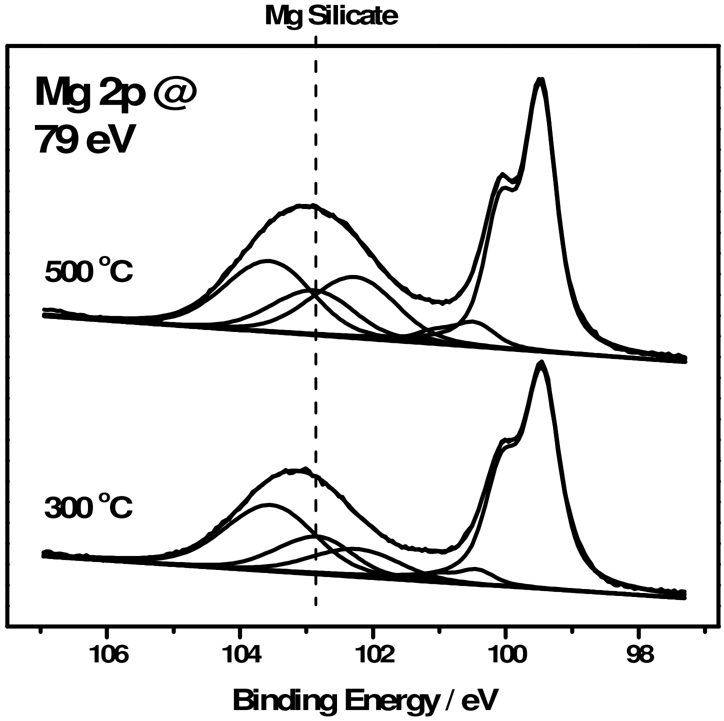

Figure 5.14 The growth of an additional peak due to thermal annealing, separated from the Si bulk peak by 3.25 eV, is attributed to the presence of Mg silicate.

The binding energy separation of 3.25 eV for Mg silicate is less than that observed in Chapter 4 figure 4.23, after deposition of stoichiometric MgO (3.4 eV). The larger binding energy separation in the previous study suggests the formation of a more oxygen rich silicate phase, which is attributed to the increased levels of O present during MgO deposition. Although there is still a considerable contribution from the Si $^{4+}$ oxidation state after 500 °C annealing, which is in contrast to results seen on Si native oxide surfaces, there is evidence to suggest that Mg silicate can be formed on ultra thin Si oxides.

5.4.3 Thermal Stability of Mg silicide on H-terminated Si surfaces

The role which interfacial SiO_2 plays in the thermal stability and growth mode of Mg silicide was further studied using oxide free silicon surfaces, which were analysed using conventional XPS. Hydrogen terminated silicon surfaces were prepared by dipping n-type Si (111) wafers in a solution of 5% hydrofluoric acid (HF) for 1 minute. Samples were dried using nitrogen gas and immediately loaded into the UHV analysis system, where they were de-gassed by annealing to 300 °C for 30 minutes. The effect of ~ 2 nm Mg deposition on a hydrofluoric acid (HF) etched oxide free Si (111) surface is shown by the Si 2p core level XPS spectra in figure 5.15.

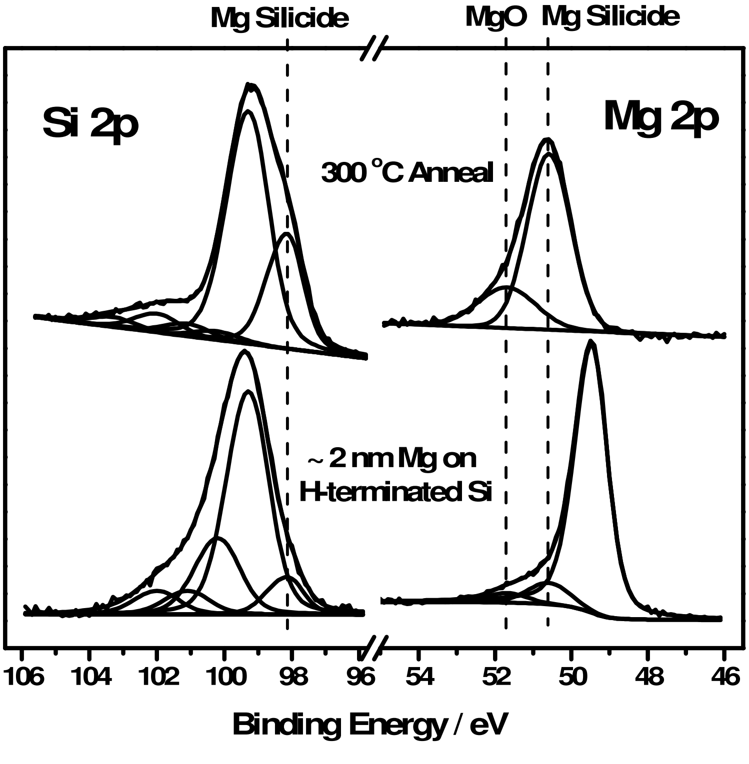

Figure 5.15 Curve fitted Si 2p and Mg 2p spectra taken using conventional XPS, showing that the growth of Mg silicide on H-terminated silicon surfaces upon deposition of ~ 2 nm Mg. Subsequent annealing to 300 °C promotes silicide growth, in contrast to the result seen on oxidised Si surfaces.

In agreement with Mg deposition on native oxide surfaces (figure 5.2) the growth of both Si sub-oxide and Mg silicide peaks is observed. The formation of Si oxide peaks on the HF last surface can be explained by the presence of residual oxygen on the surface which was either not removed by the HF etch or re-oxidised before insertion into the vacuum system. The formation of Mg silicide on both the HF last and the native oxide covered SiO_2 surfaces suggests that Mg atoms can react with both hydrogen terminated silicon and oxidised Si in order to form Mg silicide. It should also be noted that after comparable amounts of Mg deposition (~ 2 nm) there is less evidence of silicide growth on the HF last surface than that on the native oxide surfaces. This is in agreement with the work of Saiki *et al.* [49] who reported that the interaction between Mg and H-terminated Si is considerably weaker than that of Mg and the atomically clean Si surface.

The Si 2p spectrum shown in figure 5.15 taken after 300 °C thermal annealing indicates that there is considerable growth of Mg silicide on the HF treated surface, in contrast to the result seen for native oxide surfaces (figure 5.2). This is further evidenced by the corresponding Mg 2p spectra in figure 5.15, which show considerable growth of the Mg silicide component along with the removal of metallic Mg, again suggesting that Mg silicide growth was promoted by UHV annealing at 300 °C. Growth of the oxidised Mg component can also be seen from the Mg 2p peak in figure 5.15. It is suggested that this is due to the transfer of oxygen from the Si substrate to the Mg overlayer, as evidenced by a reduction in the Si sub-oxide peaks. It should also be noted that the total area of the Mg peak was reduced by a factor of 1.3 during annealing, which is considerably less than that seen for native oxide surfaces (figure 5.3) as a higher proportion of the deposited Mg layer was converted into Mg silicide and as such did not desorb from the surface.

These results suggest that the presence of oxidised Si on the native oxide covered surface between the silicide and the silicon substrate creates a barrier to Si diffusion, therefore preventing the growth of further silicide. This means that the amount of magnesium silicide which forms during the deposition process on a native oxide surface cannot be increased by thermal annealing, even if residual metallic magnesium is present. This contrasts with the behavior observed in the absence of a native oxide where the silicide can be grown at 300 °C. Therefore, the only way to control the extent of silicide formation on oxidised silicon surfaces is the deposition method used, either step-by-step or continuous deposition as outlined earlier. The formation of yttrium silicide by vacuum annealing has previously been characterised by J. E. E. Baglin *et al.* [29], who suggest that silicide growth is due to the diffusion of Si into the metal film. Given the low desorption temperature of metallic Mg on Si surfaces, in order to achieve the enhanced silicide growth observed for the HF treated surface, the diffusion of Si into the metallic Mg layer must occur below this temperature.

While it has been shown that the growth of Mg silicide can be promoted on H-terminated silicon surfaces using UHV annealing, the result has been extremely difficult to reproduce in a reliable fashion. Based on the spectra in figure 5.15 it would be reasonable to suggest that Mg silicide, once formed, is thermally stable up to 300 °C. However, in subsequent experiments, 300 °C annealing of ~ 2 nm Mg on H-terminated Si has resulted in the complete desorption of all Mg based species from the surface, including the Mg silicide species formed during Mg deposition. Similarly inconsistent results have been seen by Vantomme *et al.* [22], who have reported drastically differing levels of thermal stability for Mg silicide films, independent of film thickness and growth temperature. This inconsistency may be related to the extent to which residual oxide species remain on the surface following HF etching, as the SRXPS studies have shown that the presence of a monolayer of Si oxide is sufficient to inhibit Mg silicide growth as a function of annealing. Therefore, it is suggested that the growth of Mg silicide is inhibited by the presence of surface oxides, the low thermal stability of metallic Mg and the inconsistent desorption temperature of the formed silicide.

Although further investigation is required to determine the factors which effect thermally assisted growth of Mg silicide, this was considered to be beyond the scope of this study. As such it is concluded that while it is possible to promote Mg silicide growth on H-terminated Si using UHV annealing, a reproducible procedure for this has not be obtained. Samples were subsequently annealed to 500 °C, resulting in the complete removal of Mg silicide from the HF treated surface. The desorption temperature of Mg silicide has previously been reported to be 450 °C [50], and while it is greater than that of the metallic Mg the results of this study also suggest that Mg silicide is thermally unstable at temperatures above 500 °C.

5.4.4 Chemical Stability of Mg silicide

The chemical stability of Mg silicide grown on a native oxide Si surface has been investigated using controlled exposure to molecular oxygen (O_2) at room and elevated temperature, as shown by the evolution of the Si 2p and Mg 2p spectra in figure 5.16.

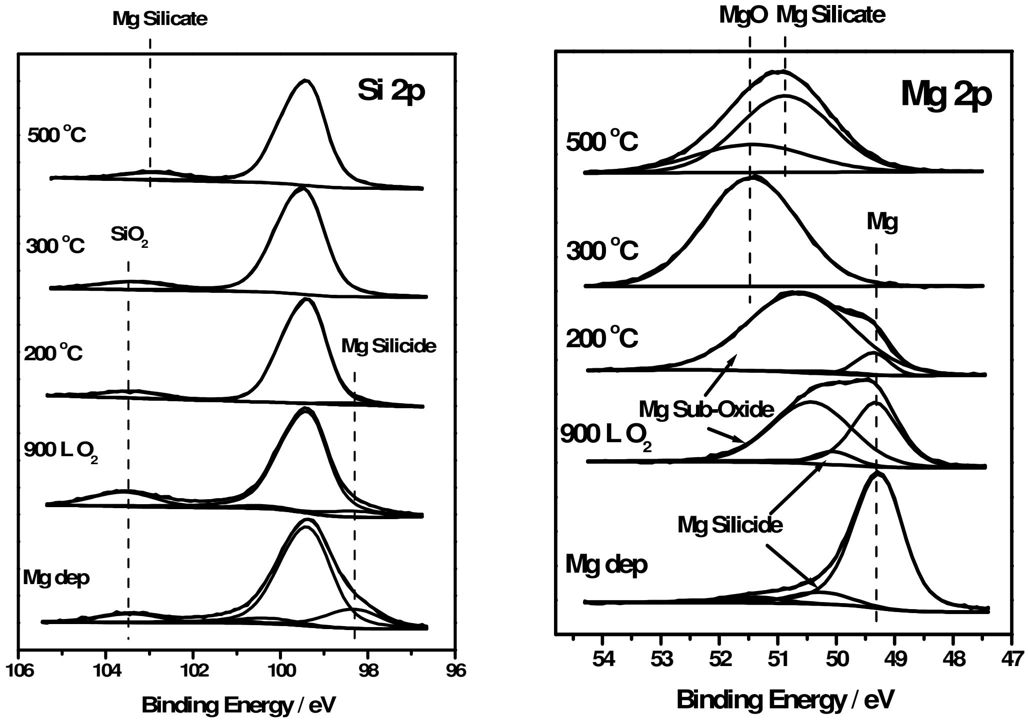

Figure 5.16 The chemical stability of Mg silicide is investigated using controlled exposure to O_2. Si 2p and Mg 2p spectra show that room temperature exposure reduces the presence of Mg silicide and partially oxidises excess metallic Mg. Annealing to 300 °C in an O_2 partial pressure of 5×10^{-7} mbar removes all evidence of Mg and Mg silicide, producing stoichiometric MgO, while further annealing to 500 °C partially converts this MgO to Mg silicate.

The Si 2p and Mg 2p spectra show that exposure to 900 L of O_2 at room temperature causes a considerable reduction in the presence of Mg silicide, in agreement with the work of Brause *et al.* [14]. The room temperature oxidation of Mg silicide shown here is in direct contrast to other silicide species such as Hf silicide [51,52] and Y silicide [3]. As such it can be stated that both the chemical and thermal stability of Mg silicide is significantly lower than that of other silicide species. The Mg 2p spectrum taken after 900 L oxygen exposure shows evidence for the formation of magnesium sub-oxide, creating a mixed phase metal/metal oxide film. Further O_2 exposure at room temperature, totaling 1500 L, resulted in no further changes to the Mg 2p or Si 2p spectra suggesting the increased stability of the mixed phase film. It should be noted that Mg 2p spectra taken using angular resolved XPS, showed no change in the relative intensity of the component peaks compared to those taken at normal emission. This suggests that there is no spatial segregation between the metallic and oxidised components of the Mg 2p. Therefore, it can be stated that the stability shown by the metal/metal oxide mixed phase is not due to oxidised Mg at the surface of the film creating a barrier to further oxidation. Given the homogenous distribution of metallic Mg within the film, it may be concluded that the "oxide" peak formed is due to partially oxidised Mg and not stoichiometric MgO.

The sample was subsequently annealed to 200 °C and 300 °C in an O_2 partial pressure of 5×10^{-7} mbar. Further reduction of Mg silicide along with further oxidation of the Mg film is shown by both the Si 2p and Mg 2p spectra. The stability of the mixed phase film is again shown by the Mg 2p spectra, which show no evidence for the desorption of Mg at 200 °C, in contrast to results seen for metallic Mg films on Si (figure 5.3). Subsequent annealing to 300 °C resulted in the complete oxidation of both metallic Mg and Mg silicide species, along with a shift in the oxidised Mg peak to a binding energy position of 51.50 eV which is indicative of fully oxidised MgO. The results suggest that the binding energy separation between metallic Mg and a fully oxidised MgO thin film is equal to 2.15 eV, in good agreement with previous Mg oxidation studies [20,21].

Further annealing to 500 °C resulted in the formation of Mg silicate, as shown by both the Si 2p and Mg 2p spectra. After silicate formation the Mg 2p peak in figure 5.16 shows a larger binding energy shift (0.61 eV) than that seen in figure 5.3 (0.2 eV). This is due to fact that fully oxidised MgO is present at a higher binding energy position than that of the partially oxidised Mg species seen in figure 5.3. The conversion of fully oxidised MgO into Mg silicate at 500 °C in this study is in contrast to the result seen in after MgO deposition in figure 5.6, and is once again attributed to the effect of silicide formation prior to annealing.

Along with evidence for Mg silicate formation it should be noted that the Mg 2p spectrum shows the presence of residual MgO after 500 °C annealing. This is in contrast to the results of figure 5.2, which showed no evidence for residual MgO after 500 °C annealing. This result is attributed to the introduction of additional O to the UHV chamber, which allowed thermally stable MgO to form on the surface during annealing. Therefore, given that the Mg present on the surface was present in the form of MgO it did not desorb, leading to more Mg remaining on the surface after 500 °C annealing. Also, given that the additional Mg present on the surface did not lead to any additional growth of Mg silicate compared to that seen in figure 5.2, it can again be suggested that Mg silicide growth is a necessary intermediate step for silicate formation.

These results show that the thermal and chemical stability of Mg based species on Si is strongly dependant on the chemical composition of the film. The factors which determine film stability, such as temperature and the availability of suitable chemical reactants, are summarised in table 5.1.

	Temperature	**Dependence on Chemical Species Present**
Metallic Mg	< 200 °C	Fully metallic Mg will only exists on Si surfaces at low temperature and in the absence of available O or Si. Mg will desorb from the surface at temperatures above ~ 200 °C, if annealed in the absence of available O or Si.
Mg Silicide	≤ 300 °C	Metallic Mg reacts with both oxidised and H-terminated Si to form Mg silicide. Step-wise deposition of Mg promotes silicide growth. Desorption of metallic Mg at low temperature makes additional growth difficult to achieve. Once formed, Mg silicide desorbs at temperatures above 300 °C.
Mg/Mg oxide Mixed Phase	< 300 °C	Forms at low levels of O_2 exposure and will not fully oxidise at room temperature. Annealing in the presence of O results in complete oxidation of Mg and prevents the desorption of Mg atoms.
Mg sub-oxide	≥ 200 °C ≤ 500 °C	Forms in the absence of either sufficient oxygen or sufficient temperature to form fully stoichiometric MgO i.e. formed from the O which is present on Si native oxide surfaces.
MgO	≤ 800 °C	MgO forms readily at all temperatures in the presence of sufficient O. Can exist at temperatures greater than 500 °C on Si surface which have not been altered by Mg silicide growth
Mg-Silicate	≥ 500 °C	Forms at temperatures above 500 °C in the presence of Mg, Si and O based species. Forms almost independently of the composition of these species however it will only form subsequent to the surface disruption caused by Mg silicide growth.

Table 5.1 Summary of the thermal and chemical stability of Mg based chemical species on Si.

5.4.5 Conclusions

The growth mode and stability of Mg silicide, formed by deposition of Mg on Si surfaces, has been investigated. The results suggest that step-wise deposition of Mg on an ultra-thin silicon oxide, with at least 1 hour between depositions, results in the formation of Mg silicide islands and the formation of excess metallic Mg on the surface of these islands. Continuous deposition of Mg results in considerably reduced silicide formation, consistent with the growth of a uniform silicide layer forming a barrier which prevents the subsequent growth of Mg silicide. The thermal stability of Mg silicide films grown on oxidised silicon and HF last silicon surfaces was also investigated. While annealing the surfaces to 300 °C resulted in the removal of silicide species from the oxidised surface, the silicide species on the HF last surface grew appreciably. This difference in silicide growth behavior is attributed to the presence of oxidised Si preventing the diffusion of Si atoms into the metallic Mg film, hence limiting the growth of further silicide species. It has also been shown that annealing the surfaces to 500 °C causes the complete removal of Mg silicide, while metallic Mg desorbs from the surface at temperatures above 300 °C. The oxidation of both Mg and Mg silicide has been studied using controlled exposure to 900 L O_2 at room temperature. This exposure resulted in a considerable reduction in the presence of Mg silicide along with the creation of a mixed phase of both metallic and partially oxidised Mg. Spectra taken after annealing to 400 °C, in an O_2 partial pressure of 5×10^{-7} mbar, show no evidence for the desorption of Mg and suggest the formation of fully oxidised MgO. Due to the increased levels of Mg present on the surface, annealing to 500 °C results in the formation of a mixed phase MgO/Mg silicate film.

Section 5.5 Investigations into the growth parameters of magnesium silicate films on silicon surfaces

In this study it has been conclusively shown that Mg silicide formation is a vital intermediate step in the growth mechanism of Mg silicate on Si native oxide surfaces. Results also indicate that UHV annealing can not be used to promote silicide growth on oxidised Si surfaces. As such, this places an upper limit on the thickness of the silicate films which can be formed on Si native oxide surfaces. Therefore, in order to form Mg silicate films of greater thickness differently prepared silicon surfaces were investigated. Given that the presence of oxidised Si has been shown to inhibit the diffusion of Si atoms towards the excess metallic Mg, Mg silicate growth was attempted on oxide free H-terminated Si (111) surfaces. The formation of Mg silicate on silicon oxide films of greater thickness was also studied, along with Mg silicate growth on ~ 2 nm thick SiON layers.

5.5.1 Growth of Mg silicate on Hydrogen Terminated Si (111) surfaces

The effect of Mg deposition on the Si 2p spectrum of H-terminated Si (111) surfaces is shown in figure 5.17.

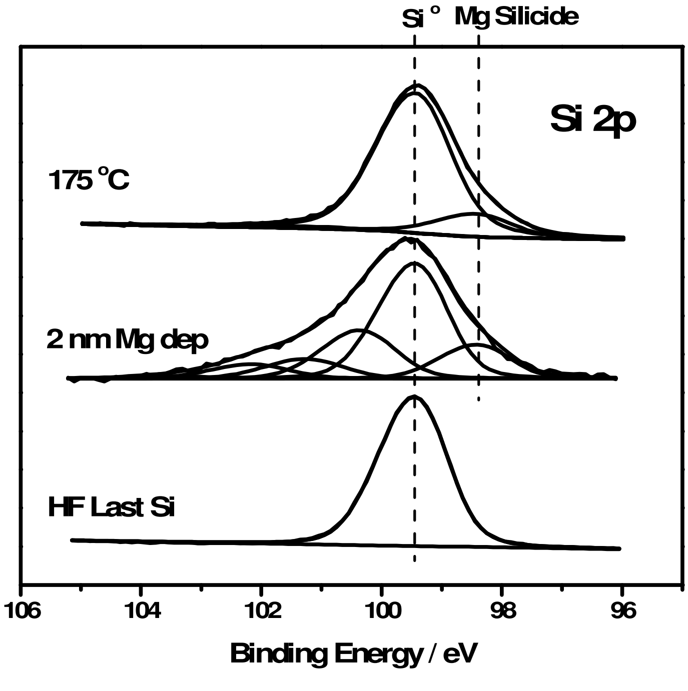

Figure 5.17 Si 2p spectra showing the effect of Mg deposition and 175 °C annealing on H-terminated Si (111) surfaces.

The spectra show that while the H-terminated surface shows no evidence of silicon oxide, Mg deposition resulted in considerable growth of sub-stoichiometric Si oxide peaks, in agreement with figure 5.15. This has again been attributed to the presence of residual surface oxygen, not removed during the HF etch. The sample was subsequently annealed to 175 °C, in order to determine if the thickness of the Mg silicide layer could be increased at elevated temperature. The Si 2p spectrum taken after 175 °C annealing, shows evidence for the complete removal of sub-stoichiometric silicon oxide species, however a 25 % reduction in the area of the Mg silicide peak is also observed. While it has been shown in figure 5.15 that is possible to promote Mg silicide growth using UHV annealing, it must again be noted that a reproducible procedure for this growth was not obtained. As such, the formation of Mg silicate on hydrogen terminated surfaces must be achieved using the Mg silicide formed during Mg deposition.

Although there is sufficient oxygen present within the SiO_2 native oxide surface to allow silicate formation the amount of surface oxygen present on H-terminated surfaces is greatly reduced, meaning that additional oxygen must be added to the UHV chamber in order to achieve silicate formation. The sample shown in figure 5.17 was subsequently annealed to 175 °C in an O_2 partial pressure of 5×10^{-7} mbar and the results of this anneal are shown in figure 5.18.

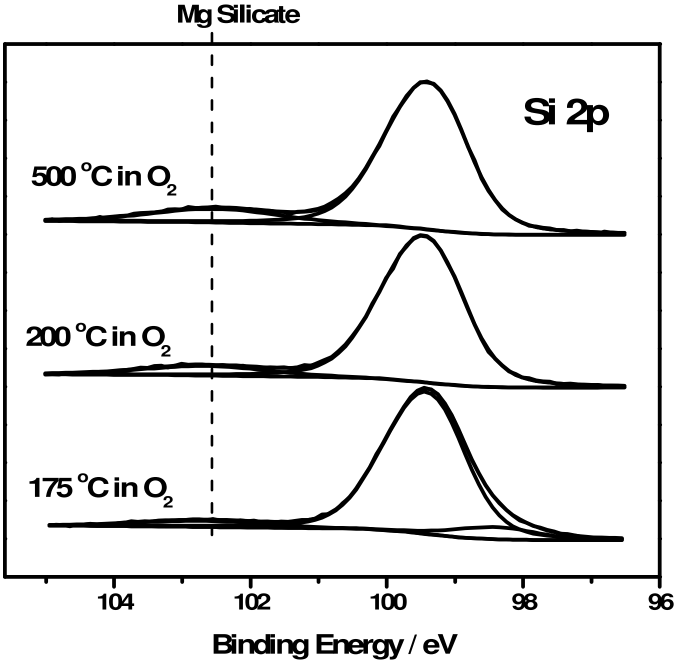

Figure 5.18 Curve fitted Si 2p spectra showing the growth of Mg silicate due to high temperature annealing of Mg on H-terminated surface in an O_2 partial pressure of 5×10^{-7} mbar.

The Si 2p spectrum taken after annealing to 175 °C in an O_2 background pressure shows a reduction in the presence of Mg silicide along with the initial formation of Mg silicate. Si 2p spectra taken after subsequent anneals to 200 ° and 500 °C are also shown in figure 5.18. It can be seen that annealing to 200 °C results in the complete removal of Mg silicide, in agreement with previous annealing studies shown in figure 5.16. Mg 2p spectra in figure 5.19 again show that annealing to 200 °C in the presence of excess oxygen results in the formation of stoichiometric MgO, and inhibits the desorption of Mg compared to that seen in figure 5.3.

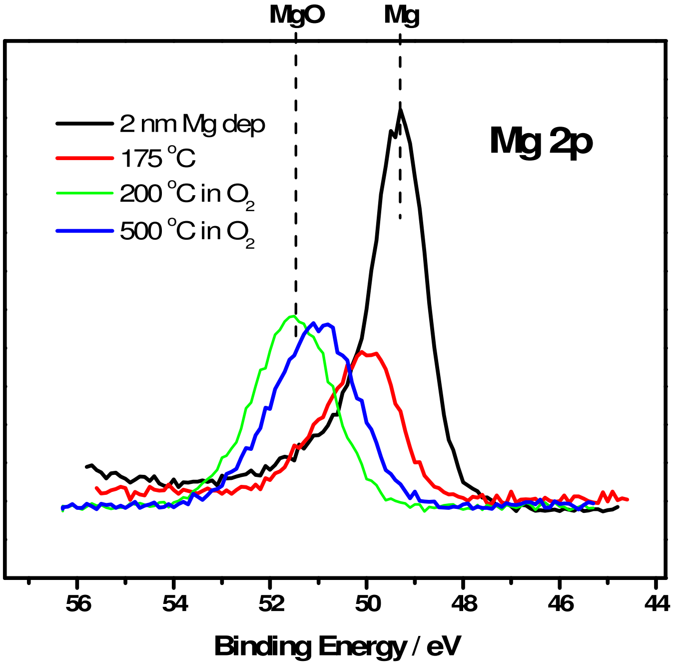

Figure 5.19 Mg 2p core level spectra show that annealing to 200 °C in 5 × 10^{-7} mbar of O_2 causes the growth of stoichiometric MgO and inhibits Mg desorption. Subsequent annealing to 500 °C causes Mg silicate growth as shown by a shift to LBE.

Subsequent annealing to 500 °C results in increased formation of Mg silicate, as evidenced by growth in the Mg silicate component peak in figure 5.18, and an associated shift to lower binding energy in the Mg 2p profile (figure 5.19).

While Mg silicate formation on H-terminated surfaces has been achieved, the thickness of this silicate is no larger than that formed on Si native oxide surfaces. This is at odds with the observation that there is more Mg present on the surface. As such, further analysis is required to determine the chemical composition of the Mg species present after 500 °C annealing. Curve fitted O 1s and Mg 2p spectra, taken after 500 °C annealing, show the presence two distinct peaks which have been attributed to the presence of Mg silicate and residual MgO (figure 5.20).

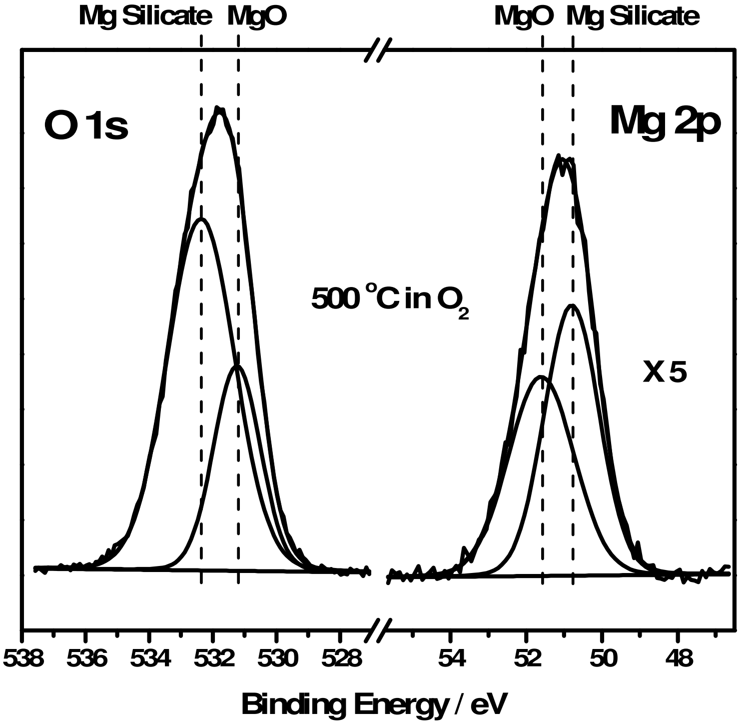

Figure 5.20 Curve fitted O 1s and Mg 2p spectra show the presence of both MgO and Mg silicate on the H-terminated surface after 500 °C.

The presence of a mixed phase MgO/Mg silicate film is in contrast to the formation of silicate films on native oxide surfaces and this discrepancy can be linked to the initial formation of Mg silicide in agreement with figure 5.16. While the presence of oxygen allowed additional Mg to remain on the surface in the form of MgO, this MgO was not converted into Mg silicate as no additional silicide formation occurred to facilitate this growth.

Therefore, it is suggested that the formation of Mg silicate on H-terminated Si surfaces at 500 °C results in the creation of a mixed phase metal oxide/metal silicate film. The formation of such mixed phase film may be prevented by ensuring that all Mg present on the surface is in the form of Mg silicide prior to the introduction of additional oxygen. However, given the thermal stability of both metallic Mg and Mg silicide it may be difficult to achieve this without causing the complete desorption of all surface magnesium. While results suggest it is difficult to achieve Mg silicide films with a thickness greater than ~ 2 nm using deposition of Mg onto Si surfaces, it has been reported that Mg silicide has been successfully formed using the simultaneous deposition of Mg and Si at elevated temperature [22,53]. Oxidation of these silicide surfaces may allow Mg silicate films with controlled thickness to be fabricated. It has also been reported that other metal silicate species may be formed by depositing metal oxide films onto silicon substrates and subsequently annealing to temperatures in excess of 750 °C [54,55]. However, the work of Wilk *et al.* [2] has suggested that high temperature silicate formation, which occurs due to silicon diffusion into metal oxide overlayers, results in uncontrolled and poor quality silicate films. Therefore, higher quality interfacial properties may be achieved using the low temperature growth mechanism described for oxidised silicon surfaces in section 5.3.

5.5.2 Mg silicate growth on silicon oxide films of greater thickness

While it has been shown that Mg silicate films can be formed on both Si native oxide and H-terminated Si surface, controlling the thickness of these films has proved difficult. These studies also suggest that the oxygen present on SiO_2 surfaces allows the composition of the final silicate layer to be more easily controlled, by placing a limit on the amount of Mg which remains on the surface at elevated temperature. In order to determine if Mg silicate layers of greater thickness can be formed on oxidised Si surfaces, metallic Mg was deposited onto a SiO_2 film of essentially infinite thickness (700 nm).

Si 2p spectra in figure 5.1 have already shown that the deposition of metallic Mg onto 700 nm SiO_2 surfaces results in the initial formation of Mg silicide. The effects of continued Mg deposition can be seen from the Si 2p and O 1s spectra in figure 5.21, which show the growth of Mg silicide along with evidence for the presence of sub-stoichiometric silicon oxides similar to those seen in figure 5.1. The integrated area of the Mg silicide peak seen in figure 5.21, is significantly larger than that seen on Si native oxide surfaces in figure 5.1. While the formation of Mg silicide on native oxide surfaces appeared to be self limiting, the increased growth seen in figure 5.21 suggests that room temperature formation of Mg silicide occurs more easily in oxidised silicon layers than in the crystalline Si bulk.

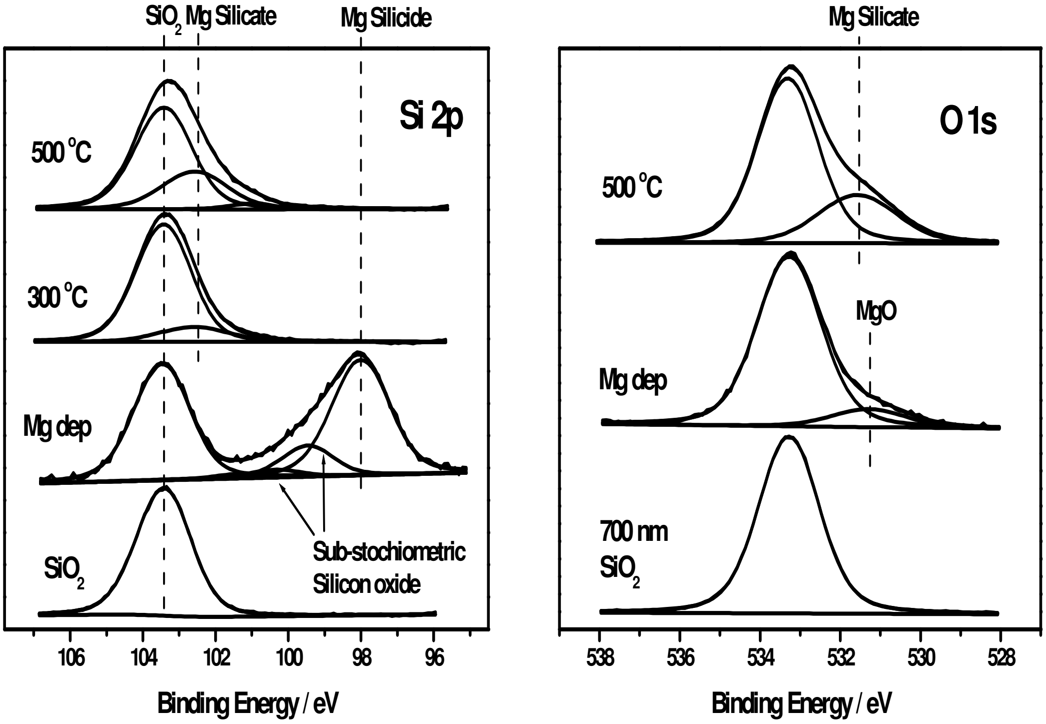

Figure 5.21 Curve fitted Si 2p and O 1s spectra showing the growth of Mg silicate on a 700 nm SiO_2 surface. The integrated area of the Si 2p Mg silicate component suggests that the thickness of the silicate layer is greater than that formed on the Si native oxide surface.

O 1s spectra show evidence for the growth of a peak at lower binding energy with respect to the SiO_2 peak, not previously seen upon deposition of Mg onto native SiO_2 surfaces before annealing.

The separation between this peak and that of the underlying SiO_2 is indicative of fully oxidised MgO, which may have formed in larger quantities on this surface due to the increased availability of O present within the 700 nm SiO_2 layer. In agreement with native oxide studies, subsequent annealing to 300 °C results in the removal of Mg silicide and Si sub-oxide peaks. However, the initial formation of an Mg silicate peak at 300 °C, separated from the SiO_2 peak by 0.75 eV, has not previously been seen at this temperature. Subsequent annealing to 500 °C results in considerable growth of Mg silicate on the surface, as seen in both the Si 2p and O 1s spectra. Given that it is difficult to conclusively determine the chemical composition of the $Mg_xSi_yO_z$ species present on the surface, XPS thickness calculations may not be accurate in determining the thickness of the Mg silicate overlayer. It can however be stated that Mg silicate can be formed on a thick SiO_2 layer and the integrated area of the Si 2p peak attributed to this silicate is approximately 3 times larger than that formed on native SiO_2 surfaces.

5.5.3 Mg silicate growth on SiON surfaces

Along with Si oxide and H-terminated surfaces, the formation of metal silicate films on nitrided Si oxide is also of technological interest. The formation of yttrium silicate on SiON and nitrided Si (100) surfaces has previously been studied by Chambers *et al.* [56]. It has been suggested that Y silicate can be formed within SiON layers, but the presence of Si-N bonds acts as a barrier to silicate formation with the Si bulk [56]. The SiON layers used in this study were grown at IMEC in Belgium, on p-type Si (100) wafers using a 3-step decoupled plasma nitridation process [57]. A base SiO_2 layer was initially grown using rapid thermal oxidation, resulting in SiO_2 thicknesses of 0.8–1.2 nm. Nitridation of the SiO_2 film was then achieved by exposure to a pulsed-RF N_2-plasma.

SiON samples were cleaned using a standard chemical degreasing procedure and loaded into the UHV analysis chamber. The effect of Mg deposition onto SiON surfaces can be seen from the Si 2p spectra in figure 5.22, which show the growth of Mg silicide in agreement with previous results.

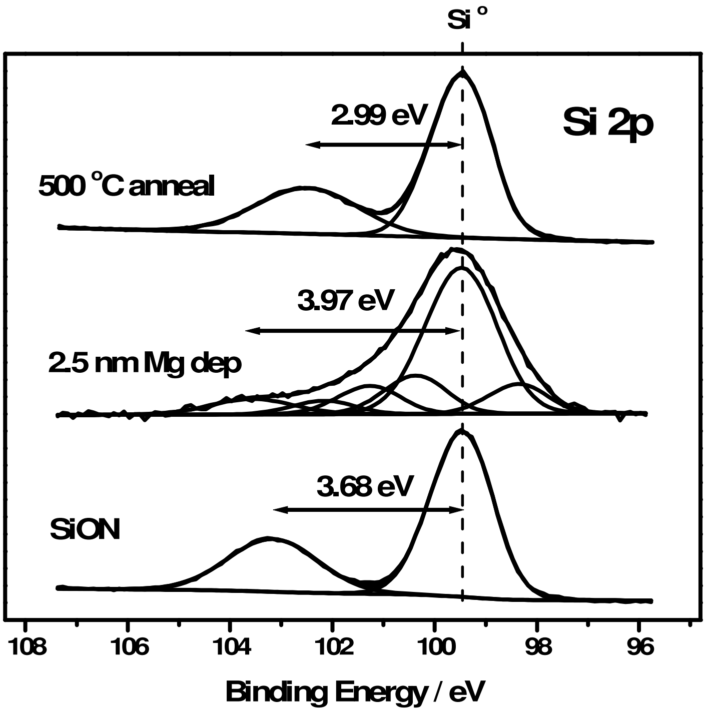

Figure 5.22 Curve fitted Si 2p spectra showing the growth of Mg silicate on a ~ 2 nm SiON layer. The binding energy position of the silicate component following 500 °C annealing may indicate that N atoms remain integrated within the film.

The spectra suggest that the integration of nitrogen atoms within the silicon oxide structure does not prevent, or inhibit, Mg silicide growth. An increase in the binding energy separation between the Si substrate and SiON peaks from 3.68 eV to 3.97 eV is also observed, indicating disruption in the SiON lattice. Subsequent annealing to 500 °C resulted in the formation of a single peak separated from the Si bulk peak by 2.99 eV, indicative of silicate formation throughout the entire film. It should also be noted that the integrated area of the N 1s peak (not shown) remained unchanged during silicate formation, indicating that nitrogen atoms within the SiON layer remained in the film during silicate formation. Possible evidence for the incorporation of N atoms within the silicate film may also be seen from the binding energy separation between the Si° and Mg silicate peaks, which is 0.26 eV less than that seen on native oxide, H-terminated and 700 nm SiO_2 surfaces.

5.5.4 Conclusions

Different possible experimental procedures aimed at forming Mg silicate films on H-terminated Si surfaces, of greater thickness than that formed on Si native oxide surfaces, have been explored. It has been shown that while Mg silicide growth can be promoted at elevated temperature, the result is difficult to recreate, with parameters such as the presence of residual surface oxides and temperature ramp rate requiring further study. The addition of oxygen, necessary for silicate formation, results in the oxidation of excess Mg to form MgO. This creates a thicker film of oxidised Mg, which is not fully converted into Mg silicate at 500 °C, forming a mixed phase MgO/Mg silicate layer in contrast to silicate films formed on native oxide surfaces. The creation of thicker Mg silicate films has been achieved using SiO_2 layers of effectively infinite thickness (700 nm). It has been shown that the deposition of Mg results in the formation of considerably more Mg silicide than that seen on native oxide surfaces, suggesting that the incorporation of Mg atoms occurs more readily in silicon oxide than in crystalline bulk silicon. Si 2p core level spectra show that subsequent annealing to 500 °C resulted in the formation of silicate films which are thicker than that formed on native oxide surfaces. Also, given that no additional oxygen was introduced during the experimental procedure there is no evidence for the presence of residual MgO after 500 °C annealing. Further studies have outlined the formation of Mg silicate films on SiON surfaces, with XPS spectra suggesting the incorporation of nitrogen within the silicate film.

5.6 Chapter Conclusions

In this study magnesium silicate films have been successfully formed on a variety of differently prepared silicon surfaces. The mechanism by which silicon native oxide surfaces are converted into Mg silicate has been investigated using XPS. Si 2p core level spectra show that room temperature deposition of metallic Mg results in the growth of Mg silicide on the silicon oxide surface. Subsequent UHV annealing to 300 °C removes all evidence of silicide and causes desorption of excess metallic Mg from the surface, leaving a chemically reactive Mg sub-oxide phase on the surface. The growth and removal of Mg silicide leads to disruption of the native oxide, which greatly increases the chemical reactivity of the surface. Further annealing to 500 °C causes the full conversion of SiO_2 to Mg silicate, as evidenced by changes in the Si 2p, Mg 2p and O 1s peak profiles. Further studies have shown that the initial growth of Mg silicide is a vital intermediate step in silicate formation, and it is suggested that the thermal instability of Mg silicide may allow Mg silicate to be formed at lower temperature than other metal silicate species. This instability also allows silicate growth to be achieved *in-situ* and without the addition of further oxygen to the system, allowing the silicate growth mechanism to be studied in greater detail than previously achieved within the literature. Once formed, the Mg silicate films were shown to be thermally stable up to 750 °C, using a series of UHV anneals.

Given the importance of Mg silicide in the proposed silicate growth mechanism, high resolution SRXPS was used to investigate the growth and stability of Mg silicide on oxidised Si surfaces. It has been shown that step-wise deposition on Mg results in higher levels of Mg silicide growth than that seen after continuous deposition, in agreement with similar studies within the literature. It is suggested that continuous deposition results in the formation of metallic Mg islands which act as a barrier to silicide growth by preventing Mg atoms from reaching the surface. Further studies have shown that the thermal and chemical stability of Mg silicide is considerably lower than other metal silicide species such as Y silicide and Hf silicide. High temperature UHV annealing studies indicate the complete desorption of Mg silicate from oxidised Si surfaces at temperatures greater than 300 °C, while the instability of Mg silicide films after room temperature exposure to O_2 (900 L) has also been shown.

In contrast to results seen for oxidised Si surfaces, it has been shown that the growth of Mg silicide can be promoted using UHV annealing of metallic Mg on H-terminated Si. This difference has been attributed to Si oxide acting as a barrier to the inter-diffusion of Si and Mg atoms during annealing, which results in excess metallic Mg desorbing from the surface prior to silicide growth. It should be noted that while results show it is possible to promote silicide growth using UHV annealing, a great deal of further study is required in order to obtain a reproducible experimental procedure for this.

In addition to the modification of Si native oxide surfaces, a series of experiments were carried out in an attempt to form Mg silicate on differently prepared Si surfaces. It has been shown that Mg silicate films of increased thickness can be formed on both 700 nm SiO_2 and SiON surfaces, using the procedure outlined for native oxide surfaces. However, exposure to an O_2 partial pressure of 5×10^{-7} mbar is required to achieve silicate growth on H-terminated Si surfaces. It has been shown that this exposure results in the formation of stoichiometric MgO which is not fully converted to Mg silicate upon annealing to 500 °C, resulting in a mixed phase MgO/Mg silicate layer.

5.7 References

[1] John Robertson, Reports of Progress in Physics **69** (2006) 327–396

[2] G.D. Wilk, R.M. Wallace, Appl. Phys. Lett. **74,** 19 (1999) 2854

[3] J. J. Chambers and G.N. Parsons, J. Appl. Phys. **90** (2001) 918-933

[4] T. Gougousi, M.J. Kelly, D.B. Terry, G.N. Parsons J. Appl. Phys. **93** (2003) 1691-1696

[5] S.-Y. Chang, M.-I. Jeong, S.V.J. Chandra, Y.-B. Lee, H.-B. Hong, V.R. Reddy, C.-J. Choi, Mater. Sci. Semicond. Process. **11** (2008) 122

[6] T. Komabayashi, K. Hirose, E. Sugimura, N. Sata, Y. Ohishi, L.S. Dubrovinsky, Earth and Planetary Science Letters **265** (2008) 515–524

[7] A. Posadas, F. J. Walker, C. H. Ahn, T. L. Goodrich, Z. Cai and K. S. Ziemer, Appl. Phys. Lett. **92** (2008) 233511

[8] P. Casey, E. O'Connor, R. Long, B. Brennan, S.A. Krasnikov, D. O'Connell, P.K. Hurley, G. Hughes, Microelectron. Eng. **86** (2009) 1711–1714

[9] L. Yan, C. M. Lopez, R. P. Shrestha, E. A. Irene, A. A. Suvorova and M. Saunders, Appl. Phys. Lett. **88** (2006) 142901.

[10] J.H. Boo, S.B. Lee, K.S. Yu, W. Koh, Y. Kim, Thin Solid Films **341**, (1999) 63

[11] J.-M Cho, K.-H. Lee, C. Il Cheon, N. I. Choc, J. S. Kim, J. Eur. Ceram. Soc. **30,** 481 (2010)

[12] K.H. Kim, M.S. Lee, J.S. Choi, J.P. Ahn, Thin Solid Films **517** (2009) 3995

[13] R. O'Connor, G. Hughes, P. Casey, S.B. Newcomb, J. Appl. Phys. **107,** 024501 (2010)

[14] M. Brause, B. Braun, D. Ochs, W. Maw-Friedrichs, V. Kempter, Surface Science **398** (1998) 184-194

[15] M. C. Zeman, C. C. Fulton, G. Lucovsky, R. J. Nemanich, W.-C. Yang, J. Appl. Phys **99** (2006) 023519

[16] J.J.Chambers and G.N.Parsons, Appl. Phys. Lett. **77** 2385 (2000)

[17] J-H. Lee, M. Ichikawa, J. Appl. Phys. **92**, 4 (2002) 1929

[18] K.N. Galkin, M. Kumar, Govind, S.M. Shivaprasad, V.V. Korobtsov, N.G. Galkin, Thin Solid Films **515,** (2007) 8192

[19] M.R.J. van Buuren, F.Voermans and H.van Kempen, J.Phys.Chem **99** (1995) 9519

[20] C. Chen, S.J. Splinter, T. Do, N.S. Mclntyre, Surface Science **382** (1997) L652-L657

[21] M. Kurth, P.C.J. Graat, E.J. Mittemeijer, Appl. Surf. Sci. **220** (2003) 60–78.

[22] A. Vantomme, G. Langouche, J.E. Mahan, J.P. Becker, Microelectronic Engineering **50** (2000) 237–242

[23] C. D. Wagner, L. E. Davis, M. V. Zeller, J. A. Taylor, R. M. Raymond and L. H. Gale, Surf. Interface Anal. **3**. (1981) 211

[24] J. Sugihara, K. Kakimoto, I. Kagomiya, H. Ohsato, J. Eur. Ceram. Soc. **27** (2007) 3105–3108

[25] K. Hirose, H. Nohira, T. Koike, K. Sakano, T. Hattori, Phys. Rev. B **59**, 8 (1999) 5617

[26] S. Y Chiam, W. K. Chim, A. C. H. Huan, J. Zhang, J. S. Pan, JVST A, **25**, 3 (2007) 500-507

[27] X P.Punchaipetch, G.Pant, M.Quevedo-Lopez, H.Zhang, M. El-Bouanani, M.J.Kim, R.M.Wallace, B.E.Gnade, Thin Solid Films **425** (2003) 68

[28] H. Ono and T. Katsumata, Appl. Phys. Lett. **78** (2001) 1832

[29] J. E. E. Baglin, F. M. d'Heurle, and C. S. Petersson J. Appl. Phys. **52** (1981) 2841

[30] A. M. Sonnet, C. L. Hinkle, M. N. Jivani, R. A. Chapman, G. P. Pollack, R. M. Wallace, E. M. Vogel Appl. Phys. Letts. **93** (2008) 122109

[31] Y.-L. Jiang, Q. Xie, C. Detavernier, R. L. V. Meirhaeghe, G.-P. Ru, X.-P. Qu, B.-Z. Li, and P. K. Chu, J. Appl. Phys. **102**, (2007) 033508

[32] M. Ghaffour, M. Bouslama, Z. Lounis, A. Nouri, C. Jardin, Y. Monteil, H. Dumont, J. Electron Spectrosc. Relat. Phenom. **134**, (2004) 81

[33] J. Morais, E. B. O. da Rosa, L. Miotti, R. P. Pezzi, I. J. R. Baumvol, Appl. Phys. Lett. **78**, 17 (2001) 2446

[34] D. Lee, G. Lee, S. Kim, C. Hwang, J.-Y. Koo, H. Lee. Journ. of Phys: Condensed Matter **19** (2007) 266004

[35] K. S. An, R. J. Park, J. S. Kim, C. Y. Park, S. B. Lee, T. Abukawa, S. Kono, T. Kinoshita, A. Kakizaki, T. lshii, J. Appl. Phys. **78**, 2 (1995) 1151-1155

[36] E.S. Cho, C.H. Lee, C.C. Hwang, J.C. Moon, J.h. Oh, K. Ono, M. Oshima, K.S. An, C.Y. Park, Surface Science **523** (2003) 30–36

[37] K.S. An, R.J. Park, J.S. Kim, C.Y. Park, C.Y. Kim, J.W. Chung, T. Abukawa, S. Kono, T. Kinoshita, A. Kakizaki, T. Ishii, Surface Science **337** (1995) L789-L794

[38] P. Shukrynau, V. Dudr, M. Švec, M. Vondrácek, P. Mutombo, T. Skála, F. Šutara, V. Matolín, K.C. Prince, V. Cháb. Surface Science **603** (2009) 469–476

[39] M. Wanke, M. Franz, M. Vetterlein, G. Pruskil, B. Höpfner, C. Prohl, I. Engelhardt, P. Stojanov, E. Huwald, J.D. Riley, M. Dähne. Surface Science **603** (2009) 2808–2814

[40] F. J. Himpsel, F.R. McFreely, A. Taleb-Ibrahimi, J.A. Yarmoff and G. Hollinger, Phys. Rev. B **38** (1988) 6084

[41] N. Miyata, M. Ichikawa, T. Nabatame, T. Horikawa, A. Toriumi, Jpn. J. Appl. Phys. **42** (2003) L 138

[42] M. R. J. van Buuren, F. Voermans, and H. van Kempen. Journal of Physical Chemistry **99** (1995) 9519-9522

[43] R. Pretorius Thin Solid Films **290-291** (1996) 477-484

[44] R. Beyers, J. Appl. Phys. **56**, 1 (1984) 147

[45] K.S. An, R.J. Park, J.S. Kim, C.Y. Park, C.Y. Kim, J.W. Chung, T. Kinoshita, and A. Kakizakff. Journal of Electron Spectroscopy and Related Phenomena **80** (1996) 165-168

[46] O.M. Ndwandwea, Q.Y. Hlatshwayo, R. Pretorius, Materials Chemistry and Physics **92** (2005) 487–491

[47] B.Brennan, S. McDonnell, G. Hughes, Thin Solid Films **518** (2010) 1980–1984

[48] H.T. Johnson-Steigelman, A.V. Brinck, S.S. Parihar, P.F. Lyman, Phys. Rev. B **69**, (2004) 235322

[49] K. Saiki, K. Nishita, Y. Ariga, A. Koma, Journal of Vacuum Science and Technology A **17**, 5 (1999) 2911-2914

[50] W. Xi-Na, W. Yong, Z. Jin, Z. Tian-Chong, M. Zeng-Xia, G. Yang, X. Qi-Kun, D. Xiao-Long, Z. Xiao-Na, H. Xiao-Dong, Z. Ze. Chinese Physics B **18**, 7 (2009) 3079-3083

[51] J.-H. Lee, M. Ichikawa, J. Appl. Phys. **92**, 4 (2002) 1929

[52] J.-H. Lee, N. Miyata, M. Kundu, M. Ichikawa, Phys. Rev. B **66**, (2002) 233309

[53] E. Goranova, B. Amov, M. Baleva, E.P. Trifonova, P. Yordanov, Journ. Mat. Sci. **39** (2004) 1857-1859

[54] M. Copel, E. Cartier, F. M. Ross, Appl. Phys. Lett. **78**, 11 (2001) 1607

[55] J. A. Gupta, D. Landheer, J. P. McCaffrey, G. I. Sproule, Appl. Phys. Lett. **78**, 12 (2001) 1718

[56] J.J. Chambers, B.W. Busch, W.H. Schulte, T. Gustafsson, E. Garfunkel, S. Wang, D.M. Maher, T.M. Klein, G.N. Parsons, Appl. Surf. Sci. **181** (2001) 78-93

[57] R. O’Connor, S. McDonnell, G. Hughes, K.E. Smith, Surface Science **600** (2006) 532–536

Chapter 6

The effects of Oxide Removal and Chemical Modification of InP surfaces prior to MgO deposition

6.1 Introduction

As outlined in Chapter 1, metal oxide semiconductor field effect transistors (MOSFETs) on III-V compound semiconductors have the potential to offer significant advantages over conventional silicon based devices [1]. While the advantages of these materials are well known, the main obstacle to the integration of alternative semiconductors remains controlling the interfacial properties between the substrate and the deposited gate dielectric [2]. Indium phosphide (InP) has been the subject of some interest due to its high carrier mobility [3], direct optical band gap [4], and reported resistance to Fermi level pinning [5]. As with other III-V semiconductors such as InGaAs [6], the preferred fabrication method for InP MOS structures is through growth techniques such as molecular beam epitaxy (MBE) [7,8] and metalorganic vapour phase epitaxy (MOVPE) [9,10] which are commonly performed using an excess phosphorous background pressure. These techniques allow for the growth of stoichiometric and well order surfaces, free from surface oxide and other impurities [7,11]. Following growth, InP surfaces may then be capped using thin Sb or As layers allowing the films to be exposed to ambient conditions for short periods without degrading surface properties [12]. While these techniques have been successful in growing high quality InP epitaxial layers the toxicity of the metalorganic and hydride species used in the growth process have limited there use. As such, the focus of this study is to investigate surface preparation methods which can be used to modify and improve the interfacial properties of InP surfaces following prolonged exposure to ambient conditions. Recent studies have shown that high quality interfacial properties and Fermi level unpinning can be achieved using Al_2O_3 thin films on InP [5,13,14], while Hollinger *et al.* [15] have suggested that Al_2O_3 acts to passivate the InP surface. Magnesium Oxide (MgO), which has a similar dielectric constant to Al_2O_3 [16,17], has shown promising results as an alternative gate dielectric on Si due to its large bandgap (7.8 eV), and high thermal stability [18, 19].

While comparatively few studies have investigated the properties of MgO thin films on III-V substrates, promising electrical characteristics have been reported for MgO on InP [20] and GaAs [21]. This study presents an initial investigation into how the interfacial chemistry of MgO/InP based devices can be modified and improved. Numerous preparation methods, including HCl [22,23], H_2SO_4 [24], Ar Ion sputtering [25,26], surface nitridation [27], hydrofluoric acid [28] and bromine based solutions [29], have been suggested for the optimisation of InP surfaces. However, many studies within the literature concentrate purely on the removal of surface oxide. Given that simply removing surface oxygen does not passivate the surface and, in fact, increases interface state density [30] investigating the chemical stability of the cleaned surface is thought to be of vital interest.

In this study the effectiveness of surface preparation methods will be classified, not only based on oxide removal, but also on the creation of chemically stable interfaces with magnesium oxide thin films. The chemical stability of the surfaces will be investigated by depositing MgO and monitoring the resulting interfacial oxide growth using XPS. As such, it can be considered that deposition of MgO has been used to "probe" the stability of both native oxide and wet chemically etched InP surfaces. The surface preparation methods initially discussed in this study include a 2-stage wet chemical etch and sulphur passivation using ammonium sulphide solution. Initial electrical characterisation was also performed on MgO/InP based MOS devices fabricated using these surfaces preparation methods, and the electrical results obtained are discussed in relation to the XPS data. Given that MOS devices prepared using wet chemical etching exhibit Fermi level pinning, the use of atomic hydrogen (H*) cleaning is also discussed as an alternative method for the preparation of contaminant free InP surfaces. Due to the reportedly low thermal stability of InP surfaces [31] lowering the substrate temperature used during H* cleaning is of key importance [32]. H* cleaning of InP native oxide surfaces was carried out over a range of temperatures, with XPS being subsequently used to investigate the removal of surface contaminants and the chemical stability of the cleaned surface. It was found that while effective cleaning of the surface could be achieved at temperatures greater than 300 °C, subsequent MgO deposition onto the cleaned surface resulted in significant interfacial oxide growth. A series of *in-situ* thermal anneals of the InP native oxide surface was then carried out which showed that this interfacial oxide growth can be directly related to the thermal stability of InP, and the temperature at which the H* cleaning was performed.

While the surface cleaning methods mentioned above are primarily designed to remove surface oxide species, modifying the chemical composition of the native oxides which form on these surfaces may also be of technological interest. Previous studies have shown that the deposition of Ge [33] and Si interfacial control layers (ICL) onto III-V substrates can improve electrical results [34-36]. Recent studies by Chen *et al.* [37] and Ok *et al.* [38] have reported that the deposition of an amorphous Si control layer on InP prior to HfO_2 deposition can improve the electrical characteristics of the device. While the electrical benefits of Si ICL have been studied in some detail, the chemical interactions which occur within the InP/Si ICL/dielectric interfacial region are less well known. In this study *in-situ* XPS analysis is used to investigate the interfacial chemistry of thin silicon and Mg silicate layers on InP native oxide surfaces. The chemical stability of both the Si layer and the underlying InP following MgO deposition and subsequent 500 °C annealing is also investigated.

6.2 Experimental Procedure

XPS characterisation of the InP native oxide surface was carried out on n-type substrates, with a doping concentration of 5×10^{18} cm^{-3}, cleaned using the standard degreasing procedure outlined in Chapter 3, section 3.4. The 2-stage wet chemical etch is that developed by Sun *et al.* [22] and consisted of a 1 minute etch in a 4:1:100 solution of H_2SO_4:H_2O_2:H_2O followed by a 30 second etch in 1:3 HCL:H_2O and subsequent rinsing using deionised water. Sulphur passivation was carried out using a 20 minute etch in 20% ammonium sulphide solution at room temperature. Care was taken to ensure that samples were rinsed in deionised water immediately after being removed from the ammonium sulphide in order to prevent excess solution drying on the surface. Following analysis of the wet chemically etched surfaces, MgO thin films were deposited *in-situ* using the evaporation of magnesium metal in an oxygen partial pressure of 5×10^{-7} mBar [39] (as described in Chapter 3, section 3.2.2). All MgO films analysed in this chapter using XPS were deposited using this technique. MgO/InP based metal oxide semiconductor (MOS) structures were fabricated using electron beam evaporation from polycrystalline MgO pellets with a purity of 99.99 %.

MOS devices were metallised using the FUSI process outlined in Chapter 3, following the deposition of a 100 nm *in-situ* Si capping layer. C-V and I-V measurements taken were acquired using the apparatus and procedure outlined in Chapter 3, section 3.6.

Atomic hydrogen was generated using the Oxford Applied Research TC-50 Thermal Gas Cracker described in Chapter 3, using a total hydrogen partial pressure ($H^* + H_2$) equal to 1×10^{-7} mbar. To determine optimum cleaning conditions InP native oxide samples were exposed to atomic hydrogen at room temperature and at elevated temperature (300 - 400 °C) for exposure times from 30 minutes to 1 hour. Silicon interfacial control layers (Si ICL) with an approximate thickness of 1 nm were deposited onto InP native oxide surfaces using electron beam evaporation from an Oxford Applied Research EGC04 mini e-beam evaporator four pocket source. An optimum deposition temperature of 200 °C was used after initial depositions were carried out over a range of temperatures between room temperature and 200 °C. In the final phase of these studies, pure magnesium metal (99.9%) was deposited at room temperature at a pressure of 1×10^{-9} mbar onto the silicon control layer surface using thermal evaporation to investigate interface modification.

6.3 Photoemission and electrical characterisation of MgO films deposited onto InP native oxide and wet chemically etched surfaces

6.3.1 Composition and Stability of InP native oxide surfaces

While the focus of this study is primarily the use of surface preparation methods and their effectiveness in removing oxide based contaminants, initial studies into the chemical composition of the InP native oxide surface were also carried out. Information relating to oxide composition is vital in determining both the chemical stability of the surface, and how effective surface preparation methods are at removing this oxide. Specifically, given that XPS is the main analysis technique used in this study, the photoemission spectral components relating to the InP native oxide must first be conclusively identified before the removal of this oxide can be investigated. Hollinger *et al.* [40] have previously investigated the chemical composition of InP native oxide surfaces using XPS. In their study, core level P 2p and In 3d spectra taken from the native oxide surface were compared to spectra taken from stoichiometric indium oxide and phosphorous oxide compounds. Their study has shown that it is inaccurate to view the InP native oxide as a composition of separate stoichiometric compounds, for instance $InPO_4$ and $In(OH)_2$. In fact, the nature of the InP native oxide is better described as a composition of both indium and phosphorous oxides, with these composites being classified into three categories which have similar properties to the species $In(OH)_3$, $InPO_4$ and $In(PO)_3$. This is the classification approach adopted in these studies.

In order to determine the composition of the InP native oxide using XPS, accurate curve fitting parameters must be determined for the oxide species on both the P 2p and $In3d_{5/2}$ (subsequently referred to as In 3d) spectra. While the large separation between the P 2p bulk and oxide peaks allows for comparatively easy identification of oxide species present, it is much more difficult to accurately retrieve chemical information relating to the specific In oxides on the surface based on curve fitting of the In3d spectrum. As such, a more plausible approach is to use the separation of the P 2p oxide peak from the substrate component in order to identify the oxide species present and hence determine how the In 3d peak should be curve fitted.

The P 2p native oxide spectrum in figure 6.1 shows a single P oxide peak separated from the InP substrate peak by 4.58 eV.

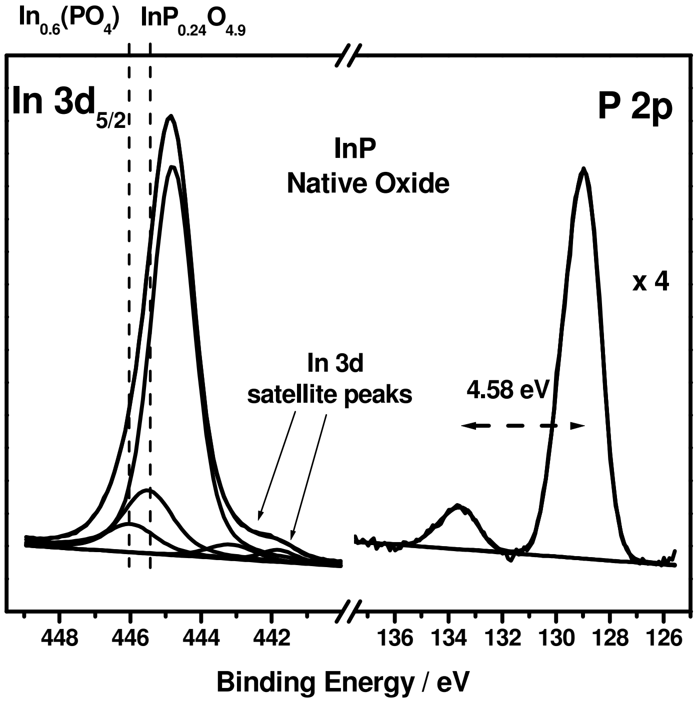

Figure 6.1 Curve fitted In 3d and P 2p spectra taken from the InP native oxide surface. Fitting parameters for the In 3d spectrum were determined based on the B.E. separation between the P 2p bulk and oxide signals, and the work of Hollinger *et al.* [40]. The origin of the In 3d satellite peaks is discussed in the appendix section at the end of this chapter.

The work of Hollinger *et al.* [40] states that this separation can be indicative of two different forms of InP composite oxide, namely $InP_{0.24}O_{4.9}$ and $In_{0.6}(PO_4)$. The curve fitted In 3d spectrum, using the relevant oxide separation of $InP_{0.24}O_{4.9}$ (0.7 eV) and $In_{0.6}(PO_4)$ (1.2 eV), is also shown in figure 6.1. The FWHM of the In 3d bulk peak was taken from a sulphur passivated InP surface, which had been etched using ammonium sulphide, as this was the most oxide free surface obtained in this study. The curve fitting parameters used for the P 2p and In 3d native oxide peaks are summarised in table 6.1.

	P 2p Bulk	**P 2p Oxide**	**In $3d_{5/2}$ Bulk**	**In $3d_{5/2}$ InP_xO_y**	**In $3d_{5/2}$ $In_x(PO_y)$**
B.E. separation from bulk signal	-------	4.58 eV	-------	0.70 eV	1.20 eV
Gaussian FWHM	1.16 eV	1.69 eV	1.11 eV	1.20 eV	1.20 eV
Lorentzian FWHM	0.15 eV	0.15 eV	0.48 eV	0.48 eV	0.48 eV
Spin-Orbit Split	0.86 eV	0.86 eV	Singlet	Singlet	Singlet

Table 6.1 Curve fitting parameters used to fit P 2p and In $3d_{5/2}$ spectra taken from the InP native oxide surface.

It should be noted that it is difficult to conclusively determine if the InP oxide compounds mentioned above are an accurate classification of the chemical species present on the surface, especially given that non-stoichiometric oxides may exist in a wide compositional range within the native oxide [40]. As a consequence of this, the oxide component peaks of the In 3d spectrum will be labelled as InP_xO_y and $In_x(PO_y)$ in all subsequent discussions. However, it can be said that the peak fitting parameters obtained using this analysis can be used to consistently fit P 2p and In 3d oxide peaks taken from a variety of differently treated surfaces.

MgO thin films were subsequently deposited onto the InP native oxide surface using the deposition of Mg in an partial pressure of O_2, as mentioned above. The effect which MgO deposition has on the native oxide core level spectra can be used as a measure of the chemical reactivity of the surface, and this is shown using the curve fitted In 3d and P 2p spectra in figure 6.2, and the relevant fitting data in table 6.2.

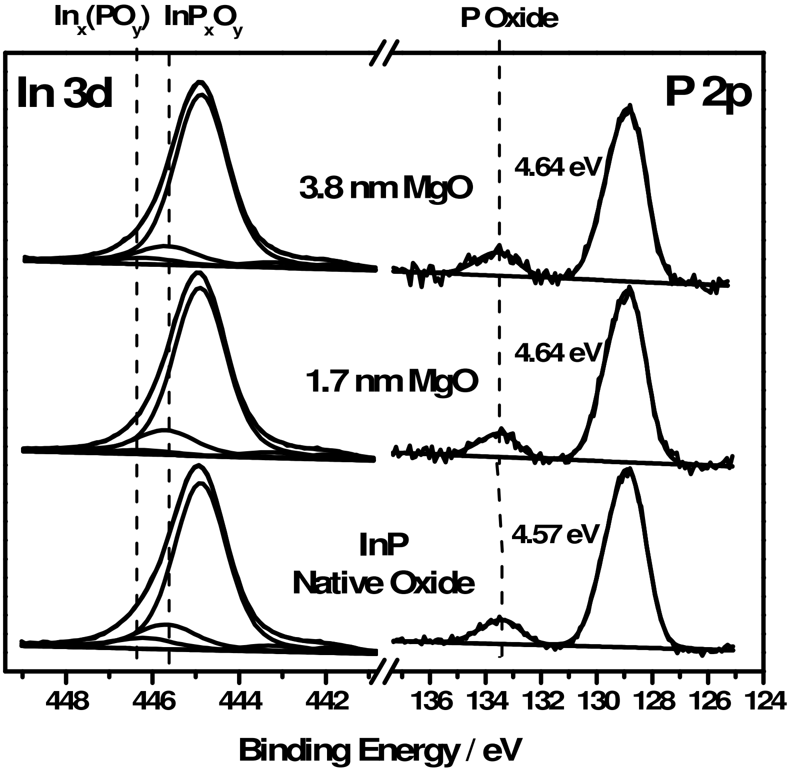

Figure 6.2 P 2p and In 3d spectra showing a change in the chemical composition of the InP native oxide surface as a result of MgO deposition.

	Total In oxide %	InP_xO_y %	$In_x(PO_y)$ %	Total P oxide %	Stoichiometry P %
InP native oxide	19.5 %	13.6 %	6.0 %	14.0 %	46.9 %
1.7 nm MgO	16.3 %	13.2 %	3.1 %	13.7 %	-
3.8 nm MgO	14.4 %	11.2 %	3.2 %	13.6 %	-

Table 6.2 Curve fitting data taken from the spectra in figure 6.2 which suggest segregation in the native oxide evidenced by a reduction of indium oxide.

P 2p spectra, taken after MgO deposition, show a slight shift in the phosphorous oxide peak to higher binding energy by 0.07eV. This can be attributed to a lessoning indium contribution within the InP composite oxide [22,40], which may be indicative of disruption or segregation within the native oxide layer. Similar evidence for disruption can be seen from the curve fitted In 3d core level data, which indicate changes in the native oxide composition. It should be noted that while In 3d spectra show a slight reduction in the integrated area attributed to indium oxide, this does not necessarily mean a reduction in the number of oxygen atoms within the oxide layer. Given the reported chemical stability of stoichiometric MgO it is unlikely that the transfer of O from the InP surface to the deposited MgO would occur. However, such a reduction in the In oxide contribution may be due to the formation of a more phosphorous oxide rich species, in agreement with the observed binding energy shift in the P 2p oxide signal.

While it is difficult to conclusively determine the effect of MgO deposition using XPS, there is sufficient evidence to suggest that MgO deposition has resulted in disruption to the chemical composition of the native oxide layer. Given that the semiconductor/dielectric interfacial region plays a critical role in determining the electrical properties of the InP substrate, the disruption shown may be detrimental to electrical characteristics. The chemical interactions on the native oxide surface after MgO deposition will now be compared with that of wet chemically etched InP surfaces.

6.3.2 Wet Chemical Etching

It has been suggested that Fermi level pinning in III-V devices may be caused by the poor quality of their native oxides [1] and numerous methods for removing these oxide layers have been developed. In this study the effect of two wet chemical etching procedures are investigated based upon the removal of surface oxygen, and the chemical stability of the etched surface as determined by MgO deposition. A 2-stage wet chemical etching procedure has been suggested by Sun *et al.* [22], using H_2SO_4 and HCl. This etch is designed to remove the native oxide as well as removing carbon based contamination from the InP surface. The effect of this 2-stage etch can be seen from the In 3d, P 2p and O 1s spectra in figure 6.3.

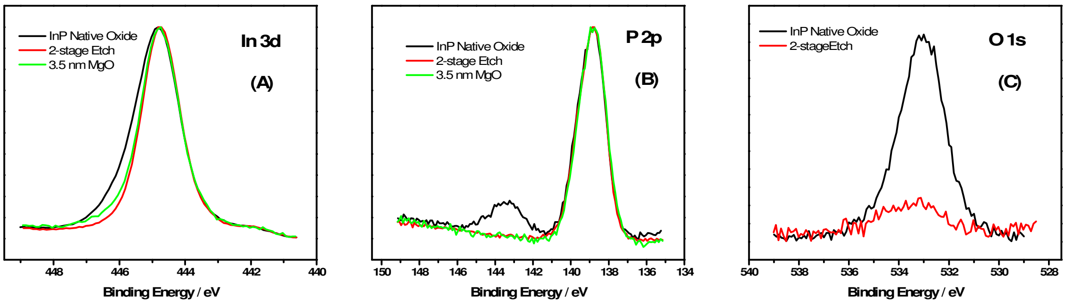

Figure 6.3 In 3d, P 2p and O 1s spectra showing the removal of surface oxide after 2-stage wet chemical etching. The spectra suggest the subsequent MgO deposition resulted in interfacial In oxide growth.

The “raw” In 3d and P 2p spectra show definite evidence for the removal of the InP native oxide (figure 6.3a,b). This is also reflected in an 80 % reduction in the integrated area of the O 1s peak (figure 6.10c). Based on the magnitude of the O 1s peak the residual oxide coverage is estimated to be less than one monolayer. As the 2-stage etch does not passivate the surface the O 1s peak measured after etching may in part be due to the re-growth of oxide which occurred while the sample was being loaded into the vacuum system.

Further analysis of the etching process, as well as the effects of MgO deposition, can be seen from the curve fitted spectra in figure 6.3 and relevant data in table 6.3.

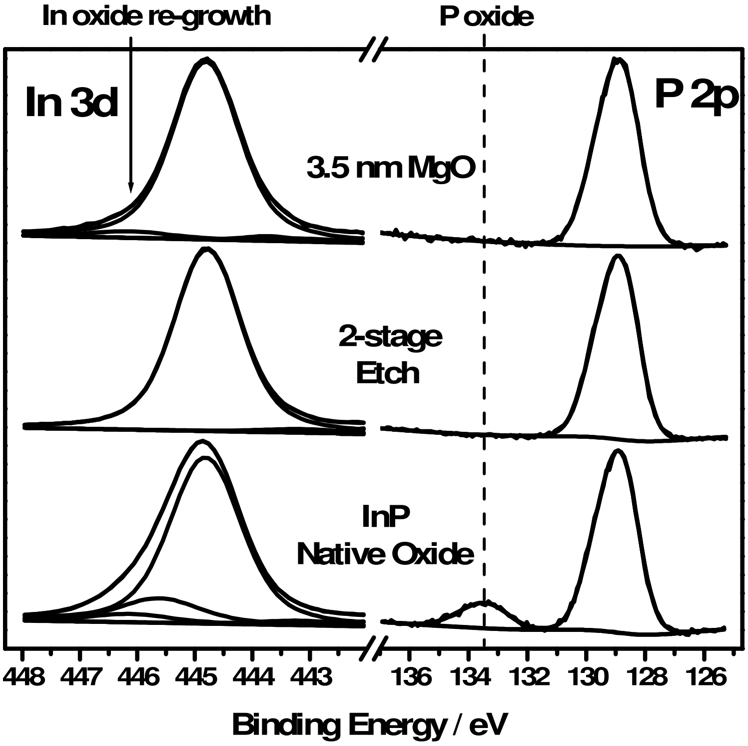

Figure 6.4 In 3d and P 2p spectra show no evidence for surface oxide after 2-stage etching, and indicate the preferential growth of In oxide after MgO deposition.

	Total In oxide %	**InP_xO_y %**	**$In_x(PO_y)$ %**	**Total P oxide %**	**O 1s %**	**Stoichiometry: P %**
InP native oxide	22.3 %	14.9 %	7.4 %	14.1 %	100 %	47.1 %
2-stage etch	0 %	0 %	0 %	0 %	19.7 %	51 %
3.5 nm MgO	4.1 %	0 %	4.1 %	0 %	-	-

Table 6.3 Curve fitting data taken from figure 6.4 suggest that 2-stage etching produced a P terminated InP surface free of P and In oxide species. The preferential growth of In oxide after MgO deposition is also shown.

While the O 1s peak has not been fully removed, curve fitted In 3d and P 2p spectra show no evidence for the presence of surface oxide following the 2-stage chemical etch. This inconsistency can be explained by the limited surface sensitivity offered by conventional XPS when compared with synchrotron radiation based photoemission and could also be attributed to inaccuracy in the peak fitting procedure. As stated previously the difficulty in curve fitting the In 3d spectrum makes it comparatively more difficult to identify the presence of In oxide species on the etched surface. The accuracy of the In 3d core level fitting procedure used in this study is dependant on the FWHM value used for the In 3d substrate component. While the value used was taken from the most oxide free InP surface obtained in this study it may be too large, and as such this may misrepresent the level of In oxide species remaining on the surface. Therefore, it can be stated that while it is difficult to conclusively determine the extent to which In and P oxide species have been removed from the surface using conventional XPS, it can be stated the etching process did significantly reduce the presence of surface oxide.

Another notable result of the etching process is a significant change in surface stoichiometry compared to that seen from the native oxide surface. While the stoichiometry of the native oxide was found to be slightly In rich, the 2-stage etching process resulted in a higher concentration of phosphorous atoms at the surface, with both results being in agreement with previous findings [22,41]. The In 3d spectrum taken after MgO deposition on the etched surface, shows evidence for the growth of indium oxide at the InP/MgO interface. The exact chemical nature of this interfacial oxide is difficult to determine, however it does exhibit a binding energy separation from the InP bulk peak of 1.3 eV, larger than that seen from the native oxide. Also, it should be noted that there is no evidence for the re-growth of P oxide after MgO deposition and as such there is no evidence that this oxide takes the form of an InP composite oxide as described by Hollinger *et al.* [40].

The second wet chemical etching procedure discussed in this study is that of sulphur passivation (S-pass) using a 20 % ammonium sulphide solution, which is designed to remove the native oxide and leave a monolayer of S bonded to the surface of substrate [42,43]. The substrates were etched using a 20 minute dip at room temperature followed by an immediate rinse in deionised water and then dried in N_2. It should be noted that the presence of sulphur on the InP surface following ammonium sulphide etching was confirmed by the presence of the S 2p core level peak (not shown). However the poor signal to noise ratio obtained from the S 2p made it difficult to analyse the chemical composition of the sulphur species present and as such further analysis of the S 2p peak was not performed. The process of sulphur passivation and the effect of subsequent MgO deposition are analysed using the unfitted In 3d, P 2p and O 1s core level spectra in figure 6.5.

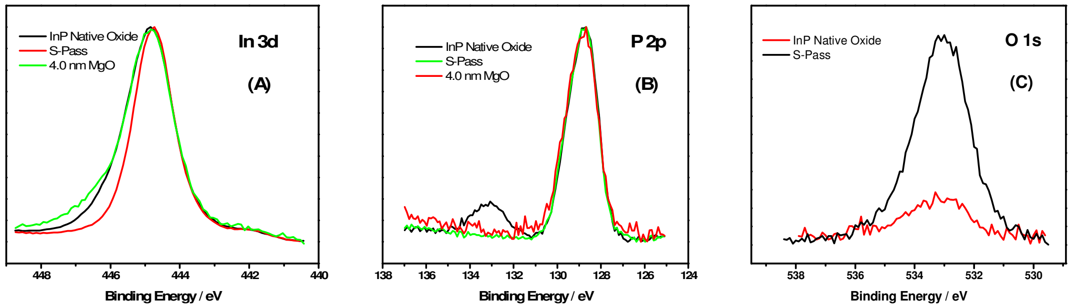

Figure 6.5 In 3d, P 2p and O 1s spectra showing the removal of surface oxide using sulphur passivation. In 3d spectra show increased levels of In oxide growth upon MgO deposition.

The results shown by these spectra are similar to those observed after the 2-stage chemical etch (figure 6.3), and suggest a significant reduction in the presence of surface oxide. The reduction of the O 1s peak (81 %) is slightly larger than that seen after 2-stage etching possibly due to less oxide re-growth prior to inserting the sample into the vacuum system, however, the difference between the two is minimal and there is little evidence for this from the P 2p and In 3d peak profiles. This either indicates that the oxides signal on the core levels is below the resolution limit of the XPS or may also indicate that the oxide signal is associated with physisorbed contaminants which do not contribute to the In 3d and P 2p core level spectra. Curve fitted spectra in figure 6.6 and the analysis presented in table 6.4 again suggest that the wet chemical etching process was effective in the removal of surface oxygen, and also resulted in a similar increase in phosphorous concentration at the InP surface to that seen after the 2-stage etch.

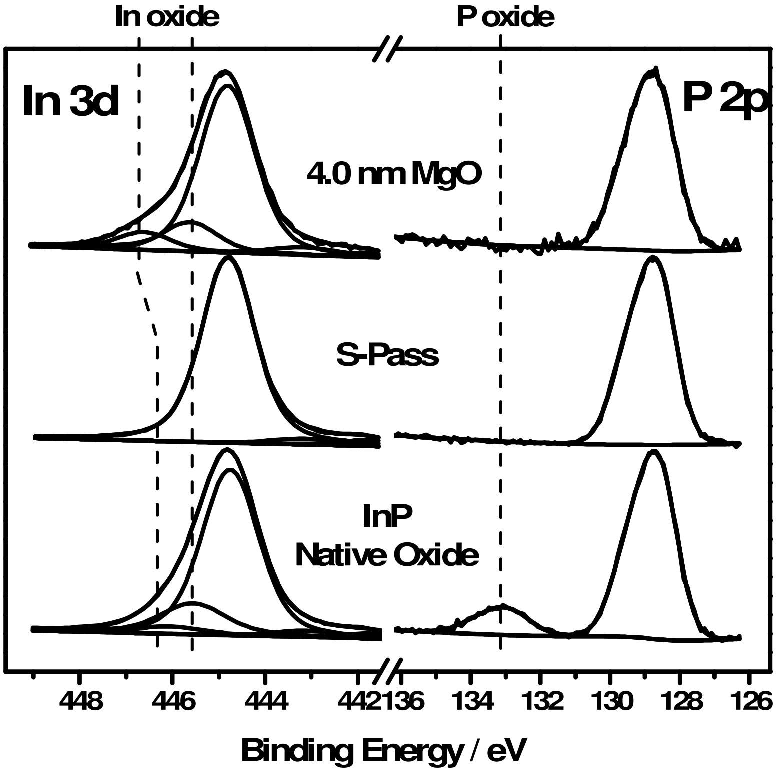

Figure 6.6 Curve fitted In 3d and P 2p spectra showing the complete removal of In and P oxide due to s-pass etching and the preferential growth of In oxide upon MgO deposition.

	Total In oxide %	**InP_xO_y %**	**$In_x(PO_y)$ %**	**Total P oxide %**	**O 1s %**	**Stoichiometry: P %**
InP native oxide	22.3 %	14.9 %	7.4 %	14.1 %	100 %	47.1 %
S-Pass	0 %	0 %	0 %	0 %	18.9 %	53 %
4 nm MgO	21.8 %	13.6 %	8.2 %	0 %	-	-

Table 6.4 Curve fitting data taken from figure 6.6 which suggest that that MgO deposition on s-pass surfaces results in greater levels of interfacial oxide growth than that seen after 2-stage etching.

However, the interfacial oxide growth seen following MgO deposition on the s-pass surface is significantly increased from that observed on the 2-stage etch sample.

While the P 2p spectrum remains unchanged, there is considerable evidence for interfacial oxide growth within the In 3d spectrum (figure 6.6). Taken as a function of peak area the interfacial oxide is now slightly greater than that seen on the native oxide surface before etching. Given these results it can be suggested that interfacial oxide growth seen after MgO deposition onto wet chemically etched surfaces is primarily indium based, as there is no evidence for the re-growth of P oxide in either figure 6.4 or figure 6.6. This is in contrast to the work of Cheng *et al.* [44] who have shown that the deposition of Al_2O_3 onto hydrofluoric acid etched InP results in significant interfacial P oxide growth.

XPS analysis has shown that MgO deposition on the InP native oxide surface results in disruption to the composition of the oxide layer. It has also been shown that wet chemical etching procedures may be used to remove surface oxide species and produce phosphorous rich surfaces. However, subsequent MgO deposition onto the etched surfaces shows evidence for In based interfacial oxide growth, with the In oxide growth on the S-pass surface comparable to that seen from the un-etched surface.

6.3.3 Electrical characterisation of MgO films on native oxide and wet chemically etched InP (100) surfaces

In order to complement these photoemission results, the electrical characteristics of MgO films deposited onto native oxide and wet chemically etched InP surfaces was also investigated. InP based MOS devices were fabricated at the Tyndall national institute using the FUSI metallisation process. I-V characteristics taken from 20 nm MgO films deposited on the differently prepared n-type and p-type InP substrates, shown in figure 6.7, suggest that devices prepared using the 2-stage etch have on average significantly higher leakage currents than those deposited on s-pass and native oxide covered substrates. This trend is shown by both n-type and p-type devices. The noise in the I-V profiles is similar to that observed on Si based devices also prepared using the FUSI method (Chapter 4 figure 4.13) and as such is again attributed to the fabrication process.

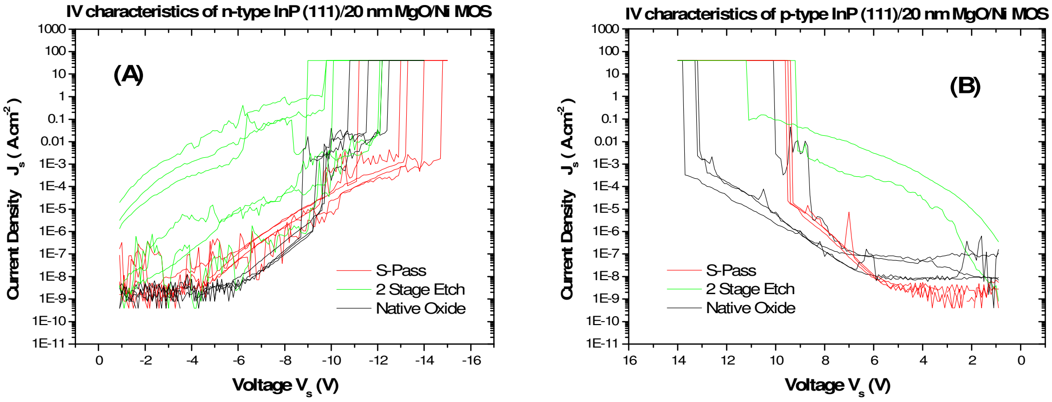

Figure 6.7 I-V characteristics taken from 20 nm MgO films on n-type (A) and p-type (B) InP surfaces. The results suggest 2-stage etch devices have on average higher leakage currents than native oxide and s-pass substrates.

It should be noted that the breakdown voltages seen for the 20 nm MgO films on InP vary significantly as a function of surface preparation method. However, breakdown voltage values as high as 14 V are seen from the S-pass n-type devices, relating to a breakdown field of ~7 × 10^6 V/cm. This value is considerably higher than that seen from the Si based devices in Chapter 4 figure 4.13, which were also prepared using the FUSI metallisation process. As such it can be suggested that MgO/InP MOS structures prepared using wet chemical etching may be more suitable for high voltage device applications, than comparable Si based devices.

C-V characteristics taken from 20 nm MgO films on n and p-doped InP substrates are shown in figure 6.8.

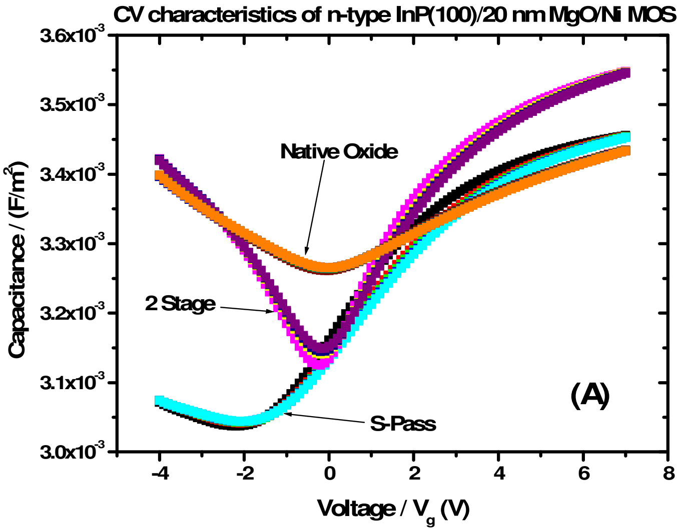

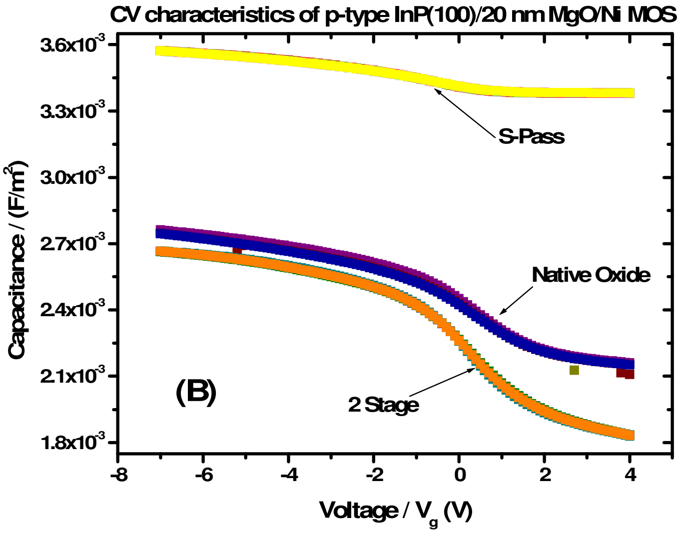

Figure 6.8 CV characteristics taken from 20 nm MgO films on n-type (A) and p-type (B) InP, showing lower values than expected for the difference (ΔC) between C_{max} and C_{min} attributed to Fermi level pinning.

The capacitance difference (ΔC) between C_{max} and C_{min} shown by the n-type devices in figure 6.8A is much smaller than expected. The maximum capacitance, of approximately 3.5 mF/m^2, is the same as that shown by 20 nm MgO films deposited on Si (111) substrates (Chapter 4, table 4.5), however, the minimum capacitance value is much higher than expected. Taking into account film thickness and substrate doping, the minimum capacitance values expected from the n-type devices was calculated to be ~ 2.3 mF/m^2 which is substantially lower than the C_{min} values measured from the n-type devices in figure 6.8A. It should be noted that the effects of surface charging, previously seen in the p-type Si wafers, are seen here on the n-type InP devices. As such, C_{min} values quoted in table 6.5 are taken from the lowest point on the CV curve, before the surface charging takes affect.

	C_{max} (mF/m^2)	**C_{min} (mF/m^2)**
Expected	3.6	2.3
n-type native oxide	3.4	3.3
n-type 2 stage	3.6	3.1
n-type s-pass	3.5	3.0

Table 6.5 A comparison between the measured and expected values for C_{max} and C_{min} from 20 nm MgO films on n-type InP. The data suggests that while measured C_{max} values are correct, C_{min} values are too high.

Capacitance values taken from the n-type devices suggest that while the correct C_{max} value is being obtained in accumulation, the C_{min} values are much higher than those expected for inversion. It should again be noted that the surface charging effects shown by the n-type InP devices may have caused inaccuracy in the C_{min} values shown above, as such the p-type devices, which do not show the effects of surface charging, may provide more accurate results.

The CV curves taken from the p-type InP devices also show a much smaller ΔC value than expected. The C_{max} and C_{min} values measured from these devices are compared to the expected values in the table 6.6.

	C_{max} (F/m^2)	**C_{min} (F/m^2)**
Expected	3.6	2.1
p-type native oxide	2.7	2.2
p-type 2 stage	2.7	1.8
p-type s-pass	3.6	3.4

Table 6.6 A comparison between the measured & expected values for C_{max} & C_{min} from 20 nm MgO films on p-type InP. Native oxide & 2-stage devices are in contrast to corresponding n-type devices as they show correct C_{min} and incorrect C_{max} values.

The data shows that while the native oxide and 2-stage devices show an approximately correct C_{min} value, the C_{max} is much lower than expected. Conversely the C_{max} value taken from the s-pass device is correct but the C_{min} is too high, suggesting that the affect can be linked to the interfacial properties of the device. While it is possible to attribute the incorrect C_{min} values seen in figure 6.8A to the affects of peripheral inversion, this charging affect can not be used to explain the decreased C_{max} value exhibited by the p-type devices. Peripheral charging affects are also inconsistent with the fact that the measured ΔC value can be linked to the InP surface preparation method used. Therefore, the results seen for both the n-type and p-type devices in figure 6.8 are attributed to Fermi level pinning, which is reported to cause a reduction in the measured ΔC value [45].

In order to better determine the viability of MgO/InP based transistor devices, the characteristics of thinner dielectric gate layers must also be studied. Therefore, 5 nm MgO films were deposited onto n-type InP substrates prepared using identical fabrication procedures as those used for the 20 nm devices. CV characteristics taken from the 5 nm MgO devices, shown in figure 6.9, display a similar trend to that seen for the 20 nm devices.

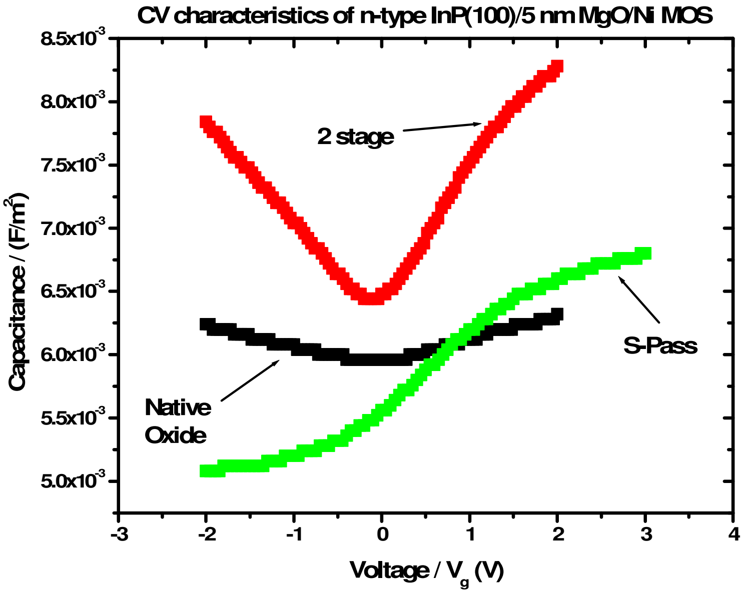

Figure 6.9 CV characteristics taken from 5 nm MgO films on n-type InP. The dependence of measured capacitance on the surface preparation techniques is similar to that seen from 20 nm devices.

Along with a similar reduction in the expected ΔC value, it should also be noted that the surface preparation methods used resulted in similar capacitance trends for both the 20 nm and 5 nm devices. It can be seen from the n-type devices in both figure 6.8 and 6.9, that surfaces prepared using the 2-stage chemical etch show a larger maximum capacitance value than the native oxide and s-pass surfaces. Assuming that the dielectric constant of the InP interfacial oxide is less than that of MgO, the reduced interfacial oxide growth seen after MgO deposition onto 2-stage etched surfaces (figure 6.4) would allow for a higher maximum capacitance value to be measured. Therefore the XPS analysis of figure 6.4 is in agreement with the CV characteristics taken from the 20 nm (figure 6.8) and 5 nm (figure 6.9) n-type devices, which show considerably larger C_{max} values for the 2-stage etch devices than for the native oxide and s-pass based devices.

6.3.4 Conclusions

In this study it has been shown that CV characteristics taken from InP based devices fabricated using native oxide and wet chemically etched surfaces show strong evidence for Fermi level pinning. XPS analysis relating to these electrical results suggest that MgO deposition on native oxide surfaces causes disruption within the oxide layer, and changes to the chemical composition of the oxide which are indicative of chemical segregation within the oxide layer. While wet chemical etching procedures were successful in removing the native oxide layer, subsequent MgO deposition saw significant growth of an indium based interfacial oxide region. In agreement with C_{max} values found during CV characterisation, interfacial oxide growth on 2-stage etched surfaces was found to be less than that seen after sulphur passivation. It is suggested that interfacial oxide growth seen upon MgO deposition could lead to an interface state density high enough to cause Fermi level pinning, as such it is difficult to conclusively determine if the interfacial oxide growth seen following MgO deposition lead to the Fermi level pinning affects seen using CV characterisation.

6.4 Atomic Hydrogen Cleaning of InP native oxide surfaces

6.4.1 Oxide removal and chemical stability of the cleaned surface

While wet chemical etching procedures were found to be unsuccessful in the formation of favourable MgO/InP interfacial characteristics, the technique of atomic hydrogen cleaning has been suggested as an alternative method of optimising the surface of III-V semiconductors. Using this method promising results have been achieved on GaAs substrates [46], while previous studies have also shown that InP surfaces can also be cleaned using this method [41]. The focus of this study was therefore to analyse the effectiveness of atomic hydrogen cleaning based on the removal of oxygen and carbon based surface contaminants, along with the chemical stability of the cleaned surface. Chemical stability was again investigated by depositing MgO on the cleaned surface and monitoring the resulting interfacial chemistry using XPS.

InP native oxide surfaces were prepared using a standard degreasing procedure, as described above, to remove carbon contamination and immediately loaded into the UHV chamber. The substrate temperature used during atomic hydrogen cleaning has been shown to be crucial in determining the effectiveness of the technique [2,41]. In contrast to the results of Wolan *et al.* [47], room temperature H* cleaning performed in this study resulted in no evidence for the removal of surface oxide species. This discrepancy is attributed to the fact that surfaces analysed by Wolan *et al.* [47] were subjected to ion sputtering prior to H* cleaning. Given that ion bombardment of InP is known to effect surface stoichiometry [25,26] the technique was not employed in this study, and therefore H* cleaning was facilitated using elevated temperature. Numerous studies have reported that atomic hydrogen cleaning may be used to effectively remove surface contaminants (oxide & carbonate) from InP at substrate temperatures between 350 °C and 380 °C [32,41,48]. In this study the effect of atomic hydrogen (H*) cleaning was investigated over a range of temperatures between 300 °C and 400 °C, using an optimum exposure time of 45 minutes. Unfitted In 3d and P 2p spectra taken after H* cleaning at 300 °C, 350 °C and 400 °C (seen in figure 6.10), show that H* exposure at 300 °C has resulted in a considerable reduction in the presence of both In and P oxide species.

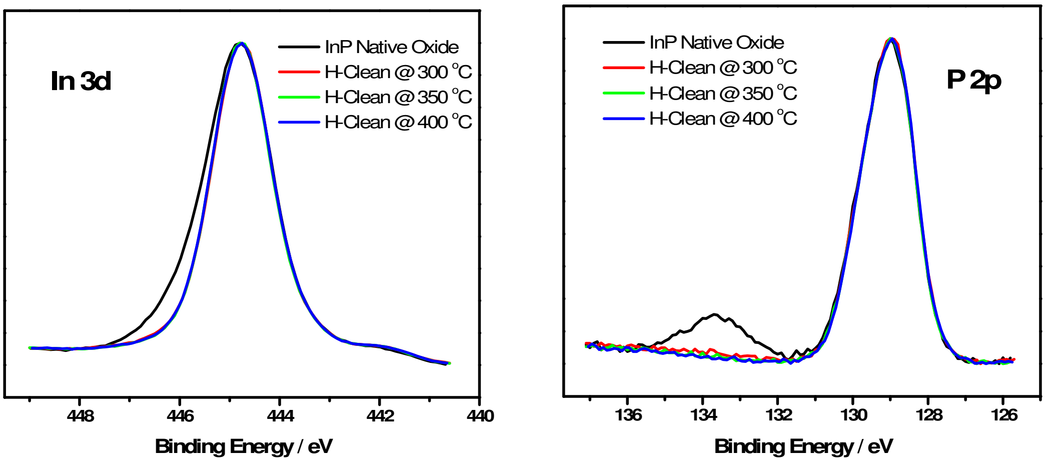

Figure 6.10 In 3d and P 2p spectra show large decreases in surface oxide upon H* cleaning at 300°C, and slight decreases upon subsequent cleaning at 350 & 400 °C.

In 3d spectra show little evidence of any additional In oxide removal at temperatures above 300 °C, while P 2p spectra suggest that H* cleaning at 350 °C produced only a slight further oxide decrease. The curve fitted In 3d and P 2p spectra in figure 6.11 show the removal of the InP native oxide after H* cleaning at 400 °C.

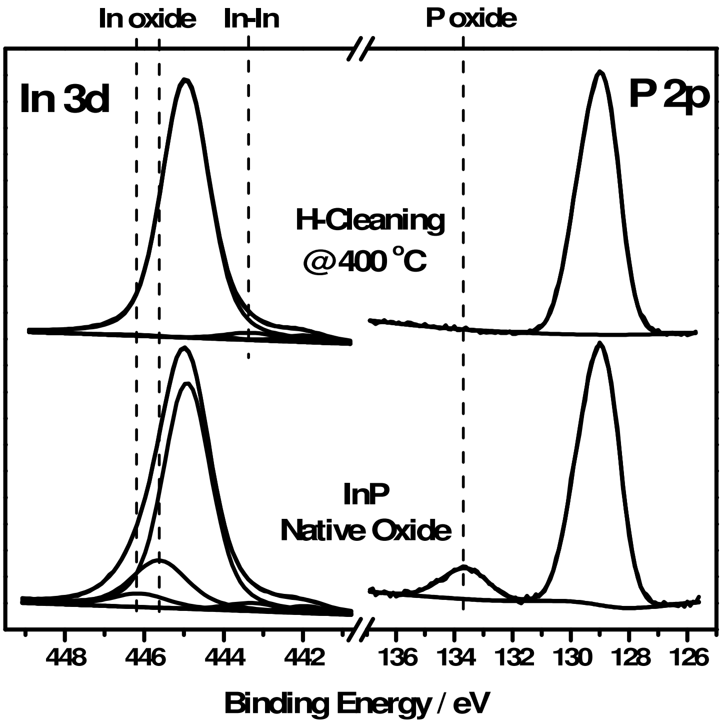

Figure 6.11 Curve fitted spectra taken after 400 °C H* cleaning which show complete removal of In & P oxide species, & evidence for the growth of In-In bonds.

In 3d spectra taken after 400 °C H* cleaning show no evidence for the presence of In oxide, while P 2p spectra also indicate the complete removal of phosphorous oxide at this temperature. The growth of an additional peak at 1.1 eV LBE to the InP bulk peak within the In 3d spectrum can also be seen, and is attributed to the presence of In-In bonds in agreement with the work of Muranka *et al.* [41]. This result is in agreement with Stietz *et al.* [49] and Bruno *et al.* [50] who have reported that H* exposure increases the concentration of indium on InP surfaces. While In 3d and P 2p spectra suggest the complete removal of surface oxygen, the difficulty of curve fitting the In 3d spectra and the relative lack of surface sensitivity offered by the P 2p peak must be noted. As such, a more accurate measure of the removal of surface contaminants may be given by the O 1s, C 1s and survey spectra seen in figure 6.12, which show the initial reduction of surface contaminants after H* cleaning at 300 °C.

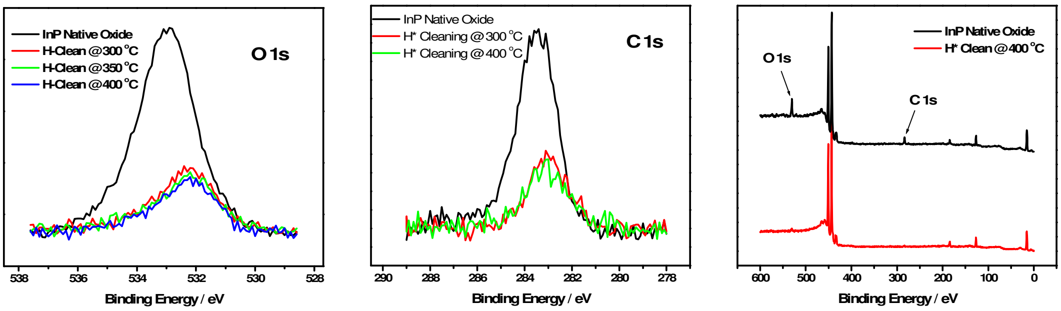

Figure 6.12 XPS O 1s, C 1s and survey (0 – 600 eV) spectra which show considerable decreases in surface contaminants after H* cleaning.

However, it is again evident that subsequent increases in substrate temperature resulted in only slight decreases in the oxygen and carbon signals, and as such were of little benefit to preparing a contamination free surface. The overall effect of H* cleaning on factors such as oxide removal and surface stoichiometry are collated in table 6.7.

	Total In oxide %	**InP_xO_y %**	**$In_x(PO_y)$ %**	**Total P oxide %**	**C 1s %**	**O 1s %**	**Stoichiometry: P %**
InP native oxide	22.3 %	14.9 %	7.4 %	14.1 %	100 %	100 %	47.1 %
300 °C	1.0 %	1.0 %	0 %	2 %	33.1 %	31.2 %	47.0 %
350 °C	0 %	0 %	0 %	0 %	30.8 %	29.8 %	46.9
400 °C	0 %	0 %	0 %	0 %	29.5 %	27.4 %	46.8

Table 6.7 Curve fitting data suggests that H* cracking had little effect on surface stoichiometry, reducing the presence of surface oxide and producing an In rich surface, in contrast to results seen after wet chemical etching.

XPS analysis suggests surface stoichiometry was unchanged by H* cleaning, and remained In rich, a result that is in contrast to previous studies [41,47] which reported near 1:1 stoichiometry for H* cleaned InP surfaces. While it may be suggested that this discrepancy is due to differences in experimental parameters, in particular the use of argon ion bombardment, this has not been conclusively determined in this study. Given the importance of minimising the thermal budget during the processing of III-V substrates [51] and the limited benefit shown by increasing substrate temperature to 350 °C and 400 °C, a temperature of 300 °C was used for all further H* cleaning studies.

While XPS results suggest the process of H* cleaning is effective in the removal of surface oxide, the chemical stability of the cleaned surface must also be investigated. The chemical stability of H* cleaned InP surfaces was analysed using MgO deposition, and compared to that of wet chemically etched surfaces. Unfitted In 3d and P 2p spectra taken after H* cleaning at 300 °C, and subsequent step-wise deposition of MgO, are shown in figures 6.13.

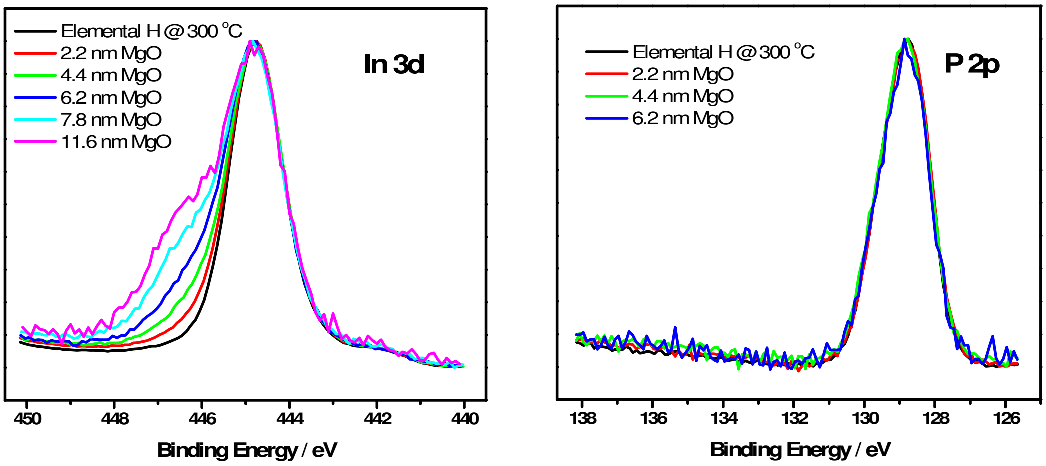

Figure 6.13 In 3d and P 2p spectra showing the large scale growth of In oxide as a result of MgO deposition after H* cleaning at 300°C, considerably greater than that seen after wet chemical etching.

While P 2p spectra show no evidence for P oxide growth as a result of MgO deposition, the interfacial indium oxide growth shown in figure 6.13 is considerably greater than that seen after MgO deposition on wet chemical etched surfaces. This increased reactivity is also reflected in the experimental procedure in that there was a considerable increase in the sticking coefficient of MgO on the surface, which necessitated a large reduction in MgO deposition time. It should be noted at this stage that the preferential growth of In interfacial oxide, as a result of MgO deposition, has been observed on both P-rich (2-stage etch) and In-rich (H* clean) surfaces. This result is in contrast to the work of Chen *et al.* [52] which suggests that the creation of In-O-In bonds is less energetically favourable than that of P-O-P or In-O-P bonds. This discrepancy suggests that the In oxide growth seen here is due to interfacial chemistry which is specific to MgO deposition, and may possibly indicate that Mg atoms are incorporated within the interfacial oxide. It should also be noted that exposing the H* cleaned surface to an O_2 partial pressure of 5×10^{-7} for 30 minutes did not result in any evidence of In oxide growth, suggesting that MgO deposition promoted oxide growth either through the incorporation of Mg or by having a catalytic effect on the surface. However, the incorporation of Mg within the interfacial oxide has not been conclusively determined in this study.

The growth of interfacial In oxide on H* cleaned surfaces can be further analysed using the curve fitted In 3d spectra in figure 6.14, which show the growth of two distinct oxide species. The largest oxide peak seen after MgO deposition shows a separation from the InP bulk peak equal to 1.3 eV, a value similar to that seen from MgO/InP interfacial oxide growth on wet chemically etched surfaces.

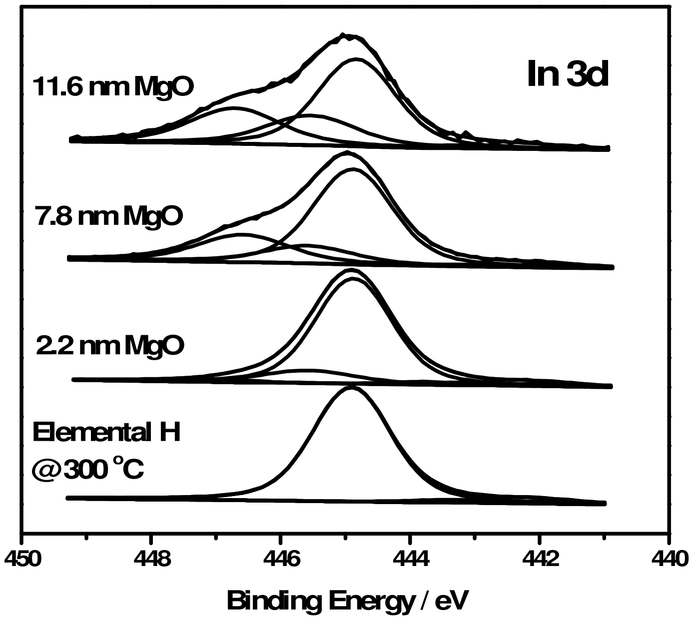

Figure 6.14 Curve fitted In 3d spectra showing the continued growth of In oxide as a function of MgO deposition.

Another notable aspect of the In 3d evolution is the continued growth of In oxide as a function of MgO deposition. XPS based thickness calculations suggest that the interfacial oxide continues to grow even after the thickness of the deposited MgO layer has become greater than 10 nm. Given that the accuracy of XPS thickness calculations is strongly dependant on the formation of a uniform overlayer and knowledge of the overlayer chemical composition, some error may exist on the thickness values shown. However, the continuous interfacial oxide growth seen after H* cleaning is still in marked contrast to that shown after wet chemical surface preparations and may be indicative of increased surface roughness causing intermixing of In and MgO. Atomic intermixing during the fabrication of MgO/InP based MOS devices has previously been reported by T.W. Kim *et al.* [20]. In order to further analyse the interfacial conditions which lead to such high levels of oxide formation, AFM was performed on an InP native oxide surface before and after H* cleaning at 300 °C (figure 6.15), with the cleaned surface being exposed to ambient conditions for ~1 hour during the acquisition of AFM images.

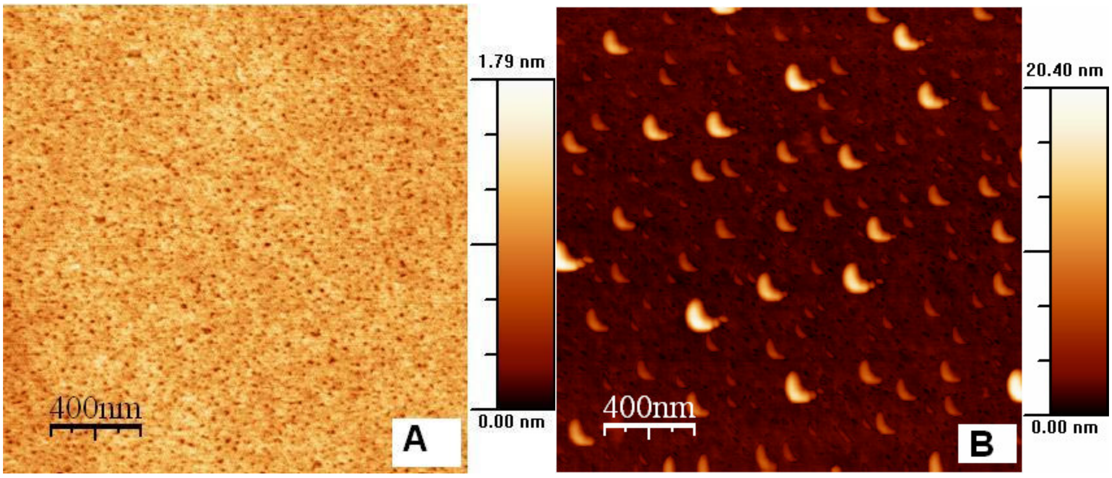

Figure 6.15 2 µm × 2µm AFM images taken from an InP native oxide surface before (A) and after H* cleaning at 300 °C (B). The H* cleaned surface clearly shows the presence of island structures which can be linked to the high levels of In oxide growth seen in figure 6.14.

	RMS roughness	**Average Height**	**Max Height**
Native Oxide Surface	0.2 nm	1.1 nm	1.8 nm
H* clean at 300 °C	1.6 nm	2.7 nm	19.3 nm

Table 6.8 AFM roughness data corresponding to the images in figure 6.15 show the surface disruption caused by H* cleaning at 300 °C.

The AFM images shown in figure 6.15, along with the relevant surface roughness data acquired from these images, suggest that the process of H* cleaning at 300 °C has resulted in considerable roughening of the InP surface. The images show the presence of island structures distributed across the surface with an average height of 13 nm and average width of 100 nm. While the regularity of the structures may suggest that they are an artefact of the scan parameters, further analysis such as changing scanning angle, tapping frequency and image size all suggest that the island features are real. It is suggested that the continuous interfacial oxide growth seen in figure 6.14 is due to the presence of these island structures i.e. the increased surface roughness may allow deposited MgO to continue interacting with the substrate at these island sites, even when the InP substrate signal has been attenuated.

The affects of H* cleaning were further analysed using I-V measurements taken from a 10 nm MgO film deposited on a n-type InP (100) substrate after H* cleaning at 300 °C (figure 6.16). This structure was fabricated in DCU using the procedure outlined in the final paragraph of Chapter 3 section 3.5.

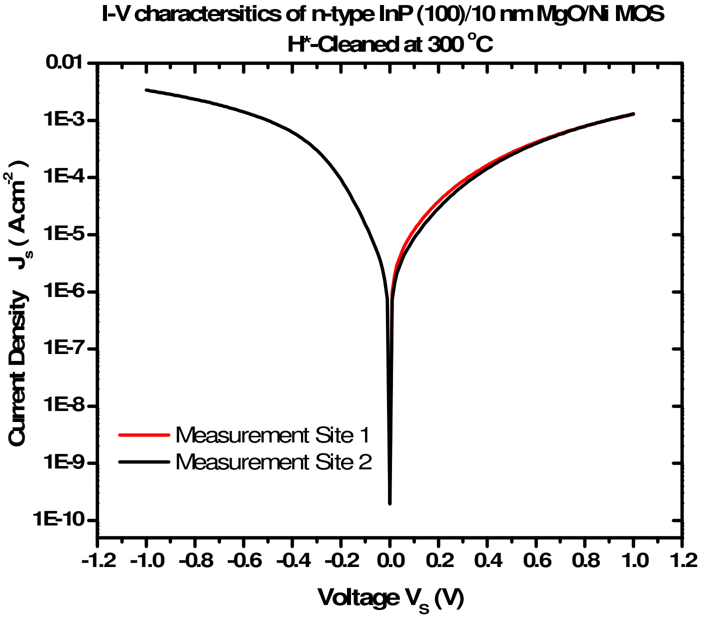

Figure 6.16 I-V characteristics taken from a 10 nm MgO film deposited on a n-type InP (100) substrate after H* cleaning at 300°C. Extremely high leakage current is indicative of nonuniformity in the dielectric layer caused by similar island features to that seen in 6.15.

The high leakage currents shown in figure 6.16 indicate that the H* cleaned MOS device was not operating as an effective capacitor, a result which can be attributed to nonuniformity in the dielectric layer. This result can be linked to the island structures seen in figure 6.15, and offers further evidence for the detrimental affects of H* cleaning at 300 °C. It should also be noted that due to the high leakage currents shown in figure 6.16, a measurable capacitance could not be acquired from the H* cleaned device.

Although the data suggests that the process of atomic hydrogen cleaning was effective in removing the InP native oxide, it has also resulted in considerable surface roughening and increased chemical reactivity upon deposition of MgO. The formation of similar island structures on InP has previously been reported [53,54] and is suggested to be due to the thermal desorption of surface atoms. However, the work of Stietz *et al.* [49] has also shown that exposure to atomic hydrogen results in the formation of In droplets on InP surfaces. While Bruno *et al.* [50] have outlined the mechanism by which H* exposure may cause desorption of surface P. As a consequence of this, doubt exists as to whether the surface disruption seen in this experiment is due to atomic H* exposure, or if it is due to the intrinsic thermal stability of the InP native oxide surface. In order to determine whether the changes in surface roughness were a result of the elevated annealing temperature or the atomic hydrogen treatment, a separate set of XPS and AFM measurements were carrier out on InP native oxide surfaces which had been annealed in UHV at temperatures ranging from 200 °C to 500 °C. The chemical stability of the annealed surfaces was subsequently analysed using *in-situ* deposition of MgO.

6.4.2 The effect of thermal annealing on the native oxide composition and surface roughness of InP.

Thermal annealing studies were performed on n-type InP native oxide substrates, with samples being held at the target temperature for 20 minutes, at a pressure of 5×10^{-9} mbar. After annealing samples were allowed to cool for 1 hour prior to XPS analysis. The chemical stability of the annealed surfaces was investigated using MgO deposition and compared to that seen after H* cleaning. Given the significant In oxide growth seen on the H* cleaned surfaces, even at MgO overlayer thicknesses approaching 12 nm, it was important to determine if similar levels of oxide growth occurred on the annealed surfaces. Therefore, sequential MgO deposition steps were continued until the interfacial oxide had ceased growing or until the substrate peaks had been fully attenuated. While deposition was carried out in a “step-wise” manner only the spectra which relate to the final MgO depositions are shown, in order to indicate the full extent of interfacial oxide growth. The effect of 200 °C annealing on an InP native oxide surface, and subsequent MgO deposition, is shown in the curve fitted In 3d and P 2p spectra in figure 6.17.

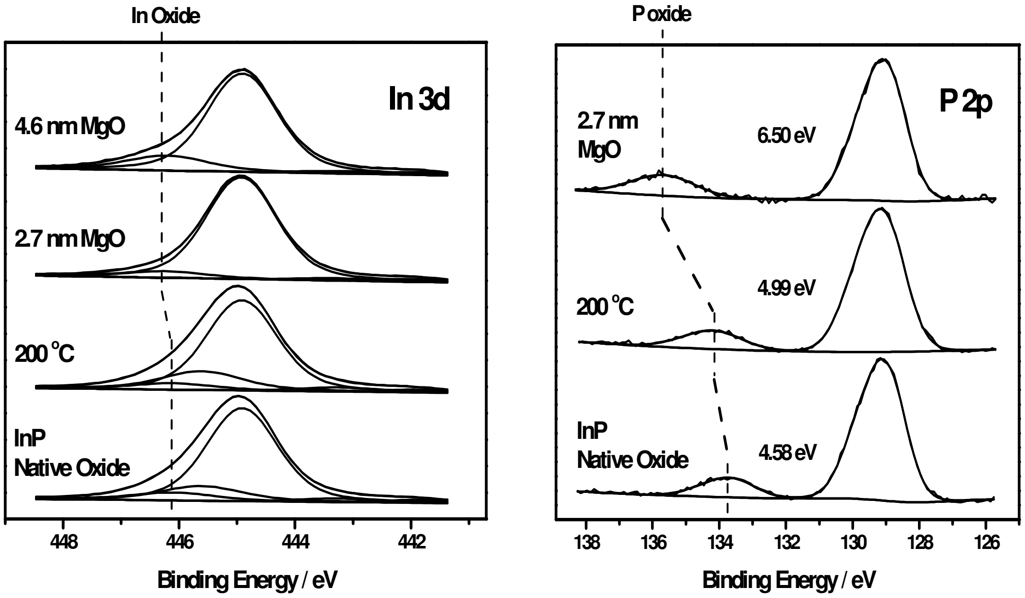

Figure 6.17 MgO deposition onto native oxide surfaces subsequent to 200 °C annealing causes a shift to HBE in the P oxide peak. The binding energy separation of the P 2p bulk and oxide peaks is indicative of a phosphorous rich oxide species.

	Total In oxide %	**InP$_x$O$_y$ %**	**In$_x$(PO$_y$) %**	**Total P oxide %**	**Stoichiometry: P %**
InP native oxide	22.8 %	14.7 %	8.1 %	13.4 %	47.0 %
200 °C	25.3 %	18.8 %	6.5 %	13.2 %	47.9 %
2.7 nm MgO	7.1 %	0 %	7.1 %	16.2 %	-
4.6 nm MgO	15.5 %	0 %	15.5 %	16.3 %	-

Table 6.9 Curve fitting data suggests the growth of an In oxide peak separated from the P bulk peak by 1.3 eV.

P 2p spectra in figure 6.17 show that the 200 °C anneal resulted in a slight shift in the P oxide peak to higher binding energy, indicative of disruption within the native oxide surface. A similar shift in the P oxide peak after thermal annealing has previously been observed by Sun *et al.* [22] and attributed to a reduction in indium contribution within the oxide, similar to that seen in figure 6.2. The effect of MgO deposition after 200 °C annealing can be seen from the P 2p spectrum in figure 6.17, with a further shift in the P oxide peak to higher binding energy being detected. The separation between the P oxide and InP bulk peak is now 6.50 eV, a value larger than anything quoted by Hollinger *et al.* [40] for an InP composite oxide species. This separation is indicative of the species P_2O_4 [40], suggesting that the P oxide present on the surface is no longer in the form of a composite InP oxide and can now be more accurately described as a phosphorous rich poly phosphate species. As no changes in the P 2p spectrum are observed at MgO coverages greater than 2.7 nm, spectra from subsequent depositions are not included. Changes in the chemical composition of the In oxide species after MgO deposition can also be seen. The spectra show the growth of an oxide state separated from the InP bulk peak by 1.3 eV, similar to that seen after MgO deposition onto wet chemically and H* cleaned surfaces. The changes in surface chemistry resulting from MgO deposition on the annealed surface are considerably greater than that seen after MgO deposition on the unannealed native oxide surface (figure 6.2). This suggests that the disruption caused by low temperature thermal annealing greatly reduces the chemical stability of the surface. The effect of 300 °C annealing of the native oxide covered InP surface and subsequent MgO deposition is shown in figure 6.18.

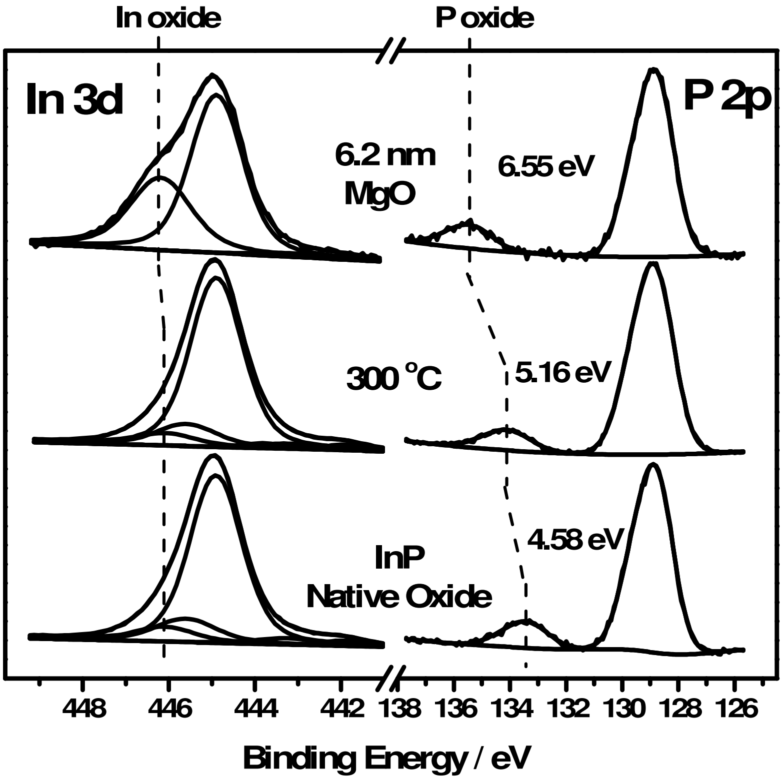

Figure 6.18 P 2p spectra taken after 300 °C annealing and subsequent MgO deposition show a shift to HBE in the P oxide peak, indicative of segregation in the oxide layer.

	Total In oxide %	**InP_xO_y %**	**$In_x(PO_y)$ %**	**Total P oxide %**	**Stoichiometry: P %**
InP native oxide	21.8 %	13.4 %	8.4 %	14.1 %	47.1 %
300 °C	19.6 %	12.5 %	7.1 %	10.9 %	47.7 %
MgO dep	35.9 %	0 %	35.9 %	12.6 %	-

Table 6.10 Curve fitting data suggest 300 °C annealing had little effect on surface stoichiometry but did result in considerable In oxide growth upon deposition of MgO

Further evidence that thermal annealing reduces In contribution to the native oxide composition can be seen in figure 6.18, with a phosphorous oxide separation of 5.16 eV being observed after 300 °C annealing. In agreement with H* cleaning studies at this temperature only slight changes in surface stoichiometry are detected. It should also be noted that there is no significant evidence for the removal of surface oxide at this temperature, which indicates that the oxide removal seen after 300 °C H* cleaning is not simply due to thermal desorption.

The effect of 300 °C annealing on the chemical stability of the surface is again shown using MgO deposition, with the P oxide peak now exhibiting a BE separation of 6.55 eV after deposition, similar to that seen following the 200 °C anneal in figure 6.17. It should also be noted that the integrated area of the P oxide peak remains largely unchanged by the deposition of MgO, suggesting that the while the chemical environment in which the P oxide exists has been changed there is little change in the number of oxygen atoms bonded to phosphorous. Considerable differences can be seen in the scale of interfacial In oxide growth after 300 °C to that seen after 200 °C annealing. It has been shown that similar rates of indium oxide growth, seen after H* cleaning at 300 °C, can be been linked to the presence of island features on the InP surface. Therefore, the topography of InP native oxide surfaces annealed to 300 °C was analysed by AFM and the resulting images are shown in figure 6.19.

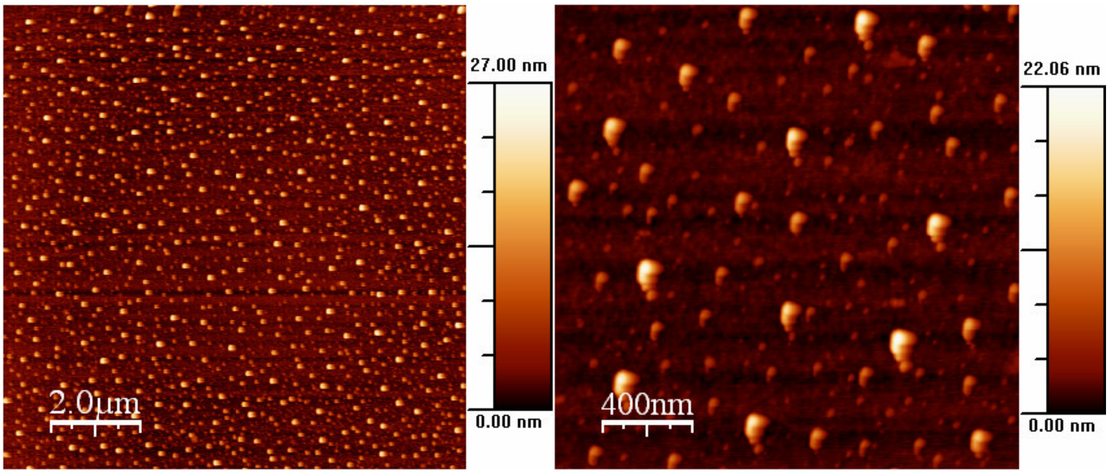

Figure 6.19 10 µm × 10 µm and 2 µm × 2 µm AFM images taken from InP native oxide surface after annealing to 300 °C shows evidence for considerable surface roughening and the presence of island structures evenly distributed across the surface.

	RMS roughness	**Average Height**	**Max Height**
Native Oxide Surface	0.2 nm	1.1 nm	1.8 nm
300 °C	1.9 nm	3.0 nm	23.6 nm

Table 6.11 AFM roughness data taken after 300 °C annealing of InP native oxide surfaces is similar to that seen after H* cleaning at the same temperature.

The 10 µm × 10µm and 2 µm × 2 µm AFM images show evidence for the presence of island structures almost identical to those observed after H* cleaning at 300 °C. The presence of these islands features, along with the interfacial oxide growth seen after MgO deposition, may suggest that the effects of H* cleaning (fig 6.14, 6.15) are primarily due to the temperature at which the cleaning was performed and not exclusively due to exposure to atomic hydrogen.

In summary, the annealing studies performed at 200 °C and 300 °C show evidence for increasing disruption within the native oxide surface leading to increased interfacial indium oxide growth upon MgO deposition. AFM images of the surface after 300 °C annealing show evidence for the presence of island features which may be attributed to metallic In clusters, similar to that seen by Reisz *et al.* [53,54], which form due to the desorption of surface phosphorous.

While the XPS stoichiometry calculations in table 6.10 do not necessarily support the formation of metallic In clusters after 300 °C annealing, Massies *et al.* [55] have suggested that the desorption of P at this temperature is counteracted by the out diffusion of P from the InP subsurface, leading to the simultaneous accumulation of surface P along with the growth of In clusters. These results suggest that the initial stages of P desorption and In cluster formation occur at temperatures as low as 300 °C, however, the process may be seen more clearly in the spectra in figure 6.20 following a 500 °C anneal and subsequent MgO deposition.

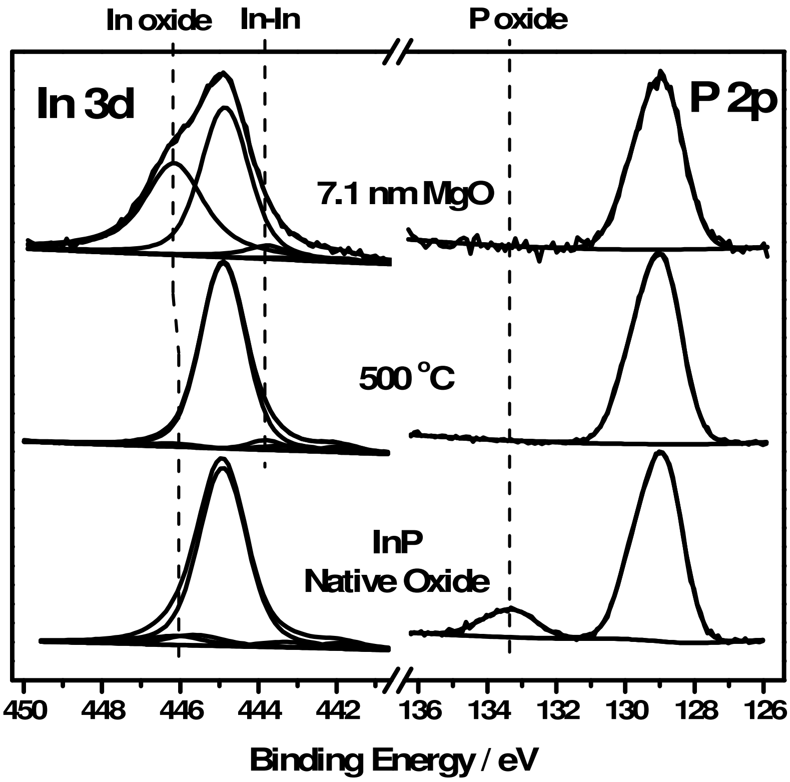

Figure 6.20 XPS core level spectra suggest the desorption of surface oxide at 500 °C, while subsequent MgO deposition results in preferential In oxide growth similar to that seen at 300 °C.

XPS core level spectra suggest that annealing to 500 °C has resulted in a considerable desorption of the InP surface oxide, which is in agreement with the work of Olivier *et al.* [25]. This reduction can also be seen in O 1s spectra taken from the surface before and after annealing shown in figure 6.21, and in the relevant surface stoichiometry data in Table 6.12.

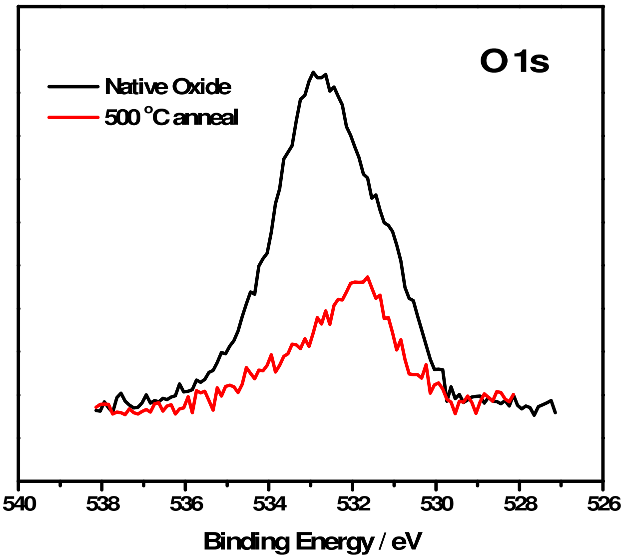

Figure 6.21 O 1s spectra offer further evidence for the desorption of surface oxygen at 500 °C.

	Total In oxide %	**InP_xO_y %**	**$In_x(PO_y)$ %**	**Total P oxide %**	**Stoichiometry P %**
InP native oxide	11.8 %	6.6 %	5.2 %	13.4 %	47.0 %
500 °C	2.0 %	0 %	2.0 %	0 %	41 %
MgO dep1	20.7 %	4.0 %	16.7 %	0 %	-
MgO dep2	41.8 %	0 %	41.8 %	0 %	-

Table 6.12 Stoichiometry data taken from the native oxide surface after 500 °C suggests considerable desorption of surface P.

Along with the loss of surface oxygen there is also evidence for a marked change in surface stoichiometry due to phosphorous desorption. Spectra taken after MgO deposition on the annealed surface (figure 6.20) once again show the continued growth of In oxide as a function of MgO deposition, similar to that seen on the 300 °C annealed sample.

The effect of 500 °C on surface roughness is shown by the AFM image in figure 6.22.

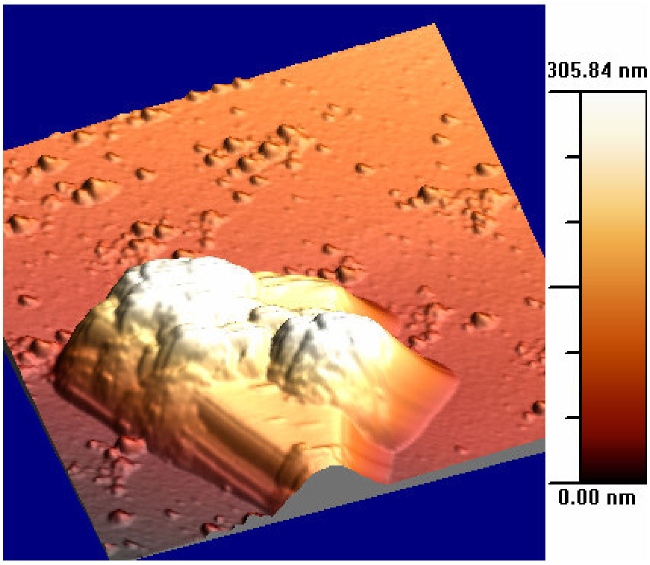

Figure 6.22 A 5 µm × 5 µm AFM image showing evidence for considerable island growth and surface disruption after 500 °C annealing. Due to their size, the island structures seen in AFM image are more easily seen using a 3 dimensional representation of the image.

	RMS roughness	**Average Height**	**Max Height**
Native Oxide Surface	0.2 nm	1.1 nm	1.8 nm
300 °C	1.9 nm	3.0 nm	23.6 nm
500 °C	62.1 nm	98.6 nm	311.3 nm

Table 6.13 AFM roughness data suggest the level of surface roughening caused by 500 °C annealing.

The 5 µm × 5 µm AFM image in figure 6.22 shows evidenced for considerably increased island growth, with the largest of these islands having an average height greater than 200 nm and average width of 2 µm. The large change in surface stoichiometry observed from the XPS studies for the 500 °C annealed sample is consistent with the surface being indium rich and the formation of "In puddles" as previously reported [53,54], which appear as a result of large scale desorption of P from the surface. The desorption of P from InP native oxide surfaces at temperatures below 500 °C is conclusively shown using temperature programmed desorption data in figure 6.23, a similar experiment to that performed by Bayliss *et al.* [31].

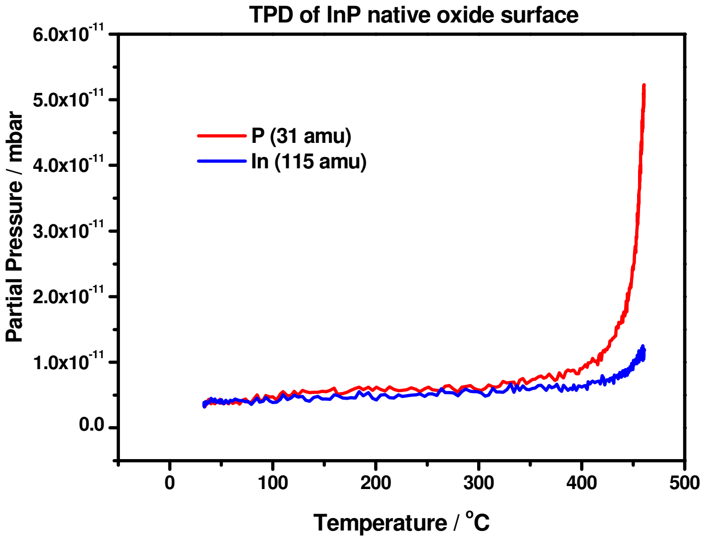

Figure 6.23 TPD spectra taken from an InP native oxide surface suggests the accelerated thermal desorption of P at temperatures above 460 °C.

TPD spectra show evidence for the desorption of P from the surface at approximately 460 °C, as such the island structures seen in figure 6.22 and stoichiometry changes seen in table 6.13 can be strongly linked to the desorption of P from the InP native oxide surface. It should be noted that annealing studies of InP native oxide surfaces after MgO deposition (not shown) show no evidence for stoichiometry change at 500 °C, suggesting that the MgO overlayer acts as a barrier to P desorption increasing the thermal stability of the surface. This result is in agreement with previous results seen for Sb capped InP surfaces [56] and is of crucial importance due to the requirement for high temperature thermal processing in transistor devices.

6.4.3 Conclusions

Based on the results of this study it is suggested that thermal annealing of InP native oxide surfaces results in the formation of indium clusters at temperatures as low as 300°C. While numerous studies [53,54] have reported the formation of island features due to thermal desorption of P from InP at temperatures above 480 °C, the creation of islands at 300 °C suggests that thermal disruption is initiated at much lower temperatures.

Further studies within the literature have also reported the desorption of surface atoms at 300 °C, and suggest that this acts as a precursor for the severe phosphorous loss seen at higher temperatures [31,57]. It is also suggested that the desorption of P at low temperature is initially counteracted by the out diffusion of P from the InP subsurface [55,58], leading to both partial P accumulation and In cluster growth at the same time [55]. This is in agreement with the XPS stoichiometry calculations (table 6.10) and AFM images (figure 6.19) taken after 300 °C annealing, suggesting that surface roughening at this temperature is due to thermal desorption of surface P and subsequent In cluster growth.

Contradictions exist between the results of this study and those within the literature, relating to the effectiveness of H* cleaning and the thermal stability of InP. In this study room temperature H* cleaning did not show evidence for oxygen removal from the InP native oxide surface, necessitating the use of substrate temperatures greater than 300 °C. However, Wolan *et al.* [47] have suggested that H* cleaning can be achieved at room temperature. While this result could not be reproduced in this study, further investigation into experimental parameters such as the use of ion bombardment cleaning prior to atomic hydrogen exposure may have yielded improved results. Also, Bruno *et al.* [50,59] have reported that a high energy remote hydrogen plasma source can achieve effective H* cleaning at 230 °C, without damaging the InP surface. As such no definitive conclusions can be made in relation to the viability of low temperature H* cleaning on InP surfaces. In contrast to this it can be stated that the removal of surface oxygen can be readily achieved using H* cleaning at temperatures greater than 300 °C. However, it has been shown that the thermal instability of InP native oxide surfaces makes it extremely difficult to prevent P desorption and In cluster growth at this temperature.

The surface disruption seen in figures 6.14 and 6.15 is in contrast to published results which have used electron diffraction techniques to study the affects of high temperature H* cleaning, and report well ordered and P stabilized surfaces [32,48,60]. However, analysis of related studies within the literature suggests that these techniques may have been unable to detect the initial stages of surface disruption. In the work of Elamrawi *et al.* [60], no evidence for island formation was identified at temperatures below 530 °C. However, numerous AFM studies [53,54] as well as the results in this study show evidence for major disruption to the InP surface at this temperature. Also, Stietz *et al.* [49] have measured 1 × 1 LEED patterns from InP surfaces containing In clusters up to 0.2 μm in width. As such, it can be suggested that AFM may resolve the initial stages of surface disruption more effectively than diffraction techniques such as RHEED.

6.5 InP interface modification using Si interlayers.

Results obtained thus far suggest that while methods such as wet chemical etching and atomic hydrogen cleaning are effective in the removal of InP native oxide, the chemical instability of the cleaned surface results in varying degrees of interfacial oxide growth upon metal oxide deposition. More favourable interfacial characteristics may therefore be achieved by modifying the chemical nature of the oxide instead of removing it. Previous studies have shown that the deposition of thin silicon layers onto III-V semiconductor surfaces, prior to dielectric deposition, can improve electrical characteristics [36]. This improvement has been attributed to the Si layer passivating surface states, and reducing the interface state density by providing a good bonding match to both the insulator and the semiconductor [54]. The work of Takahashi *et al.* [30] has suggested that strain induced by the formation of ultra thin epitaxial Si layers on III-V surfaces results in a reduction in the Si bandgap. Theoretical models have also suggested that the conduction and valence band states of the so called Si interface control layer (ICL) behave as electrically active defect states within the InP energy gap, pinning the Fermi level of the device [61,62]. However, given that these results are based on the formation of epitaxial Si layers, they may not be directly applicable to amorphous Si films. Also, recent studies by Chen *et al.* [37] and Ok *et al.* [38] have shown that the deposition of an amorphous Si control layer on InP prior to HfO_2 deposition can improve electrical results. While the electrical benefits of Si ICL have been studied in some detail, the chemical interactions which occur within the InP/Si ICL/dielectric region are less well known. As such the interfacial chemistry of amorphous Si ICL, deposited onto InP using electron beam evaporation may be of interest. Also, given that the nitridation of the Si ICL on InP has been reported to dramatically reduce the effects of Fermi level pinning [45,63,64], converting Si layers to Mg silicate will also be investigated as an alternative method of interface modification.

6.5.1 Si interfacial control layers on InP native oxide surface

Experiments aimed at investigating the interface chemistry between thin silicon layers and the InP native oxide surface were therefore undertaken. Subsequent MgO deposition on these surfaces allowed interface formation to be compared with the previous studies in this chapter. In order to ensure that the Si being deposited from the electron beam evaporator was in the form of unoxidised Si, a thick (> 10 nm) Si film was deposited on a wet chemically etched InP substrate. The Si 2p spectrum taken from this thick Si film, shown in figure 6.24, confirms that there is very little Si oxide present within the film, with only a slight contribution from the Si $^{1+}$ oxidation state. A thin Si layer was subsequently deposited on an InP native oxide surface, at an elevated substrate temperature of 200 °C. The thickness of the silicon control layer was ~ 1 nm as determined using XPS thickness calculations, which is in agreement with the optimum thickness of 1.5 nm suggested by Oktyabrsky *et al.* [65]. Silicon layers were initially deposited at a range of temperatures between room temperature (RT) and 200 °C, with the best results in terms of oxygen transfer from the substrate to the Si layer being achieved at 200 °C.

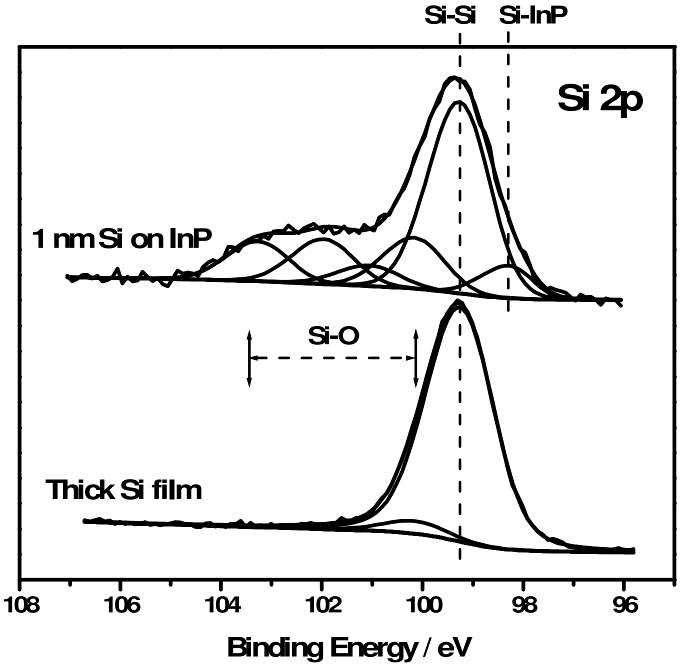

Figure 6.24 Si 2p core level spectra taken after Si control layer deposition on InP native oxide surfaces show the transfer of O from the substrate. A peak at the LBE side of the Si-Si peak is attributed to Si-InP bonds.

Evidence for the transfer of oxygen from the InP substrate to the Si interlayer can be seen in the Si 2p spectrum taken after Si deposition which shows considerable evidence of oxidation, with the Si-Si peak accounting for 51 % of the total Si 2p signal. The curve fitted components on the HBE side of the Si 2p peak reflect the oxidation states observed within the SiO_2/Si layer. They are equally spaced at 0.9 eV apart [66] and are presented more as a guide to resolving the peak profile rather than a definitive analysis of chemical composition. Previous studies involving the deposition of a Si ICL onto GaAs surfaces are in agreement with this result and show similar levels of oxidation within the control layer [67,68]. Given that angular resolved Si 2p spectra (not shown) are identical to those taken at normal emission, it is suggested that O atoms taken from the InP surface are uniformly distributed within the Si layer. The Si 2p spectrum also shows evidence for a peak at 0.9 eV LBE from the Si-Si peak, which has been attributed to the presence of Si-InP bonds. While there is clear evidence for the presence of "Si-substrate" bonding on the LBE side of the Si-Si peak it should be noted that a similar peak may also exist on the HBE side, in agreement with previous results seen for Si ICL on GaAs [67,69,70]. However, given the abundance of SiO_x bonds it is difficult to conclusively identify Si-substrate bonding on the HBE side of the Si-Si peak.

The effect of Si deposition on the native oxide covered InP surface can be seen from the In 3d and P 2p core level spectra shown in figure 6.25, which show that the deposition of Si has resulted in a considerable reduction in the presence of both the In and P oxide species. The P oxide peak also exhibits a shift to HBE of approximately 1.82 eV, seen previously in this chapter to indicate a reduction in In contribution to the oxide. The deposition of Si has also resulted in the emergence of a peak on the LBE side of both the P 2p and In 3d bulk peaks attributed to the presence of P-Si and In-Si bonds respectively, in agreement with observations on the Si 2p spectrum. The presence of Ga-Si and As-Si bonds has previously been reported by Ivanco *et al.* [67] after deposition of a Si passivation layer onto the GaAs surface, and it is suggested in their analysis that replacing Ga-O bonds with Ga-Si bonds is key to unpinning the Fermi level.

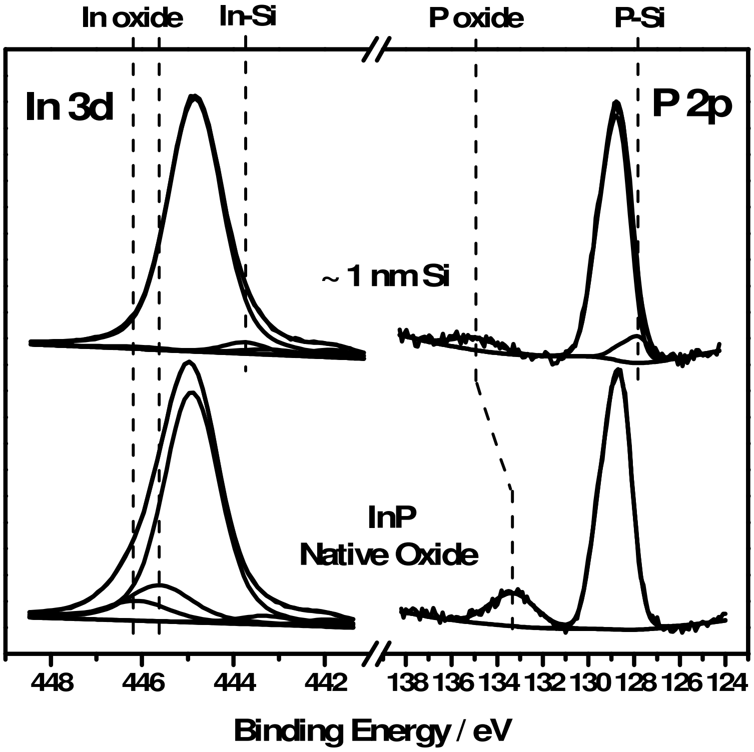

Figure 6.25 In 3d and P 2p spectra both indicate the transfer of O from the substrate to the Si control layer, and offer further evidence for the presence of S-P and Si-In bonds.

MgO was subsequently deposited onto the surface in order to determine the chemical stability of the Si passivation layer, and compare it to that seen after wet chemical etching and H cracking of InP surfaces. The spectra in figure 6.26 show that MgO deposition does not result in the growth of interfacial InP oxide, suggesting that the ~ 1 nm Si layer is an effective method of InP surface passivation.

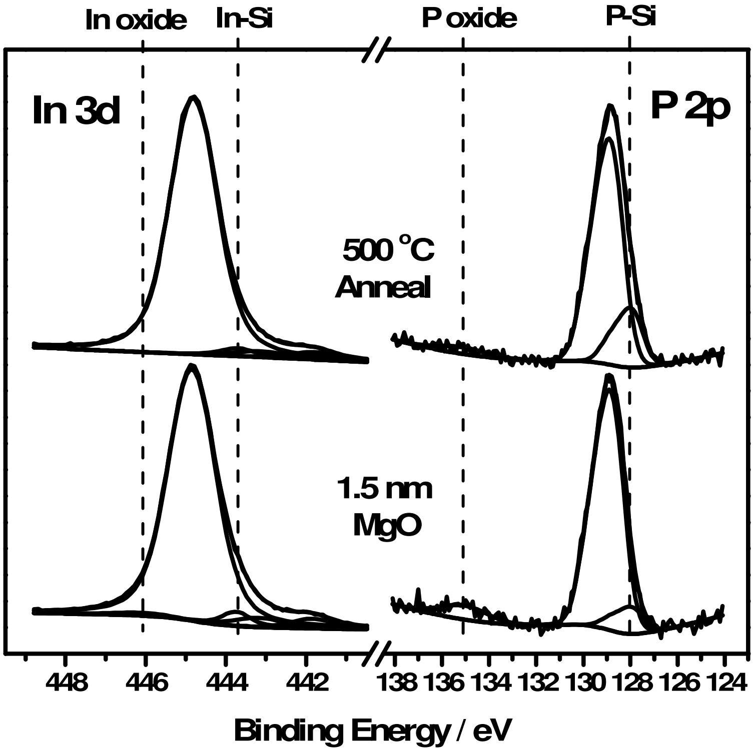

Figure 6.26 XPS spectra suggest the presence of a Si ICL layer prevented the growth of interfacial InP oxide upon MgO deposition and subsequent 500 °C annealing.

The chemical stability of III-V substrates as a result of Si ICL deposition has previously been reported by Hinkle *et al.* [71,72] using the deposition of Al_2O_3 dielectric layers and Hasegawa *et al.* [62] using O exposure. Given that an elevated surface temperature of 200 °C was used during Si deposition, it should be noted that the absence of interfacial InP oxide growth is in contrast to that seen after MgO deposition onto InP surfaces after 200 °C annealing (figure 6.17).

The effect of MgO deposition on the Si interlayer can be seen in the Si 2p spectra in figure 6.27. The spectra show that MgO deposition results in further oxidation of the Si layer, with growth in each of the 4 oxidation states and a corresponding reduction in the integrated area of the Si-Si peak. The presented curve fit is consistent with the growth of an additional peak separated from the Si-Si peak by 3.25 eV, which is indicative of the formation of Mg silicate.

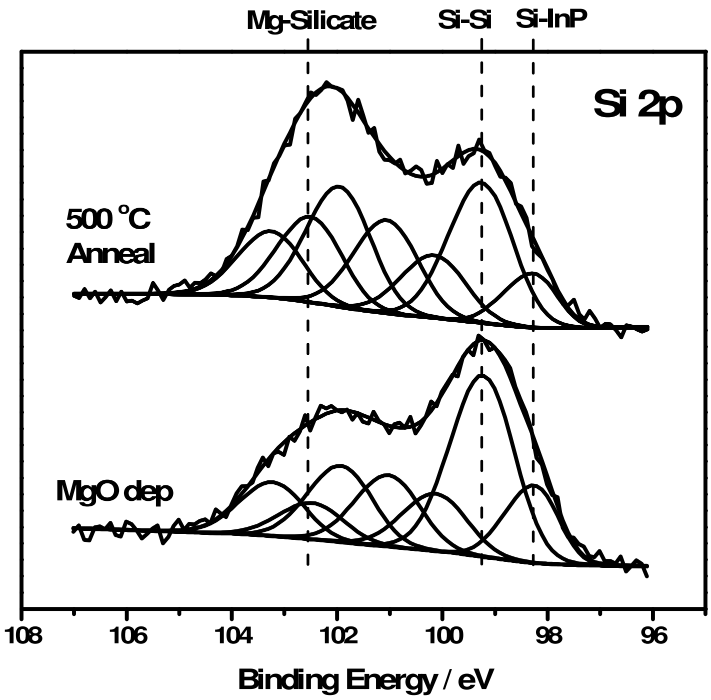

Figure 6.27 Si 2p core level spectra show the continued oxidation of the Si CL layer due to MgO deposition and 500 °C annealing. Curve fitting of the spectra also indicate the presence of Mg silicate within the film.

In a similar study performed by Ok *et al.* [38] a Si ICL was deposited onto InP, followed by subsequent deposition of Al_2O_3. In their study the presence of SiO_2 within the Si ICL was reported, however the exact nature of this interfacial oxide may be difficult to determine based on the TEM analysis used. In this study the nature of the interfacial oxide seen after MgO deposition has been further investigated using XPS characterisation, and it can be clearly stated that the oxide region in confined to the Si ICL and does not result in oxidation of the InP substrate.

In order to determine the thermal stability of the Si interlayer the MgO covered sample was annealed in UHV to 500 °C. The P 2p and In 3d spectra (figure 6.26) each show further reduction of the interfacial oxide, suggesting the Si interlayer is an effective barrier to InP interfacial oxide growth after both high-*k* deposition and high temperature annealing. The Si 2p spectrum (figure 6.27) taken after the 500 °C anneal shows further oxidation of the Si interlayer, evidenced by a reduction in the Si-Si peak from 51 % to 23 % of the total Si 2p signal. There is also considerable growth of the Mg silicate peak, making it larger than the Si $^{4+}$ oxidation state. It should also be noted that annealing to 500 °C results in considerable growth in the Si-P component of the P 2p peak, which may be attributed to the diffusion of P atoms into the Si ICL at high temperature. This result is in agreement with the work of Oktyabrsky *et al.* [65] who report the thermal diffusion of As atoms into Si ICL deposited onto GaAs substrates.

While the results of this study indicate that the deposition of a Si interlayer onto InP native oxide surfaces can be used to remove both the P and In oxide species, the formation of silicon oxide may still be detrimental to the electrical characteristics of any possible InP based transistor devices [5]. Modifying the Si oxide layer by converting it to magnesium silicate may improve the electrical characteristics of the deposited Si layer by increasing the dielectric constant and thermal stability of the layer. Also, Oktyabrsky *et al.* [65] have stated that the presence of unoxidised Si at the Si/GaAs interface is required in order to prevent Fermi level pinning. Therefore, modifying the interface in an attempt to inhibit oxidation within the Si control layers may also be of benefit.

6.5.2 InP interface Modification using Mg silicate interlayers.

It is suggested that the low temperature Mg silicate growth mechanism, outlined in Chapter 5, may make it suitable for modifying the interfacial properties of III-V substrates. In order to determine if a partially oxidised Si layer can be converted into Mg silicate, an ultra thin (~ 1 nm) Si layer was deposited on an InP native oxide surface using the procedure outlined in section 6.5.1. Metal Mg was subsequently deposited and the surface analysed using XPS. The Si 2p core level spectrum taken after Si deposition, shown in figure 6.28, has a similar profile to that observed in the previous experiment with evidence of significant oxidation and Si-InP bond formation on the LBE side of the unoxidised peak.

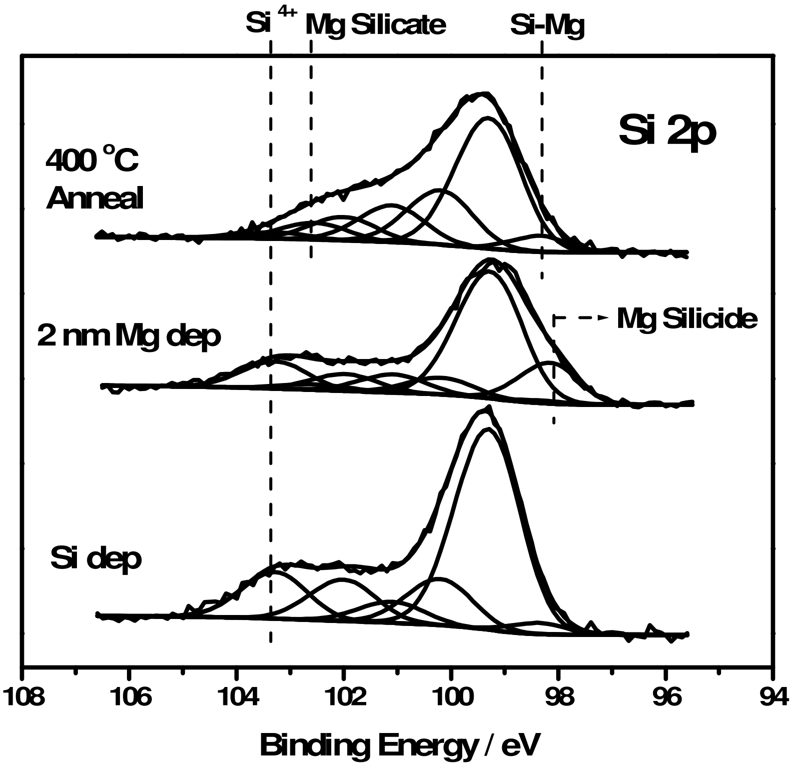

Figure 6.28 Si 2p spectra show evidence for the growth of Mg silicide as a result of Mg deposition onto the Si ICL on InP native oxide. Subsequent annealing to 500 °C results in Mg silicate growth, in agreement with studies on Si native oxide surfaces.

Subsequent deposition of metallic Mg results in the formation of Mg silicide within the Si interlayer, which is apparent from the appearance of a LBE component shifted by 1.1 eV from the unoxidised peak. The growth of silicide appeared to be self limiting and reached a saturation point i.e. Mg deposition beyond this point did not result in further growth of the Si 2p Mg silicide peak. Jiang *et al.* [73] have recently reported than thin amorphous Si layers on Si (100) substrates can be converted into Yb silicide, however, the high temperature required to achieve this (400 °C - 800 °C) may be detrimental to III-V substrates.

The Si 2p spectrum taken after 400 °C annealing shows the removal of the Mg silicide peak at 1.1 eV LBE, however it can be seen that a peak at 0.9 eV LBE is still present and is attributed to the Si-InP bonding observed previously. There is also evidence for the growth of an additional peak separated from the Si-Si peak by 3.25 eV and attributed to the presence of Mg silicate. The reduction in the area of the Si $^{4+}$ peak should also be noted as it suggests the conversion of oxidised Si into Mg silicate, as seen previously in the similar study on silicon native oxide surfaces in Chapter 5. The results suggest that Mg silicate has been formed within the Si interlayer, however there is still considerable contributions from the Si 1+, 2+ and 3+ oxidation states. The presence of these peaks may suggest that sub-stoichiometric Si oxide species are more difficult to convert into Mg silicate, or alternatively, the peaks may also be due to the presence of less oxygen rich silicate phases. In order to asses the chemical and thermal stability of the Mg silicate layer, and compare it to that of the unmodified Si interlayer, MgO oxide was deposited on the surface and subsequently annealed to 500 °C with the resulting Si spectra shown in figure 6.29.

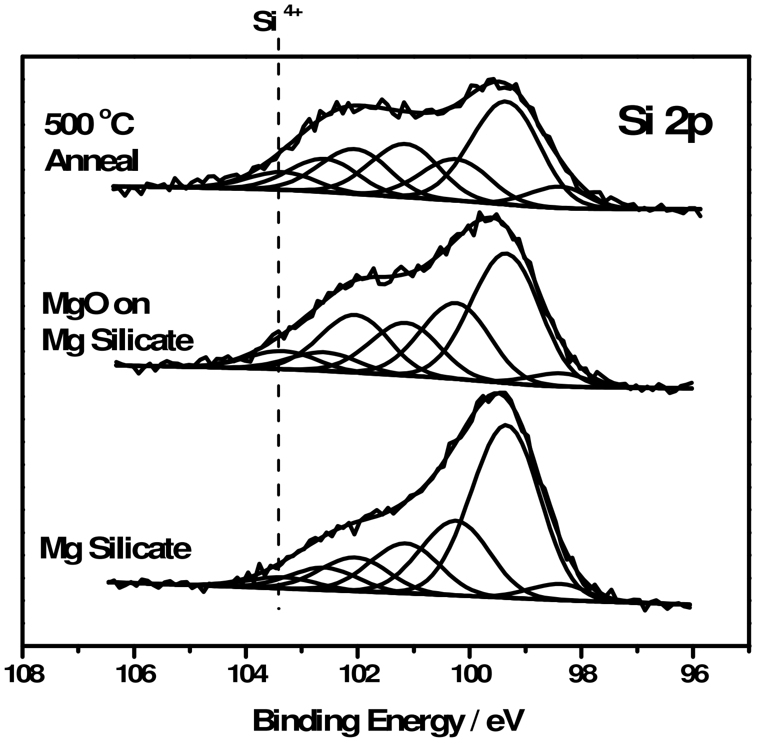

Figure 6.29 Modification of Si ICL via Mg silicate formation is seen to inhibit the growth of Si oxide after ~ 1.5 nm MgO deposition and 500 °C annealing.

The spectra indicate that the growth of Si oxide following MgO deposition was inhibited on the Mg silicate surface, in comparison to the changes observed in spectra taken from the unmodified Si interlayer (figure 6.27). The growth of the overall oxide signal and the Si $^{4+}$ signal after MgO deposition on modified and as deposited Si interlayers are listed in table 6.14.

	% Si Oxide	**% Si 4+**
Si interlayer	41.7	10
MgO on Si	54.8	11
MgO on Si: 500 °C	70	12.3
Mg silicate	50	2.8
MgO on Mg silicate	59	5.1
MgO on Mg silicate: 500 °C	60	5.7

Table 6.14 Si 2p data showing the growth of Si oxide on as deposited and modified Si control layers.

The XPS curve fitting data suggests that Mg silicate formation was successful in inhibiting the oxidation of the silicon ICL after MgO deposition, hence limiting the thickness of the low-*k* interfacial region and reducing the EOT of the device [74], in addition to preserving the unoxidised Si atoms which are key to the electrical characteristics of the interface [65].

While the formation of Mg silicate layers on InP surfaces have shown promising results, the effect of silicate formation on the underlying InP is also of key importance. In order to explore this further, the effect of metal Mg deposition on the Si ICL on InP substrate is shown in the In 3d and P 2p peaks in figure 6.30. The indium 3d spectra show that Mg deposition results in the growth of a prominent peak 1.00 eV on the LBE side of the InP bulk peak. The LBE peak has been attributed to the formation of direct In-Mg bonds, in agreement with the relative electronegativity values of Mg (1.31), In (1.78) and P (2.19). Evidence for the formation of direct P-Mg bonds can also be seen in the P 2p spectrum with the emergence of a peak on the low binding energy side separated from the substrate peak by 0.72 eV. The formation of direct In-Mg and P-Si bonds is analogous to the formation of Mg silicide during the Mg silicate growth studies presented in Chapter 5. However, the thermal stability of these bonds may be greater than that of Mg silicide and the presence of such metallic bonds may be detrimental to the electrical characteristics of any possible transistor devices [74].

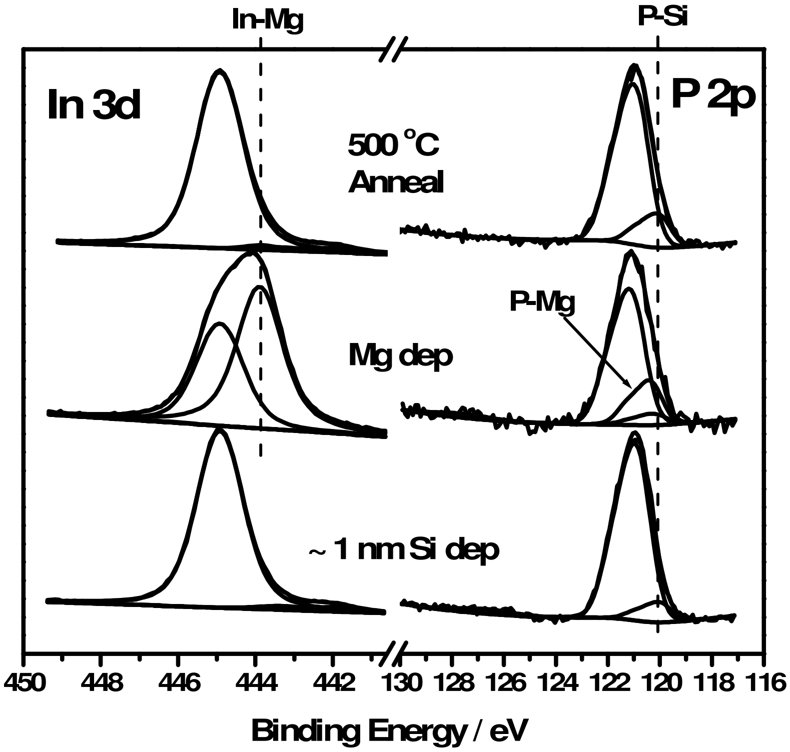

Figure 6.30 In 3d and P 2p spectra, relating to the Si 2p spectra in figures 6.28 & 6.29, suggest the formation of direct Mg-In and Mg-P bonds as a function of Mg deposition onto the ~ 1 nm silicon overlayer. XPS data suggests these bonds are successfully removed from the surface at 500 °C.

Although it has been shown that annealing to 400 °C is sufficient to create Mg silicate within the Si overlayer, P 2p and In 3d spectra taken after this anneal still show the presence of Mg-InP bonds. In an attempt to remove these bonds the sample was annealed to higher temperature, and the effect of 500 °C annealing on the InP substrate can be seen in fig 6.30. All evidence of In-Mg bonds has been removed from the In 3d spectra, returning it to a condition identical to that seen before Mg deposition. The P 2p spectra also show a considerable reduction in the LBE features, consistent with the removal of P-Mg bonds and a slight increase in P-Si bonds, similar to that seen in fig 6.26. While the spectra suggest that Mg-InP bonds are removed at 500 °C, this temperature is considerably higher than that required to remove Mg silicide. It should also be noted that while Mg silicate formation at 400 °C had no effect on the InP stoichiometry, annealing to 500 °C resulted in an increase in surface P signal changing the stoichiometry of the surface from ~ 50 % to ~ 53 % P. This may indicate the diffusion of P from the InP surface into the Mg silicate overlayer, as evidenced by the increased P-Si peak in the P 2p spectra. While it has been suggested that P deficiency at the surface of capped InP layers can be compensated by P out diffusion from the bulk [56], the disruption of surface stoichiometry may still be detrimental to the electrical characteristics of the InP. Therefore, even though the results suggest that Mg silicate can be formed at temperatures low enough to prevent disruption of the InP surface, the removal of Mg-InP bonds at 500 °C annealing appears to result in P diffusion into the silicate layer.

The formation of Mg-InP bonds during silicate formation is comparable to the formation of P-N bonds during prolonged nitridation of Si ICL which has been linked to an increase in interfacial state density [30]. As such, further research is required in order to prevent the initial formation of Mg-InP bonds. The formation of these In-Mg bonds is in direct contrast to MgO deposition on Si ICL and may be explained by the diffusion of Mg through the Si interlayer or by discontinuity in the Si film. To further investigate the morphology of the film atomic force microscopy was performed on the surface of a Si control-layer deposited onto InP native oxide at a substrate temperature of 200 °C.

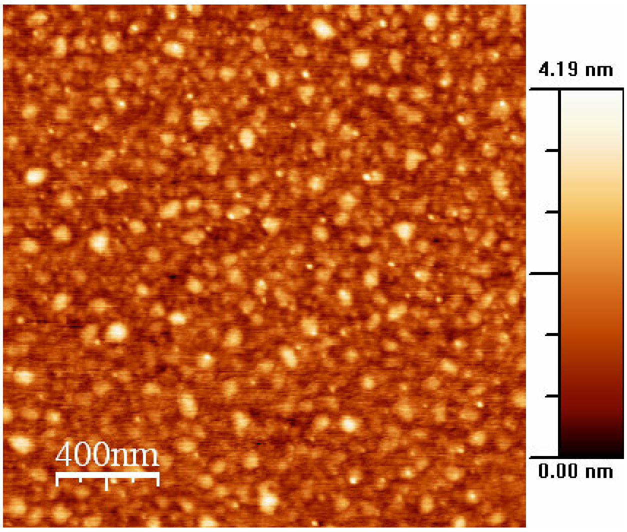

Figure 6.31 2 μm × 2 μm AFM images show no evidence for discontinuity in Si control layers on InP native oxide, suggesting that Mg-InP bonds are caused by Mg diffusion through the Si film.

Surface roughness data taken from multiple sites across the surface provide an RMS roughness of 0.5 nm, suggesting the Si layer has formed a flat continuous film upon the InP surface. While there is evidence of island features with a maximum height of approximately 4 nm such features are infrequent, with islands greater than 2 nm in height accounting for an average of 8 % of the surface and islands of greater than 3 nm accounting for less than 1 %. As such, AFM measurements offer no direct evidence that discontinuity in the Si film is the cause of Mg-InP bond formation, suggesting that Mg diffusion through the Si film may occur during Mg deposition. If this is the case diffusion may only be prevented by the deposition of thicker Si films.

6.5.3 Conclusions

Deposition of ~ 1 nm silicon interface control layers (Si ICL) onto InP native oxide results in the transfer of oxygen from the substrate to the Si layer and the formation of Si-InP bonds. Subsequent MgO deposition and 500 °C annealing results in oxidation of the Si ICL but shows no evidence for the growth of In or P oxide species. The silicon interface control layers were then modified by depositing metallic Mg and annealing to form Mg silicate. Silicate formation was shown to inhibit oxidation in the control layer, preserving Si-Si bonds within the layer. However, silicate formation resulted in the diffusion of Mg through the ultra thin silicon layer. While the resulting Mg-InP bonds were removed using high temperature annealing, the temperature required to achieve this appeared to cause P diffusion into the silicate layer.

6.6 Chapter Conclusions

In this study initial electrical and chemical characterisation of MgO films deposited onto native oxide and wet chemically etched InP surfaces has been performed. The capacitance difference (ΔC) between C_{max} and C_{min} shown by both p-type and n-type devices is much smaller than expected, which has been linked to Fermi level pinning. XPS analysis suggests that while wet chemical etching techniques are effective in removing InP native oxide, subsequent MgO deposition results in significant interfacial oxide growth. Interfacial oxide is predominantly in the form of In oxide, with MgO films deposited onto sulphur passivated surfaces showing the highest level of interfacial oxide growth, which can be directly correlated with CV results.

An atomic hydrogen (H*) cleaning study of InP native oxide surfaces has also been performed. Results suggest that effective surface cleaning can be achieved at temperatures above 300 °C, with significant reductions in the presence of both surface oxide and carbon based contamination. However, MgO deposition onto surfaces prepared using H* cleaning at 300 °C show high levels of interfacial indium oxide growth, considerably larger than that seen after wet chemical etching. AFM images taken from the H* cleaned surfaces show the presence of island features with an average height of 13 nm and average width of 100 nm distributed across the surface. It is suggested that these islands lead to atomic intermixing which explains the continuous growth of In oxide as a function of MgO deposition. Studies relating to the thermal stability of InP native oxide surfaces suggest that UHV annealing to temperatures above 300 °C results in P desorption from the surface, leading to the formation of similar island structures to that seen after H* cleaning. As such it can be suggested that while H* cleaning performed at high temperature is effective in the removal of surface oxide and carbonate species, the surface degradation caused during annealing result in considerable interfacial oxide growth.

The deposition of ultra thin (~ 1 nm) silicon intefacial control layers onto InP native oxide surfaces has proved to be successful in modifying the chemical composition of the surface oxide. XPS results suggest that Si deposition at 200 °C results in the transfer of oxygen from the InP surface to the Si interlayer, creating a partially oxidised film which shows contributions from all 4 silicon oxidation states. The subsequent deposition of MgO resulted in further oxidation within the Si but showed no evidence for the reformation of In or P oxides. Having shown the effective passivation of InP surfaces using Si interlayers, metallic magnesium was subsequently deposited in an attempt to convert the Si oxide into Mg silicate. XPS results have shown that the partial formation of Mg silicate achieved after 400 °C annealing was sufficient to inhibit the growth of Si oxide growth after MgO deposition. Inhibiting Si oxide growth acts to preserve Si-Si bonds at the InP interface which are vital to improving electrical characteristics [65]. However, there is also evidence for the formation of direct Mg-InP bond as a result of Mg diffusion through the Si interlayer. Annealing to 500 °C was required to remove Mg-InP bonds, which resulted in disruption of the InP surface and evidence for P diffusion into the Si layer.

6.7 Appendix to Chapter 6

The In 3d spectral components labelled as satellite peaks in figure 4.1 are artefacts of the non-monochromated Mg Kα X-ray source which was used in this study. As stated in Chapter 3, the Mg X-ray source is dominated by the $K\alpha_{1,2}$ emission spectrum, which emits X-rays at a photon energy of 1253.6 eV. However, for non-monochromated sources the doubly ionised ($K\alpha_{3,4}$) emission line is also present at a photon energy of ~ 1263.6 eV [75]. This produces photoelectron satellite peaks which are ~ 8 % of the main peak intensity and separated from the main peak by ~ 10 eV on the lower binding energy side. Therefore, it is suggested that the satellite peaks in the In 3d $_{5/2}$ spectrum are satellite features emanating from the In 3d $_{3/2}$ peak. Given that the intensity of such satellite peaks is only 8 % of the main line they are commonly not resolved above the spectral background, except in the case of "strong" core level features such as the In 3d. Figure 6.32 shows a photoemission spectrum taken from an InP native oxide surface which encompassed both the In 3d $_{5/2}$ and In 3d $_{3/2}$ peaks.

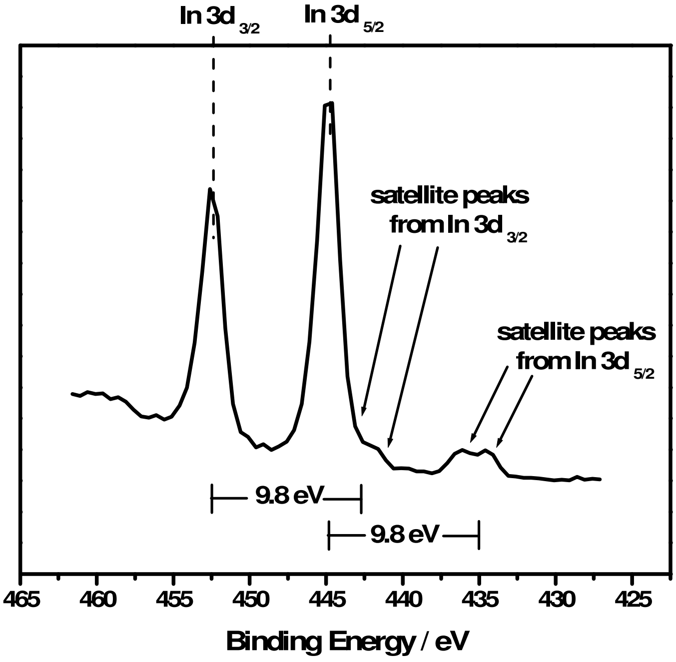

Figure 6.32 In 3d spectrum showing the correlation between the In 3d $_{3/2}$ main peak and the satellite peaks which form part of the overall In 3d $_{5/2}$ peak profile

The spectrum clearly shows the correlation between the In 3d $_{3/2}$ main peak and the satellite peaks which form part of the overall In 3d $_{5/2}$ peak profile. The presence of additional, slightly larger, satellite peaks emanating from In 3d $_{5/2}$ main feature further supports the analysis. It should be noted that the satellite features form a "double peak" shape which is in contrast to the main line (k$\alpha_{1,2}$) features from which they emanate. However, this is simply due to the spectral width of the K$\alpha_{3,4}$ doublet, which is considerably larger than the dominant K$\alpha_{1,2}$ doublet (0.7 eV). This difference is clearly illustrated in Figure 3.10, on page 98 of reference 68.

The assertion that these features are satellite peaks, and are not representative of chemical states present within the sample surface, is further evidenced by the fact that similar peaks are not present on the LBE side of the In 3d $_{3/2}$ or In 4d profiles. Therefore, the contribution of the satellite peaks was identified using curve fitting and disregarded during experimental analysis. Figure 6.33 shows an enlarged image of the curve fitted satellite peaks within the In 3d $_{5/2}$ spectrum, while the curve fitting parameters used to fit these satellite peaks are listed in table 6.15.

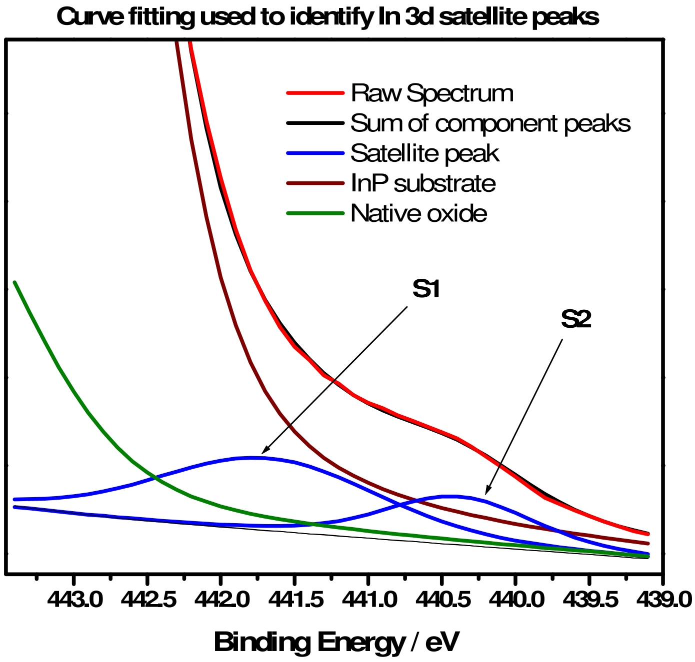

Figure 6.33 curve fitted In 3d spectrum taken from a InP native oxide surface. The LBE side of the peak profile is enlarged to more clearly show the curve fitting components which were used throughout this study to identify the satellite peaks labelled S1 and S2.

	Gaussian FWHM	**Lorenztian FWHM**	**B.E. separation from InP substrate peak**
Satellite peak 1 (S1)	1.45 eV	0.5 eV	1.7 eV
Satellite peak 1 (S2)	0.95 eV	0.5 eV	3.0 eV

Table 6.15 showing the relevant curve fitting parameters used throughout this study to fit the In 3d satellite peaks seen in figure 6.33

These parameters were used to consistently and accurately fit In 3d spectra taken from native oxide, 2-stage wet chemically etched and sulphur passivated InP surfaces, as well as spectra taken after MgO deposition onto these surfaces. However, when the parameters in table 6.15 did not provide an accurate peak fit of the measured In 3d spectrum, the addition of a further component peak was required during the curve fitting process. The additional component peaks used in this study, along with the circumstances under which they were observed, are listed as follows;

- Atomic hydrogen cleaned InP (In – In bonds, separated from the substrate peak by 1.10 eV)
- Native oxide surfaces annealed above 300 °C (In – In bonds, separated from the substrate peak by 1.10 eV)
- Silicon deposition onto InP native oxide surfaces (In - Si bonds, separated from the substrate peak by 1.08 eV)
- Mg deposition onto Si ICL covered InP surfaces (In-Mg bonds, separated from the substrate peak by 1.00 eV)

The origin of these peaks, and the curve fitting parameters used to identify them, are discussed in greater detail within the relevant sections of Chapter 6.

6.8 References

[1] J. Robertson, and B. Falabretti, J. Appl. Phys. **100** (2006) 014111

[2] M. Passlack, J.K. Abrokwah, R. Droopad, Yu Zhiyi, C Overgaard, S. In Yi, M. Hale, J. Sexton, A.C. Kummel, *Electron* Device Letters, IEEE **23**, no.9, (2003) 508-510

[3] P. van Staa, H. Rombach, R. Kassing J. Appl. Phys. **54** (1983) 4014

[4] F. J. Leonberger, P. F. Moulton, Appl. Phys. Lett., **35**, 9 (1979) 712

[5] Y. Q. Wu, Y. Xuan, T. Shen, P. D. Ye, Z. Cheng, A. Lochtefeld, Appl. Phys. Lett. **91** (2007) 022108

[6] E. O'Connor, R. D. Long, K. Cherkaoui, K. K. Thomas, F. Chalvet, I. M. Povey, M. E. Pemble, B. Brennan, G. Hughes, S. Newcomb, P.K. Hurley, Appl. Phys. Lett. **92** (2008) 022902

[7] H. Q. Zheng, K. Radahakrishnan, S. F. Yoon, G. I. Ng, Journ. Appl. Phys. **87** 11 (2000) 7988

[8] J. N. Baillargeon, A. Y, Cho, R. J. Fischer, P. J. Pearah, K. Y. Cheng, J. Vac. Sci. Technol. B 12 **2**, (1994) 1106

[9] J.E. Epler, H.P. Schweizer, J. Pedersen, J. Sochtig, Appl. Phys. Lett. 12 **66** (1995) 1472

[10] N.F. Gardner, Q.J. Hartmann, S.A. Stockman, G.E. Stillman, J.E. Baker, J.I. Malin, K.C. Hsieh, Appl. Phys. Lett. **65** 3 (1994) 359

[11] G. Zimmermann, A. Ougazzaden, A. Gloukhian, E.V.K. Rao, D. Delprat, A. Ramdane, A. Mircea, Journ. Crystal Growth **170** (1997) 645 – 649

[12] C. Mailhiot, C. B. Duke, D. J. Chadi, Phys. Rev. B **31**, (1985) 2213

[13] H. Zhao, D. Shahrjerdi, F. Zhu, M. Zhang, H.-S. Kim, I. Ok, J.H. Yum, S. Il Park, S.K. Banerjee, J.C. Lee, Appl. Phys. Lett. **92** (2008) 233508

[14] H. Zhao, D. Shahrjerdi, F. Zhu, H.-S. Kim, I. Ok, M. Zhang, J. H. Yum, S.K. Banerjee, J.C. Lee, Electrochemical and Solid-State Letters **11**, 8 (2008) H233-H235

[15] G. Hollinger, R. Blanchet, M. Gendry, C. Santinelli, R. Skheyta, P. Viktorovitch, J.. Appl. Phys. **67**, 9 (1990) 4173

[16] A. Posadas, F. J. Walker, C. H. Ahn, T. L. Goodrich, Z. Cai and K. S. Ziemer, Appl. Phys. Lett. **92** (2008) 233511

[17] J. Senzaki, K. Kurihara, N. Nomura, O. Mitsunaga, Y. Iwasaki, T. Ueno, Jpn. J. Appl. Phys. Vol. **37** (1998) 5150-5153

[18] L. Yan, C. M. Lopez, R. P. Shrestha, E. A. Irene, A. A. Suvorova and M. Saunders, Appl. Phys. Lett. **88**, (2006) 142901

[19] P. Casey, E. O'Connor, R. Long, B. Brennan, S.A. Krasnikov, D. O'Connell, P.K. Hurley, G. Hughes, Microelect. Eng. **86** (2009) 1711–1714

[20] T.W. Kim, Y.S. You, Appl. Surf. Sci. **180** (2001) 162-167

[21] W. Prusseit, S. Corskpius, F. Baudenbacher, K. Hirata, P. Berberich, H. Kinder, Appl. Phys. Lett. **61**, 15 (1992) 1841

[22] Y. Sun, Z. Liu, F. Machua, P. Pianetta, W.E. Spicer, J. Appl. Phys. **97** (2005) 124902

[23] Y. Sun, Z. Liu, F. Machua, P. Pianetta, W.E. Spicer, J. Vac. Sci. Technol. A **21**, 1 (2003) 219

[24] Y. Tao, A. Yelon, E. Sacher, Z.H. Lu, M. J. Graham, Appl. Phys. Lett. **60**, 21 (1992) 2669

[25] J. Olivier, P. Faulconnier, R. Poirier, J. Appl. Phys. **51**, 9 (1980) 4990

[26] A. Abdellaoui, M. Ghaffour, A. Ouerdane, K. Hamaida, Y. Monteil, N. Berrouachedi, Z. Lounis, M. Bouslama, Applied Surface Science **254** (2008) 4024–4028

[27] M. Petit, Y. Ould-Metidji, C. Robert, L. Bideux, B. Gruzza, V. Matolin, Appl. Surf. Sci. **212–213** (2003) 601–606

[28] S.K. Krawczyk, G. Hollinger, Appl. Phys. Lett. **45**, 8 (1984) 870

[29] A. Guivarc'h, H. L'Haridon, G. Pelous, G. Hollinger, P. Pertosa, J. Appl. Phys. **55**, 4 (1984) 1139

[30] H. Takahashi, T. Hashizume, H. Hasegawa, Jpn. J. Appl. Phys. **38** (1998) 1128-1132

[31] C.R. Bayliss, D.L. Kirk, Journ. Phys. D: Appl. Phys., Vol. **9**, (1979) 233

[32] Y.J. Chun, T. Sugaya, Y. Okada, M. Kawabe, Jpn. J. Appl. Phys. **32** (1993) L 287-L 289

[33] H.-S. Kim, I. Ok, M. Zhang, F. Zhu, S. Park, J. Yum, H. Zhao, J.C. Lee, P. Majhi, Appl. Phys. Lett. **93** (2008) 102906

[34] A.M. Sonnet, C.L. Hinkle, M.N. Jivani, R.A. Chapman, G.P. Pollack, R.M. Wallace, E.M. Vogel, Appl. Phys. Lett. **93** (2008) 122109

[35] J. Ivanco, T. Kubota, H. Kobayashi, J. Appl. Phys. **97** (2005) 073712

[36] H. Hasegawa, Thin Solid Films **367** (2000) 58-67

[37] Y.-T. Chen, H. Zhao, J.H. Yum, Y. Wang, and J.C. Lee, Appl. Phys. Lett. **94** (2009) 213505

[38] I. Ok, H. Kim, M. Zhang, F. Zhu, S. Park, J. Yum, H. Zhao, D. Garcia, P. Majhi, N. Goel, W. Tsai, C.K. Gaspe, M.B. Santos, J.C. Lee, Appl. Phys. Lett. **92** (2008) 202903

[39] J.S. Corneille, J.W. He, D.W. Goodman, Surf. Sci., **306**, (1994) 269

[40] G.Hollinger, E. Bergignat, J. Joseph, Y. Robach, J. Vac. Sci. Technol. A. **3**, 6 (1985) 2082

[41] T. Muranaka, C. Jiang, A. Ito, H. Hasegawa, Jpn. J. Appl. Phys. **40** (2001) 1874-1877

[42] Z. H. Lu, M.J. Graham, X.H. Feng, B.X. Yang, Appl. Phys. Lett. **60**, 22 (1992) 2773

[43] T. Chassé, H. Peisert, P. Streubel, R. Szargan, Surface Science **331-333** (1995) 434-440

[44] X. Cheng, D. Xu, Q.-Q. Sun, D. He, Z. Wang, Appl. Phys. Lett. **96** (2010) 022904

[45] Z. Fu, S. Kasai, H. Hasegawa, Applied Surface Science **190** (2002) 298–301

[46] T. Sugaya, M. Kawabe, Jpn. J. Appl. Phys. **30**, 3A (1991) L 402 – L 404

[47] J.T. Wolan, G.B. Hoflund, J. Vac. Sci. Technol. A **16**, 4 (1998) 2546

[48] M.A. Hafez, H.E. Elsayed-Ali, J. Appl. Phys. **91**, 3 (2002) RHEED

[49] F. Stietz, T. Allinger, V. Polyakov, J. Woll, A. Goldmann, W. Erfurth, G.J. Lapeyre, J.A. Schaefer, Applied Surface Science **104/105** (1996) 169-175

[50] G. Bruno, M. Losurdo, P. Capezzuto, V. Capozzi, T. Trovato, G. Perna, and G. F. Lorusso, Appl. Phys. Lett. **69**, 5 (1996) 685

[51] M. Ghaffour, M. Bouslama, Z. Lounis, A. Nouri, C. Jardin, Y. Monteil, H. Dumont, J. Electron Spectrosc. Relat. Phenom. **134** (2004) 81

[52] G. Chen, S.B. Visbeck, D.C. Law, R.F. Hicks, J. Appl. Phys. **91**, 11 (2002) 9362

[53] F. Riesz, L. Dobos, J. Karanyi, J. Vac. Sci. Technol. B **16**, 5 (1998) 2672

[54] F. Riesz, L. Dobos, C. Vignali, C. Pelosi, Materials Science and Engineering B **80** (2001) 54–59

[55] J. Massies, F. Lemaire-Dezaly, J. Appl. Phys. **57**, 2 (1985) 237

[56] M. Yamada, A.M. Green, A. Herrera-Gomez, T. Kendelewicz, W.E. Spicer, Jpn. J. App. Phys. **30**, 11B (1991) L 1982 – 1984

[57] F. Riesz, C. Vignali, C. Pelosi, K. Rakennus, T. Hakkarainen, J. Appl. Phys. **83**, 1 (1998) 246

[58] P. Ebert, M. Heinrich, M. Simon, K. Urban, M.G. Lagally, Phys. Rev. B **51**, 15 (1995) 9696

[59] G. Bruno, P. Capezzuto, and M. Losurdo, Phys. Rev. B **54**, 23 (1996) 175

[60] K.A. Elamrawi, M.A. Hafez, H.E. Elsayed-Ali, J. Appl. Phys. **84**, 8 (1998) 4568

[61] H. Hasegawa, M. Akazawa, K.-I. Matsuzaki, H. Ishii, H. Ohno, Jpn. J. Appl. Phys. **27**, 12 (1998) L 2265 – L 2267

[62] H. Hasegawa, M. Akazawa, H. Ishii, K.-I. Matsuzaki, J. Vac. Sci. Technol. B **7**, 4 (1989) 870

[63] Z. Fu, H. Takahashi, S. Kasai, H. Hasegawa, Jpn. J. Journ. Appl. Phys. **41** (2002) 1062 – 1066

[64] Z. Jin, K. Uchida, S. Nozaki, W. Prost, F.-J. Tegude, Applied Surface Science **252** (2006) 7664–7670

[65] S. Oktyabrsky, V. Tokranov, M. Yakimov, R. Moore, S. Koveshnikov, W. Tsai, F. Zhu, J.C. Lee, Materials Science and Engineering B **135** (2006) 272–276

[66] F. J. Himpsel, F.R. McFreely, A. Taleb-Ibrahimi, J.A. Yarmoff and G. Hollinger, Phys. Rev. B **38**, (1988) 6084

[67] J. Ivanco, T. Kubota, H. Kobayashi, J. Appl. Phys. **97** (2005) 073712

[68] I. Jiménez, F.J. Palomares, J.L. Sacedón, Phys. Rev. B **49**, 16 (1994) 117

[69] M. Akazawa, H. Hasegawa, Materials Science and Engineering B **165** (2009) 122–125

[70] H. Hasegawa, M. Akazawa, Applied Surface Science **255** (2008) 628–632,

[71] C.L. Hinkle, M. Milojevic, E.M. Vogel, R.M. Wallace, Microelectronic Engineering **86** (2009) 1544–1549

[72] C. L. Hinkle, M. Milojevic, B. Brennan, A.M. Sonnet, F.S. Aguirre-Tostado, G. J. Hughes, E.M. Vogel, R.M. Wallace, Appl. Phys. Lett. **94** (2009) 162101

[73] Y.-L. Jiang, Q. Xie, C. Detavernier, R.L. Van Meirhaeghe, G.-P. Ru, X.-P. Qu, B.-Z. Li, P.K. Chu, J. Appl. Phys. **102** (2007) 033508

[74] J. Robertson, Reports of Progress in Physics **69** (2006) 327–396

[75] D.P. Woodruff, T.A. Delchar, Modern techniques of surface science, Cambridge Solid State Science Series (1986)

Chapter 7

Conclusions and Future Work

7.1 Conclusions

In this study the use of MgO and Mg silicate as alternative gate dielectric materials on both Si and InP, has been investigated. While the main focus of this work has been the use of photoelectron spectroscopy to analyse dielectric-semiconductor interface formation, other techniques such as AFM, TPD and electrical characterisation have also been employed.

7.1.1 MgO thin films on Si

Initial electrical characterisation of MgO thin films on Si allow the dielectric constant of MgO to be calculated as 8.1, however, devices also showed evidence for high interface density and poor capacitance scaling with thickness. Investigations into the ambient stability of MgO suggest that this poor capacitance scaling is due to the rapid growth of magnesium hydroxide and carbonate species on the MgO surface, during the *ex-situ* Pd metallisation process. In order to prevent the detrimental affects of ambient exposure an amorphous Si capping layer (~100 nm) was deposited *in-situ* onto MgO/Si based devices, prior to exposure. The FUSI metallisation process, which included annealing to 500 °C for 30 seconds, was subsequently used to facilitate electrical characterisation of these MgO films. C-V characteristics taken from the FUSI devices showed a significant reduction in interface state density along with increased maximum capacitance values compared to that seen from the Pd devices. I-V characterisation of the FUSI devices showed a typical reduction in leakage current density of ~ 10 A cm^{-2} compared to those metallised using the *ex-situ* Pd process. However, FUSI devices also exhibited a significant decrease in dielectric strength, as evidenced by a reduction in the I-V breakdown voltage. This reduction has been attributed to the presence of columnar crystallite grains within the MgO, which have been clearly identified using cross sectional TEM images taken from both the 20 nm and 5 nm H-terminated FUSI devices. TEM images also show the presence of a thin (< 1 nm) amorphous interfacial region, which has been identified as magnesium silicate using high resolution synchrotron based photoemission. Photoemission studies show no evidence for SiO_2 formation upon deposition of MgO on to H-terminated or oxidised Si surfaces, while thermal annealing has also been shown to result in the preferential growth of Mg silicate. While the dielectric constant of MgO thin films (~ 10) is less than that of other high *k* metal oxide candidates, it is suggested that the favourable interfacial characteristics and thermal stability of MgO on Si may make it a viable candidate for use in gate oxide stacks along with high-*k* materials such as HfO_2 or TiO_3.

7.1.2 Growth of magnesium silicate thin films on Si

The growth of magnesium silicate thin films on silicon has been investigated as a method of modifying the interfacial properties of Si. In this study Mg silicate has been formed on a variety of substrates, including native oxide and H-terminated silicon surfaces. The mechanism by which silicon native oxide surfaces are converted into Mg silicate has been investigated using XPS. It has been shown that room temperature deposition of metallic Mg results in the formation of Mg silicide within the surface oxide layer. Subsequent annealing to 300 °C causes the complete removal of both Mg silicide and excess metallic Mg, leaving a partially oxidised Mg species on the SiO_2 surface. Further annealing to 500 °C causes the full conversion of SiO_2 to Mg silicate, as evidenced by changes in the Si 2p, Mg 2p and O 1s peak profiles. Subsequent studies have shown that the growth and desorption of Mg silicide is a vital intermediate step in silicate formation, and it is suggested that the thermal instability of Mg silicide may allow Mg silicate to be formed at lower temperature than other metal silicate species. Given the importance of Mg silicide in the silicate growth mechanism, further studies were undertaken in order to determine the factors which effect the growth and stability of Mg silicide layers on Si.

High resolution SRXPS was used to investigate the growth mode of Mg silicide on ultra-thin Si oxide surfaces. It has been shown that step-wise deposition on Mg results in higher levels of Mg silicide growth than that seen after continuous deposition, in agreement with similar studies within the literature. It is suggested that continuous deposition results in the formation of metallic Mg islands which act as a barrier to silicide growth by preventing subsequent Mg atoms from reaching the surface. It has also been shown that UHV annealing can not be used to promote the growth of Mg silicide on Si oxide surfaces, as the oxide layer acts as a barrier to the inter-diffusion of Si and Mg atoms. As such, it is suggested that the only method which can be used to control silicide growth on oxidised surfaces is the use of either step-wise or continuous Mg deposition. Controlled exposure to low levels of O_2 has been used to investigate the chemical stability of Mg silicide. It has been shown that room temperature exposure to 900 L of O_2 caused a significant decrease in the presence of Mg silicide, which is in contrast to the reported stability of other metal silicide species such as Hf silicide and Y silicide.

In addition to the modification of Si native oxide surfaces, a series of experiments were carried out in an attempt to form Mg silicate on differently prepared Si surfaces. While Mg silicate films of increased thickness can be formed on both 700 nm SiO_2 and SiON surfaces using the procedure outlined for native oxide surfaces, exposure to an O_2 partial pressure of 5×10^{-7} mbar is required to achieve silicate growth on H-terminated Si. It has been shown that this exposure prevents the desorption of excess Mg and results in the formation of stoichiometric MgO which is not fully converted to Mg silicate upon annealing to 500 °C, resulting in a mixed phase MgO/Mg silicate layer.

7.1.3 InP surface preparation methods

Methods by which the interfacial properties of indium phosphide (InP) can be modified and improved have also been investigated in this study. Initial electrical and chemical characterisation of MgO films deposited onto native oxide and wet chemically etched InP surfaces has been performed. The capacitance difference (ΔC) between C_{max} and C_{min} shown by both p-type and n-type devices is much smaller than the expected theoretical value, which has been linked to Fermi level pinning. XPS analysis suggests that while wet chemical etching techniques are effective in removing InP native oxide, subsequent MgO deposition results in significant interfacial oxide growth. The interfacial oxide is shown to be predominantly in the form of In oxide, with MgO films deposited onto sulphur passivated surfaces showing the highest level of interfacial oxide growth, a result which can be directly correlated with C-V device characteristics.

Given that devices fabricated using wet chemical etching resulted in Fermi level pinning, atomic hydrogen (H*) cleaning of InP native oxide surfaces was attempted as an alternative method of surface preparation. As room temperature H* cleaning showed no evidence for the removal of surface contaminants, H* cleaning at elevated substrate temperature was subsequently attempted. While H* cleaning at temperatures greater than 300 °C was successful in the removal of surface oxide and carbonate species, MgO deposition onto the cleaned surface was shown to result in high levels of interfacial indium oxide growth. In addition to this, AFM images taken from H* cleaned InP surfaces show evidence for the growth of island structures with an average height of 13 nm and average width of 100 nm distributed across the surface. Separate high temperature vacuum annealing studies have shown that both of these results can be directly linked to the thermal desorption of surface P from the InP native oxide surface at temperatures as low as 300 °C. As such, it can be suggested that while H* cleaning performed at high temperature is effective in the removal of surface oxide and carbonate species, the process also results in significant disruption to the InP surface.

Recent studies within the literature have shown extremely promising electrical results relating to the use of silicon interfacial control layers (ICL) on InP. However, the chemical interactions which occur within the {InP/Si/high-*k*} interfacial region are not yet fully understood. In this study it has been shown that depositing ~ 1 nm Si onto the InP native oxide surface results in the transfer of surface oxygen to the Si ICL, and the formation of Si-InP bonds. Subsequent MgO deposition was shown to result in further oxidation of the Si layer, however, XPS analysis showed no evidence for the growth of In or P oxide species after MgO deposition or subsequent 500 °C annealing. As such it can be said that the interfacial oxide region is confined to Si interfacial control layer. The interfacial chemistry of InP was further modified by the formation of Mg silicate interfacial control layers. XPS analysis suggests that Mg silicate films can be successfully formed at temperatures as low as 400 °C, following the successive deposition of Si and metallic Mg. It has also been shown that the modified silicate layers act to inhibit oxidation within the control layer, preserving the Si-Si bonds which are thought to be crucial to unpinning the Fermi level. However, there is also evidence for the formation of direct Mg-InP bond as a result of Mg diffusion through the Si interlayer. Further annealing to 500 °C was required to remove Mg-InP bonds, which resulted in disruption of the InP surface evidenced by P diffusion into the Si layer

7.2 Future Work

The primary aspects arising from this study which require further investigation are outlined as follows.

7.2.1 MgO as part of gate oxide stack

In Chapter 4 the properties of MgO which make it suitable for use in dielectric stacks have been outlined. The primary benefit of MgO is its favourable interfacial properties with Si, however, if MgO is to be used as part of a dielectric stack then the interaction between MgO and other dielectric layers must also be investigated. The increased resolution and surface sensitivity offered by SRXPS may be of benefit to investigating the interfacial chemistry of MgO and other metal oxide species such as HfO_2. It has also been shown in Chapter 4 that MgO films crystallise upon annealing, reducing the lifetime of the device. Therefore, if MgO is to be used as part of a gate dielectric stack further investigation must be carried out to determine if the thickness of the MgO layer can be reduced to a point which allows the films to remain amorphous upon high temperature annealing.

7.2.2 Electrical characterisation of Mg silicate thin films

While the low temperature conversion of silicon dioxide into magnesium silicate has shown has shown promising results as a method of modifying the surface chemistry of Si, Mg silicate films of sufficient thickness must be fabricated in order to determine their electrical characteristics. As described in Chapter 5, it is difficult to promote the growth of Mg silicide using high temperature vacuum annealing, and this limits the achievable thickness of the eventual silicate layer. However, a number of possible solutions exist which may be worthy of further investigation. The deposition of metal silicate layers from a metal silicate evaporation target has shown promising results for other species such as Hf silicate [1], Gd silicate [2], Zr silicate [3] and Ti silicate [4]. Another method of device fabrication reported by Chang et al [5] for the growth of Er silicate dielectric layers, may also be of some interest. Chang et al have deposited 45 nm metallic Er layers onto 5 nm SiO_2 films at room temperature, followed by the deposition of 25 nm W before annealing to 250 °C. The use of this 25 nm W capping layer prevents the thermal desorption of Er prior to silicate formation, and may be of particular use in the Mg silicate system in order to prevent the low temperature desorption of metallic Mg. Therefore, a possible method for the fabrication of Mg silicate devices may be the deposition of excess Mg onto thick (≥ 5 nm) SiO_2 layers, followed by the deposition of a metallic capping layer. Samples may then be annealed to 500 °C in other to achieve silicate formation, while excess metallic Mg may be subsequently removed using wet chemical etching as described by Chang et al [5]. Investigating the crystallographic structure of the silicate layers may also be of some interest, in order to determine if silicate films show a greater resistance to the formation of crystallite regions than that shown by MgO.

7.2.3 Electrical characterisation of Si ICL on InP

The main aspect arising from Chapter 6 which requires further investigation is the fabrication of MOS devices using silicon interfacial control layers prior to MgO deposition. Recent studies have shown that Si ICL are beneficial to the electrical characteristics of InP devices [6,7] and such MgO/Si based devices would allow direct comparison to the MgO devices measured in Chapter 6 which were fabricated using wet chemical etching.

7.3 References

[1] G. D. Wilk, R. M. Wallace, Appl. Phys. Lett. **74**, 19 (1999) 2854

[2] J.A. Gupta, D. Landheer, J.P. McCaffrey, G.I. Sproule, Appl. Phys. Lett. **78**, 12 (2001) 1718

[3] J. Morais, E.B.O. da Rosa, L. Miotti, R.P. Pezzi, I.J.R. Baumvol, A.L.P. Rotondaro, M.J. Bevan, L. Colombo, Appl. Phys. Lett. **78**, 17 (2001) 2446

[4] D. Brassard, M.A. El Khakani, L. Ouellet, J, Appl. Phys. **102** (2007) 034106

[5] S.-Y. Chang, M.-I. Jeong, S.V. Jagadeesh Chandra, Y.-B. Lee, H.-B. Hong, V. Rajagopal Reddy, C.-J. Choi Materials Science in Semiconductor Processing **11** (2008) 122–125

[6] Y.-T. Chen, H. Zhao, J.H. Yum, Y. Wang, and J.C. Lee, Appl. Phys. Lett. **94** (2009) 213505

[7] I. Ok, H. Kim, M. Zhang, F. Zhu, S. Park, J. Yum, H. Zhao, D. Garcia, P. Majhi, N. Goel, W. Tsai, C.K. Gaspe, M.B. Santos, J.C. Lee, Appl. Phys. Lett. **92** (2008) 202903